

UNCLASSIFIED

AD NUMBER

AD875744

LIMITATION CHANGES

TO:

Approved for public release; distribution is unlimited.

FROM:

Distribution authorized to U.S. Gov't. agencies and their contractors;  
Administrative/Operational Use; JUL 1970. Other requests shall be referred to Army Aviation Materiel Labs., Fort Eustis, VA 23604.

AUTHORITY

USAAVLABS ltr 18 Jun 1971

THIS PAGE IS UNCLASSIFIED

AD875744

20 SP  
AD

## USAALABS TECHNICAL REPORT 70-35

### A WIND-TUNNEL INVESTIGATION OF THE AERODYNAMIC ENVIRONMENT OF A FULL-SCALE HELICOPTER ROTOR IN FORWARD FLIGHT

AD No. /  
AD 875744  
COPY

By

T. H. Bowden

G. A. Shockley

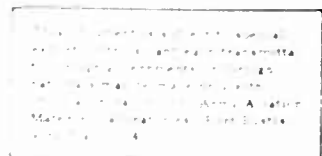
July 1970

U. S. ARMY AVIATION MATERIEL LABORATORIES  
FORT EUSTIS, VIRGINIA

CONTRACT DAAJ02-69-C-0031

BELL HELICOPTER COMPANY

FORT WORTH, TEXAS



141

Disclaimers

The findings in this report are not to be construed as an official Department of the Army position unless so designated by other authorized documents.

When Government drawings, specifications, or other data are used for any purpose other than in connection with a definitely related Government procurement operation, the United States Government thereby incurs no responsibility nor any obligation whatsoever; and the fact that the Government may have formulated, furnished, or in any way supplied the said drawings, specifications, or other data is not to be regarded by implication or otherwise as in any manner licensing the holder or any other person or corporation, or conveying any rights or permission, to manufacture, use, or sell any patented invention that may in any way be related thereto.

Disposition Instructions

Destroy this report when no longer needed. Do not return it to the originator.







DEPARTMENT OF THE ARMY  
HEADQUARTERS US ARMY AVIATION MATERIEL LABORATORIES  
FORT EUSTIS, VIRGINIA 23604

This report has been reviewed by the U.S. Army Aviation Materiel Laboratories and is considered to be technically sound. The report is published for the exchange of information and the stimulation of ideas.

Task 1F162204A13903  
Contract DAAJ02-69-C-0031  
USAAVLABS Technical Report 70-35  
July 1970

A WIND-TUNNEL INVESTIGATION OF THE AERODYNAMIC ENVIRONMENT  
OF A FULL-SCALE HELICOPTER ROTOR IN FORWARD FLIGHT

Final Report

Bell Helicopter Company Report 576-099-054

By

T. H. Bowden  
G. A. Shockey

Prepared by

Bell Helicopter Company  
Fort Worth, Texas

for

U. S. ARMY AVIATION MATERIEL LABORATORIES  
FORT EUSTIS, VIRGINIA

This document is subject to special export controls, and  
each transmittal to foreign governments or foreign nationals  
may be made only with prior approval of U.S. Army Aviation  
Materiel Laboratories, Fort Eustis, Virginia 23604.

## SUMMARY

A wind tunnel test was conducted to determine the aerodynamic environment of a full-scale helicopter rotor in forward flight. Aerodynamic data were measured at one blade radius station as the initial phase of a program designed to define the aerodynamic environment over the entire rotor disc. The rotor was instrumented to measure stagnation point location, radial flow direction, and pressure distributions. These data were then used to determine angle of attack; effective airfoil profile; section normal force, chord force, and pitching moment; and stall and unsteady aerodynamics effects. The test data were compared with two-dimensional empirical data and theory. Four cases were analyzed in some detail. They showed the variations in airfoil pressure, angle of attack, and radial flow as functions of azimuth and advance ratio. Deviations in the pressure distributions between test data and theory are believed to be due to the rotor wake and unsteady aerodynamic effects.

## FOREWORD

The investigation described herein was conducted in the NASA-Ames 40- x 80-foot wind tunnel under U.S. Army Contract DAAJ02-69-C-0031, Task 1F162204A13903. The program was sponsored by the U.S. Army Aviation Materiel Laboratories, Fort Eustis, Virginia, and was administered by Mr. Patrick Cancro. The active participation of James Biggers and Michael Falarski of the NASA-Ames Research Center in organizing and conducting the tests is gratefully acknowledged. The contributions of Robert Wohlfeld, George Massey, and John Penner of Bell Helicopter Company are appreciated by the authors. The analytical techniques used in this report and the advanced instrumentation were developed as part of the Bell Helicopter Company Independent Research and Development Program.

TABLE OF CONTENTS

	<u>Page</u>
SUMMARY . . . . .	iii
FOREWORD . . . . .	iv
LIST OF ILLUSTRATIONS . . . . .	viii
LIST OF SYMBOLS . . . . .	xiii
INTRODUCTION . . . . .	1
TEST EQUIPMENT. . . . .	2
ROTOR TEST MODULE . . . . .	2
ROTOR . . . . .	2
GLOVE . . . . .	2
SURFACE STATIC PRESSURES . . . . .	3
BOUNDARY LAYER BUTTON. . . . .	4
LEADING-EDGE HOT WIRE ANEMOMETER . . . . .	5
DATA ACQUISITION . . . . .	5
SYSTEM OPERATION . . . . .	7
DATA REDUCTION . . . . .	9
TESTS. . . . .	10
GENERAL DISCUSSION. . . . .	10
TESTING PROCEDURE . . . . .	10
TEST RESULTS AND DISCUSSION . . . . .	14
MEASURED SURFACE PRESSURES . . . . .	14
STAGNATION POINT MEASUREMENTS . . . . .	17
BOUNDARY LAYER BUTTON RESULTS . . . . .	18
DISCUSSION OF FOUR TEST CONDITIONS . . . . .	21
CONCLUSIONS. . . . .	26
LITERATURE CITED . . . . .	74
APPENDIX. . . . .	76
DISTRIBUTION . . . . .	125

## LIST OF ILLUSTRATIONS

<u>Figure</u>	<u>Page</u>
1      Gloved Section of Rotor With Hot Wire Anemometer in Leading Edge and Boundary Layer Buttons Along the Chord . . . . .	27
2      Installation of Static Pressure Transducers in Gloved Section of Rotor . . . . .	28
3      Detailed View of Boundary Layer Button . . . . .	29
4      Installation of Hot Wire Anemometer on Leading Edge, and Schematic of the Circuit. . . . . . . . . . .	30
5      Block Diagram of Data Acquisition System. . . . .	31
6      Repeatability of Test Data for Three Revolutions of the Rotor . . . . .	32
7      Repeatability of Pressure Data for the Four Test Runs . . . . .	33
8      Comparison of Absolute and Differential Pressure Distributions, Run 2, Point 3; $\mu = 0.20, M_{(1.0, 90)} = 0.30, \theta_{.75R} = 11.0^\circ,$ $\dot{\beta} \approx \ddot{\beta} \approx 0, \psi = 240^\circ, \alpha = 14.5^\circ . . . . .$	34
9      Comparison of Absolute and Differential Pressure Distributions, Run 2, Point 15; $\mu = 0.50, M_{(1.0, 90)} = 0.37, \theta_{.75R} = 7.2^\circ,$ $\dot{\beta} \approx \ddot{\beta} \approx 0, \psi = 210^\circ, \alpha = 8.3^\circ . . . . .$	35
10     Influence of Vortex on Freestream Velocity Vector . . . . .	36
11     Section Angle of Attack Versus Azimuth; $\mu = 0.20, M_{(1.0, 90)} = 0.30 . . . . .$	37
12     Section Angle of Attack Versus Azimuth; $\mu = 0.30, M_{(1.0, 90)} = 0.32 . . . . .$	38
13     Section Angle of Attack Versus Azimuth; $\mu = 0.40, M_{(1.0, 90)} = 0.34 . . . . .$	39
14     Section Angle of Attack Versus Azimuth; $\mu = 0.50, M_{(1.0, 90)} = 0.37 . . . . .$	40

<u>Figure</u>	<u>Page</u>
15 Measurement of Velocity Vector With Boundary Layer Button . . . . .	41
16 Local Velocity Angle Relative to Chord Measured With BLBs . . . . .	42
17 Local Resultant Velocity Measured With BLBs on Upper Surface at Three Chord Stations, $h = 0.0625$ in. . . . .	48
18 Resultant Velocity of Three Heights Above the Airfoil Surface Versus Azimuth, $x/c = 0.90$ . . . . .	49
19 Top View of Tip Vortex Core Path for Two-Bladed Rotor, $\mu = 0.20$ . . . . .	50
20 Chordwise Pressure Distribution (Run 2, Point 1); $\mu = 0.20$ , $M_{(1.0, 90)} = 0.30$ , $\theta_{.75R} = 3.1^\circ$ , $\dot{\beta} \equiv \ddot{\beta} \equiv 0$ . . . . .	51
21 Integrated Normal Force, Chord Force, and Pitching Moment Coefficients Versus Azimuth; $\mu = 0.20$ , $M_{(1.0, 90)} = 0.30$ , $\theta_{.75R} = 3.1^\circ$ , $\dot{\beta} \equiv \ddot{\beta} \equiv 0$ . . . . .	54
22 Chordwise Pressure Distribution (Run 2, Point 3); $\mu = 0.20$ , $M_{(1.0, 90)} = 0.30$ , $\theta_{.75R} = 11.0^\circ$ , $\dot{\beta} \equiv \ddot{\beta} \equiv 0$ . . . . .	55
23 Integrated Normal Force Coefficient Versus Azimuth; $\mu = 0.20$ , $M_{(1.0, 90)} = 0.30$ , $\theta_{.75R} = 11.0^\circ$ , $\dot{\beta} \equiv \ddot{\beta} \equiv 0$ . . . . .	58
24 Integrated Chord Force Coefficient Versus Azimuth; $\mu = 0.20$ , $M_{(1.0, 90)} = 0.30$ , $\theta_{.75R} = 11.0^\circ$ , $\dot{\beta} \equiv \ddot{\beta} \equiv 0$ . . . . .	59
25 Integrated Pitching Moment Coefficient Versus Azimuth; $\mu = 0.20$ , $M_{(1.0, 90)} = 0.30$ , $\theta_{.75R} = 11.0^\circ$ , $\dot{\beta} \equiv \ddot{\beta} \equiv 0$ . . . . .	60

<u>Figure</u>	<u>Page</u>
26 Top View of Tip Vortex Core Path for Two-Bladed Rotor, $\mu = 0.50$ . . . . .	61
27 Chordwise Pressure Distribution (Run 2, Point 13); $\mu = 0.50$ , $M_{(1.0, 90)} = 0.37$ , $\theta_{.75R} = 3.1^\circ$ , $\dot{\beta} \equiv \ddot{\beta} \equiv 0$ . . . . .	62
28 Integrated Normal Force Coefficient Versus Azimuth; $\mu = 0.50$ , $M_{(1.0, 90)} = 0.37$ , $\theta_{.75R} = 3.1^\circ$ , $\dot{\beta} \equiv \ddot{\beta} \equiv 0$ . . . . .	65
29 Integrated Chord Force Coefficient Versus Azimuth; $\mu = 0.50$ , $M_{(1.0, 90)} = 0.37$ , $\theta_{.75R} = 3.1^\circ$ , $\dot{\beta} \equiv \ddot{\beta} \equiv 0$ . . . . .	66
30 Integrated Pitching Moment Coefficient Versus Azimuth, $\mu = 0.50$ , $M_{(1.0, 90)} = 0.37$ , $\theta_{.75R} = 3.1^\circ$ , $\dot{\beta} \equiv \ddot{\beta} \equiv 0$ . . . . .	67
31 Chordwise Pressure Distribution (Run 2, Point 15); $\mu = 0.50$ , $M_{(1.0, 90)} = 0.37$ , $\theta_{.75R} = 7.2^\circ$ , $\dot{\beta} \equiv \ddot{\beta} \equiv 0$ . . . . .	68
32 Integrated Normal Force Coefficient Versus Azimuth; $\mu = 0.50$ , $M_{(1.0, 90)} = 0.37$ , $\theta_{.75R} = 7.2^\circ$ , $\dot{\beta} \equiv \ddot{\beta} \equiv 0$ . . . . .	71
33 Integrated Chord Force Coefficient Versus Azimuth; $\mu = 0.50$ , $M_{(1.0, 90)} = 0.37$ , $\theta_{.75R} = 7.2^\circ$ , $\dot{\beta} \equiv \ddot{\beta} \equiv 0$ . . . . .	72
34 Integrated Pitching Moment Coefficient Versus Azimuth; $\mu = 0.50$ , $M_{(1.0, 90)} = 0.37$ , $\theta_{.75R} = 7.2^\circ$ , $\dot{\beta} \equiv \ddot{\beta} \equiv 0$ . . . . .	73
35 Chordwise Pressure Distribution (Run 2, Point 1); $\mu = 0.20$ , $M_{(1.0, 90)} = 0.30$ , $\theta_{.75R} = 3.1^\circ$ , $\dot{\beta} \equiv \ddot{\beta} \equiv 0$ . . . . .	77

<u>Figure</u>	<u>Page</u>
36 Chordwise Pressure Distribution (Run 2, Point 2); $\mu = 0.20$ , $M_{(1.0, 90)} = 0.30$ , $\theta_{.75R} = 3.1^\circ$ , $\dot{\theta} \approx \ddot{\theta} \approx 0$ . . . . .	80
37 Chordwise Pressure Distribution (Run 2, Point 3); $\mu = 0.20$ , $M_{(1.0, 90)} = 0.30$ , $\theta_{.75R} = 11.0^\circ$ , $\dot{\beta} \approx \ddot{\beta} \approx 0$ . . . . .	83
38 Chordwise Pressure Distribution (Run 2, Point 4); $\mu = 0.20$ , $M_{(1.0, 90)} = 0.30$ , $\theta_{.75R} = 11.0^\circ$ , $\dot{\theta} \approx \ddot{\theta} \approx 0$ . . . . .	86
39 Chordwise Pressure Distribution (Run 2, Point 5); $\mu = 0.30$ , $M_{(1.0, 90)} = 0.32$ , $\theta_{.75R} = 3.1^\circ$ , $\dot{\beta} \approx \ddot{\beta} \approx 0$ . . . . .	89
40 Chordwise Pressure Distribution (Run 2, Point 6); $\mu = 0.30$ , $M_{(1.0, 90)} = 0.32$ , $\theta_{.75R} = 3.1^\circ$ , $\dot{\theta} \approx \ddot{\theta} \approx 0$ . . . . .	92
41 Chordwise Pressure Distribution (Run 2, Point 7); $\mu = 0.30$ , $M_{(1.0, 90)} = 0.32$ , $\theta_{.75R} = 9.1^\circ$ , $\dot{\beta} \approx \ddot{\beta} \approx 0$ . . . . .	95
42 Chordwise Pressure Distribution (Run 2, Point 8); $\mu = 0.30$ , $M_{(1.0, 90)} = 0.32$ , $\theta_{.75R} = 9.1^\circ$ , $\dot{\theta} \approx \ddot{\theta} \approx 0$ . . . . .	98
43 Chordwise Pressure Distribution (Run 2, Point 9); $\mu = 0.40$ , $M_{(1.0, 90)} = 0.34$ , $\theta_{.75R} = 3.1^\circ$ , $\dot{\beta} \approx \ddot{\beta} \approx 0$ . . . . .	101
44 Chordwise Pressure Distribution (Run 2, Point 10); $\mu = 0.40$ , $M_{(1.0, 90)} = 0.34$ , $\theta_{.75R} = 3.1^\circ$ , $\dot{\theta} \approx \ddot{\theta} \approx 0$ . . . . .	104
45 Chordwise Pressure Distribution (Run 2, Point 11); $\mu = 0.40$ , $M_{(1.0, 90)} = 0.34$ , $\theta_{.75R} = 8.1^\circ$ , $\dot{\beta} \approx \ddot{\beta} \approx 0$ . . . . .	107

<u>Figure</u>	<u>Page</u>
46      Chordwise Pressure Distribution (Run 2, Point 12); $\mu = 0.40$ , $M_{(1.0, 90)} = 0.34$ , $\theta_{.75R} = 8.1^\circ$ , $\dot{\theta} \approx \ddot{\theta} \approx 0$ . . . . .	110
47      Chordwise Pressure Distribution (Run 2, Point 13); $\mu = 0.50$ , $M_{(1.0, 90)} = 0.37$ , $\theta_{.75R} = 3.1^\circ$ , $\dot{\theta} \approx \ddot{\theta} \approx 0$ . . . . .	113
48      Chordwise Pressure Distribution (Run 2, Point 14); $\mu = 0.50$ , $M_{(1.0, 90)} = 0.37$ , $\theta_{.75R} = 3.1^\circ$ , $\dot{\theta} \approx \ddot{\theta} \approx 0$ . . . . .	116
49      Chordwise Pressure Distribution (Run 2, Point 15); $\mu = 0.50$ , $M_{(1.0, 90)} = 0.37$ , $\theta_{.75R} = 7.2^\circ$ , $\dot{\theta} \approx \ddot{\theta} \approx 0$ . . . . .	119
50      Chordwise Pressure Distribution (Run 2, Point 16); $\mu = 0.50$ , $M_{(1.0, 90)} = 0.37$ , $\theta_{.75R} = 7.2^\circ$ , $\dot{\theta} \approx \ddot{\theta} \approx 0$ . . . . .	122

### LIST OF SYMBOLS

$A_{1S}$	lateral cyclic pitch control with respect to the shaft axis, deg
$b$	number of blades
$B_{1S}$	longitudinal cyclic pitch with respect to the shaft axis, deg
$c$	blade chord, ft
$C_c$	airfoil section chord force coefficient, $C_c = \int C_p d(y/c)$
$C_{L/\sigma}$	rotor lift coefficient, $C_{L/\sigma} = L/\rho b c R(\Omega R)^2$
$C_m c/4$	airfoil section pitching moment coefficient about the quarter chord, $C_m c/4 = \int C_p (0.25-x/c) d(x/c) + \int C_p (y/c) d(y/c)$
$C_n$	airfoil section normal force coefficient, $C_n = \int C_p d(x/c)$
$C_p$	absolute pressure coefficient, $C_p = \frac{P_{\text{measured}} - P_{\text{tunnel static}}}{q}$
$\Delta C_p$	differential pressure coefficient, $\Delta C_p = \frac{P_{\text{measured(upper surface)}} - P_{\text{measured(lower surface)}}}{q}$ $= C_{p_{\text{upper surface}}} - C_{p_{\text{lower surface}}}$
$f$	frequency of rotor motion, Hz
$h$	height of boundary layer button static tubes above the airfoil surface, in.
$k$	reduced frequency, $\pi f c/V$
$L$	total rotor lift, lb

$M_{(1.0, 90)}$	advancing tip Mach number
$P$	static pressure, psi
$q$	dynamic pressure, $\text{lb}/\text{ft}^2$ $q = 1/2 \rho_\infty (\Omega r + V_\infty \sin \psi)^2$
$r$	radial distance to blade element, ft
$R$	rotor radius, ft
$V$	local free-stream velocity, ft/sec $V = \Omega r + V_\infty \sin \psi$
$V_\infty$	free-stream forward speed, ft/sec
$V_1$	local velocity component measured by inboard boundary layer button total tube, ft/sec
$V_2$	local velocity component measured by outboard boundary layer button total tube, ft/sec
$V_l$	local velocity, ft/sec
$V_r$	local resultant velocity, ft/sec
$V_v$	local line vortex velocity, ft/sec
$x/c$	nondimensional distance along the chord
$y/c$	nondimensional distance perpendicular to the chord
$\alpha$	instantaneous local section angle of attack, deg
$\beta$	flapping angle at any azimuth position referred to the plane normal to the shaft axis, positive up, deg
$\dot{\beta}$	flapping velocity, deg/sec
$\ddot{\beta}$	flapping acceleration, $\text{deg}/\text{sec}^2$
$\gamma$	radial flow angle, deg
$\theta$	blade section pitch feathering, angle at any azimuth position referred to the shaft axis, deg
$\theta_{.75R}$	blade collective pitch angle measured at $0.75R$ , deg

$\dot{\theta}$	feathering velocity, deg/sec
$\ddot{\theta}$	feathering acceleration, deg/sec <sup>2</sup>
$\Lambda$	yaw angle, positive for sweepback, deg
$\mu$	advance ratio, $\mu = \frac{V_\infty}{\Omega R}$
$\rho_\infty$	free-stream density of air, slugs/ft <sup>3</sup>
$\psi$	blade azimuth angle measured from downwind in the direction of rotation in a plane normal to the shaft axis, deg
$\Omega$	rotor shaft angular velocity, rad/sec
$\Omega r$	station rotational velocity, ft/sec
$\Omega R$	tip speed, ft/sec

## INTRODUCTION

Measurement of the aerodynamic environment of a helicopter rotor in forward flight has been the object of considerable effort for many years. The primary parameters necessary to describe the aerodynamic environment of a rotor are: local blade angle of attack, local flow velocity magnitude and direction, and chordwise pressure distributions. Recently developed advanced instrumentation has proved capable of measuring these parameters. The initial investigation of rotor aerodynamics in forward flight using one complete blade station of the advanced instrumentation is the subject of this report.

The investigation, using standard UH-1D blades reduced to 34-foot diameter, was conducted in the Ames 40- x 80-foot wind tunnel. The instrumentation was installed at one radius station. Angle of attack, radial flow direction and velocity, and chordwise pressure distribution data were continuously recorded. The simultaneous measurement of the above parameters at one radius station represents the first step toward describing the flow field about the rotor. With this further knowledge of the flow field about the rotor, improvements in forward-flight helicopter rotor design and theory, including stall, wake, and unsteady effects, can be formulated and tested. With this goal in mind, the experimental results of this investigation were compared with the following: (1) baseline two-dimensional wind-tunnel data, (2) two-dimensional potential flow theory, and (3) rigid blade nonuniform inflow theory.

The Test Results and Discussion section presents data from the various instruments and discusses the results of each type of data separately. The Discussion of Four Test Conditions section gives an integrated version of the overall results for each of four test conditions. Included in this section are comparisons of test results with theory and other empirical data. Also, some reasons are offered as explanations of the observed results. The four cases are low  $\mu$ , low and high lift, and high  $\mu$ , low and high lift.

## TEST EQUIPMENT

### ROTOR TEST MODULE

The test equipment primarily consists of a rotor test stand, a rotor, and a control console. The stand includes a mounting frame, a UH-1 pylon system, a speed-increaser gearbox, an electric-driven motor, and an aerodynamic fairing. The mounting frame, pylon, and drive system are enclosed by an aerodynamic fairing of teardrop shape. The maximum diameter of the fairing is 6.66 feet, and the length is 22 feet. Further description of the test module, power distribution panel, control module, and associated instrumentation may be found in Appendix II of Reference 1 and as basic configuration 576-099-050-101 in Enclosure A of Reference 2.

### ROTOR

A two-bladed, semirigid-type rotor using a UH-1D underslung feathering axis hub was tested. Basic data for this rotor, a standard UH-1D blade reduced to 34-foot diameter, are given below.

#### 34-Foot-Diameter Rotor

Airfoil Designation	NACA 0012
Chord	1.75 ft
Diameter	34 ft
Twist	-1.42 deg
Disc Area	908 sq ft
Solidity	0.0656
Effective Root Cutout	11.8%
Lock Number	3.62

### GLOVE

Since it is not structurally feasible to cut into the surface of a blade, a glove is used in which the instrumentation is embedded. This arrangement provides a smooth aerodynamic surface. Figure 1 shows a glove, 0.10 inch thick, and the instrumentation installed on a rotor blade. With the addition of the 0.10-inch-thick glove, the coordinates of the airfoil become:

<u>x/c</u>	<u>y/c</u>	<u>x/c</u>	<u>y/c</u>	<u>x/c</u>	<u>y/c</u>
0.000	0.000	0.030	0.031	0.348	0.062
0.001	0.004	0.052	0.039	0.417	0.059
0.002	0.009	0.074	0.045	0.486	0.056
0.004	0.013	0.096	0.049	0.555	0.051
0.007	0.016	0.119	0.052	0.624	0.045
0.010	0.020	0.142	0.055	0.692	0.039
0.014	0.022	0.165	0.057	0.761	0.031
0.018	0.025	0.181	0.059	0.829	0.024
0.022	0.027	0.211	0.060	0.898	0.015
0.026	0.029	0.288	0.062	0.966	0.006
				1.000	0.002

The basic airfoil chord was also extended from 21.0 to 21.75 inches to fair the trailing edge of the airfoil to a reasonable thickness. Termination of the extended airfoil at 21 inches would have resulted in a blunt trailing edge.

The total spanwise length of the installed glove was 3 feet 8 inches, with the center line of the glove at the 0.75 radius position. The basic glove was 3 feet long and was constructed of a stretch-formed aluminum leading edge to the 0.25 chord. From the quarter chord, the glove was formed of paper honeycomb covered with fiber glass. Except for the terminal strips at the trailing edge of the pressure blade, all wires were in channels cut into the glove and faired over to maintain a smooth aerodynamic surface. At each end of the glove, approximately 4 inches was used to fair the sharp-edged glove into the basic NACA 0012 21-inch chord airfoil.

To minimize the mutual interference between the various pieces of instrumentation, the surface static pressure transducers were installed on one blade, and the hot wire anemometer and BLBs were installed on the opposite blade.

#### SURFACE STATIC PRESSURES

Eleven surface static pressures were measured on each surface (upper and lower) plus one on the leading edge at the following chord and span stations:

<u>x/c</u>	<u>r,ft</u>	<u>x/c</u>	<u>r,ft</u>
0.000	12.750	0.142	12.750
0.007	12.667	0.208	12.750
0.015	12.817	0.314	12.750
0.030	12.736	0.543	12.750
0.051	12.658	0.731	12.750
0.081	12.750	0.96	12.750

The gages were subminiature pressure transducers of 0-20 psig. The complete installation is shown in Figure 2; a 3-inch-wide contoured metal plate was fabricated, in which the transducers were installed. Staggering of the transducers near the leading edge was necessary due to space limitation. As shown in the preceding table, all transducers were within 1.10 inches of the 0.75 radius value.

#### BOUNDARY LAYER BUTTON

The Boundary Layer Button (BLB) is a pressure measuring device developed to measure flow direction on a rotating surface. Two subminiature differential pressure transducers are contained in the button as shown in Figure 3.

Each of the total pressure tubes is connected to the top of the diaphragm of a transducer. The angle between the tubes is 90 degrees. The backside of the diaphragm of both transducers is connected to a common static port. Therefore, the output of each transducer is dynamic pressure. Using the dynamic pressure, the velocity magnitude can be calculated. The angle between the tubes is known; therefore, the flow direction can be calculated. Each BLB cap was calibrated for flow direction. The calibration is linear, and it requires no correction for an included angle of 32 degrees. First results with this instrument are published in Reference 1.

Ten BLBs were installed, five on each surface as shown in Figure 1, with the 60% chord button located at the 0.75 radius station. A 30-degree stagger was used to minimize the mutual disturbance factor between the instruments at low radial flow angles. The tube height was held constant at 0.0625 inch for six primary BLBs, and the heights for the added instruments at 90% chord were 0.1875 and 0.3125 inch.

## LEADING-EDGE HOT WIRE ANEMOMETER

The hot wire anemometer is a constant-current device using 16 sensors to measure the stagnation point location along the airfoil profile. A sketch of the hot wire installation is given in Figure 4 along with a schematic of the circuit.

All channels of the system are set to a no-wind common voltage, and the relative velocity is recorded for all channels. The stagnation point is determined by locating the sensor which has the maximum voltage. The accuracy of measuring the angle of attack depends on the spacing between the sensors with respect to the chord. For the spacing used, the maximum accuracy is within one degree of angle of attack. Two-dimensional test results with this instrument are published in Reference 3. The positions of the individual wires are given below in inches along the contour from the leading edge.

<u>Sensor No.</u>	<u>Position, in.</u>	<u>Surface</u>
1	0.24	Upper
2	0.12	Upper
3	0.00	L.E.
4	0.12	Lower
5	0.24	Lower
6	0.36	Lower
7	0.48	Lower
8	0.60	Lower
9	0.72	Lower
10	0.84	Lower
11	0.96	Lower
12	1.08	Lower
13	1.20	Lower
14	1.32	Lower
15	1.44	Lower
16	1.56	Lower

## DATA ACQUISITION

The Bell Offsite Data Acquisition Package (ODAP), as used in this test program, consisted of measurement transducers, transducer signal conditioners, test equipment rack, electronics rack, magnetic tape recorder rack, and remote monitor console. Figure 5 is a block diagram of the system. A brief description of each block follows.

1. Sensotec Transducers - These transducers are semi-conductor, strain-gage type units connected to the PR-100 signal conditioner. One absolute pressure transducer was used per static port and two differential pressure transducers were used per BLB.
2. Hot Wire Anemometer - This is the Bell Helicopter Company-developed hot wire system. Sixteen segments were connected across the leading edge of the blade, and each of the segments was measured. These segment signals were conditioned by the hot wire anemometer control box.
3. Control Loads (Rotating) - Strain-gage bridge transducers were bonded on the model at various points to measure control forces.
4. Control Positions (Nonrotating) - Linear transducers were connected to measure control positions. Potentiometers were electrically connected in 350-ohm bridges so that movement of the potentiometer varied the bridge balance. This produced a change in reading of the position indicators.
5. Slipring - A 164-ring in-the-mast slipring was used to complete the data channels from the rotating system to the signal conditioners in the nonrotating system.
6. Astronics PR-100 Signal Conditioners - These were very high input impedance amplifiers, designed for use with piezo-resistive transducers. These amplifiers were mounted on a base with 20 signal conditioners, one voltage regulator, and one calibrator per mount.
7. Hot Wire Anemometer Control Box - The signal conditioners for the segmented hot wire anemometer were contained in this box.
8. Bell Helicopter ILD 082 Amplifier Module - This unit was approximately 12 inches by 12 inches by 3 inches in size. There were nine connectors on two sides of the unit for signal inputs, outputs, and power. Inside the module were connections and locating slots for 64 signal conditioning amplifiers and associated range setting printed circuit boards. The calibration network was also located within this module.
9. Electronics Rack - This unit was 77 inches high by 22 inches wide. Mounted in the rack were the five power supplies which furnish transducer excitation voltage, signal conditioner amplifier power, 28-volt DC control,

and voltage-controlled oscillators and associated circuitry used to provide frequency division multiplexing of transducer output signals. Included in this rack were discriminators for demultiplexing the frequency division changes for quick-look and data acquisition verification purposes. On the front of the rack was a program board with positions for signal outputs and inputs of those channels in use.

10. Magnetic Tape Recorder - The magnetic tape recorder was an Ampex FR 1800 with a 14-channel capacity. Available in the tape recorder were the required record and playback electronics.
11. Monitor Display Console - This console contained a digital display, a 16-channel selector, a monitor oscilloscope, and a direct-write oscilloscope.
12. Model Control Console - This unit was not part of the ODAP, but it is shown on the block diagram to indicate that control positions and loads were furnished by the Off-Site Data Acquisition Package.
13. Direct-Write Oscilloscope - A model 5-126 CEC oscilloscope was used to read out the hot wire anemometer data. A second direct-write oscilloscope was used in the monitor display console for a quick look at any data channel while the test was in progress.

#### SYSTEM OPERATION

In the Off-Site Data Acquisition Package for this program, the data distribution followed four paths from physical stimuli to a recording medium. The Sensotec transducers were connected through the slipring to the Astronics PR-100 signal conditioner. From the PR-100's, the distribution path was through the program board to the voltage-controlled oscillators (VCO's) and thus to the magnetic tape recorder.

The hot wire anemometer measuring elements were connected through the slipring to the hot wire anemometer control box. From the control box, the data path was directly to the CEC Model 5-126 oscilloscope and the magnetic tape recorder.

The model control loads were connected through the slipring to the Bell Helicopter ILD 082 instrumentation amplifier module. From the amplifier module, the data path was through the program board to the VCOs and thus to the magnetic tape recorder. The model control positions were connected directly to the BHC amplifier module. From the module, the distribution path was through the program board to the VCOs and thus

to the magnetic tape recorder. The following description of the system operation applies to all channels that were distributed through the program board.

The location or position of each of the signals from the measurement transducers was determined by the signal conditioning amplifier position being used for that transducer. Each of the conditioned signals was available at four positions adjacent to each other on the program board. Connection by means of a patch cord could be made from one signal output to a VCO, to become one channel of a frequency-divided multiplex group. A second patch cord could be used to connect this same signal to provide a display at the monitor display console; a third patch cord could connect this signal to the model control console to display an operating load or control position; and a fourth patch cord could connect this same signal to one channel of an oscilloscope (direct write) to provide quick-look display for immediate evaluation of the measurement parameter. This same capability was available for each active channel of the test parameter assignments.

Program board positions were available for multiplex outputs, magnetic recorder channel inputs, playback outputs, and discriminator outputs. The discriminators provided the capability of playing back data previously recorded into the direct-write oscilloscope to assure data integrity, and for quick-look evaluation of the recorded data. The discriminators were not used for data reduction or for critical evaluation of recorded data. This function was reserved for the Bell Fort Worth Ground Data Center, where data manipulation and computer data evaluation are available.

Once the patching of all active data channels was complete, operation was automatic. When the desired measurement conditions were achieved at the model, the test conductor pressed the record button on the tape system remote-control logic unit. The tape transport was activated, and when it reached operating speed, actual data were recorded for a preset interval of time determined by the operator or test conductor. At the termination of the time interval, the 20-percent and 80-percent calibration indications or steps were recorded, the tape transport was stopped, and the system was again ready to repeat the cycle as required. The time intervals that could be selected were 2.5, 5.0, and 10 seconds, and infinite, which allowed the recorder to continue to run until the operator or test conductor stopped it.

## DATA REDUCTION

The various test parameters were recorded in multiplexed FM form by a magnetic tape recorder. The signals were then demodulated into voltages and converted to digital form with an analog-to-digital converter.

For each data point, a record of approximately 10 seconds was made. Of this record, three revolutions were digitized with 586 data samples per revolution. One revolution was then divided into 5-degree increments, and these data were put into digital computer programs. The outputs of the programs are pressure coefficients; integrated force coefficients; velocity vectors; flapping and feathering angular displacements, velocities, and accelerations; and angle-of-attack distributions. Some of the outputs were machine plotted as well as tabulated.

## TESTS

### GENERAL DISCUSSION

The test conditions are shown in the table on page 11. Forward-flight data obtained were: (1) angle of attack, (2) local velocity magnitude and direction, (3) chordwise pressure distributions, (4) control positions, and (5) main rotor mast torque. Continuous data were taken at a single blade station, 75 percent radius, for advance ratios of 0.2, 0.3, 0.4, and 0.5. A constant rotational speed of 160 rpm and a constant shaft angle of 0 degrees were maintained.

The chordwise pressure, radial flow, and angle-of-attack data are local airfoil section measurements. All other data, including the wind-tunnel balance data which were recorded and reduced by NASA-Ames, were resolved in the relative wind axis.

### TESTING PROCEDURE

There are four basic test cases with four corresponding tunnel speeds. These tunnel speeds were used so that, with a constant rpm of 160, data could be taken at each of the four advance ratios. The rotor rpm was varied slightly to maintain these advance ratios. For each advance ratio, four test points were taken. At a given advance ratio, a low blade angle (lift) was selected, first-harmonic flapping with respect to the shaft was minimized, and data were recorded. At this same blade angle, first-harmonic feathering with respect to the shaft was also minimized, and data were recorded. Then, a high blade angle was selected, and first-harmonic flapping and feathering were minimized. This procedure was followed for each of the four advance ratios.

Run 2 is the primary data run in which the BLB axis is at 0 degrees with respect to the blade chord line. Runs 3 and 4 are repeats of Run 2 except that the axis of each BLB is rotated inboard 22.5 degrees (negative) and outboard 22.5 degrees (positive), respectively, in relation to the chord line. Runs 5 and 7 are repeats of the minimized first-harmonic flapping test points of Run 2, in which additional boundary layer buttons were added to the trailing edge.

## TEST CONDITIONS

Run	Point	$\mu$	Mach	No.	$\theta$	$0.75R$	Lift	Drag	$A_{LS}$	$B_{LS}$	$\dot{\beta} = \ddot{\beta} = 0$	$\dot{\theta} = \ddot{\theta} = 0$
2	1	.2011	.2973	3.1	481.	96	8.03	.47	2.23	x		
	2	.2011	.2973	3.1	551.	95	26.04	0	.47		x	
	3	.2018	.2974	11.0	1346.	67	-19.30	1.36	6.67	x		
	4	.2000	.2967	11.0	1567.	55	121.72	0	0	x		
	5	.2993	.3210	3.1	486.	12	14.39	.68	2.78	x		
	6	.3004	.3196	3.1	626.	45	44.74	0	.22	x		
	7	.3011	.3198	9.13	1076.	28	-6.95	.78	7.32	x		
	8	.3003	.3193	9.13	1426.	58	154.07	0	.33	x		
	9	.4040	.3444	3.1	429.	68	17.49	.68	3.57	x		
	10	.4037	.3440	3.1	675.	03	61.17	.13	.33	x		
	11	.4034	.3445	8.13	839.	60	8.81	.68	8.11	x		
	12	.4034	.3439	8.13	1390.	46	185.54	0	.33	x		
	13	.5040	.3688	3.1	448.	74	25.51	.90	4.25	x		
	14	.5034	.3687	3.1	788.	58	89.13	0	.33	x		
	15	.5042	.3679	7.15	703.	43	26.71	.68	8.45	x		
	16	.5028	.3685	7.15	1288.	43	156.73	.13	2.90	x		
3	1	.2036	.2921	3.1	459.	91	4.38	.55	2.23	x		
	2	.1988	.2917	3.1	526.	10	20.39	0	.47		x	
	3	.2008	.2914	11.0	1295.	44	-23.27	1.36	6.67	x		
	4	.2057	.2926	11.0	1528.	96	135.33	0	0	x		
	5	.3041	.3161	3.1	483.	73	11.71	.68	2.78	x		
	6	.3044	.3154	3.1	603.	90	42.04	.13	.22	x		
	7	.2998	.3199	9.13	1078.	46	-12.60	.78	7.32	x		
	8	.2980	.3211	9.13	1428.	27	146.65	0	.47	x		
	9	.3985	.3460	3.1	457.	65	18.40	.47	3.57	x		
	10	.3980	.3462	3.1	667.	62	54.40	.13	.55	x		
	11	.3984	.3460	8.13	847.	60	2.41	.68	8.11	x		
	12	.3973	.3466	8.13	1418.	39	181.49	.22	.47	x		
	13	.4992	.3698	3.1	450.	29	23.55	.90	4.25	x		

TEST CONDITIONS - Continued										
Run	Point	$\mu$	Mach No.	$\theta_{75R}$	Lift	Drag	$A_{1S}$	$B_{1S}$	$\beta = \beta = 0$	$\dot{\theta} = \dot{\theta} = 0$
3	14	.5012	.3701	3.1	790.85	82.75	.13	.47	x	x
	15	.4994	.3703	7.15	700.54	21.66	.68	8.45	x	x
	16	.5005	.3705	7.15	1245.35	143.39	.13	2.90	x	x
4	1	.1988	.2975	3.1	505.03	2.55	.33	2.35	x	x
	2	.1991	.2971	3.1	574.98	21.54	0	.47	x	x
	3	.2003	.2966	11.0	1379.65	-28.78	1.36	6.67	x	x
	4	.1988	.2964	11.0	1610.00	131.85	0	0	x	x
	5	.2981	.3211	3.1	498.89	12.55	.60	2.78	x	x
	6	.2971	.3211	3.1	654.14	45.21	0	.13	x	x
	7	.2971	.3211	9.13	1084.07	-11.77	.68	7.32	x	x
	8	.2969	.3203	9.13	1434.47	147.87	0	.47	x	x
	9	.3977	.3455	3.1	463.11	18.54	.68	3.57	x	x
	10	.3986	.3457	3.1	667.88	60.58	.13	.47	x	x
	11	.3982	.3456	8.13	868.00	5.89	.55	8.11	x	x
	12	.3976	.3455	8.13	1361.42	189.35	0	.33	x	x
	13	.4976	.3702	3.1	450.16	23.31	.90	4.25	x	x
	14	.4987	.3705	3.1	790.57	77.11	0	.47	x	x
	15	.5002	.3708	7.15	711.18	21.31	.68	8.54	x	x
	16	.4993	.3697	7.15	1250.51	148.73	.13	2.90	x	x
5	1	.2026	.2964	3.1	486.80	3.70	.47	2.23	x	x
	2	.2037	.2964	11.0	1346.80	-24.64	1.36	6.67	x	x
	3	.3025	.3211	3.1	495.10	11.73	.68	2.78	x	x
	4	.3030	.3212	9.13	1046.39	-14.58	.74	7.32	x	x
	5	.4001	.3460	3.1	434.80	15.78	.68	3.57	x	x
	6	.4019	.3452	8.13	864.84	7.45	.68	8.11	x	x
	7	.5004	.3695	3.1	432.94	21.60	.90	4.25	x	x
	8	.5021	.3699	7.15	698.52	20.81	.68	8.45	x	x

## TEST CONDITIONS - Concluded

Run	Point	$\mu$	Mach No.	$\theta_{.75R}$	Lift	Drag	$A_{1S}$	$B_{1S}$	$\dot{\beta} = \dot{\beta} = 0$	$\dot{\beta} = \dot{\beta} = 0$
7	1	.2000	.2970	3.1	512.26	4.71	.47	2.23	x	
	2	.2005	.2963	11.0	1362.08	-24.28	1.36	6.77	x	
	3	.2995	.3216	9.13	1100.46	-8.94	.68	7.32	x	
	4	.2978	.3220	3.1	506.34	10.72	.55	2.90	x	
	5	.3967	.3474	3.1	450.18	14.42	.68	3.57	x	
	6	.3988	.3462	8.13	869.80	4.42	.68	8.11	x	
	7	.5006	.3706	7.15	708.39	22.80	.78	8.33	x	
	8	.4998	.3705	3.1	463.15	22.70	.90	4.25	x	

## TEST RESULTS AND DISCUSSION

This section presents the results of the three types of data measured with the advanced instrumentation. The data include surface static pressures, local angles of attack, and local velocity vectors. Each of the three items is presented and discussed separately.

### MEASURED SURFACE PRESSURES

The repeatability of the pressure data is illustrated in Figures 6 and 7. Figure 6 shows the cyclic repeatability for five pressure transducers for three typical revolutions. The repeatability is excellent. Figure 7 shows the repeatability of a typical pressure for the four test runs. Some small variations are apparent, but these are due to small differences in the set test conditions (see the table on page 11). In general, by taking the variation in test conditions into account, the repeatability is good.

Typical pressure plots are shown in Figures 8 and 9 for advance ratios of 0.2 and 0.5. Two-dimensional potential flow theory and experimental data from Reference 4 are included. The differential pressure coefficients appear to be conventional, and in both cases the experimental results are similar in character to the two-dimensional oscillating airfoil results shown in Reference 4. However, the absolute pressure coefficients are not conventional (two-dimensional) in character. Both advance ratios show stagnation pressure coefficients in excess of +1 and, especially in Figure 9, very large negative pressure coefficients on both surfaces. The negative pressure coefficients on the lower surface of the airfoil are most surprising. Data presented in the appendix of this report show that this condition does not exist at all azimuth positions. These unexpected results require a more detailed examination.

Oscillating airfoil effects were one of the considerations in the search for an explanation of the unusual pressure distributions. Figures 8 and 9 include oscillating airfoil data from Reference 4. The following conditions exist between the empirical data of Reference 4 and this test:

- Signs of the unsteady velocities and acceleration are the same.
- Magnitudes of velocities and accelerations are unequal.
- Reduced frequencies,  $k$ , are equal.
- Frequencies and Mach numbers are not equal.
- Airfoil profiles are similar (basically 0012), but both have been slightly modified.

Figures 8 and 9 show that the shapes of the differential pressure distribution curves are similar. No empirical data are available in the form of upper and lower surface pressure distribution; therefore, a detailed comparison could not be made. The conclusion is that some oscillating airfoil effect must be present. However, the large magnitudes of the pressures cannot be totally due to oscillating airfoils because the frequency oscillation was very low in this particular test (2.66 Hz or 1/rev at 160 rpm).

Another consideration in the investigation of the pressure distribution problem is the definition of the freestream dynamic pressure,  $q$ , in the equation for  $C_p$ .

$$C_p = \frac{P_{\text{measured}} - P_{\text{tunnel static}}}{q_\infty} \quad (1)$$

$$q_\infty = \frac{1}{2} \rho (\Omega r + V_\infty \sin \psi)^2 \quad (2)$$

Equation (1) is the definition of  $C_p$  used in this report. This equation is based on the Bernoulli relationship, which does not apply to intersecting flow fields (rotational flows). An example illustrating this and offering a possible explanation for the magnitudes of the pressure coefficients is given in Figure 10. Shown is an infinite wing at  $0^\circ$  angle of attack with the core of a line vortex above the wing, and the center line of the core parallel to the streamline. The line vortex adds a velocity  $V_v$  at  $90^\circ$  to the freestream velocity  $V_\infty$ . At any point on the wing, the local velocity is  $V_l$ . A plane view of the velocity vectors is shown in the lower sketch of Figure 10. By vector addition, the resultant velocity at each point would be  $V_r$  as shown.

$$\bar{V}_r = \bar{V}_v + \bar{V}_l \quad (3)$$

Assume  $|V_v| = |V_\infty|$

Therefore, at the leading edge

$$\begin{aligned} V_l &= V_\infty \\ \text{and, } |V_r| &= \sqrt{V_v^2 + V_l^2} \end{aligned}$$

$$v_r = \sqrt{v_\infty^2 + v_\infty^2}$$

$$v_r = \sqrt{2} v_\infty$$

Therefore, from Figure 10

$$q_\infty = 1/2 \rho v_\infty^2$$

However, based on  $v_r$  at the leading edge

$$q_r = 1/2 \rho v_r^2 = 1/2 \rho (\sqrt{2} v_\infty)^2$$

Thus,  $2q_\infty = q_r$

At the stagnation point of a two-dimensional airfoil

$$q_\infty = P_{\text{measured}} - P_{\text{tunnel static}}$$

$$C_p = q_r/q_\infty = 1$$

for the assumed case, using equation (1) and with the knowledge that  $q$  at the leading edge is  $q_r$

$$C_p = q_r/q_\infty = 2.$$

Based on the above, the conventional coefficient system equation (2) breaks down for the case of a rotor operating in the vicinity of a vortex. This condition of the vortex velocity contributing to the dynamic pressure exists in rotary-wing forward flight, and is especially important in the third and fourth quadrants of rotor azimuth. The condition of vortex position relative to the rotor blade will be discussed further in the detailed Discussion of Four Test Conditions section of this report.

The lower part of Figure 10 is also useful to illustrate the effect an additional velocity component has upon the pressure at any point on the airfoil. The actual velocity at each

point is  $V_r$  as shown. The pressure transducer is measuring the velocity  $V_r$ , not  $V_t$ , as in the classical case, and for the case drawn here,  $V_r \neq V_\infty$ . Therefore, again for this highly simplified case shown, the absolute value of the pressure is increased over a pressure corresponding to  $V_t$  and has been divided by a  $q$  which the previous paragraphs have shown to be low. The results, of course, would be a higher absolute magnitude of the pressure coefficient than is normally expected.

A second mechanism shown in this figure is that the streamline will naturally follow the resultant velocity path (i.e., tangent to  $V_r$  at each  $x/c$ ) and form a curved path over the airfoil surface as shown by the dashed line. Such results will be shown in a later section with data from the Boundary Layer Button.

The previous explanation based on Figure 10 is, of course, a highly simplified one. However, it does serve to illustrate that in the three-dimensional flow field in which the rotor is operating, the interpretation of the results in the conventional two-dimensional sense is not always possible. Also, it shows that differential pressure should not be measured since a totally different interpretation of the data can be given in looking at differential pressures versus the absolute pressures. A graphed set of data for the 16 test points at azimuth increments of 30 degrees is presented in the appendix.

#### STAGNATION POINT MEASUREMENTS

Prior to presenting the experimental results, a brief discussion of the method of using stagnation point location in determining angle of attack will be given, and the inherent assumption of the method will be reviewed. As explained in an earlier section, the velocity null about the leading edge of an airfoil is measured using a constant-current hot wire anemometer specially designed for the purpose. The location of the velocity null (stagnation point) is determined from the known locations of the hot wire segments. Using data from Reference 3 that relates stagnation point and angle of attack from a two-dimensional test, the angle of attack for the three-dimensional rotating test was determined. The assumption is that the angle of attack corresponding to a given stagnation point location is the same for both a nonrotating, two-dimensional test and a rotating, three-dimensional test.

The assumption that stagnation point location alone from two-dimensional tests can be used to determine three-dimensional angles of attack is not necessarily sufficient. For the results of a rotating test to indicate true aerodynamic

angles of attack using this method, both the stagnation point location and the local freestream direction must duplicate those of the nonrotating case. The above assumption is invalid if:

- the local freestream direction has not reached steady state; therefore, is changing with distance downstream (as a blade in the vicinity of vortex induced velocities)
- the airfoil oscillating and/or plunging velocities are not much less than the local freestream velocity.

The effect of radial flow on the determination of angle of attack was also ignored. Reference 3 shows that for radial angles within the range of  $-30^\circ$  to  $+30^\circ$  little effect upon the angle of attack versus stagnation point location is felt; however, extending this assumption to radial flow angles greater than  $30^\circ$  is highly suspect.

The test results are shown in Figures 11 through 14. The upper portion of each figure shows the minimized first-harmonic flapping cases and the lower portion shows the minimized first-harmonic feathering cases. For all test conditions at the higher lifts, voids are shown in the test data on the retreating blade. In these areas the rotor stalled, and either the test data were not interpretable or the two-dimensional baseline data of Reference 3 did not go to a sufficiently large angle-of-attack range to correlate with the stagnation point.

In general, the agreement shown between experimental and theoretical angle of attack is good. However, these comparisons can be very misleading, since both sets of data have their basic origins in the assumption of two-dimensional flow. In the data shown in Figures 11 through 14, the good agreement between experiment and theory may reflect a compatibility of assumptions rather than a valid experimental method. The hot wire data are accurate for the advancing blade where wake effects are small and unsteady velocities are much less than local freestream velocities. Portions of the data for the retreating blade are questionable because of wake effects and low local freestream velocities. When these conditions exist, the hot wire technique may be valid only to indicate relative changes in angle of attack, not absolute magnitudes.

#### BOUNDARY LAYER BUTTON RESULTS

The Boundary Layer Button is an instrument for measuring the magnitude and direction of the local velocity on a rotor blade. The BLB works on the same principle as a spherical yaw head with two total pressure tubes and one static pressure port, as shown in Figure 15. The total tubes are

oriented 90 degrees to each other and 45 degrees to each side of the center line of the instrument. The standard position of the BLB on a rotor is with the center line parallel to the rotor chord. The height of the total tubes above the rotor surface can be varied to measure velocity either in or out of the boundary layer. The resultant velocity vector is computed by the following relationships:

$$v_r = \sqrt{v_1^2 + v_2^2}$$

$$\gamma = \tan^{-1} (v_1/v_2) - 45^\circ$$

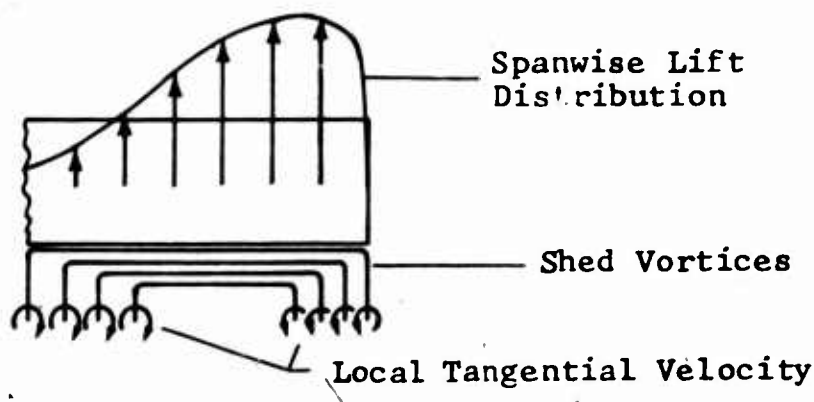
The specific application of the BLB for this test was to measure the local flow angle on the upper and lower surfaces of the blade at the 0.75 radius station. BLBs were installed at 30, 60, and 90 percent chord on both surfaces, and the tube height was 0.0625 inch above the surface. The radial flow angles are shown in Figure 16 for the low lift cases for each of the four advance ratios. High lift cases for only  $\mu = 0.20$  and 0.40 are given since the change from low to high lift is not unusual. Included in the figures are theoretical flow angles and the upper and lower surface measurements for a given chord station.

If the radial flow angle  $\gamma > 20$  degrees, the output from the BLB is nonlinear; therefore, the BLBs were rotated  $\pm 22.5$  degrees on successive runs to measure the larger angles incurred at the higher advance ratios. This technique was partially successful in that it extended the velocity measurements over a broader spectrum of the azimuth. However, the velocity vector was not mapped over the entire 360-degree azimuth range because the resultant angle was greater than the range of the BLB for certain conditions. These conditions occurred on the retreating side, usually in the fourth quadrant.

For all four advance ratios, the absolute value of the upper surface velocity angle was greater than the corresponding lower surface angle in the first and fourth quadrants. In the second and third quadrants, the absolute value of the lower surface angle was greater than the upper. There is one exception to the above, at  $\mu = 0.2$  and  $x/c = 0.90$ , which appears to be caused by the wake and is explained in more detail later. These conditions produce an effective positive camber and negative camber, respectively. Therefore, the symmetrical airfoil data normally used in theoretical performance programs should be corrected as a function of azimuth to better represent the real aerodynamic environment. The

graphs of radial flow angles show a gentle curving of the flow inboard as a function of chord. A possible explanation of this may be the strength of the shed vortices from the trailing edge as shown in the sketch below.

Because the lift distribution on a rotor is greater on the outboard section, the local tangential velocity may be greater inboard than outboard around 75 percent R, which is the BLB location.



Sketch of Shed Vortices From Lift Distribution

The curves in Figure 17 show the magnitude of the local velocity at 30, 60, and 90 percent chord on the upper surface. Because the total tubes were at a height of 0.0625 inch above the surface, they are inside the boundary layer. Since the boundary layer thickens and the local velocity decreases toward the trailing edge, the curves showing a reduction for 60 percent and 90 percent are as expected. The lower surface velocities were similar in magnitude and character to the upper surface velocities; therefore, they are not shown.

Figure 18 shows the velocity magnitude at 90-percent chord for three different tube heights and two advance ratios. In some cases, the two higher BLBs measured almost the same velocity magnitude, which indicates that they are both out of the boundary layer. In other cases, the data are incomplete and unexplainable. The sections of the graphs of both velocity magnitude and direction that are incomplete are data points where a vacuum was pulled in one or both of the total head tubes of the BLBs.

## DISCUSSION OF FOUR TEST CONDITIONS

In the Test Results section, the advanced instrumentation data were presented. This section is a more detailed discussion of the test results and presents integrated pressure force coefficients and data other than from the actual advanced instrumentation. Two different theories are used for comparison with the test data; a two-dimensional airfoil pressure distribution theory (2DPD), Reference 5, based on Theodorsen's conformal mapping technique and a rotor performance theory (BRAM) based on the transient blade flapping technique, Reference 6, with the addition of a free wake. The method of discussion is to examine four data points in some detail and interrelate the various results. These test points were selected to compare the low and high lift and low and high advance ratio conditions. The specific test points presented are from Run 2, Points 1, 3, 13, and 15 (see table, page 11). A complete analysis of all test points is not presented; however, some detailed comparisons and speculations are offered to explain the observed results.

Case I:  $\mu = 0.2$ ,  $C_L/\sigma = 0.0443$ ,  $M_{(1.0, 90.)} = 0.30$ .  
(Low  $\mu$ , low lift)

Figure 19 is the tip vortex core path for a two-bladed rotor at six azimuth positions. The circle represents the 0.75 radius of the rotor. This figure will be referred to repeatedly in the discussion of the results at  $\mu = 0.2$ .

The angle-of-attack variation with azimuth is shown in Figure 11. The theory shows that there are small interactions of the wake with the advancing blade between  $\psi = 40$  and  $\psi = 140$  degrees. The test data show some very small variations, but angular changes of 0.5 degree or less were beyond the capability of the system used. (Resolution of the system is approximately 1.0 degree.) At  $\psi = 270$  degrees, there is a significant change in angle of attack evident in both the test data and the theory.

These data are compatible with the variation which would be expected from Figure 19. At  $\psi = 40$  and 80 degrees, the blade is encountering vortices which are a revolution or more old. The effects from vortices are not strong, since they are below the plane of rotation and are produced by a blade having a total lift of only 240 pounds. Thus, the vortex effects on angle of attack are small. At  $\psi = 100$  degrees, the blade crosses the vortex from the previous blade which is 0.5 revolution old, and, as would be expected, the effect is larger. Figure 11 shows a large decrease in angle on the retreating blade. This too would be expected from Figure 19, since at

about  $\psi = 280$  degrees the blade is encountering its own tip vortex, which is about 0.75 revolution old and almost parallel to the chord at the 0.75 radius. The effect of the vortex on the blade would be larger on the retreating blade than on the advancing since the velocity  $(\Omega r + V \sin \psi)$  is at its minimum value at  $\psi = 270$  degrees. Therefore, a vortex of given strength and distance from the blade would have a larger effect on the retreating blade than on the advancing blade, where the velocities are higher. Figure 19 shows another cause for the decrease in angle of attack around  $\psi = 270$  degrees. This is the effect caused by the vortex core path traveling parallel to the blade span. The curl of the vortex is right hand. Therefore, as the blade approaches the vortex, the angle of attack would increase, and after it passes the core, the angle would decrease. This effect is evident in the angle-of-attack curve, Figure 11.

Interpretation of the radial flow angles from the BLBs, given in Figure 16, is more difficult than the hot wire data, since no theoretical analysis is available to predict the differences in radial flow between the upper and lower surfaces of an airfoil. However, some general observations can be made.

First, on the retreating blade the buildup of three-dimensional flow is obvious. The differential flow angles between surfaces are evident at 0.3 and 0.6 chord, and the flow angles at 0.9 chord become too large for the BLB to measure. Also, the figures show that a streamline over the blade follows a highly curved path. This is especially evident in the fourth quadrant. This would be expected since the hot wire data showed the strong influence of the vortex in that quadrant. However, the small effects of the vortex, shown in Figures 11 and 19, around  $\psi = 200$  degrees do not appear to be a plausible explanation for the three-dimensionality of the flow in that region. As yet, no plausible explanation has been found.

To summarize the 3L3 and hot wire results for this case:

- The aerodynamic wake effects on the advancing blade are second order, and the flow is essentially two-dimensional in character. However, these effects may be of prime importance in an aeroelastic analysis.
- There are significant three-dimensional effects on the retreating blade, some of which are explainable by the presence of the wake.

The airfoil pressure distributions for  $\mu = 0.2$   $C_l/\sigma = 0.0443$  are given in Figure 20 at azimuth increments of 30 degrees. The symbols are the test data; the solid lines are the calculated pressure distributions (2DPD) using the angle-of-attack and radial flow angles from Figures 11 and 16. The dashed lines

are the two-dimensional test results from Reference 3. Only limited cases of the two-dimensional test results are available for one-to-one comparisons. The pressure coefficients of Figure 20 tend to verify the BLB and hot wire results summarized in the preceding paragraph. On the advancing blade,  $\psi = 30$  to  $\psi = 140$  degrees, the flow is essentially two-dimensional. Here, the difference between the test and calculated results can be explained by small differences in the angles of attack (0.5 degree), as indicated on Figure 11. The tendency for the upper surface to be double peaked may result from oscillating airfoil effects. By  $\psi = 180$  degrees, there are significant differences between the test data and the calculated and experimental two-dimensional results. At  $\psi = 240$ , 270, and 300 degrees, the minimum positive pressure on the lower surface is greater than unity, and substantial negative pressures were measured on most of the lower surface. The flow appears to be highly three-dimensional.

Figure 21 presents the normal force, chord force, and pitching moment coefficients obtained from the test pressure distributions. The pressure integrations were performed at five degrees of azimuth. The dashed lines on the  $C_n$ ,  $C_c$ , and  $C_m c/4$  curves are the calculated values from BRAM and 2DPD. The normal force agreement is good and the chord force is reasonable. The higher chord forces may be due to oscillating airfoil effects. In general, the literature shows an increase in the oscillating two-dimensional drag coefficients over steady data. This could be the cause of the increase indicated in Figure 21.

Large negative pitching moments were measured as shown in Figure 21 for the symmetrical profile tested. The accurate determination of pitching moment from pressure measurements, especially from the limited number of chordwise transducers used, is subject to question. However, the data from this case, and for the cases to be shown later, indicate that the moments are certainly not zero for the symmetrical airfoil.

Case II:  $\mu = 0.20$ ,  $C_{L/\sigma} = 0.124$ ,  $M_{(1.0, 90)} = 0.30$ .  
(Low  $\mu$ , high lift)

The same data are shown in Figures 22 through 25 for Case II as were presented for Case I. Essentially, the comments to be made about this test condition are identical to Case I except the wake effects are appreciably amplified and stall is apparent on the retreating blade.

The results for this case where stall is present are summarized in Figure 23. Experimental, BRAM, and 2DPD normal force coefficients are compared. The BRAM curve is based on a total

rotor lift about 10 percent less than the experimental. The reason for this is that the mathematical model with a free wake has convergence problems when stall is present, and the program would not converge at the exact test total lift. Therefore, the calculated normal force distribution is somewhat low.

The normal force distribution calculated by BRAM is not grossly different on the advancing blade. The wake influence is felt on the advancing blade as a rapid change in force ( $\psi = 90$  degrees). The calculated wake effect is about 20 degrees out of phase with the experiment. The retreating blade shows the combination of three-dimensional effects and stall. The correlation might be significantly improved if the calculation technique included oscillating airfoil effects. Such a program is under development at Bell, but it is not presently available.

In general, it is felt that for this case a two-dimensional free-wake, oscillating-airfoil mathematical model would adequately predict the rotor performance. It is doubtful that this technique would predict all of the high-frequency motions which are most important in an aeroelastic analysis. However, such a technique would probably be an order of magnitude superior to a quasi-static uniform inflow analysis for predicting aeroelastic blade response at low advance ratios. Eventually, as the knowledge of rotor behavior is increased, an unsteady three-dimensional analysis must be evolved.

Case III:  $\mu = 0.5$ ,  $C_{L/\sigma} = 0.0424$ ,  $M_{(1.0, 90)} = 0.37$ .  
(High  $\mu$ , low lift)

Figure 26 is the tip vortex core path for  $\mu = 0.5$ . This figure will be used for Cases III and IV in a similar manner as Figure 19 was used for Cases I and II.

This case, as compared with Case I, shows the lower angles of attack on the advancing side and higher angles on the retreating side, Figure 14, as would be expected. The pressure coefficients, Figure 27, for  $30^\circ \leq \psi \leq 150^\circ$  are well behaved with respect to two-dimensional theory. However, the retreating blade pressure distributions rapidly diverge from two-dimensional theory, and the trend of negative pressures on the lower surface which appeared in Case I is amplified for this case. The integrated coefficients, Figures 28 through 30, show major excursions from theory for  $190^\circ \leq \psi \leq 260^\circ$ . However, the angle-of-attack curve of Figure 14 for Case III does not show any large angles or sudden changes that normally accompany changes in the aerodynamic coefficient. This fact raises the question of what causes large changes in the

coefficients without changing the angle of attack. One answer for the magnitude of the coefficients is that the blade is reacting to an encounter with its own tip vortex where the core is approximately parallel to the span and much closer than the  $\mu = 0.2$  case. This condition is the one described in the Stagnation Point Measurements section of the Test Results and Discussion; specifically item (1) of the assumptions. Therefore, the angle-of-attack curve for this azimuth increment may be invalid.

Case IV:  $\mu = 0.5$ ,  $C_{L/\sigma} = 0.067$ ,  $M(1.0, 90) = 0.37$ .  
(High  $\mu$ , high lift)

Case IV shows the greatest difference between theoretical and measured angle of attack, Figure 14, of the four cases discussed. Primarily, this is caused by the inability of BRAM to correctly predict rotor performance at high advance ratios, Reference 1. The pressure coefficients in this case, Figure 31, are similar to those of Case III in that on the advancing blade they are well behaved because the angle of attack is small. The only noticeable difference between Case III and IV is that the excursions of the integrated coefficients, Figures 32 through 34, on the retreating blade for Case IV are spread over a wider azimuth range than Case III. This can be explained as a combination of the condition described in Case III and retreating blade stall which would be expected for the high lift case and is predicted by theory.

For all four cases, the sudden change in the force and moment coefficients around  $\psi = 270^\circ$  is partially caused by the close proximity of the blade to a vortex which is nearly parallel to the span at  $r/R = .75$ . Of the four cases, only Case I has a complete set of both experimental and theoretical data. Neither BRAM nor 2DPD is capable of accurately predicting the aerodynamics of a rotor operating near stall at high advance ratios. Also, the experimental hot wire and BLB data are incomplete in portions of the third and fourth quadrants. The pitching moment coefficient predicted by 2DPD is for steady-state; therefore, the theoretical  $C_{mc}/4$ 's for this airfoil profile are approximately zero. The reason for the large pitching moment coefficients measured in this test must be caused by the unsteady aerodynamics, Reference 14. A complete analysis of these test data and the intermediate advance ratio data is beyond the scope of this report. Such a study is required to define more completely the unknown areas and questions posed by the test results.

## CONCLUSIONS

The wind-tunnel test and subsequent analysis of the data for determining the aerodynamic environment of a rotor in forward flight have yielded the following conclusions:

- The use of the advanced instrumentation in forward flight was shown to be feasible.
- 1. The hot wire anemometer method of measuring angle of attack is accurate, provided the flow is essentially two-dimensional.
- 2. The Boundary Layer Button showed that the radial flow angles on the upper and lower surfaces of the airfoil are different, causing an effective camber. Also, there is a gradual curving inboard of the flow as  $x/c$  increases.
- 3. Absolute static pressure measurements show unusual shapes and magnitudes for some azimuth positions; however, differential pressures and integrated coefficients generally agree with previously measured data. It is concluded that differential pressure measurements mask some of the details of the aero-environment.
- The agreement between theory and experimental data is good on the advancing blade; however, there is considerable divergence between theory and experiment on the retreating blade. The conclusion is that the environment of the 0.75R station on the advancing blade can be predicted reasonably by two-dimensional theory. Because of the unsteady effects of the blade reacting to the wake, two-dimensional theory is not capable of accurately predicting the aerodynamics of a rotor in the third and fourth quadrants. Also, the range of the instrumentation must be extended to measure the aerodynamic environment in these areas.
- The effects of the wake at high advance ratios ( $\mu = 0.4$  and 0.5) are not negligible, and should be included in rotor analysis programs.
- The measured pitching moment coefficients indicated greater magnitudes and higher frequencies than predicted by theory.



Figure 1. Gloved Section of Rotor With Hot Wire Anemometer in Leading Edge and Boundary Layer Buttons Along the Chord.



**Figure 2. Installation of Static Pressure Transducers  
in Gloved Section of Rotor.**

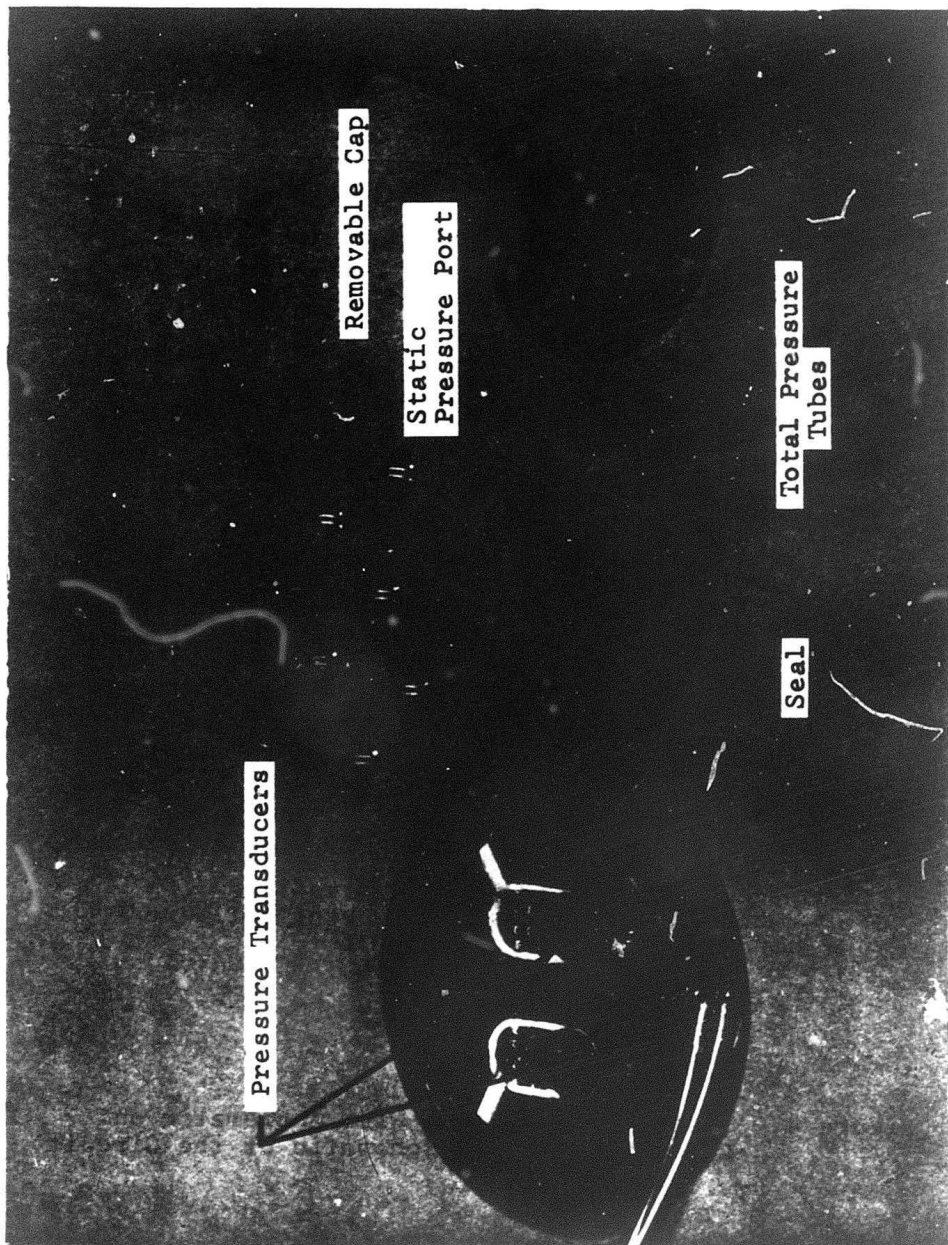
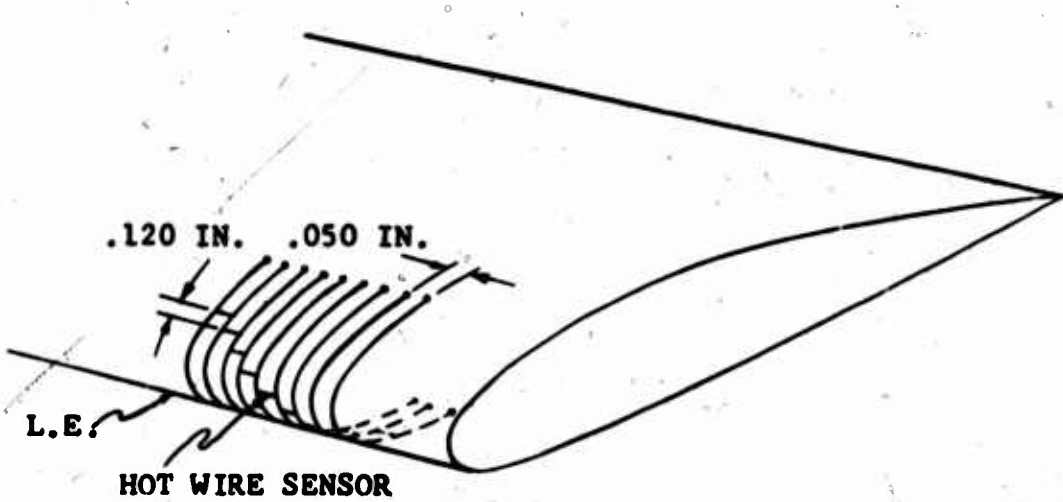
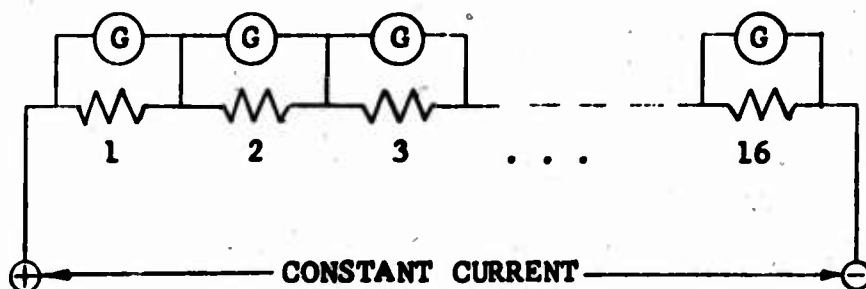


Figure 3. Detailed View of Boundary Layer Button.



Sketch of Hot Wire Anemometer Installation



Schematic of Constant-Current Hot Wire

Figure 4. Installation of Hot Wire Anemometer on Leading Edge, and Schematic of the Circuit.

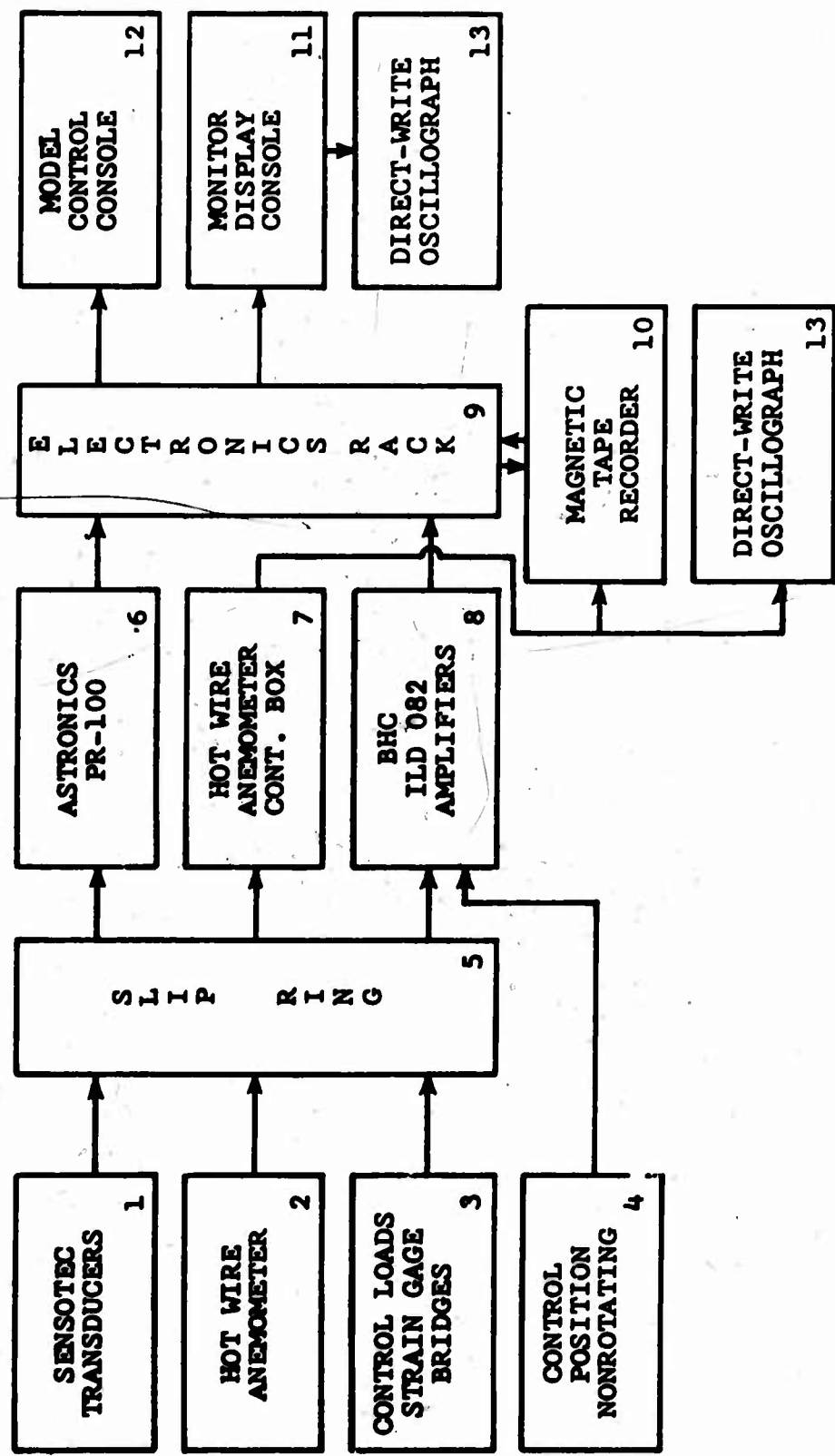


Figure 5. Block Diagram of Data Acquisition System.

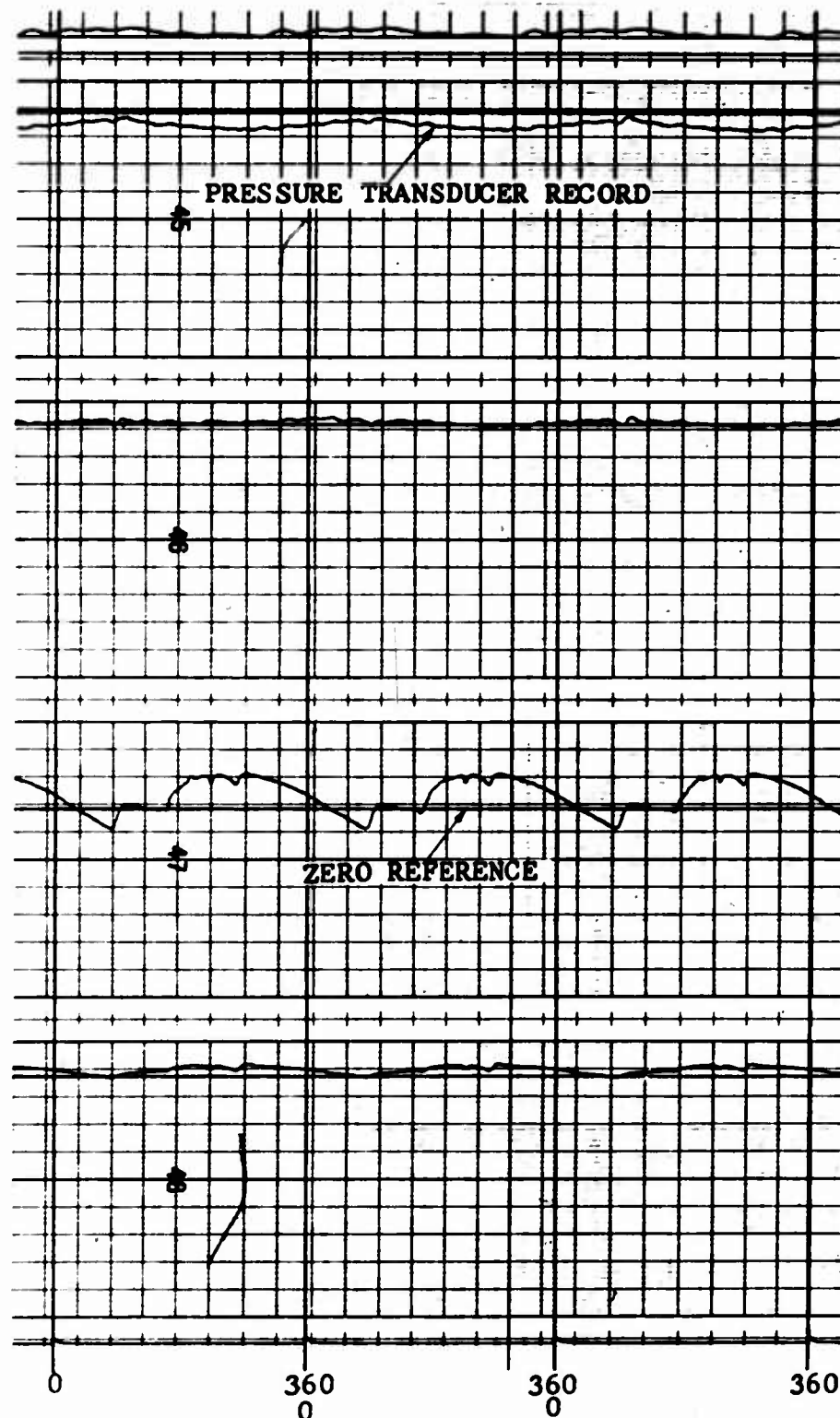
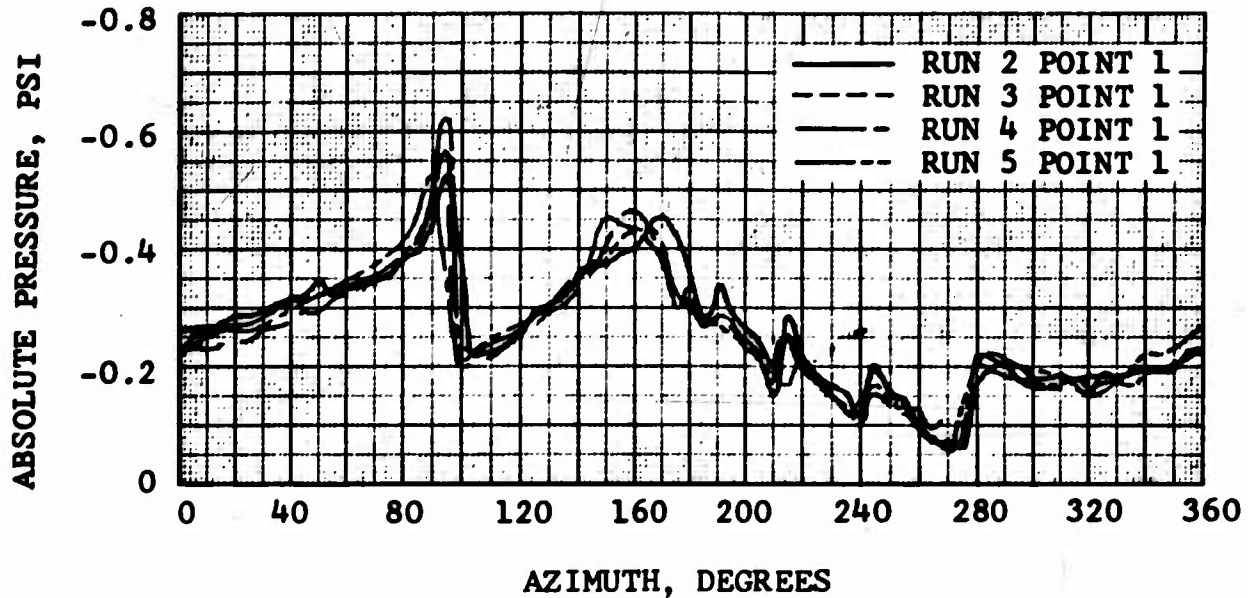
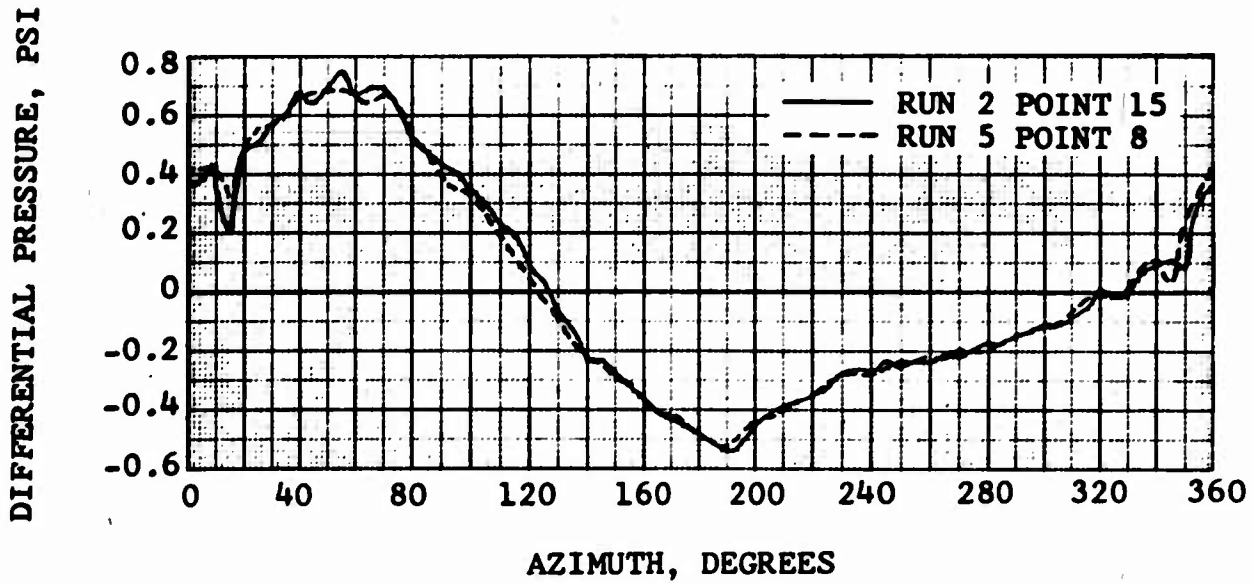


Figure 6. Repeatability of Test Data for Three Revolutions of the Rotor.



(a) Absolute Pressure ( $x/c=.007$ , Upper Surface)  
 $\mu=0.20, M_{(1.0,90)}=.30, \theta=3.1^\circ, \beta=0$ .



(b) Differential Pressure, BLB ( $x/c=.3$ , Lower Surface)  
 $\mu=0.50, M_{(1.0,90)}=.37, \theta=11.0^\circ, \beta=0$ .

Figure 7. Repeatability of Pressure Data for the Four Test Runs.

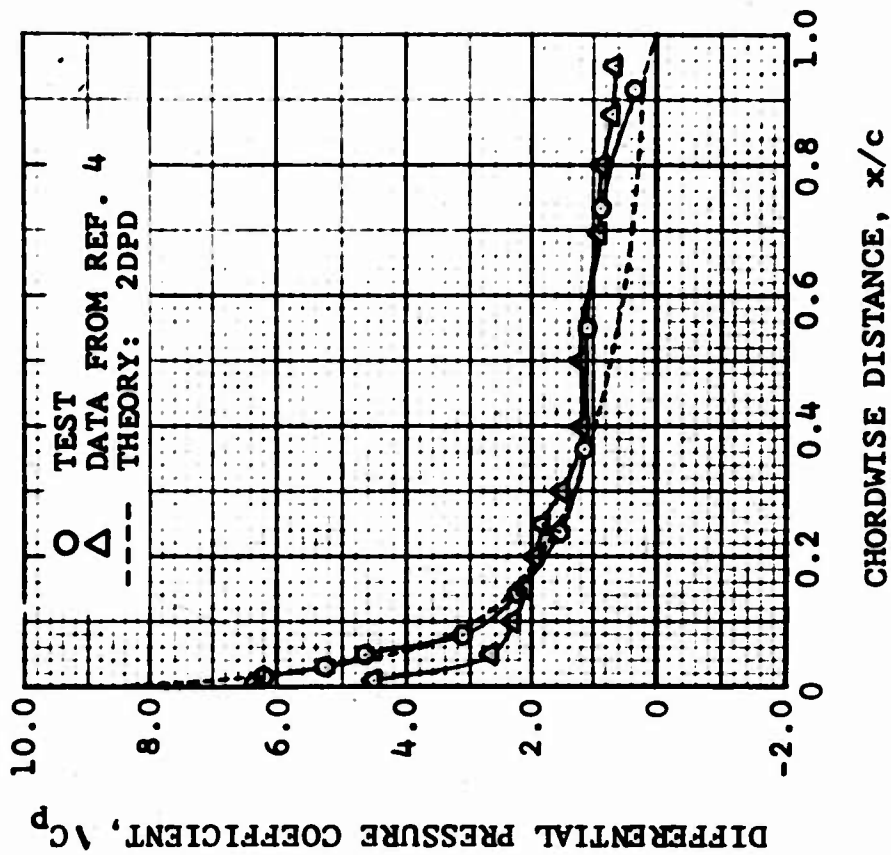
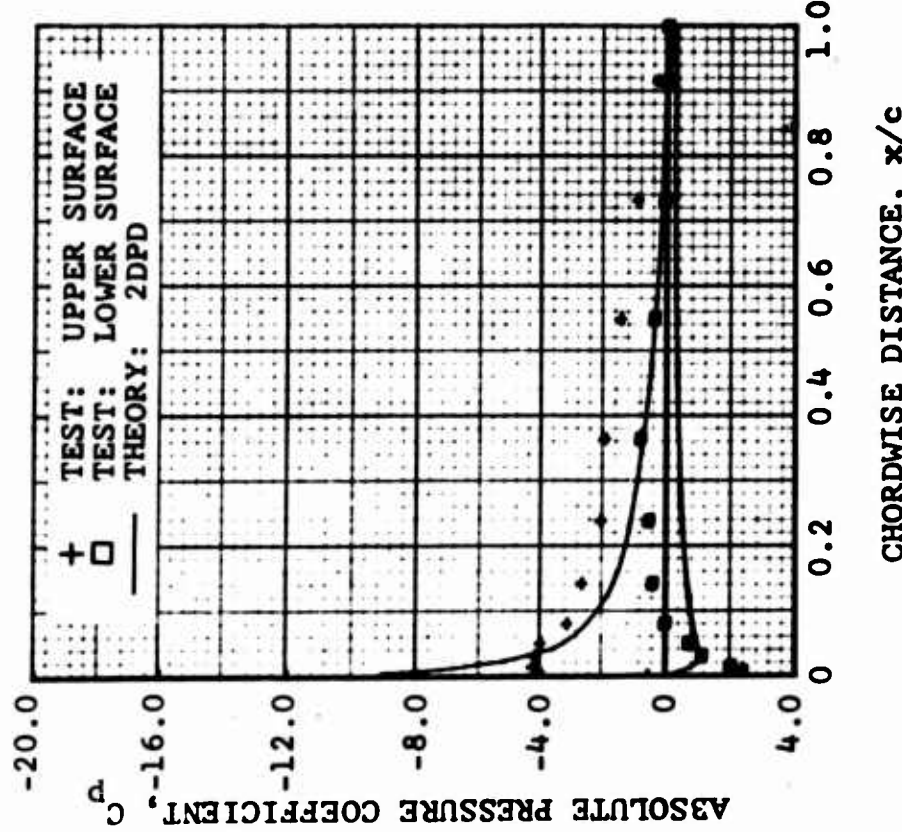


Figure 8. Comparison of Absolute and Differential Pressure Distributions, Run 2, Point 3;  $\mu = 0.20$ ,  $M(1.0, 90) = 0.30$ ,  $\theta_{75R} = 11.0^\circ$ ,  $\beta = \hat{\beta} \approx 0$ ,  $\psi = 240^\circ$ ,  $\alpha = 14.5^\circ$ .

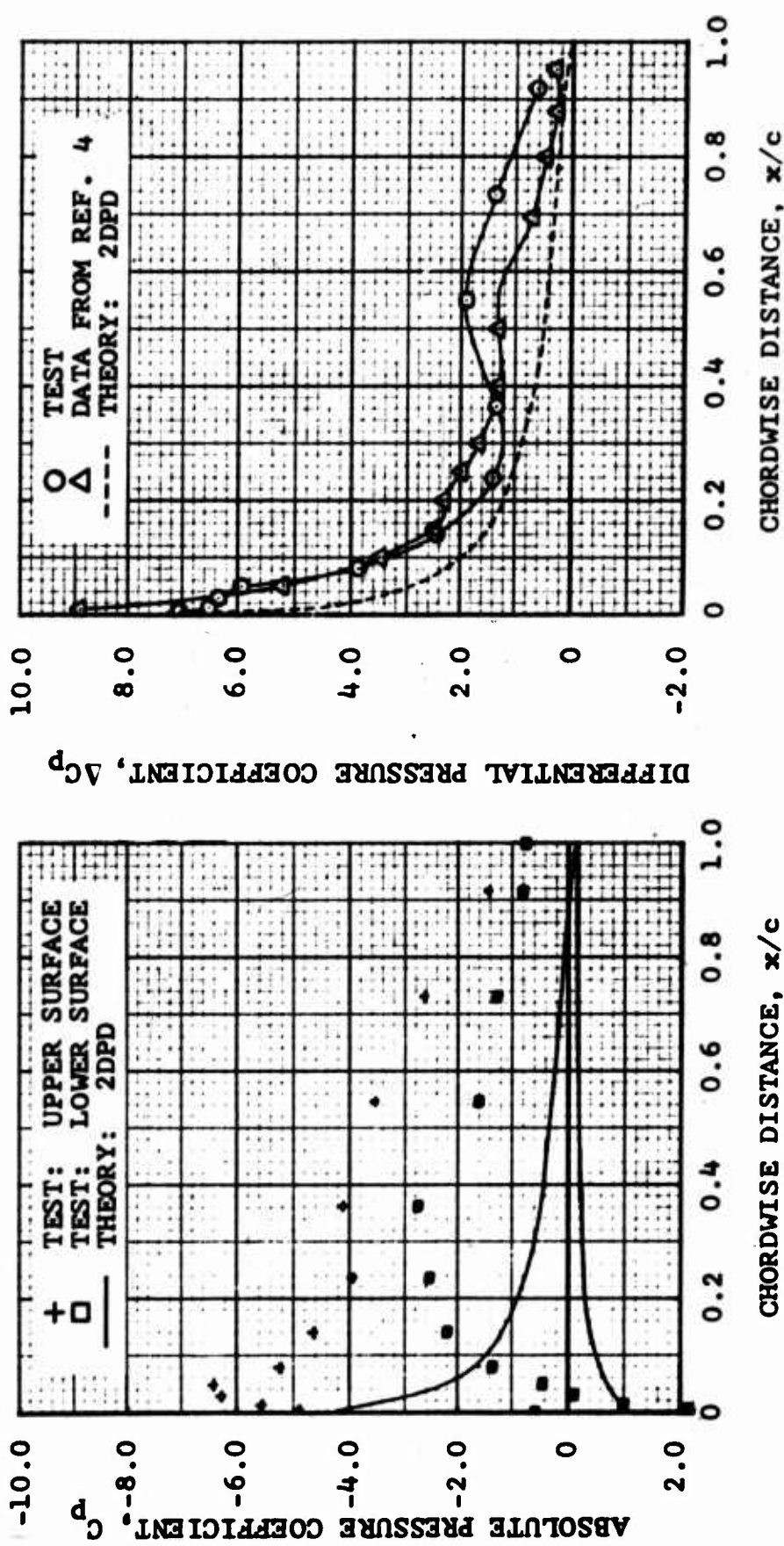


Figure 9. Comparison of Absolute and Differential Pressure Distributions,  
 Run 2; Point 15;  $\mu = 0.50$ ,  $M_{(1.0, 90)} = 0.37$ ,  $\theta_{75R} = 7.2^\circ$ ,  
 $\dot{\beta} = \dot{\beta} = 0$ ,  $\psi = 210^\circ$ ,  $\alpha = 8.3^\circ$ .

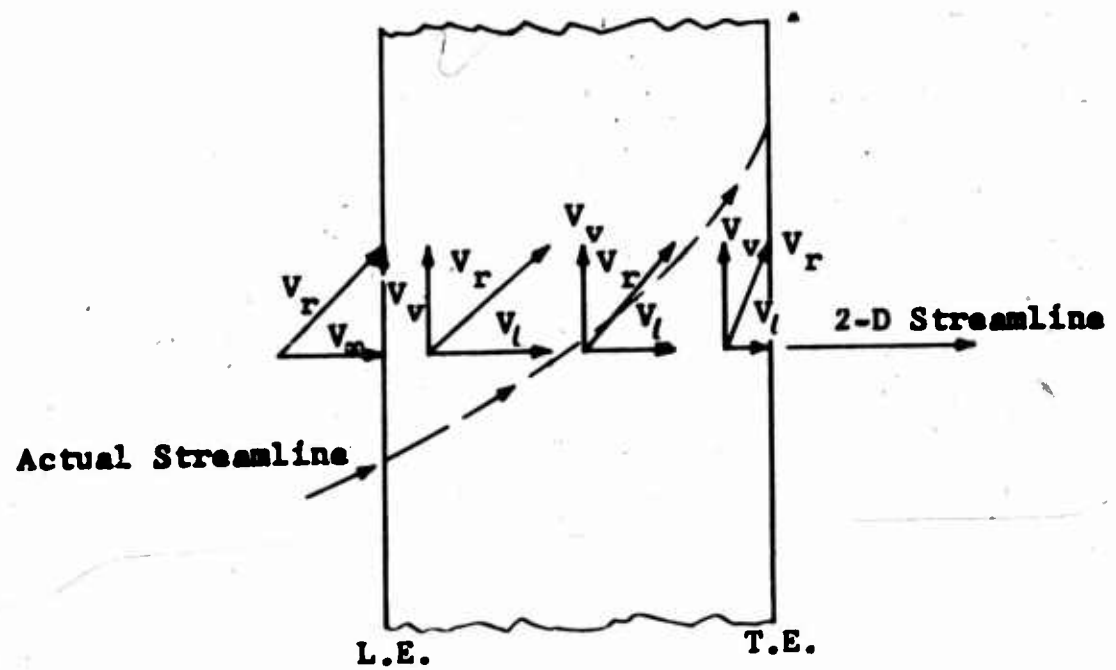
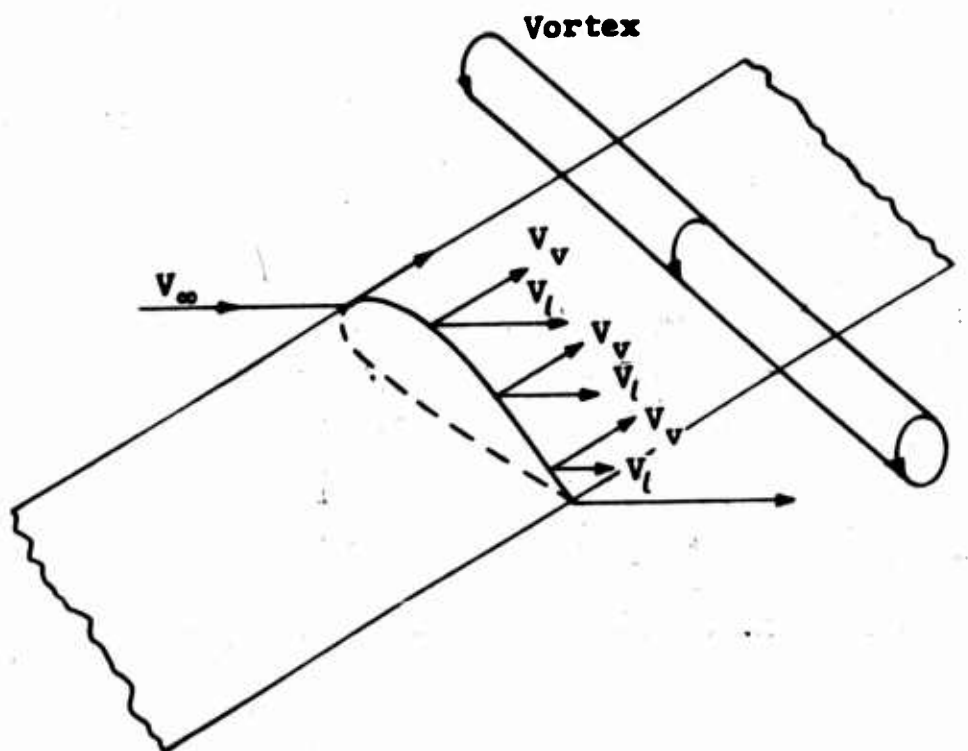


Figure 10. Influence of Vortex on Freestream Velocity Vector.

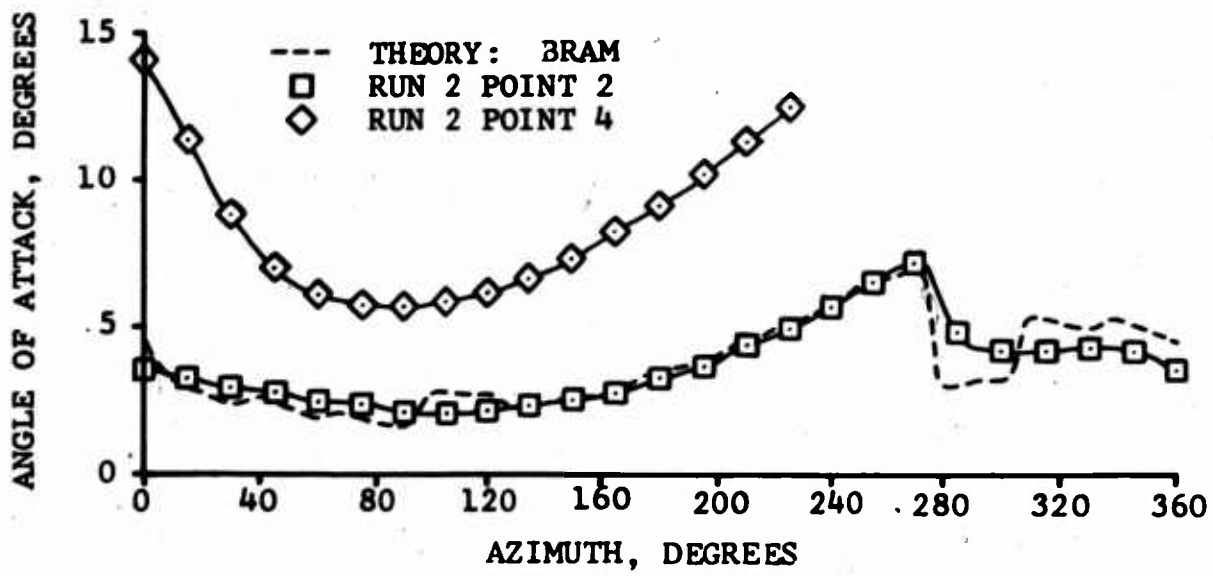
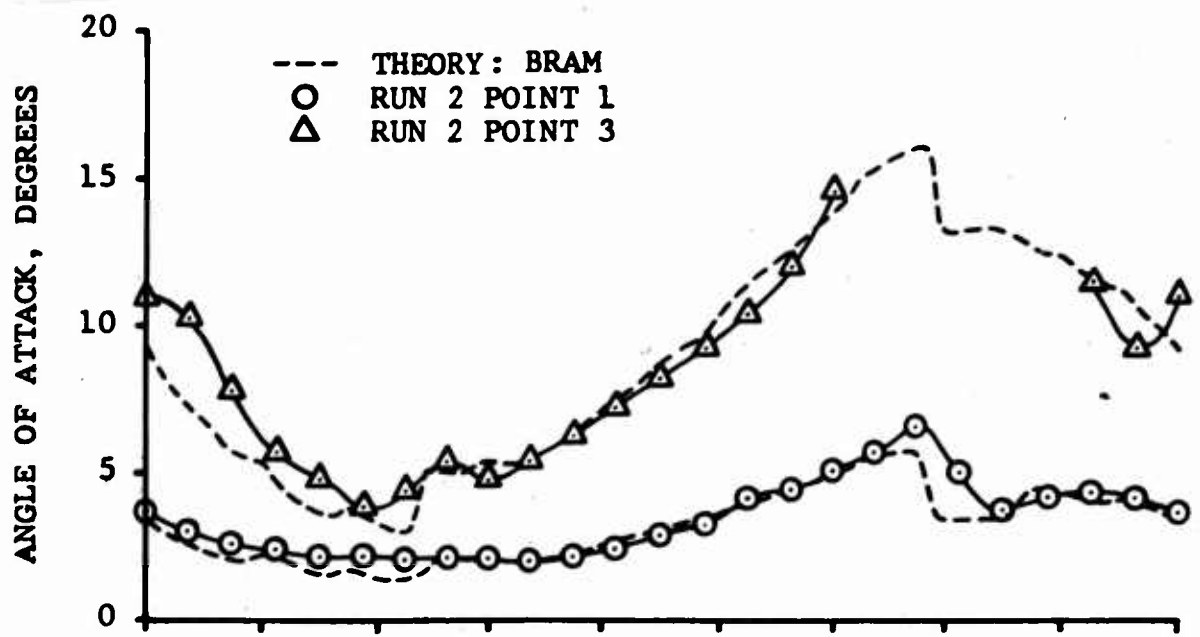


Figure 11. Section Angle of Attack Versus Azimuth;  
 $\mu = 0.20$ ,  $M_{(1.0, 90)} = 0.30$ .

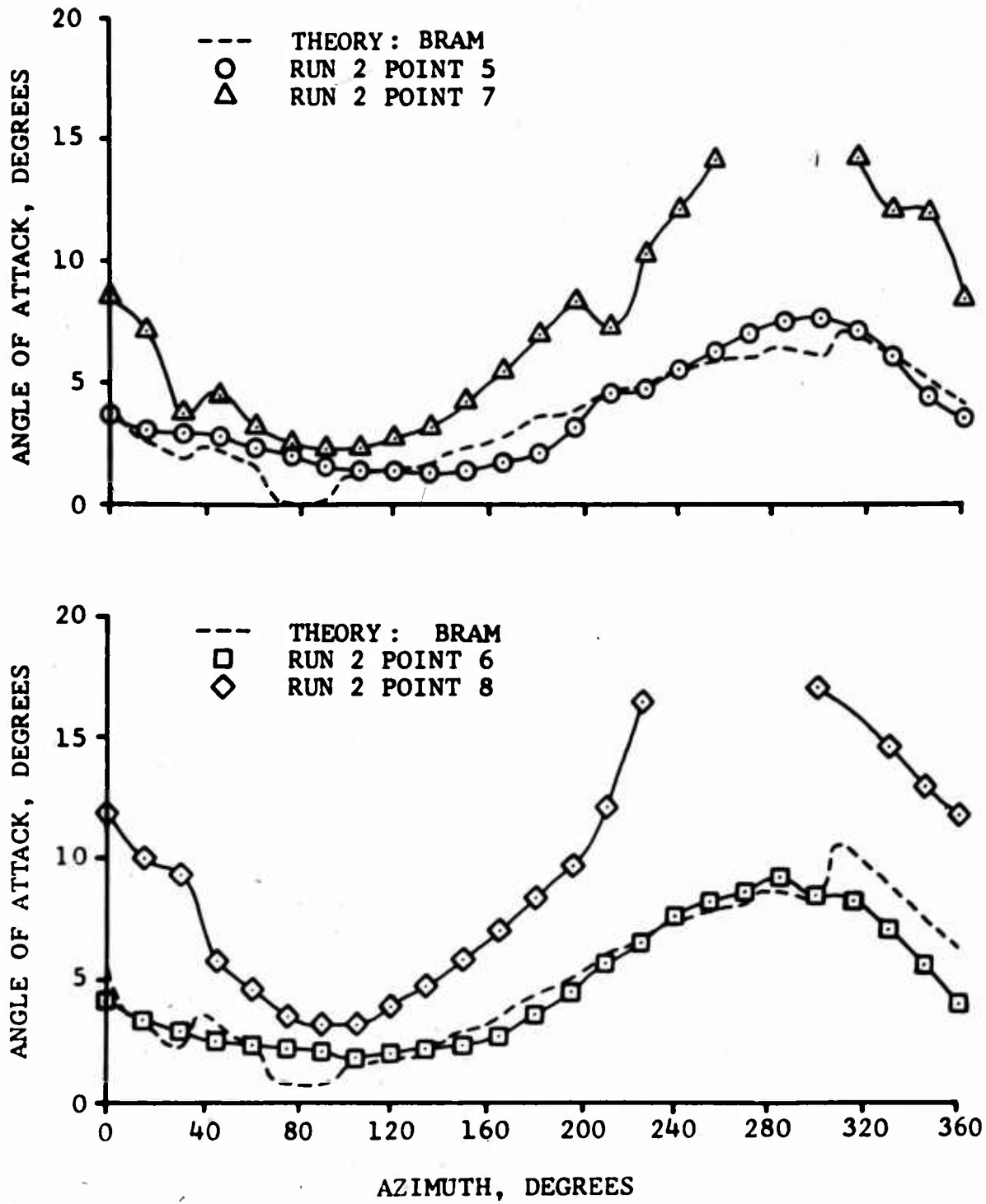


Figure 12. Section Angle of Attack Versus Azimuth;  
 $\mu = 0.30$ ,  $M_{(1.0, 90)} = 0.32$ .

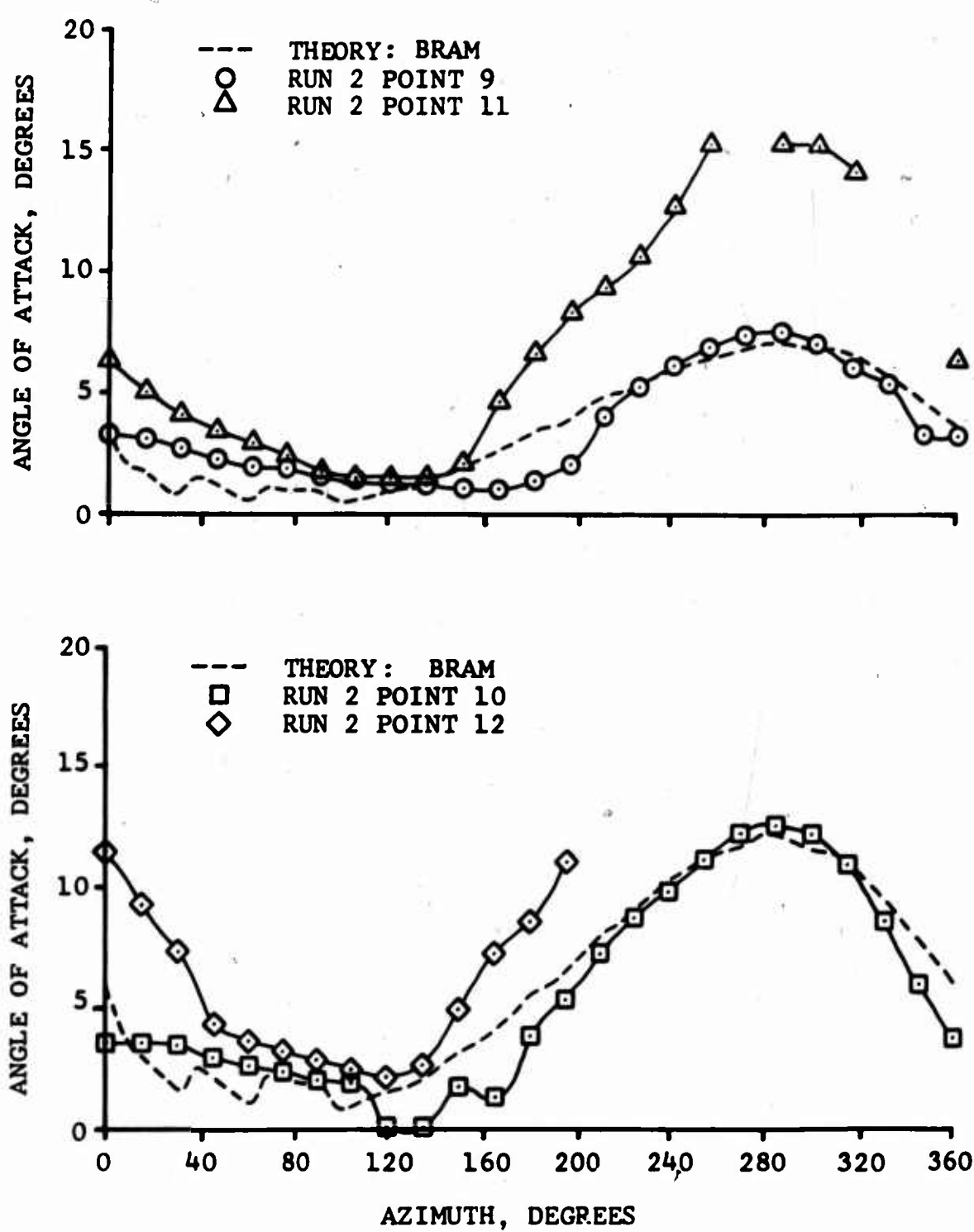


Figure 13. Section Angle of Attack Versus Azimuth;  
 $\mu = 0.40$ ,  $M_{(1.0, 90)} = 0.34$ .

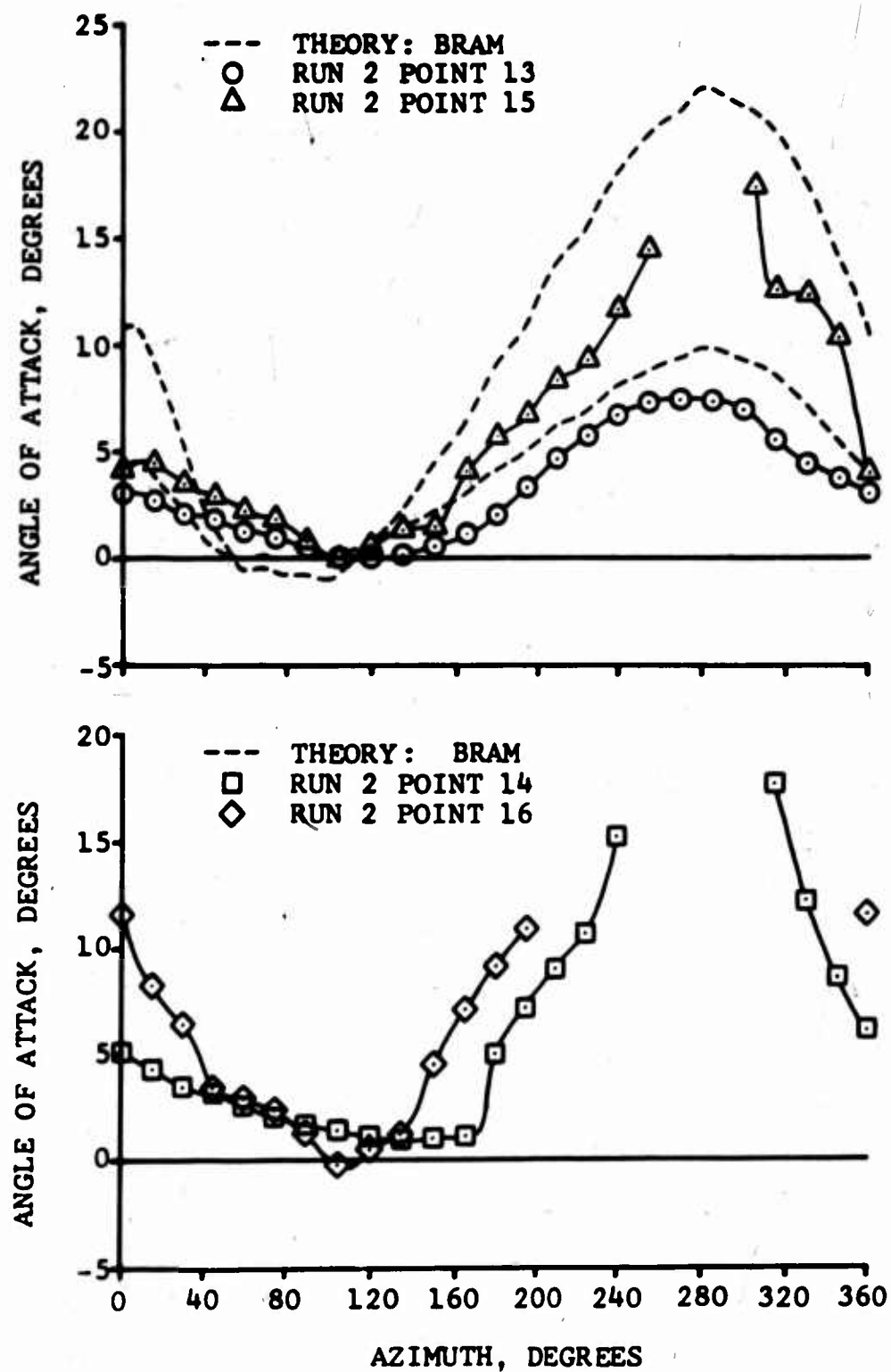


Figure 14. Section Angle of Attack Versus Azimuth;  
 $\mu = 0.50$ ,  $M_{(1.0, 90)} = 0.37$ .

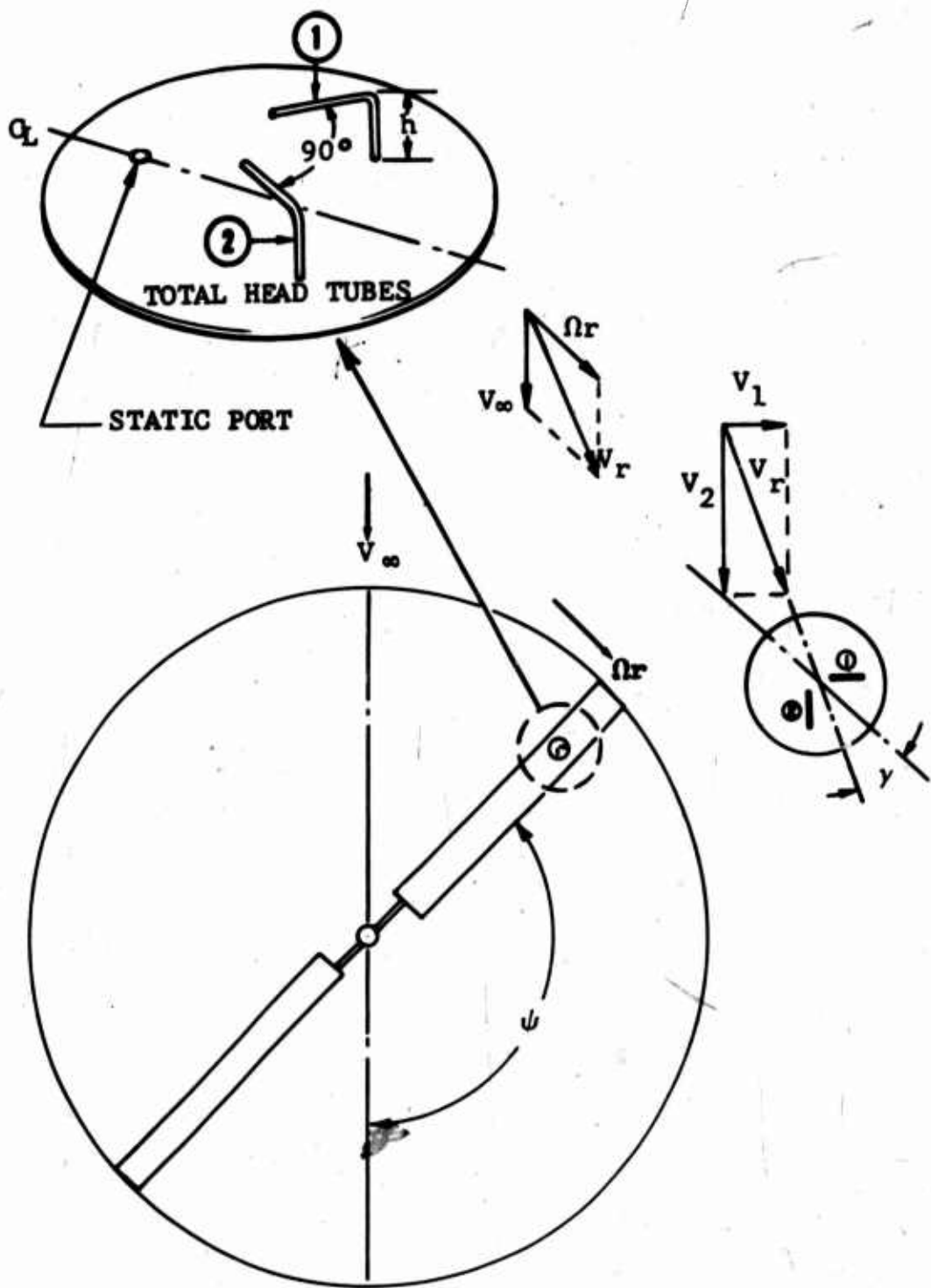


Figure 15. Measurement of Velocity Vector With Boundary Layer Button.

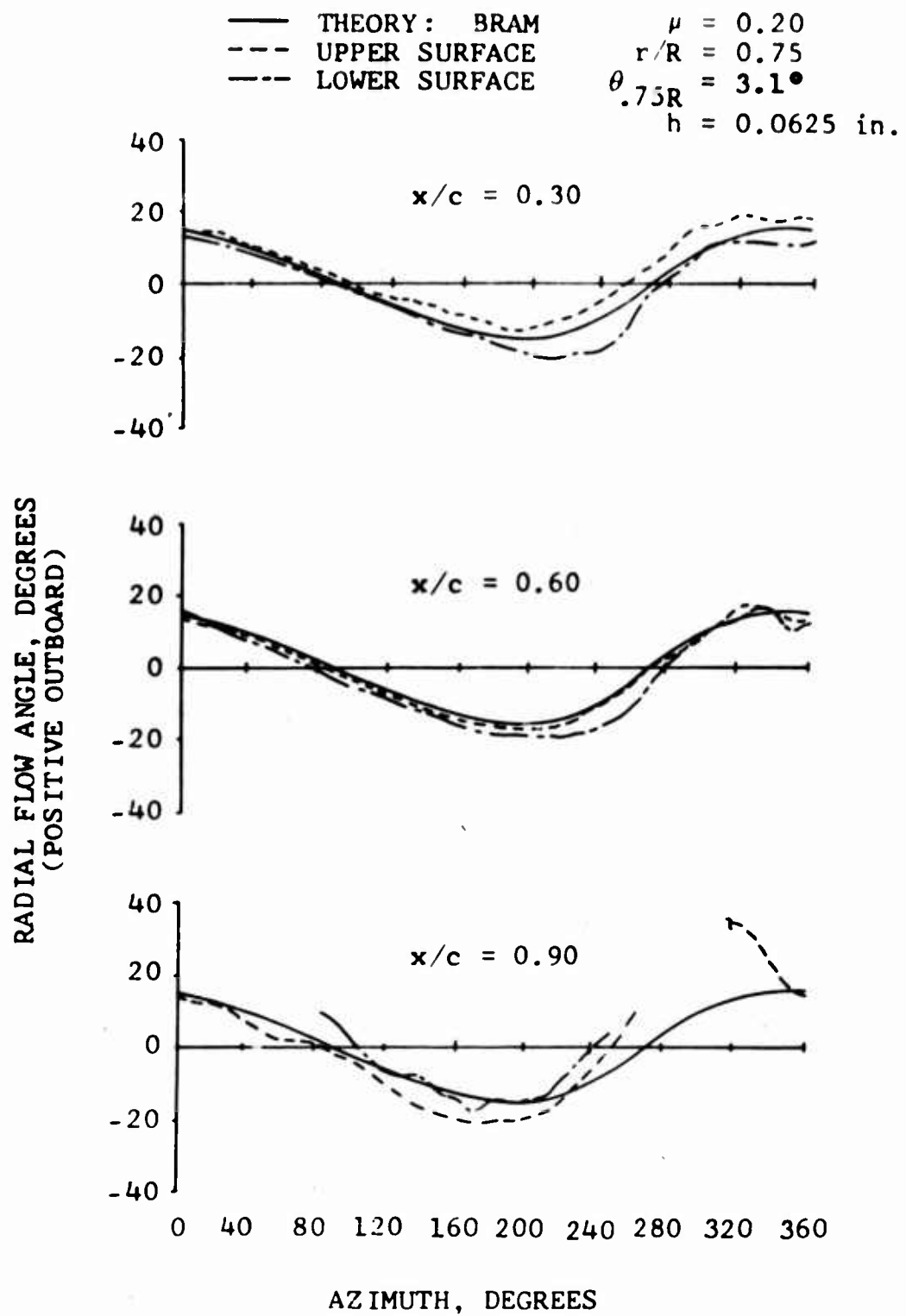


Figure 16. Local Velocity Angle Relative to Chord  
Measured With BLBs.

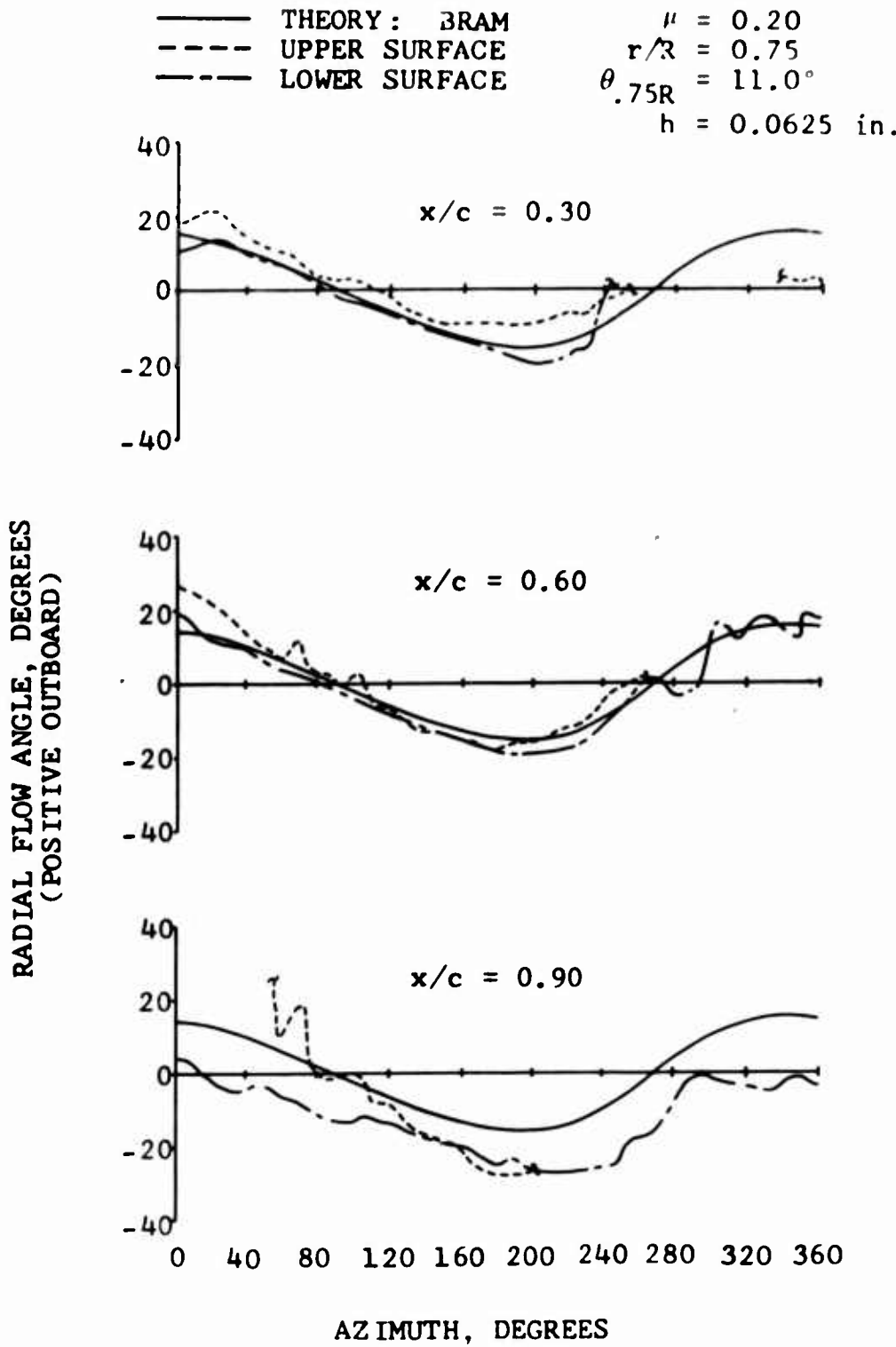


Figure 16. Continued.

——— THEORY: BRAM  
 - - - - - UPPER SURFACE  
 - - - - - LOWER SURFACE

$\mu = 0.30$   
 $r/R = 0.75$   
 $\theta_{.75R} = 3.1^\circ$   
 $h = 0.0625$  in.

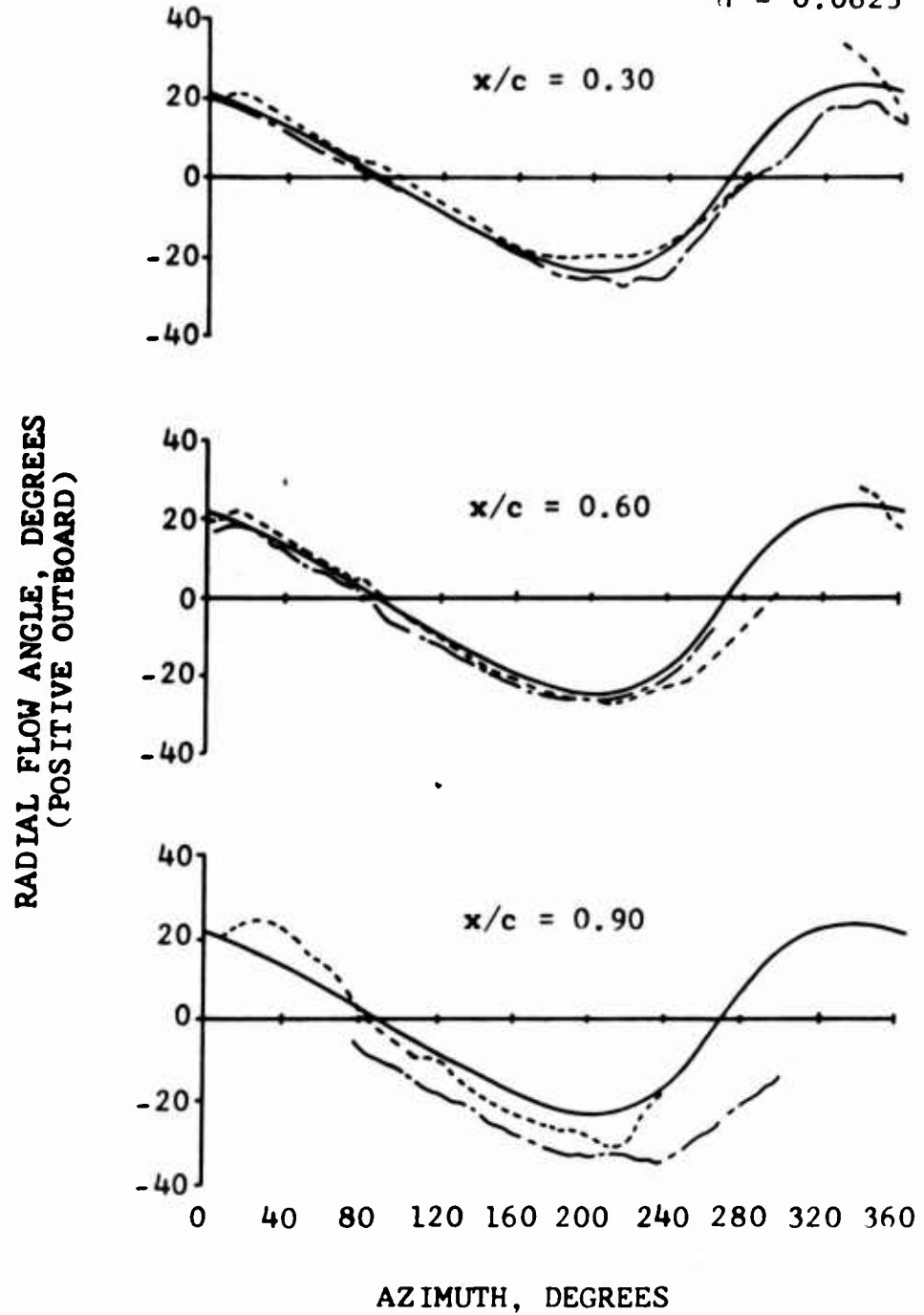


Figure 16. Continued.

——— THEORY: BRAM       $\mu = 0.40$   
 - - - - - UPPER SURFACE       $r/R = 0.75$   
 - - - - - LOWER SURFACE       $\theta_{.75R} = 3.1^\circ$   
 h = 0.0625 in.

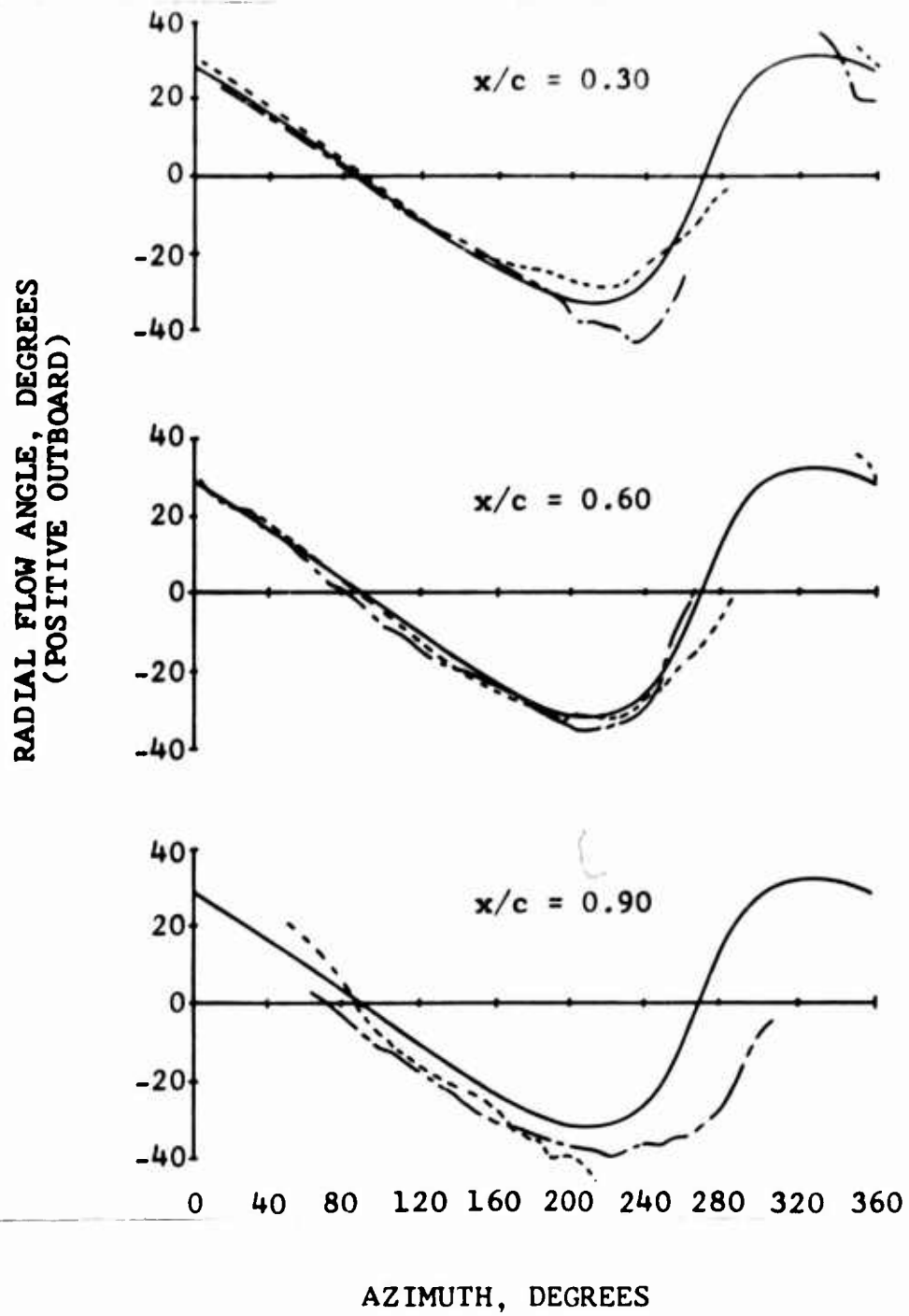


Figure 16. Continued.

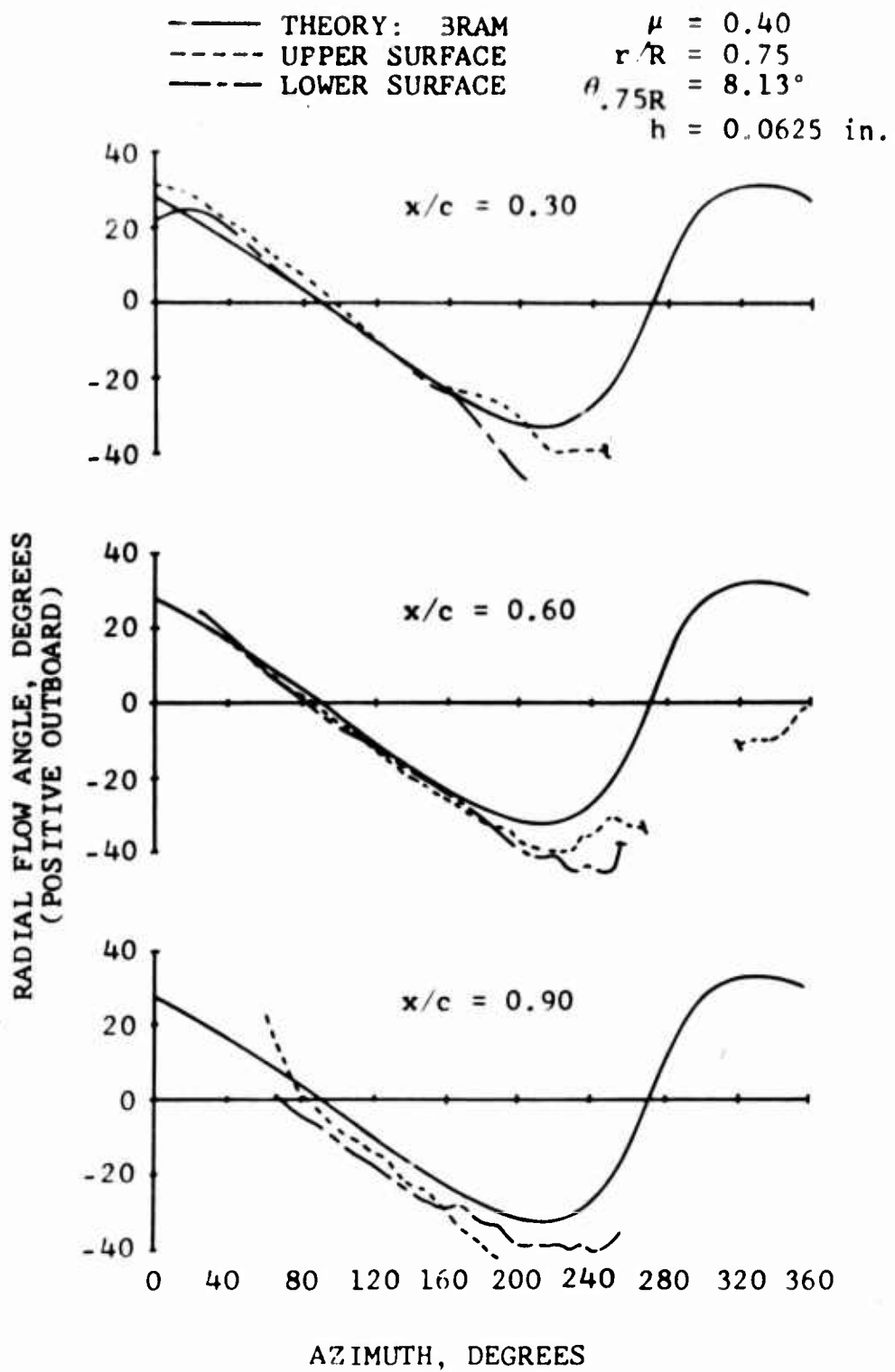
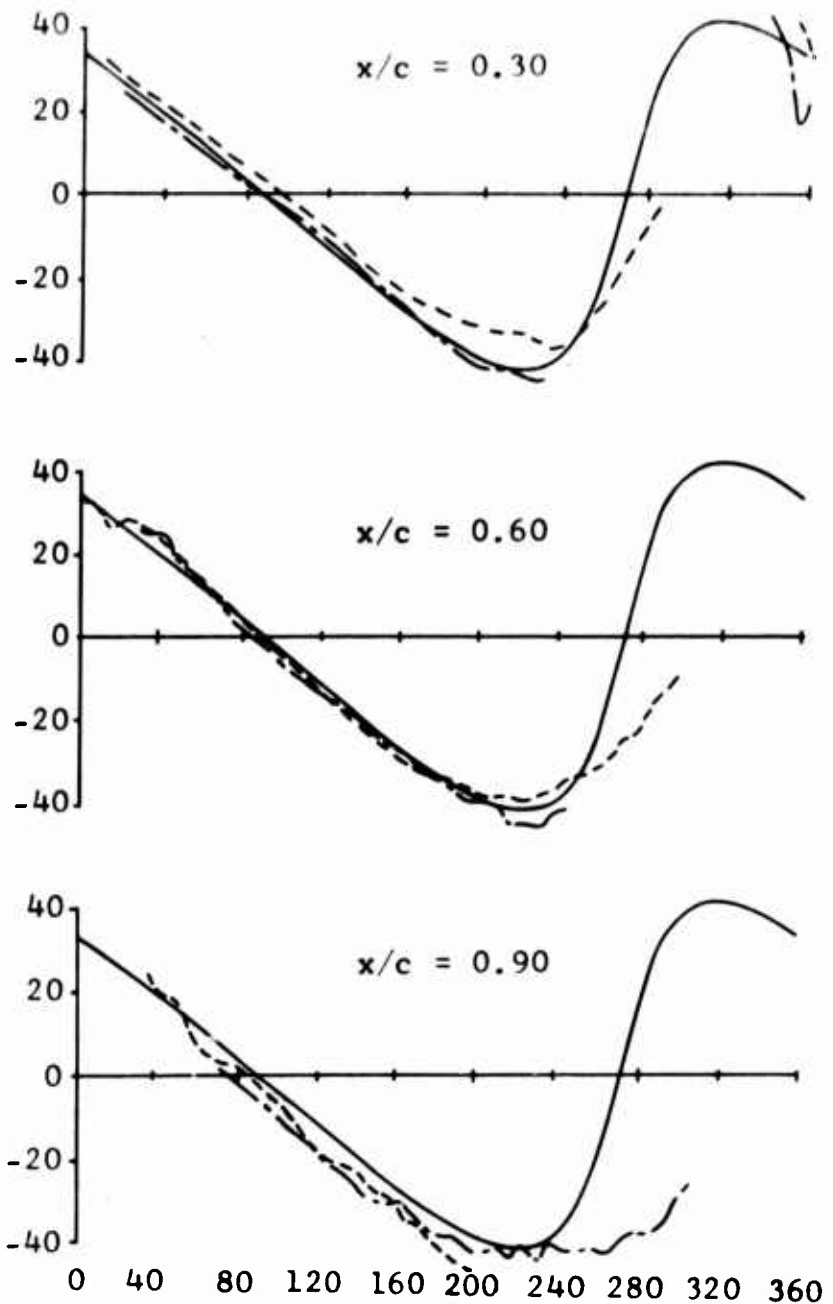


Figure 16. Continued.

— THEORY: BRAM       $\mu = 0.50$   
 - - - - - UPPER SURFACE       $r/R = 0.75$   
 - - - - - LOWER SURFACE       $\theta_{.75R} = 3.1^\circ$   
 - - - - -       $h = 0.0625$  in.

RADIAL FLOW ANGLE, DEGREES  
(POSITIVE OUTBOARD)



AZIMUTH, DEGREES

Figure 16. Concluded.

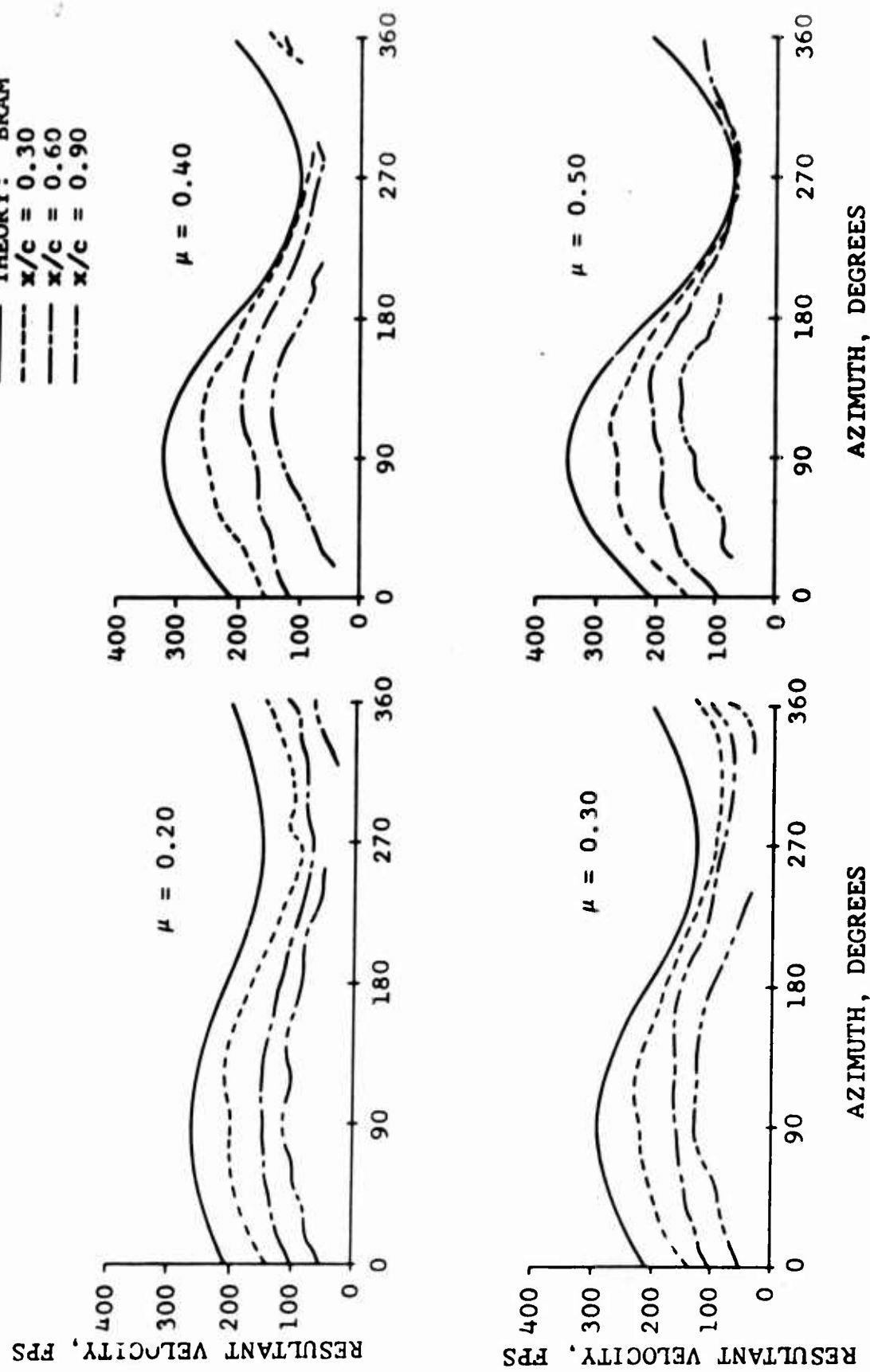


Figure 17. Local Resultant Velocity Measured With BLBs on Upper Surface at Three Chord Stations,  $h = 0.0625$  in.

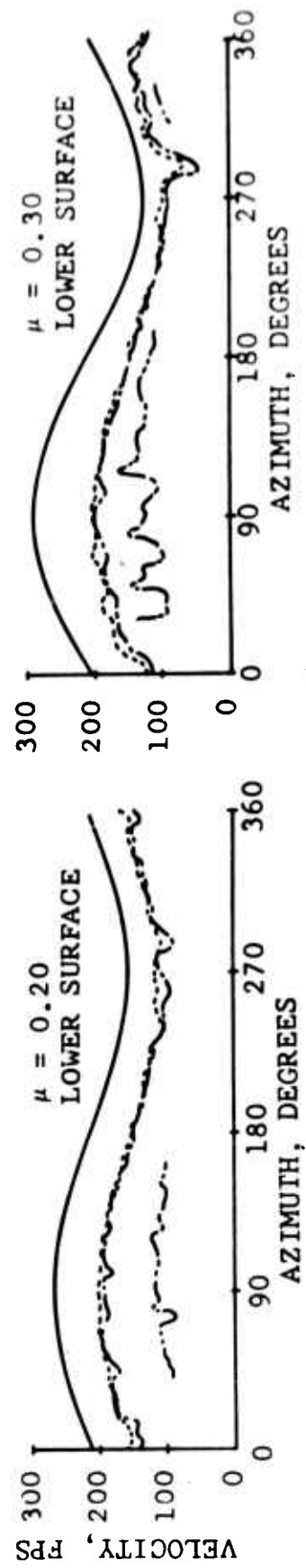
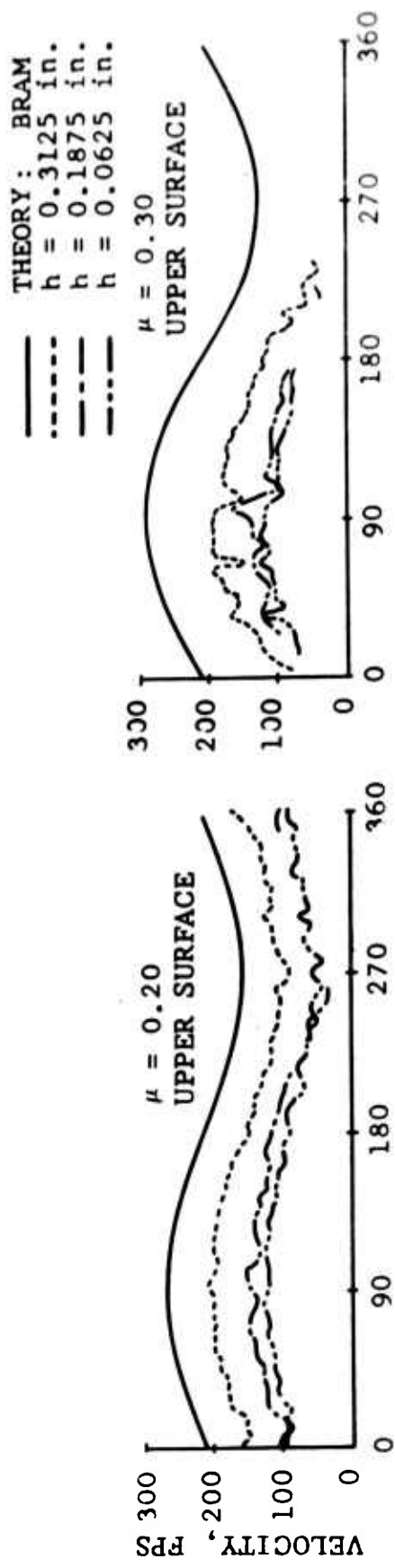


Figure 18. Resultant Velocity of Three Heights Above the Airfoil Surface Versus Azimuth,  $x/c = 0.90$ .

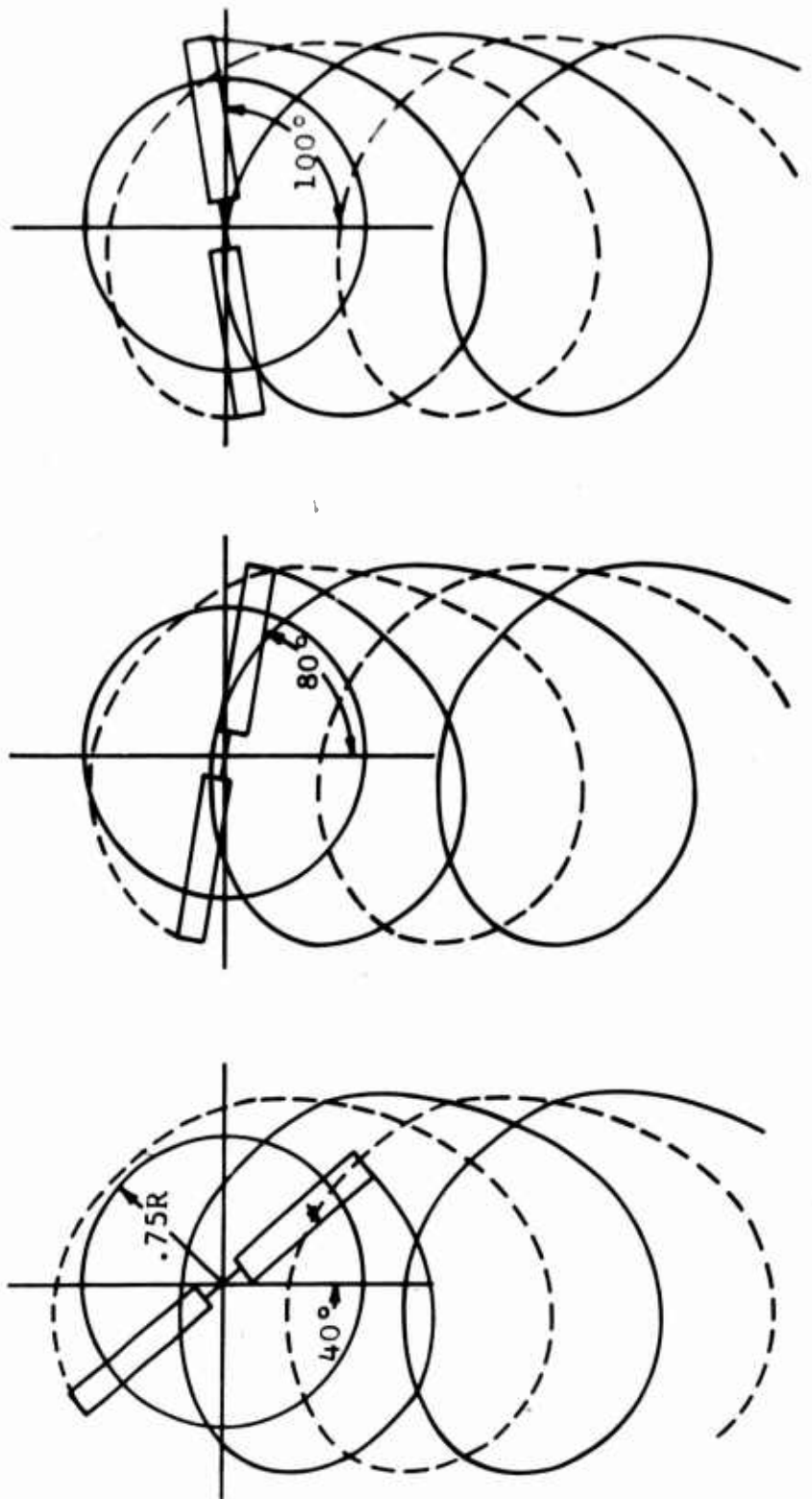
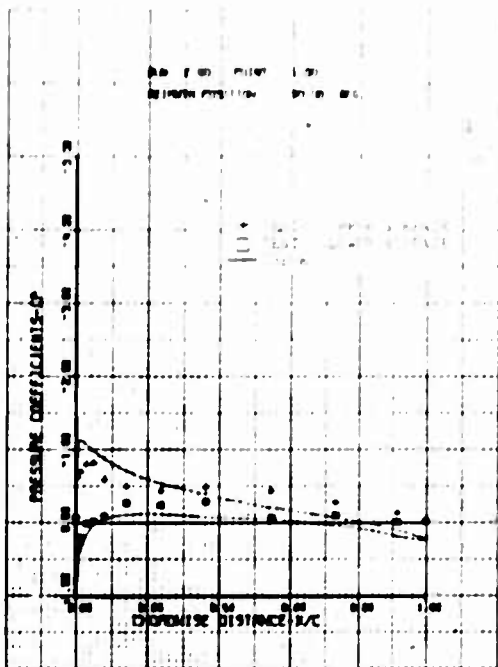
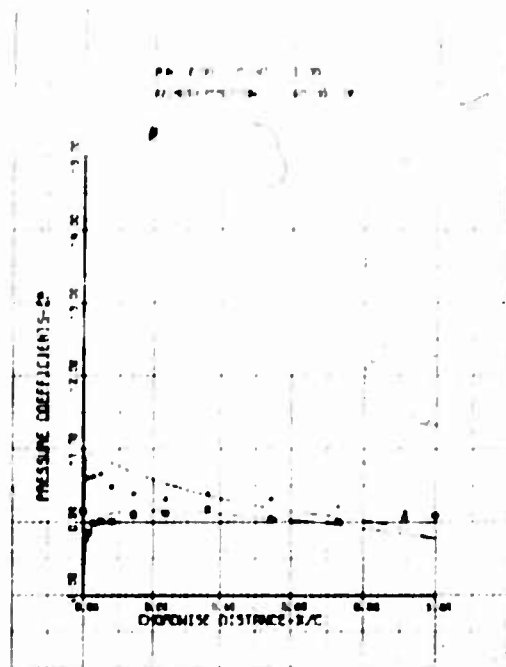


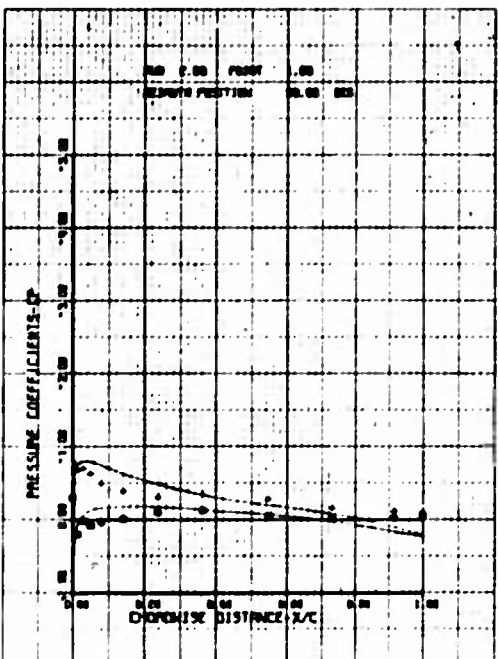
Figure 19. Top View of Tip Vortex Core Path for Two-Bladed Rotor,  $\mu = 0.20$ .



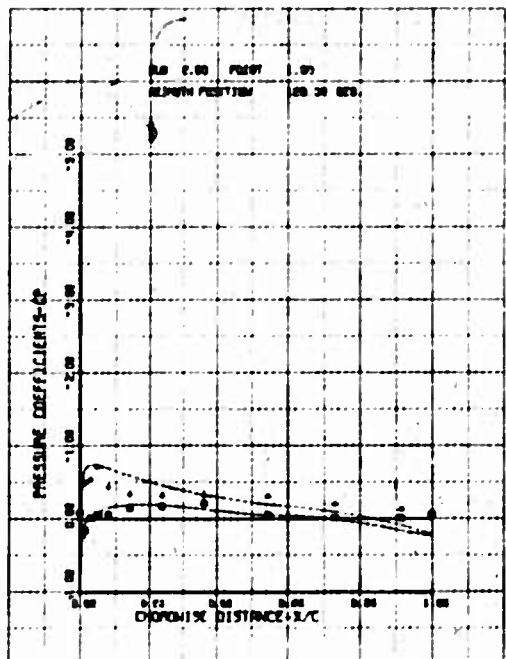
(a)  $\psi = 30^\circ$



(b)  $\psi = 60^\circ$

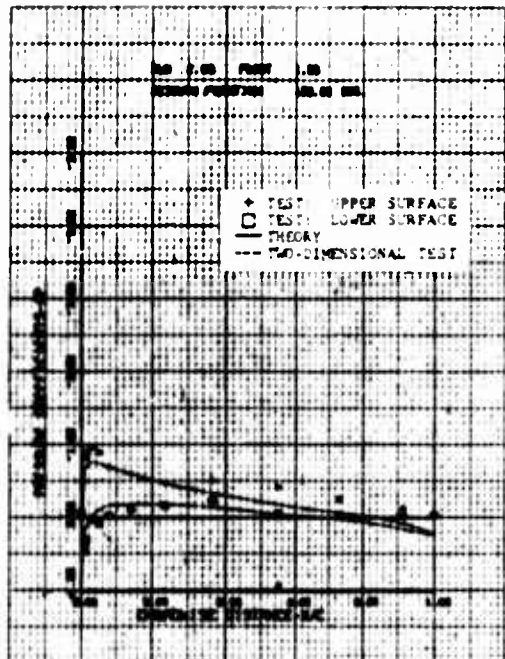


(c)  $\psi = 90^\circ$

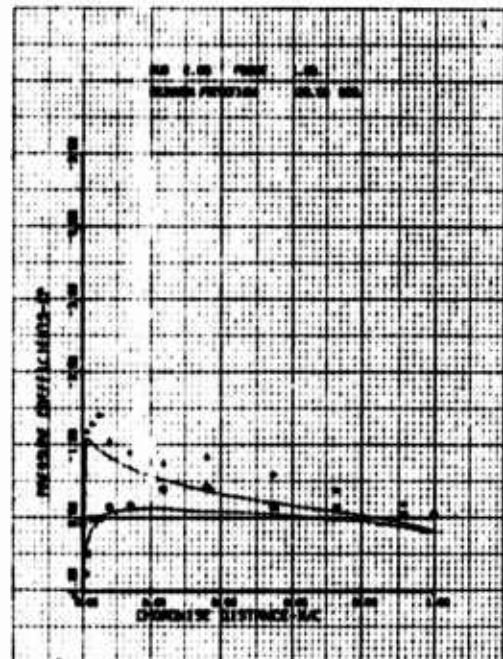


(d)  $\psi = 120^\circ$

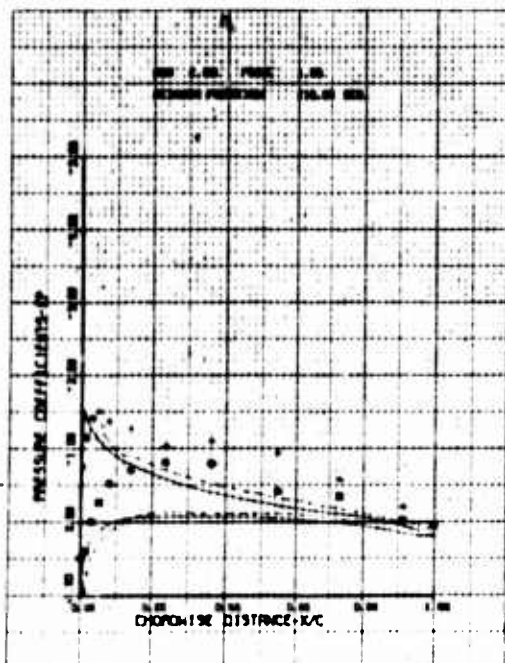
Figure 20. Chordwise Pressure Distribution (Run 2, Point 1);  
 $\mu = 0.20$ ,  $M_{(1.0, 90)} = 0.30$ ,  $\theta_{.75R} = 3.1^\circ$ ,  
 $\beta \approx \ddot{\beta} \approx 0$ .



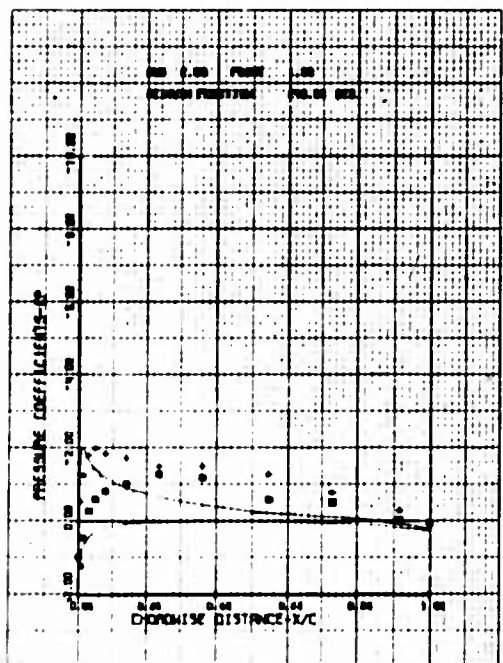
(e)  $\psi = 150^\circ$



(f)  $\psi = 180^\circ$

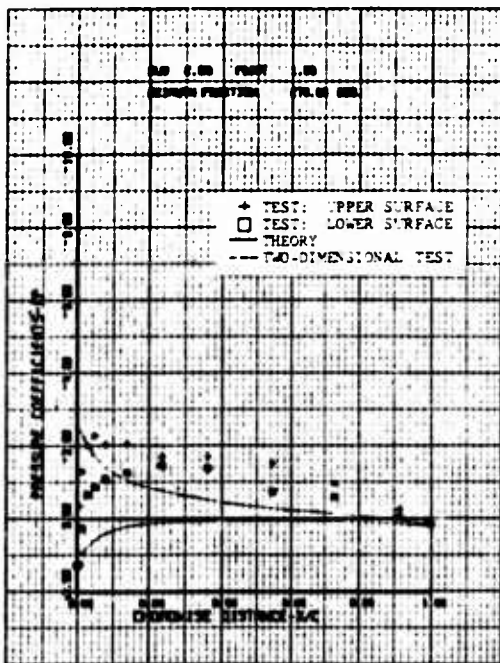


(g)  $\psi = 210^\circ$

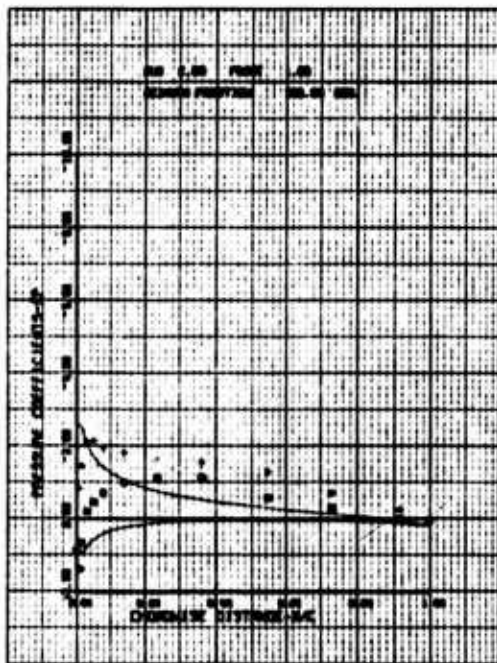


(h)  $\psi = 240^\circ$

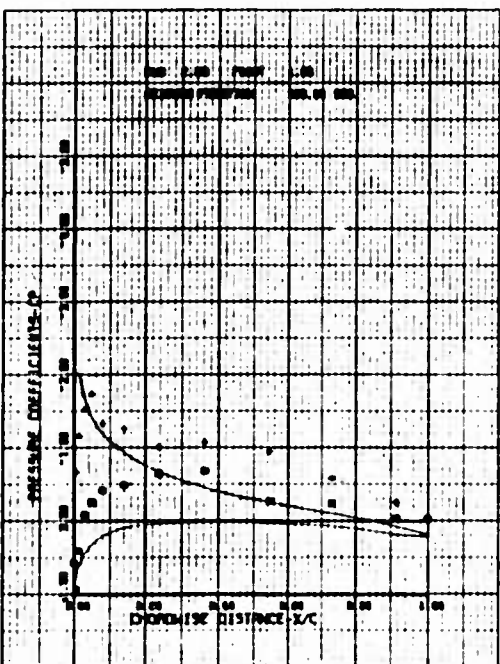
Figure 20. Continued.



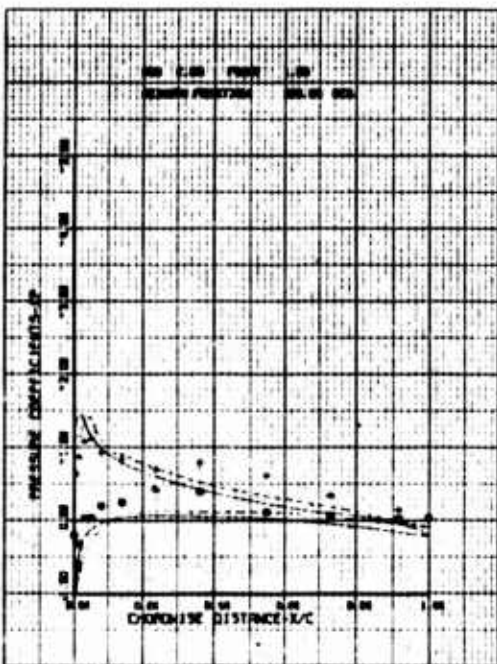
(i)  $\psi = 270^\circ$



(j)  $\psi = 300^\circ$



(k)  $\psi = 330^\circ$



(l)  $\psi = 360^\circ$

Figure 20. Concluded.

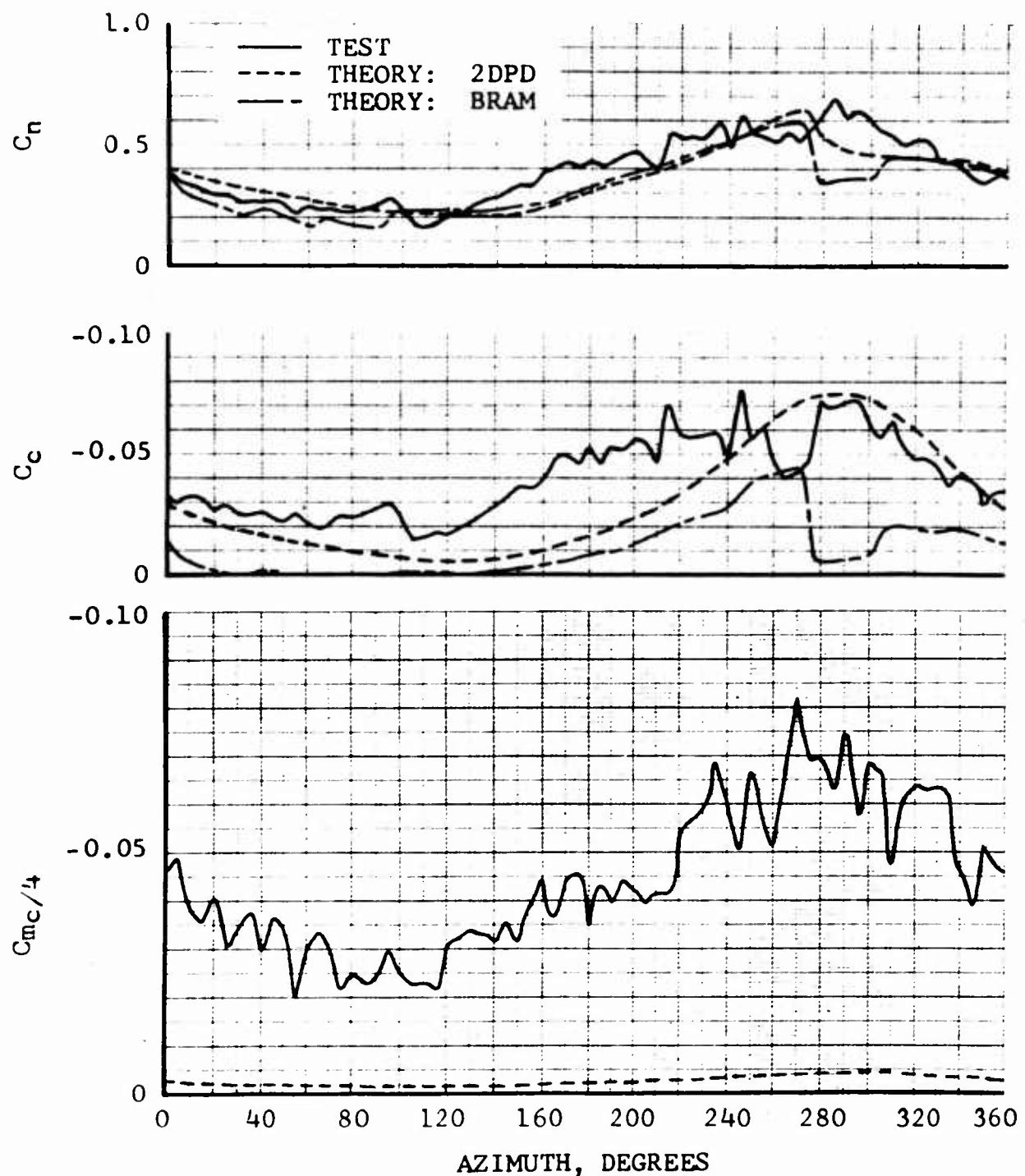
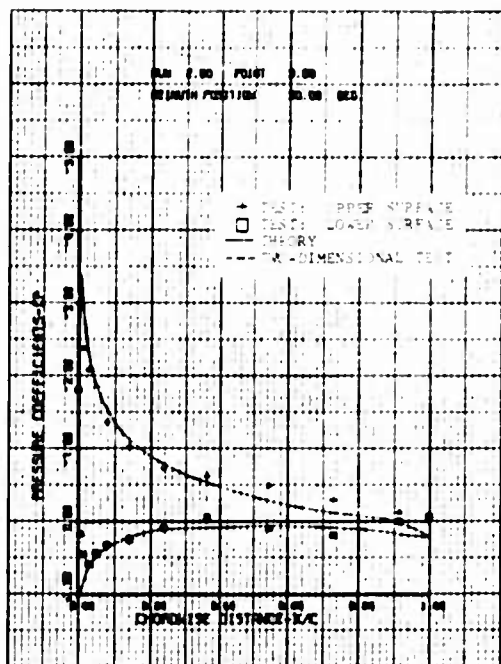
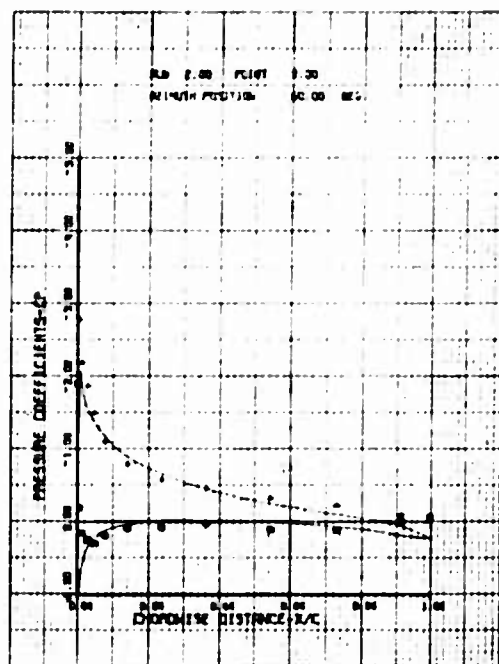


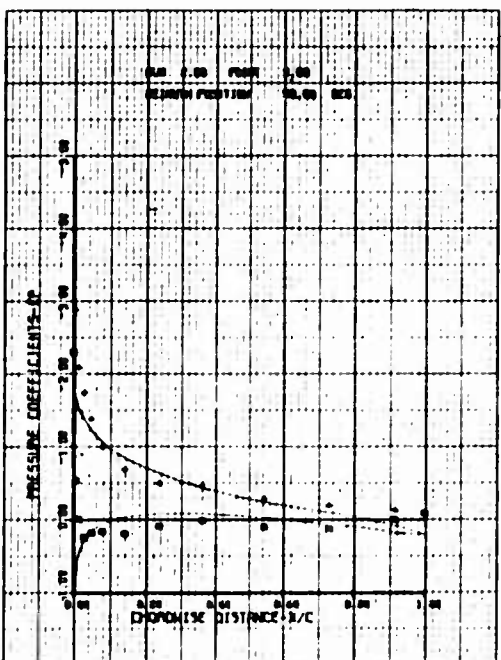
Figure 21. Integrated Normal Force, Chord Force, and Pitching Moment Coefficients Versus Azimuth;  
 $\mu = 0.20$ ,  $M_{(1.0, 90)} = 0.30$ ,  $\theta_{.75R} = 3.1^\circ$ ,  
 $\beta \approx \dot{\beta} \approx 0$ .



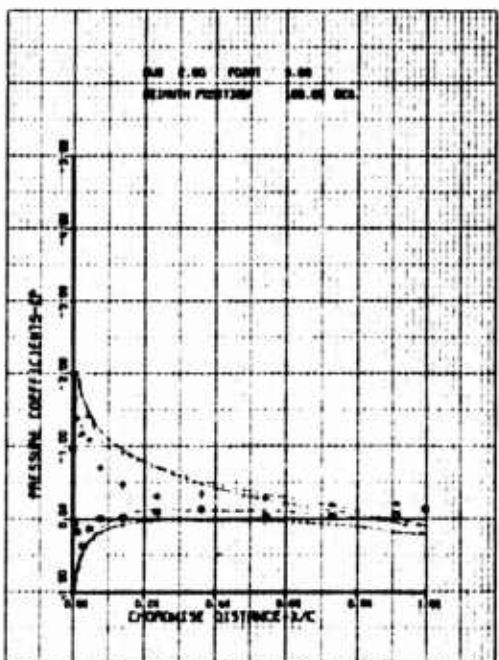
(a)  $\psi = 30^\circ$



(b)  $\psi = 60^\circ$

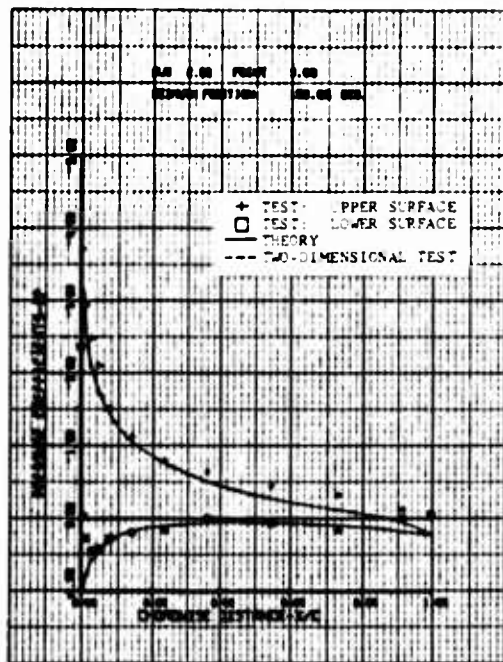


(c)  $\psi = 90^\circ$

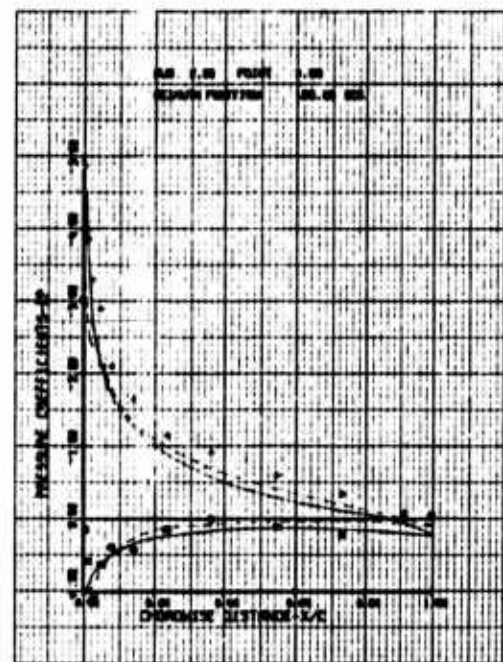


(d)  $\psi = 120^\circ$

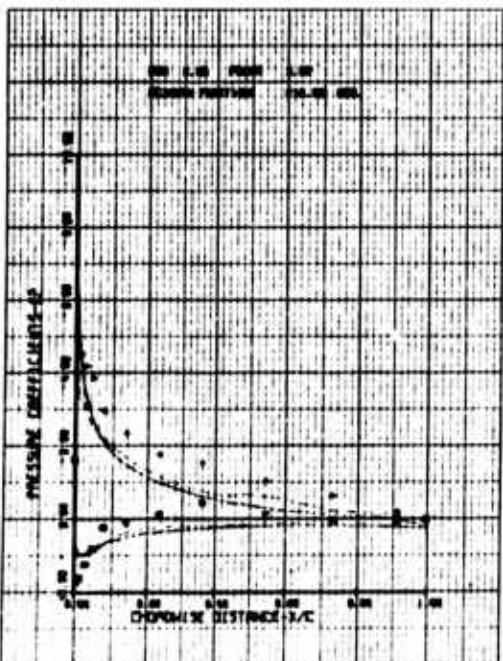
Figure 22. Chordwise Pressure Distribution (Run 2, Point 3);  
 $\mu = 0.20$ ,  $M_{(1.0, 90)} = 0.30$ ,  $\theta_{.75R} = 11.0^\circ$ ,  
 $\beta \approx \ddot{\beta} \approx 0$ .



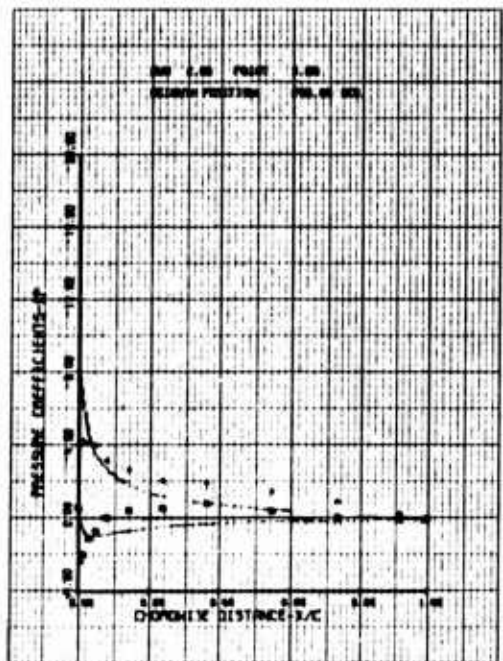
(e)  $\psi = 150^\circ$



(f)  $\psi = 180^\circ$

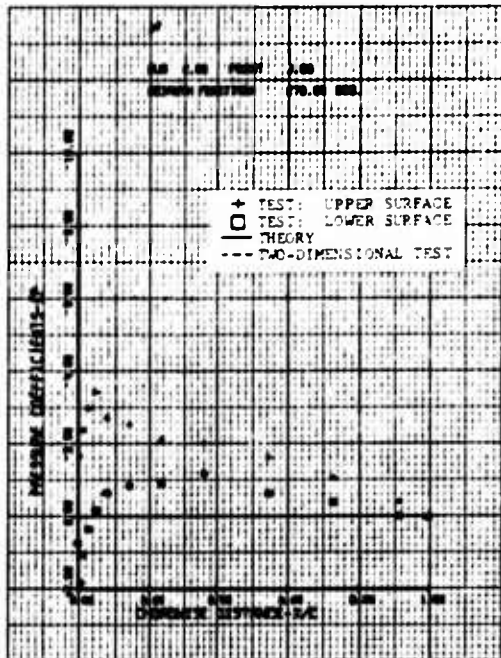


(g)  $\psi = 210^\circ$

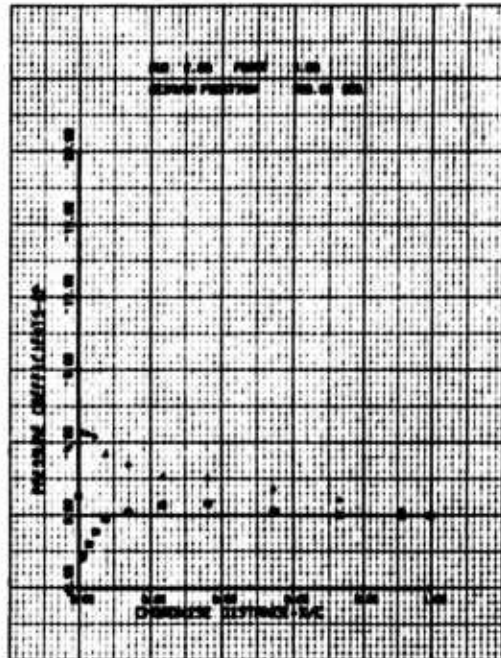


(h)  $\psi = 240^\circ$

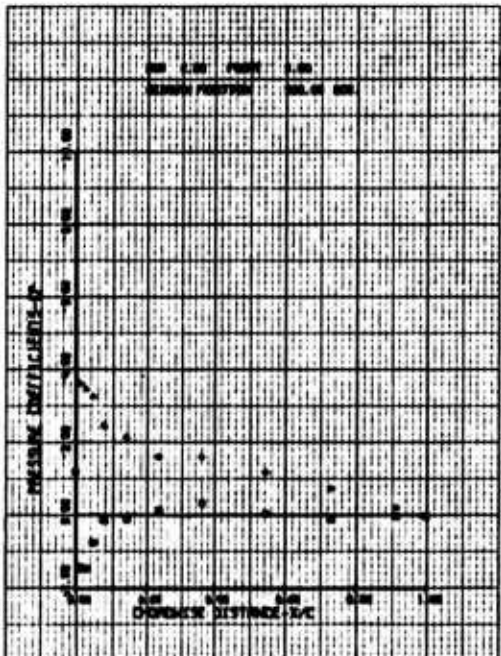
Figure 22. Continued.



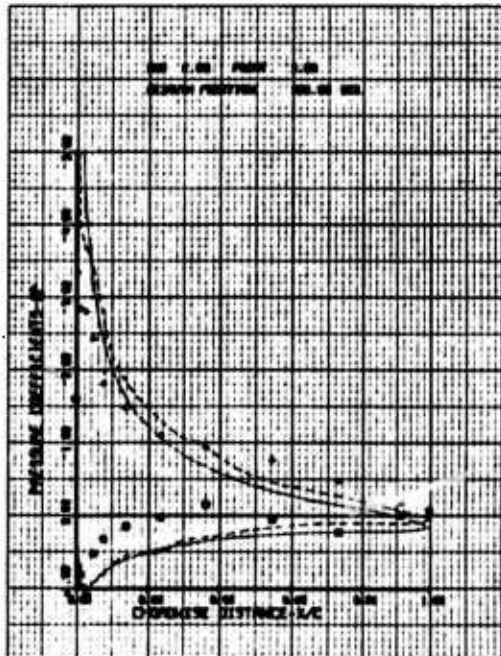
(i)  $\psi = 270^\circ$



(j)  $\psi = 300^\circ$



(k)  $\psi = 330^\circ$



(l)  $\psi = 360^\circ$

Figure 22. Concluded.

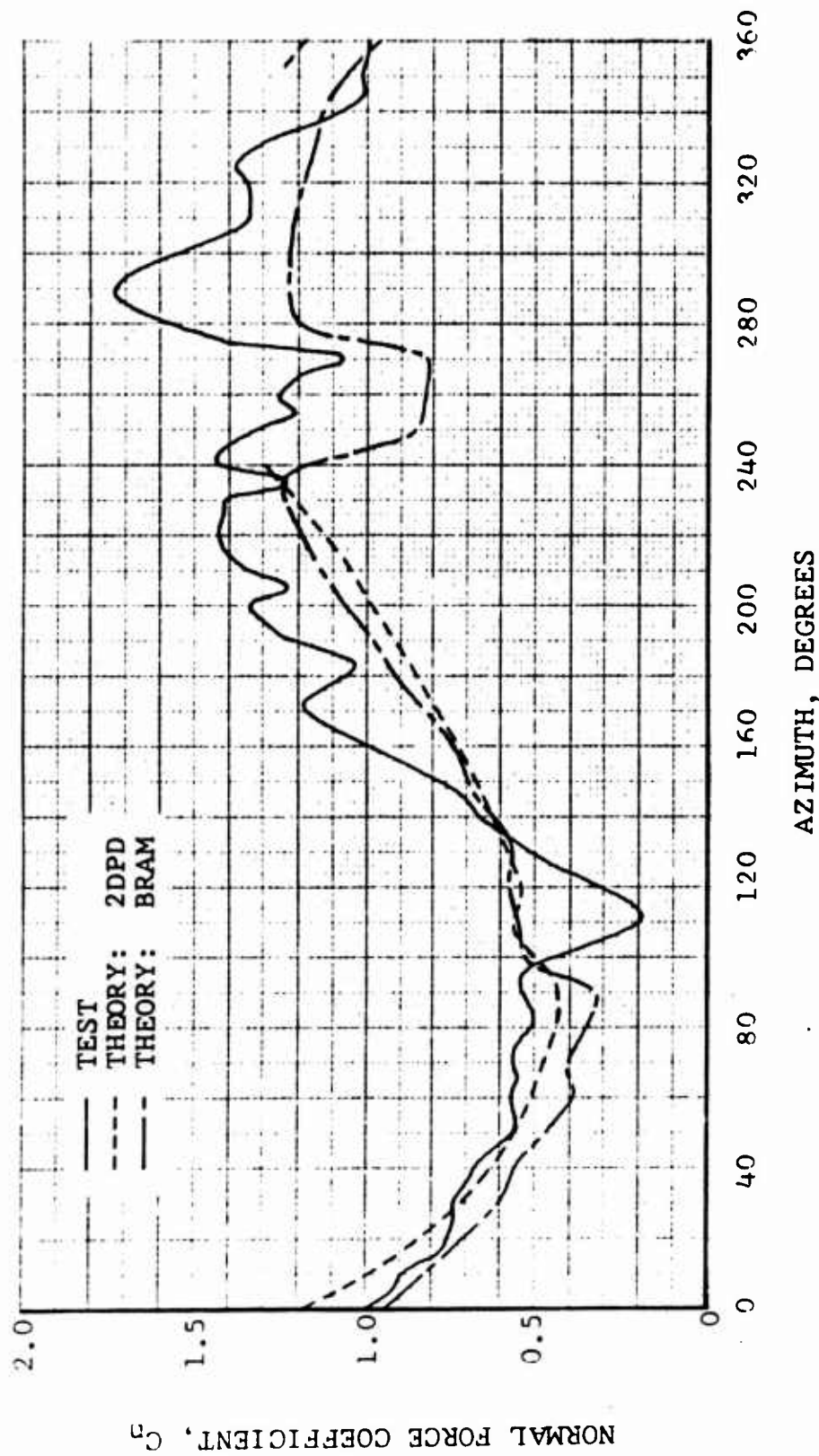


Figure 23. Integrated Normal Force Coefficient Versus Azimuth;  
 $\mu = 0.20$ ,  $M(1.0, 90) = 0.30$ ,  $\theta_{.75R} = 11.0^\circ$ ,  $\hat{\beta} \equiv \hat{\beta} \equiv 0$ .

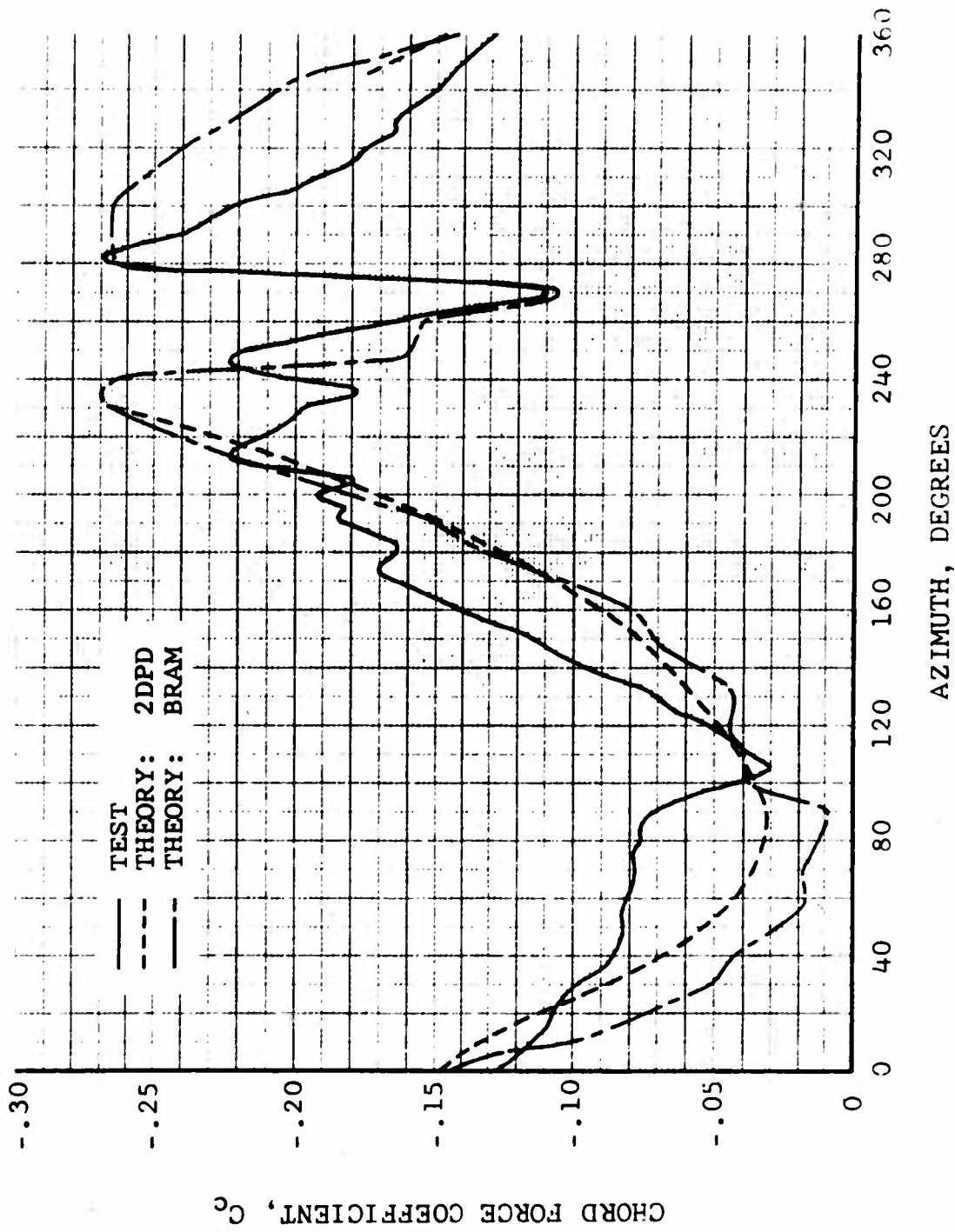


Figure 24. Integrated Chord Force Coefficient Versus Azimuth;  
 $\mu = 0.20$ ,  $M(1.0, 90) = 0.30$ ,  $\theta .75R = 11.0^\circ$ ,  $\beta \approx \ddot{\beta} \approx 0$ .

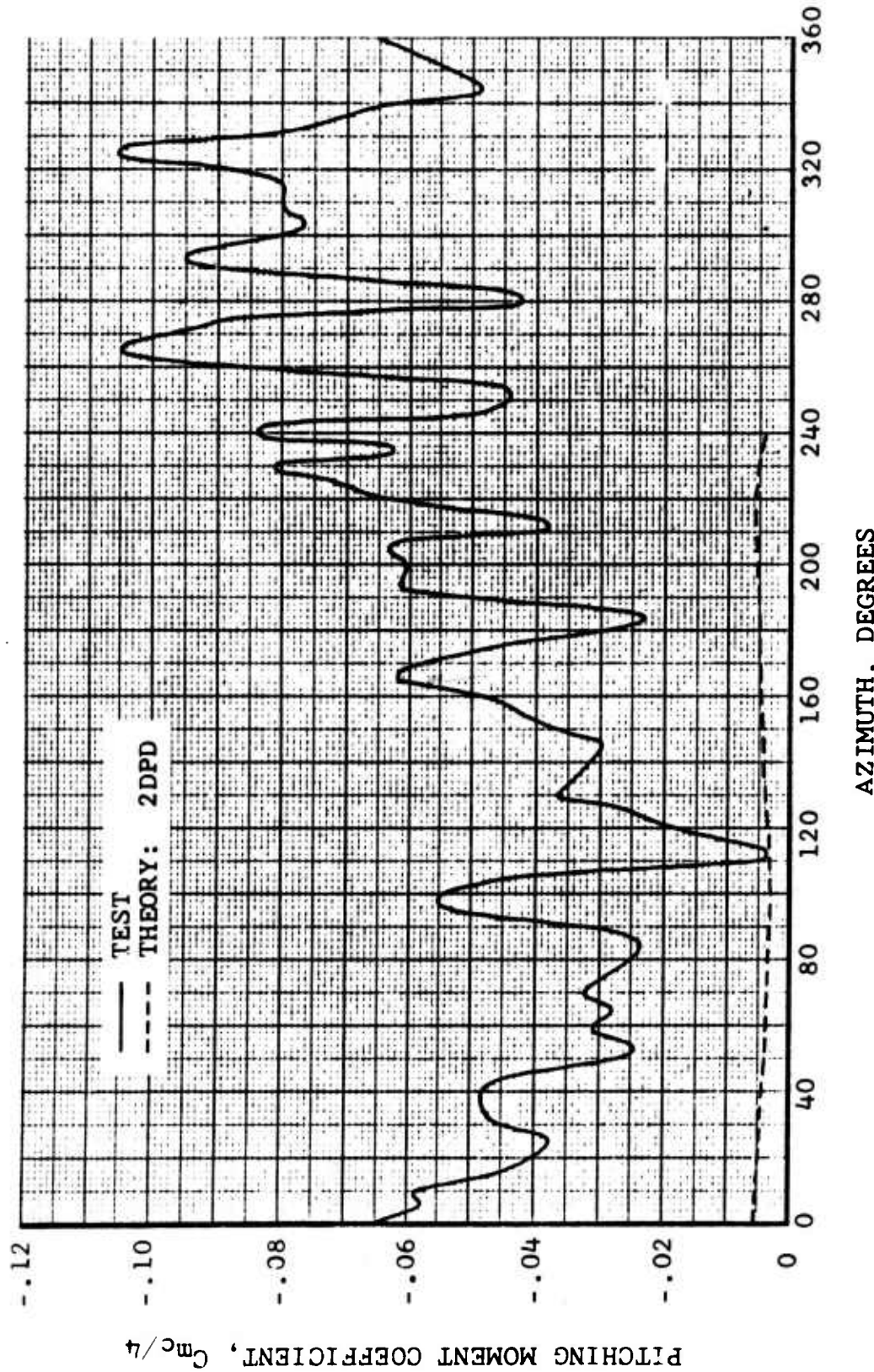


Figure 25. Integrated Pitching Moment Coefficient Versus Azimuth;  
 $\mu = 0.20$ ,  $M(1.0, 90) = 0.30$ ,  $\theta = 11.0^\circ$ ,  $\beta \equiv \ddot{\beta} \equiv 0$ .

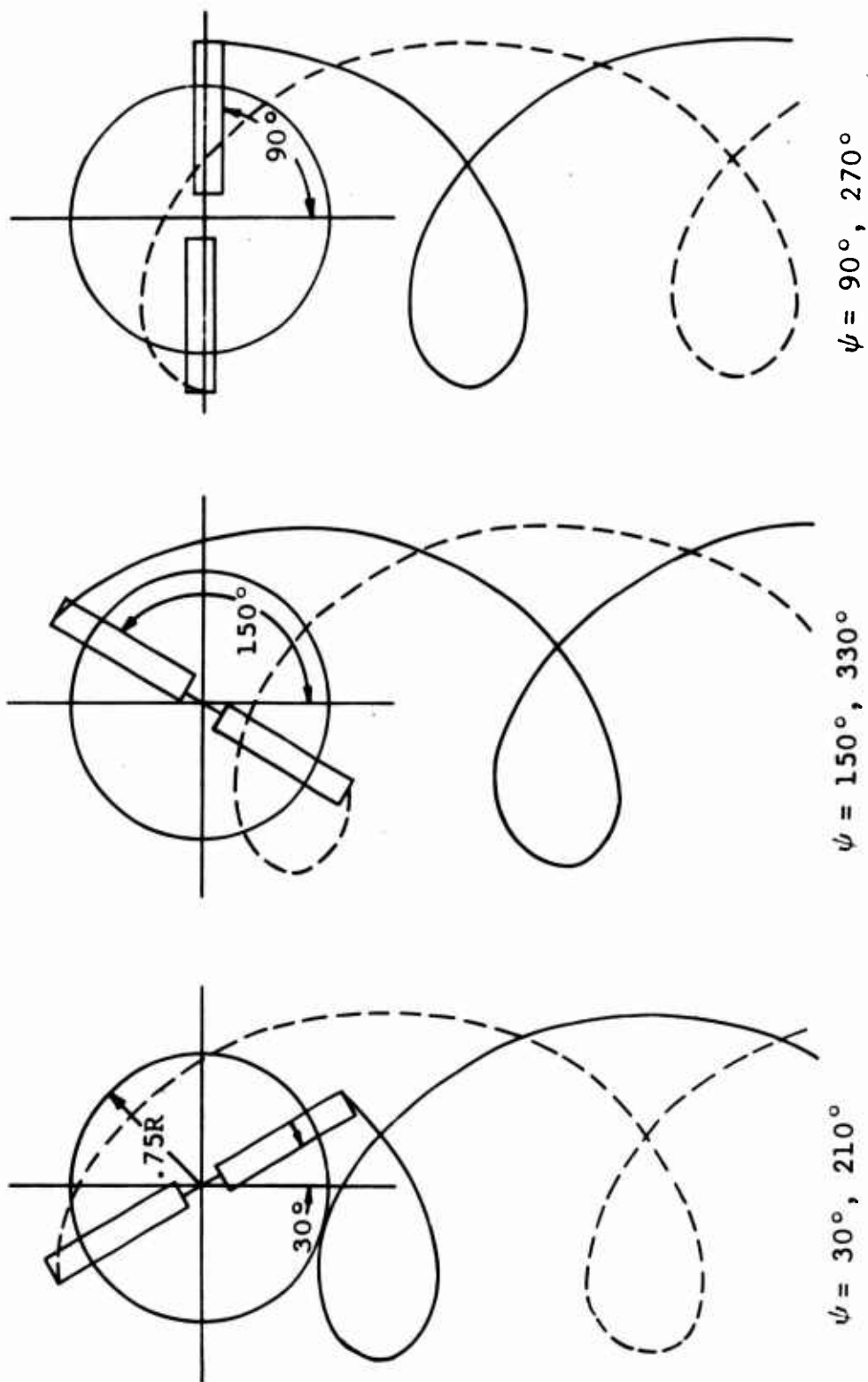
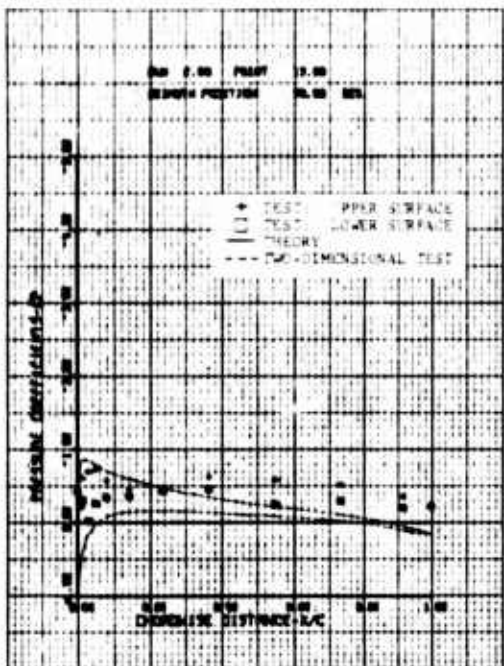
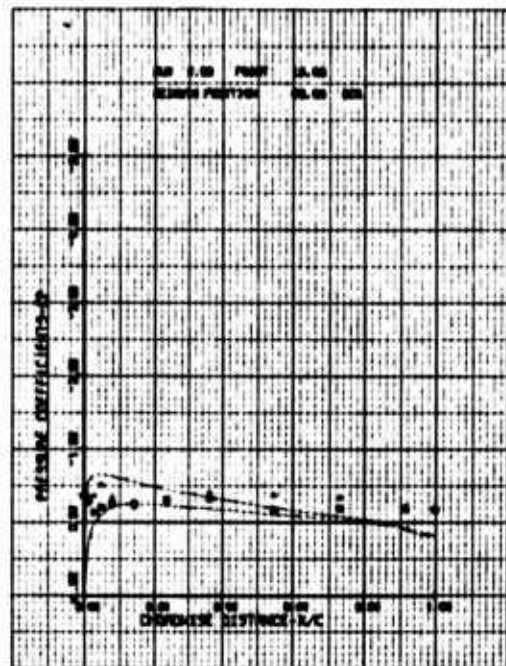


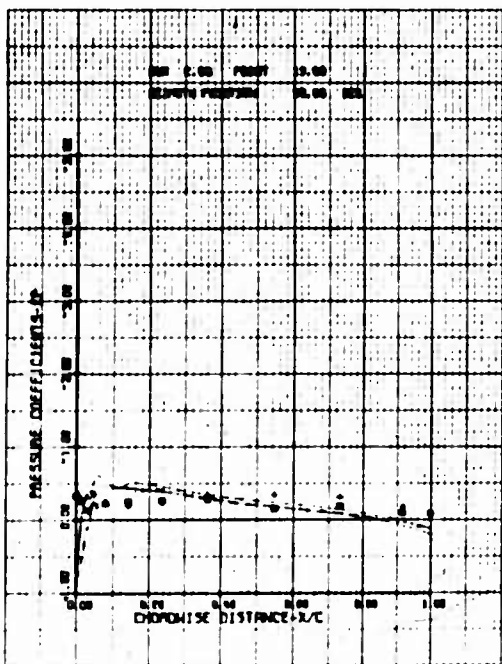
Figure 26. Top View of Tip Vortex Core Path for Two-Bladed Rotor,  $\mu = 0.50$ .



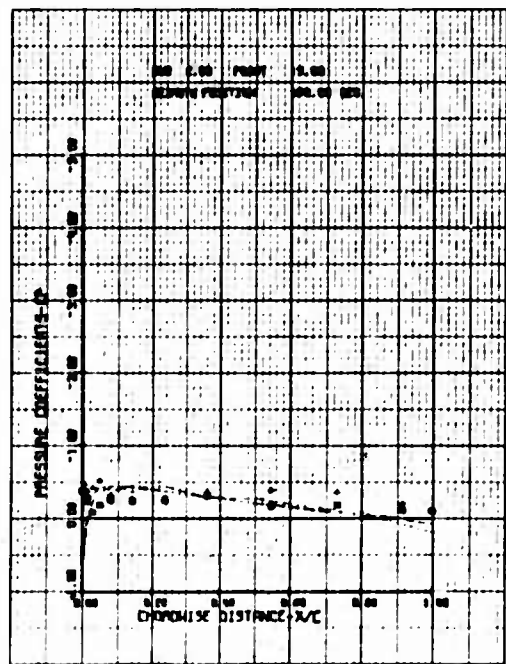
(a)  $\psi = 30^\circ$



(b)  $\psi = 60^\circ$

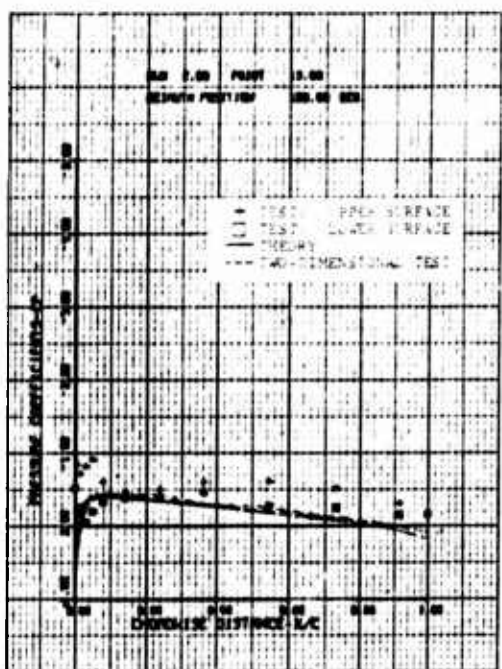


(c)  $\psi = 90^\circ$

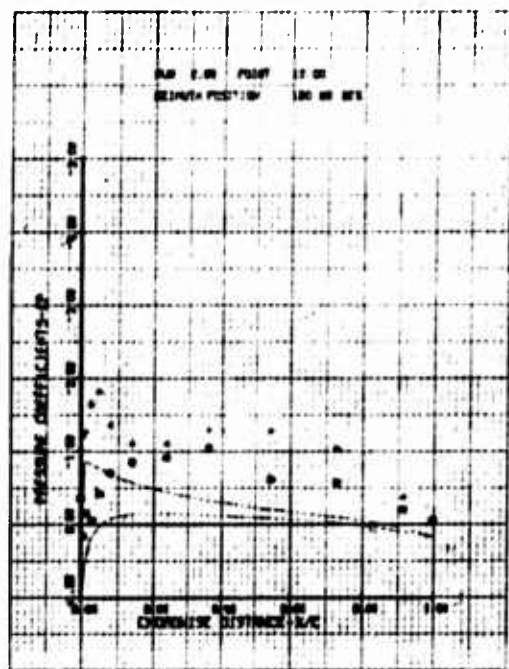


(d)  $\psi = 120^\circ$

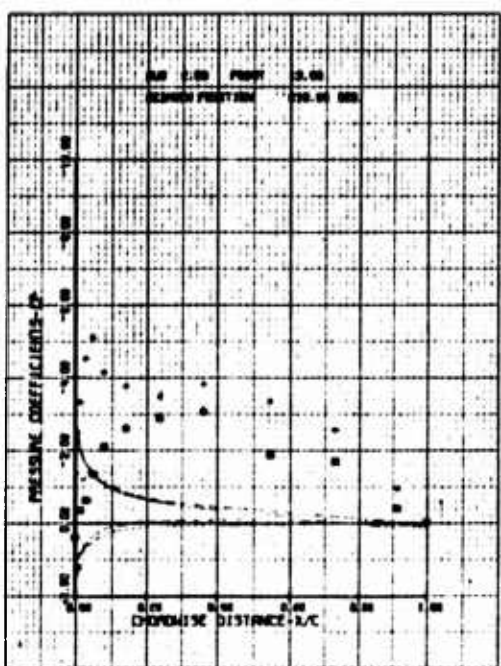
Figure 27. Chordwise Pressure Distribution (Run 2, Point 13);  
 $\mu = 0.50$ ,  $M(1.0, 90) = 0.37$ ,  $\theta_{.75R} = 3.1^\circ$ ,  
 $\dot{\beta} \approx \ddot{\beta} \approx 0$ .



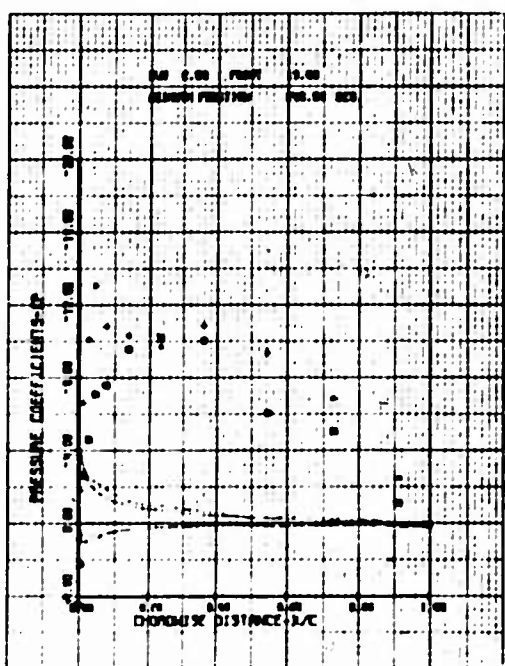
(e)  $\psi = 150^\circ$



(f)  $\psi = 180^\circ$

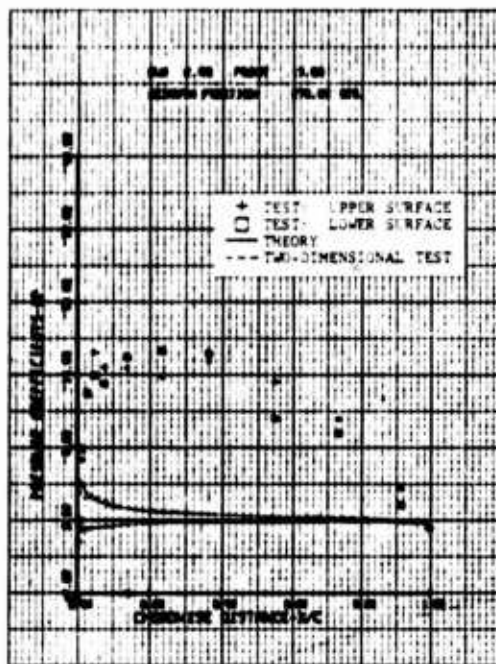


(g)  $\psi = 210^\circ$

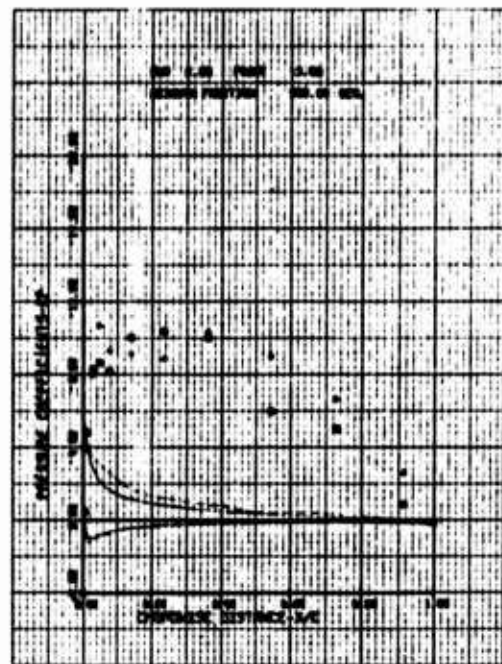


(h)  $\psi = 240^\circ$

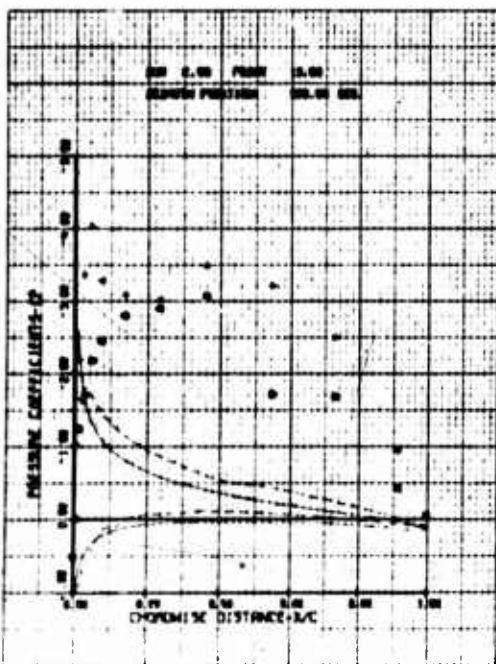
Figure 27. Continued.



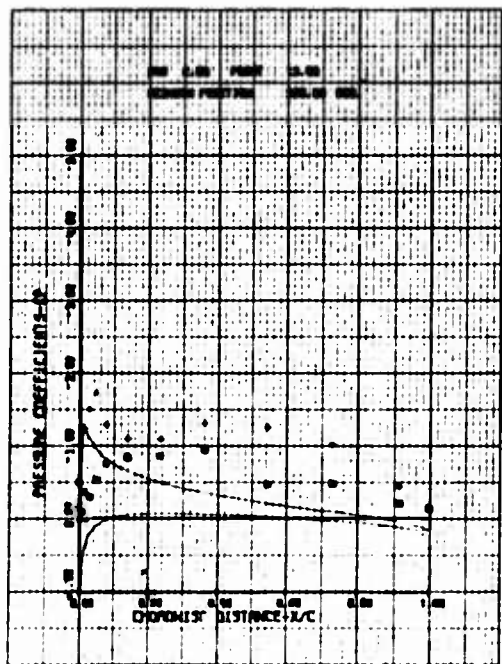
(i)  $\psi = 270^\circ$



(j)  $\psi = 300^\circ$



(k)  $\psi = 330^\circ$



(l)  $\psi = 360^\circ$

Figure 27. Concluded.

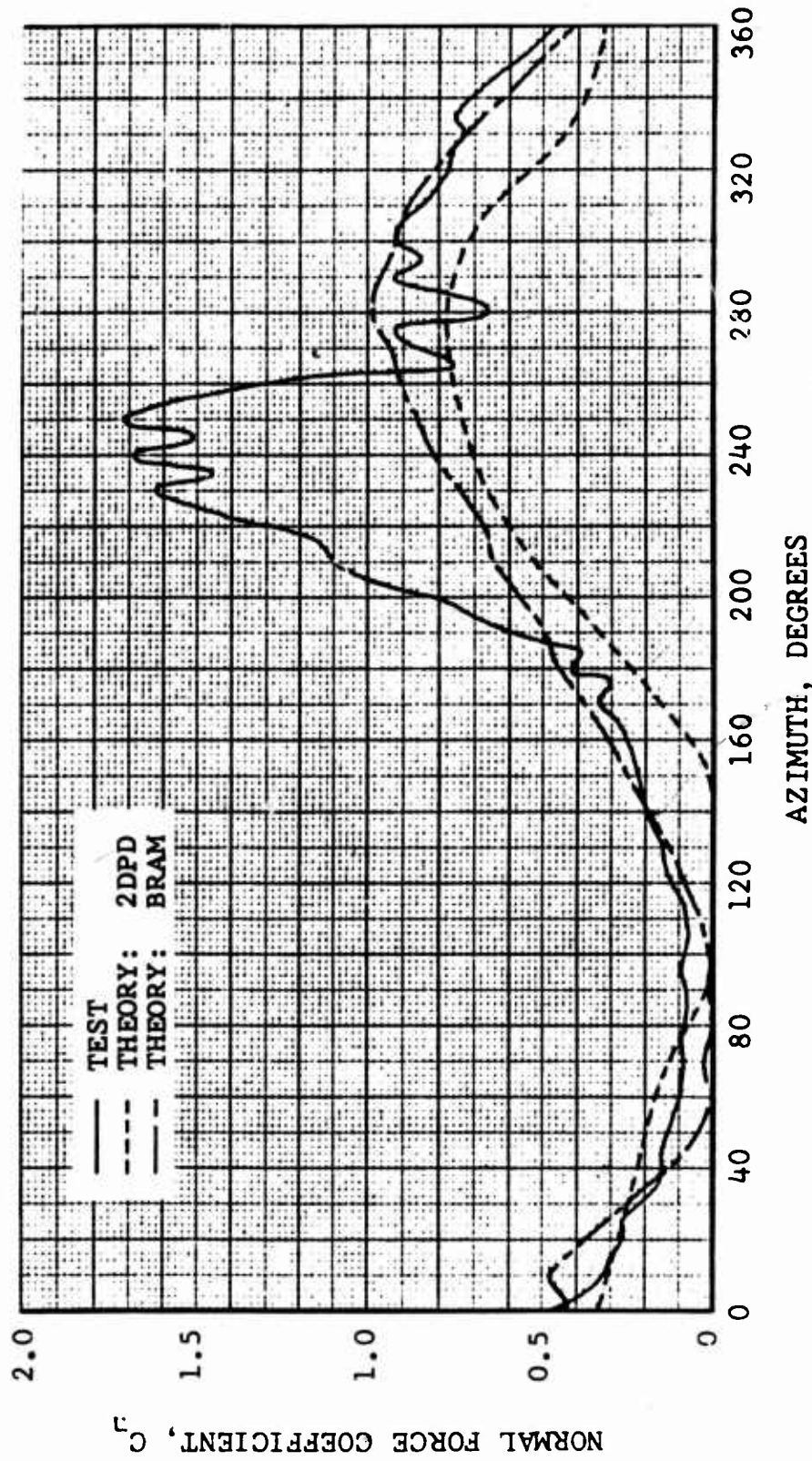


Figure 28. Integrated Normal Force Coefficient Versus Azimuth;  $\mu = 0.50$ ,  $M(1.0, 90) = 0.37$ ,  $\theta = 3.1^\circ$ ,  $\beta = 0^\circ$ .

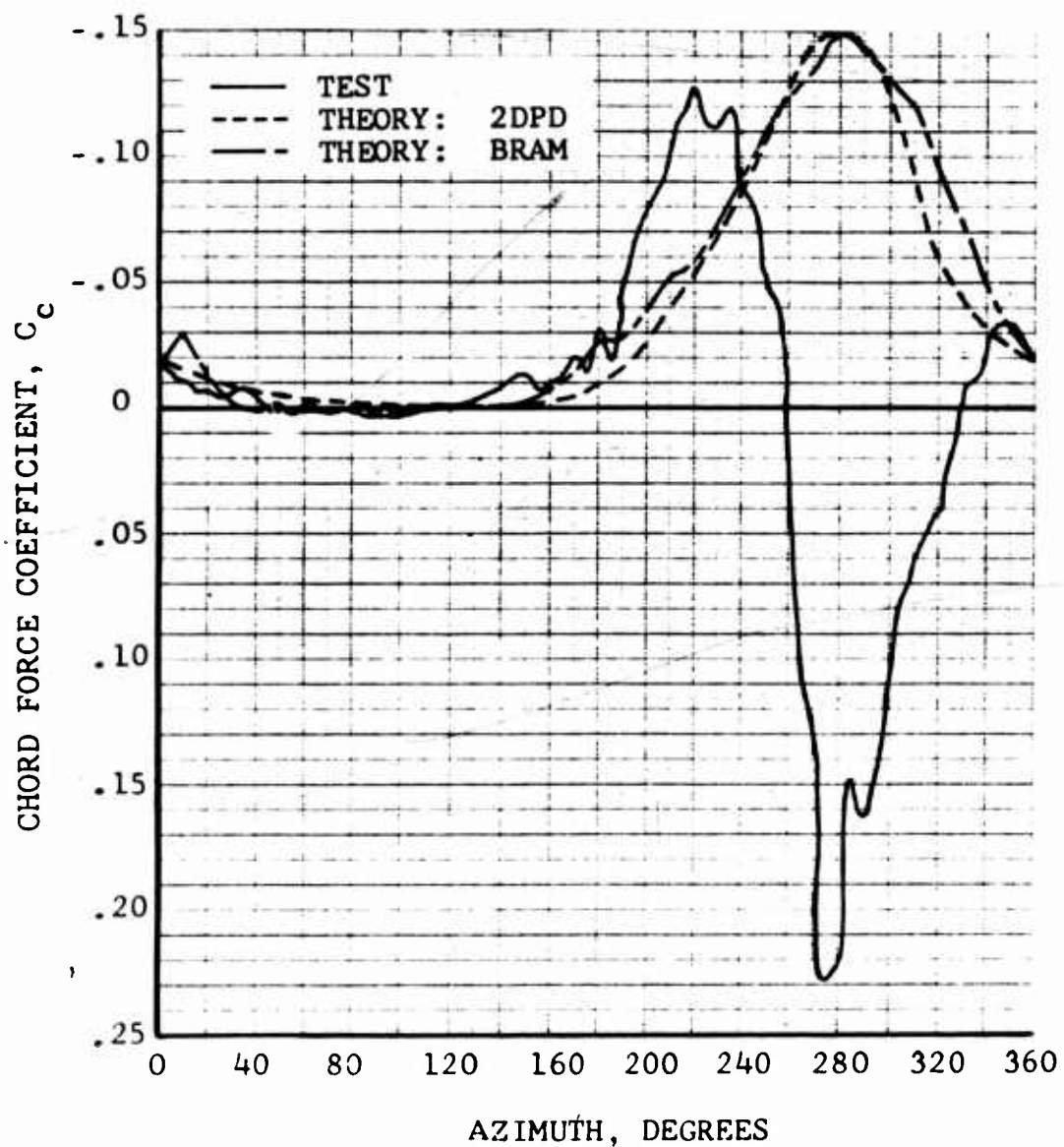


Figure 29. Integrated Chord Force Coefficient Versus Azimuth:

$\mu = 0.50$ ,  $M_{(1.0, 90)} = 0.37$ ,  $\theta_{.75R} = 3.1^\circ$ ,  
 $\beta \approx \dot{\beta} \approx 0$ .

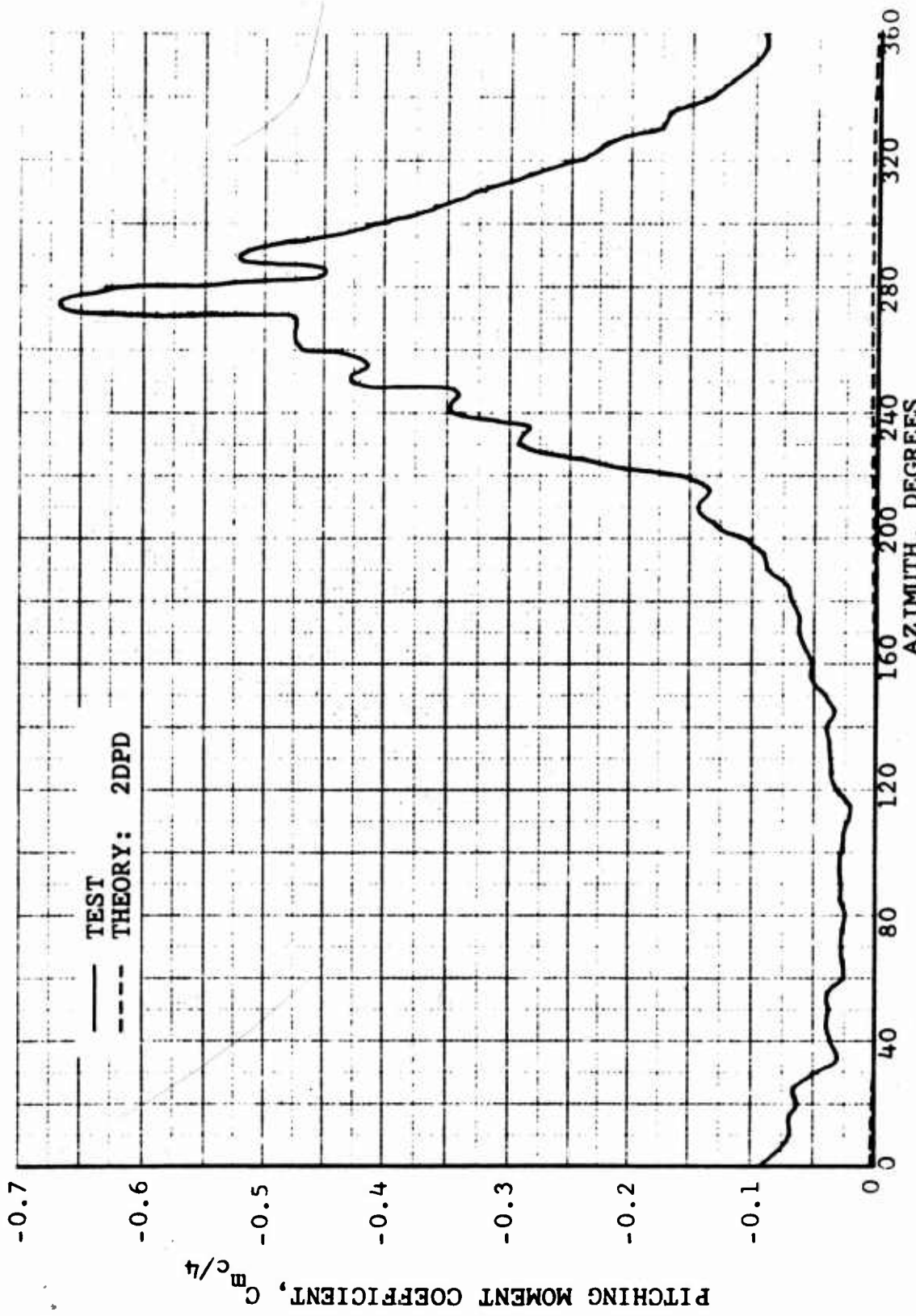
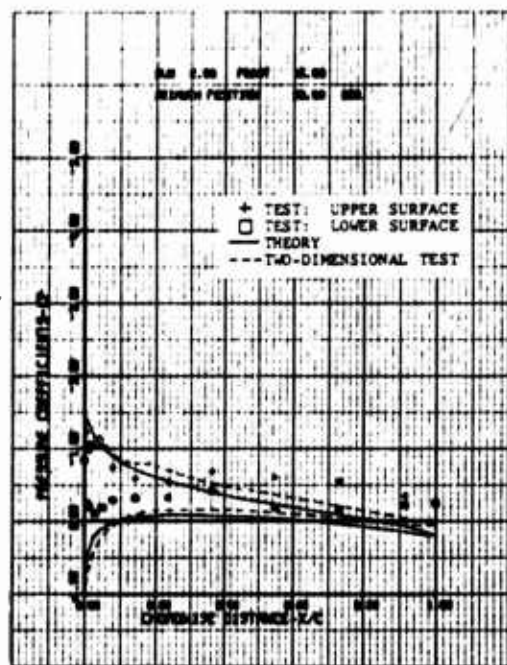
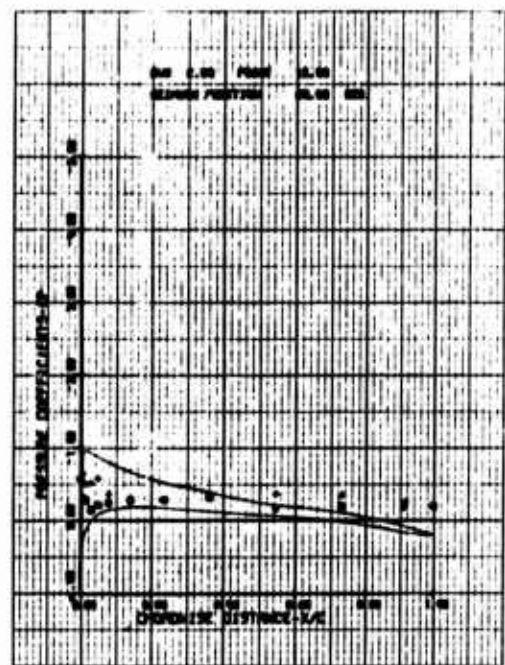


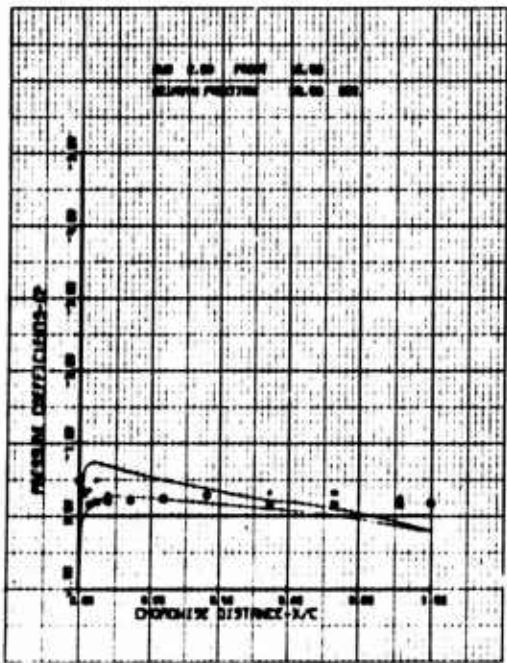
Figure 30. Integrated Pitching Moment Coefficient Versus Azimuth;  
 $\mu = 0.50$ ,  $M(1.0, 90) = 0.37$ ,  $\theta .75R = 3.1^\circ$ ,  $\beta = \beta \equiv 0$ .



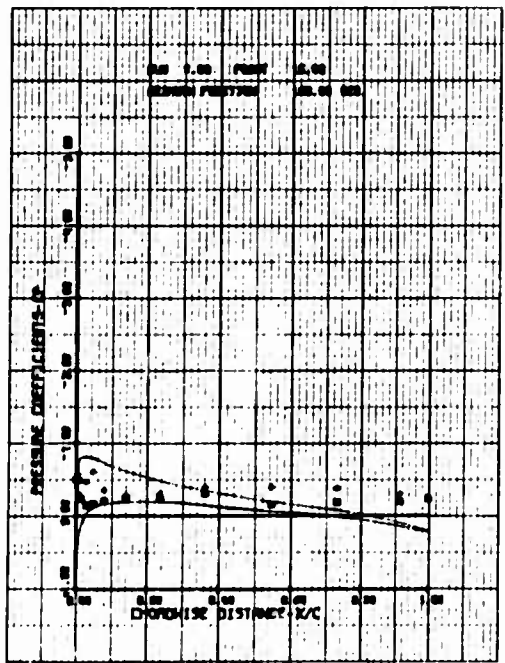
(a)  $\psi = 30^\circ$



(b)  $\psi = 60^\circ$

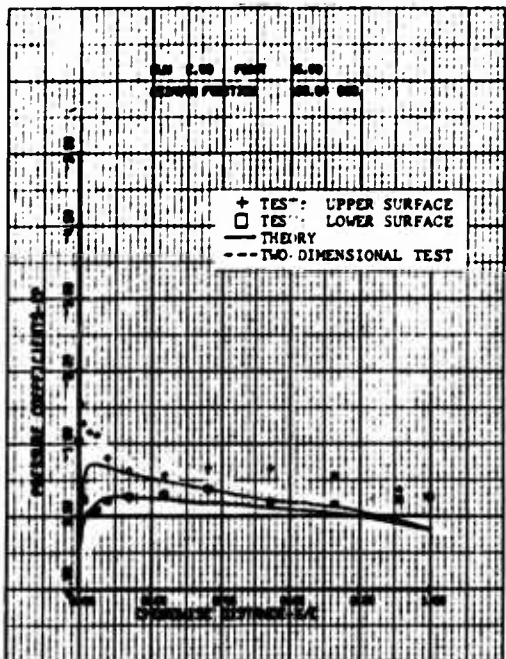


(c)  $\psi = 90^\circ$

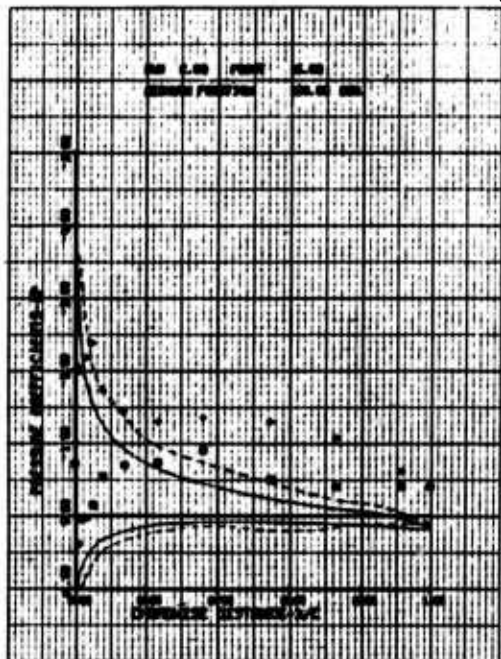


(d)  $\psi = 120^\circ$

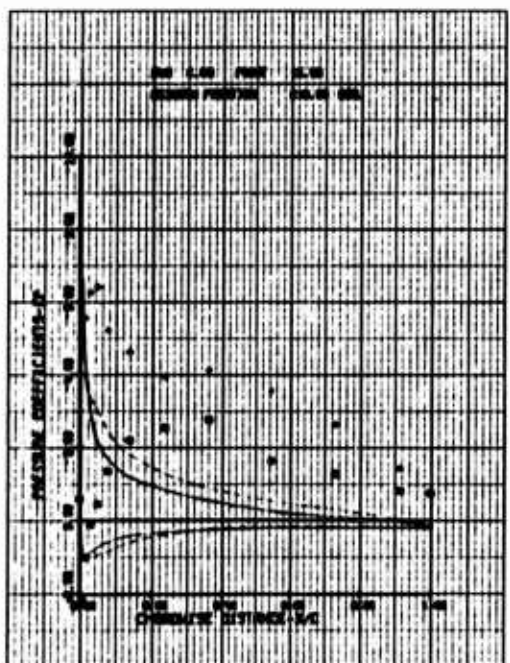
Figure 31. Chordwise Pressure Distribution (Run 2, Point 15);  
 $\mu = 0.50$ ,  $M_{(1.0, 90)} = 0.37$ ,  $\theta_{.75R} = 7.2^\circ$ ,  
 $\beta \approx \dot{\beta} \approx 0$ .



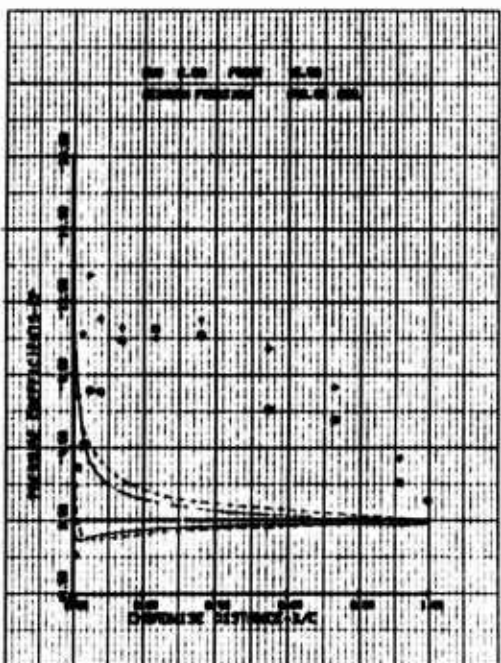
(e)  $\psi = 150^\circ$



(f)  $\psi = 180^\circ$

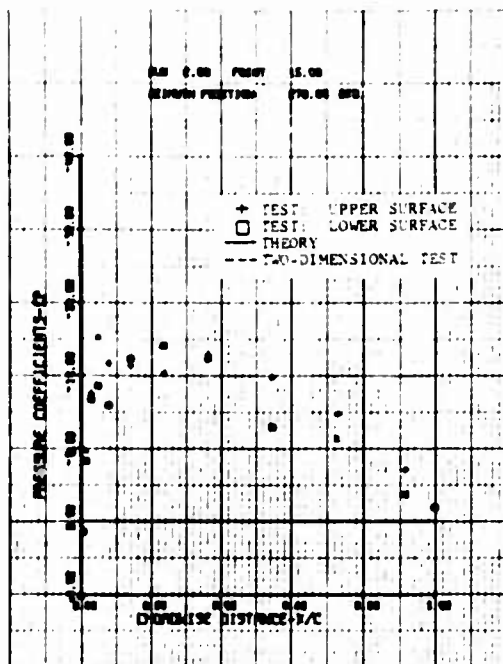


(g)  $\psi = 210^\circ$

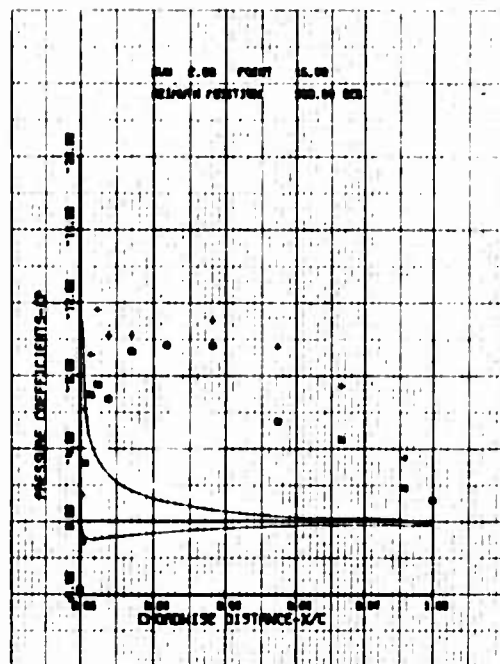


(h)  $\psi = 240^\circ$

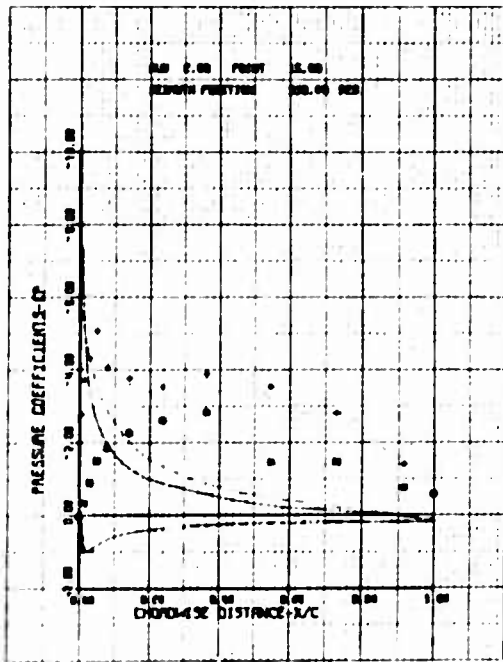
Figure 31. Continued.



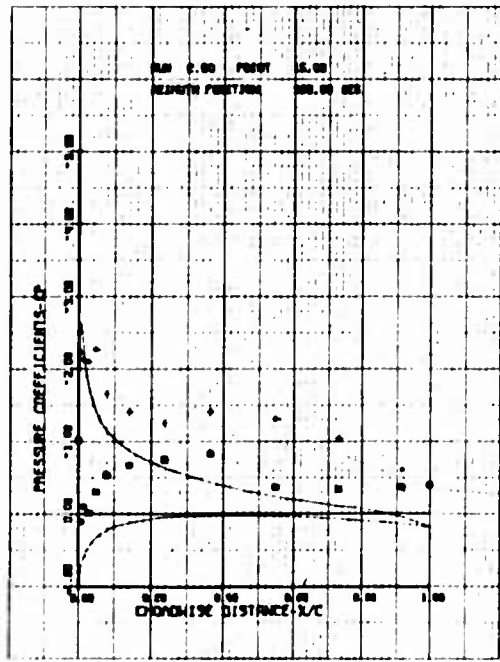
(i)  $\psi = 270^\circ$



(j)  $\psi = 300^\circ$



(k)  $\psi = 330^\circ$



(l)  $\psi = 360^\circ$

Figure 31. Concluded.

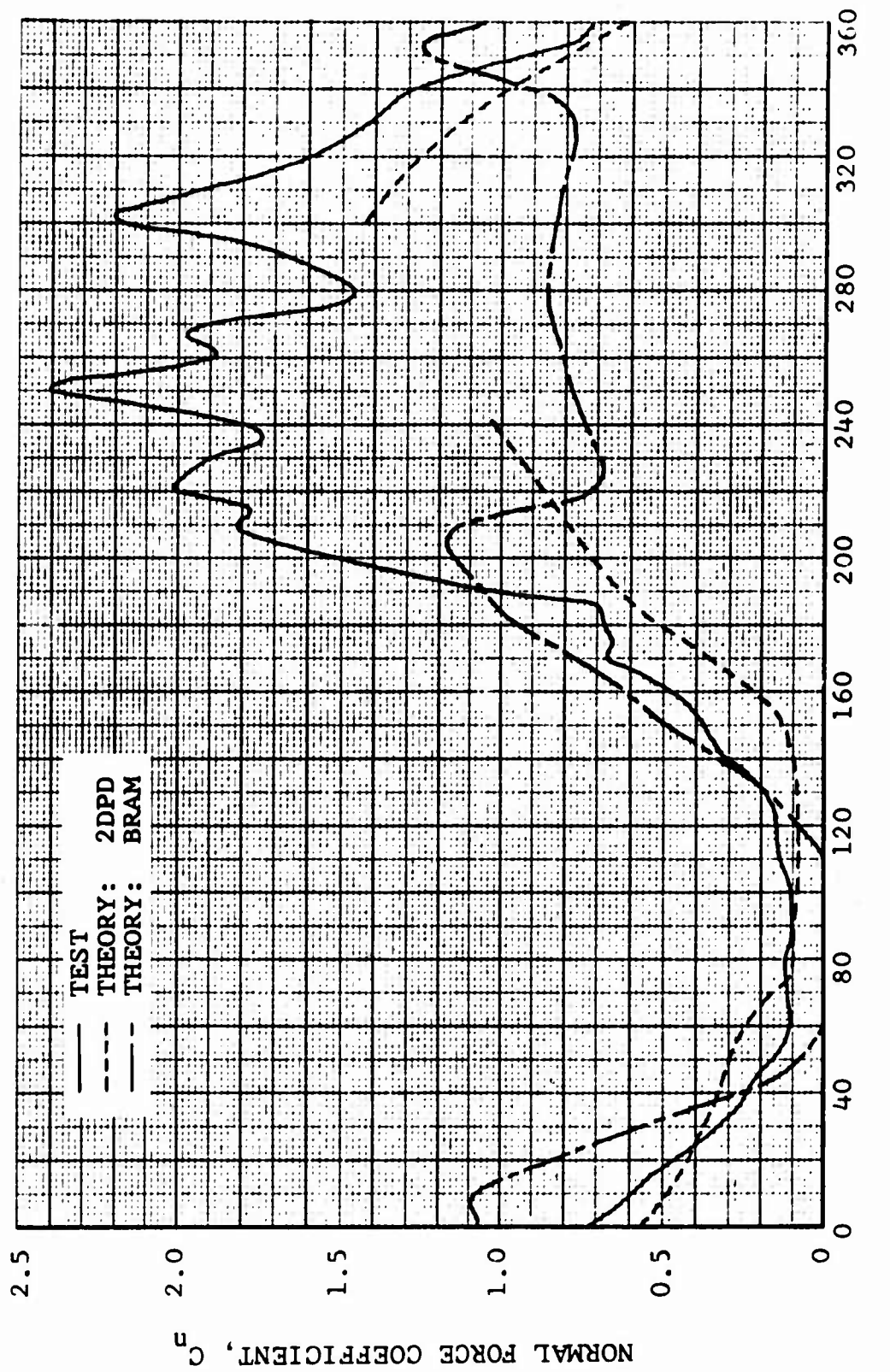


Figure 32. Integrated Normal Force Coefficient Versus Azimuth;  
 $\mu = 0.50$ ,  $M(1.0, 90) = 0.37$ ,  $\theta_{.75R} = 7.2^\circ$ ,  $\dot{\beta} \equiv \ddot{\beta} \equiv 0$ .

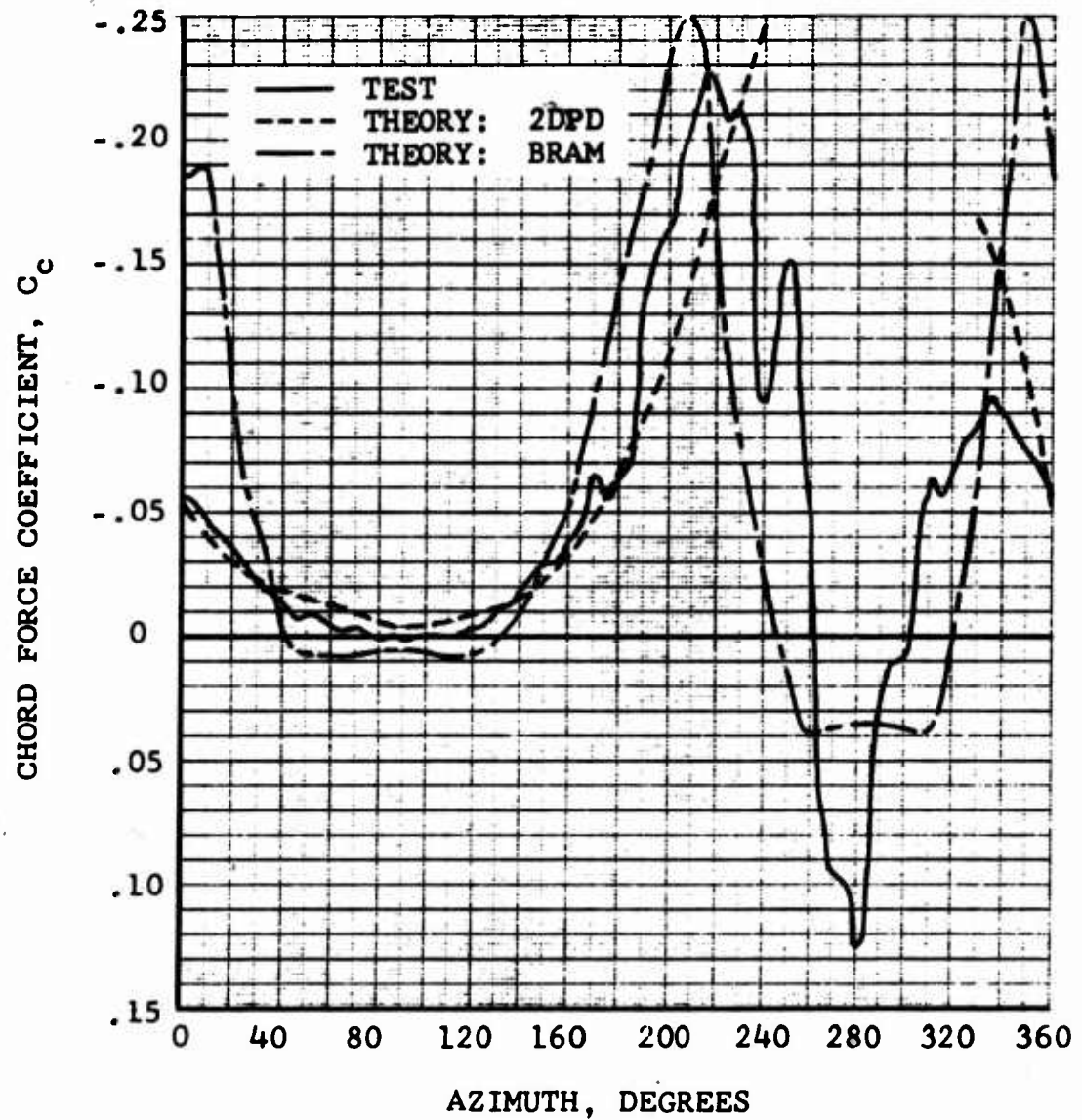


Figure 33. Integrated Chord Force Coefficient Versus Azimuth;  
 $\mu = 0.50$ ,  $M_{(1.0, 90)} = 0.37$ ,  $\theta_{.75R} = 7.2^\circ$ ,  $\dot{\beta} \approx \ddot{\beta} \approx 0$ .



Figure 34. Integrated Pitching Moment Coefficient Versus Azimuth;  
 $\mu = 0.50$ ,  $M(1.0, 90) = 0.37$ ,  $\theta_{.75R} = 7.2^\circ$ ,  $\beta \approx \bar{\beta} \approx 0$ .

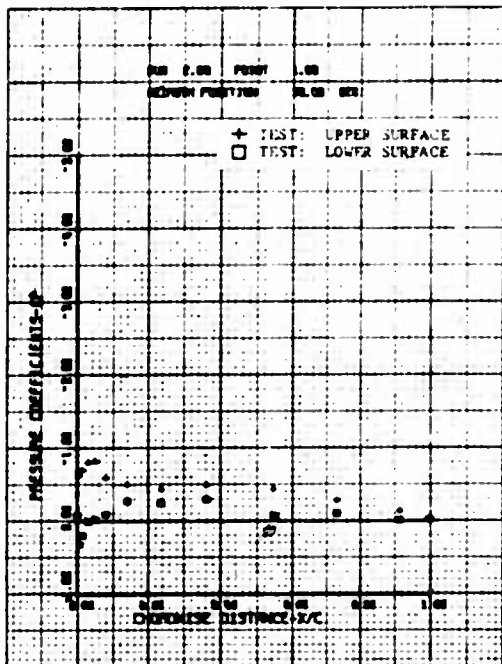
## LITERATURE CITED

1. Tanner, W. H., and Van Wyckhouse, J. F., WIND TUNNEL TESTS OF FULL-SCALE ROTORS OPERATING AT HIGH ADVANCING TIP MACH NUMBERS AND ADVANCE RATIOS, Bell Helicopter Company; USAAVLABS Technical Report 68-44, U. S. Army Aviation Materiel Laboratories, Fort Eustis, Va., July 1968, AD674188.
2. Bowden, T. H., GLOVE TESTS FOR DEVELOPMENT OF ROTOR INSTRUMENTATION, Bell Helicopter Company Report No. 576-099-017, February 1969.
3. Burpo, F. B., and Tanner, W. H., TWO DIMENSIONAL TESTS OF ADVANCED INSTRUMENTATION FOR ROTORS, Bell Helicopter Company Report No. 606-099-001, December 1968.
4. Liiva, Jaan, Davenport, F. J., Gray, Lewis, and Walton, I. C., TWO-DIMENSIONAL TESTS OF AIRFOILS OSCILLATING NEAR STALL, VOLUMES 1 AND 2, Vertol Division, The Boeing Company; USAAVLABS Technical Report 68-13A and B, U. S. Army Aviation Materiel Laboratories, Fort Eustis, Va., April 1968, AD670957 and AD670958.
5. Hughes, C. W., Jr., TWO-DIMENSIONAL PRESSURE DISTRIBUTION PROGRAM, Bell Helicopter Company Report No. 599-102-901, January 1970.
6. Gessow, Alfred, and Crim, Almer D., A METHOD OF STUDYING THE TRANSIENT BLADE-FLAPPING BEHAVIOR OF LIFTING ROTORS AT EXTREME OPERATING CONDITIONS, NACA TN 3366, 1955.
7. Crimi, Peter, THEORETICAL PREDICTION OF THE FLOW IN THE WAKE OF A HELICOPTER ROTOR, PARTS 1 AND 2, Cornell Aeronautical Laboratory, Inc., CAL No. BB-1994-S-1 and 2, September 1965.
8. Charles, B. C., and Tanner, W. H., WIND TUNNEL INVESTIGATION OF SEMIRIGID FULL-SCALE ROTORS OPERATING AT HIGH ADVANCE RATIOS, Bell Helicopter Company; USAAVLABS Technical Report 69-2, U. S. Army Aviation Materiel Laboratories, Fort Eustis, Va., January 1969, AD684396.
9. Anonymous, MEASUREMENT OF DYNAMIC AIR LOADS ON A FULL-SCALE SEMIRIGID ROTOR, USATRECOM Technical Report 62-42, December 1962, AD297940.
10. Rabbott, J. P., Lizak, A. A., and Paglina, V. M., TABULATED SIKORSKY CH-34 BLADE SURFACE PRESSURES MEASURED AT THE NASA/AMES FULL-SCALE WIND TUNNEL, Sikorsky Report No. SER-58399, January 15, 1966.

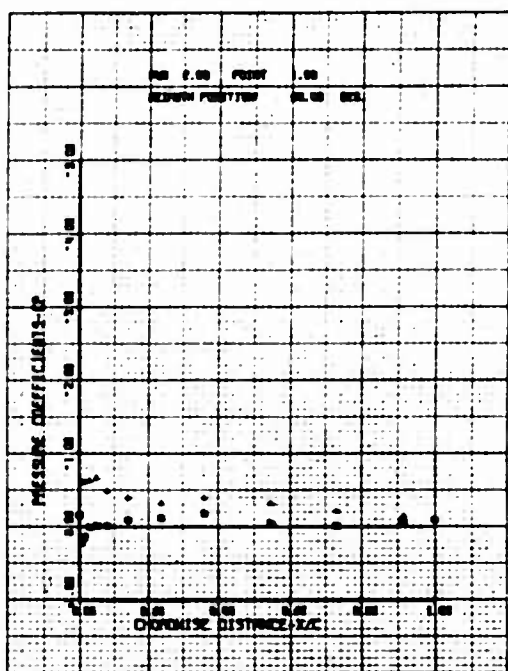
11. Scheiman, James, A TABULATION OF HELICOPTER ROTOR-BLADE DIFFERENTIAL PRESSURES, STRESSES, AND MOTIONS AS MEASURED IN FLIGHT, NASA TMX-952, March 1964.
12. Scheiman, James, and Kelley, H. L., COMPARISON OF FLIGHT-MEASURED HELICOPTER ROTOR-BLADE CHORDWISE PRESSURE DISTRIBUTIONS WITH STATIC TWO-DIMENSIONAL AIRFOIL CHARACTERISTICS, NASA TND-3936, May 1967.
13. Ericsson, L. E., COMMENT ON UNSTEADY AIRFOIL STALL, J. Aircraft, Vol. 4, No. 5, pp. 478-480, September-October 1967.
14. Liiva, Jaan, UNSTEADY AERODYNAMIC AND STALL EFFECTS ON HELICOPTER ROTOR BLADE AIRFOIL SECTIONS, J. Aircraft, Vol. 6, No. 1, pp. 46-51, January-February 1969.

## APPENDIX

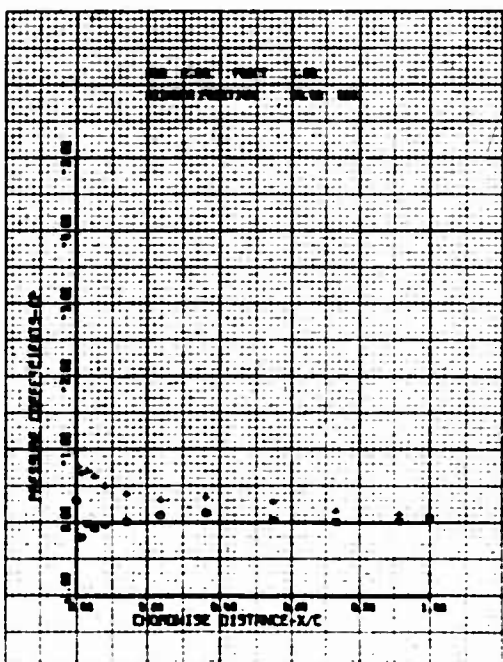
The data presented in this appendix (Figures 35 through 50) are upper- and lower-surface pressure distributions versus chord length. The data are from Run 2, Points 1 through 16, of the wind-tunnel test. They are plotted for every 30 degrees of azimuth for each point.



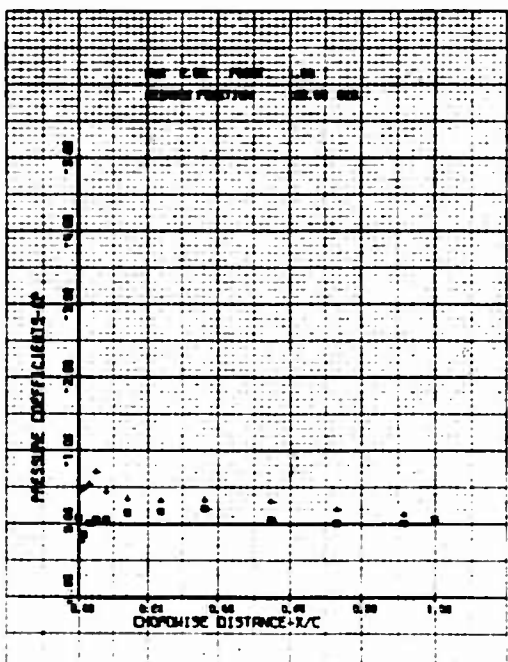
(a)  $\psi = 30^\circ$



(b)  $\psi = 60^\circ$

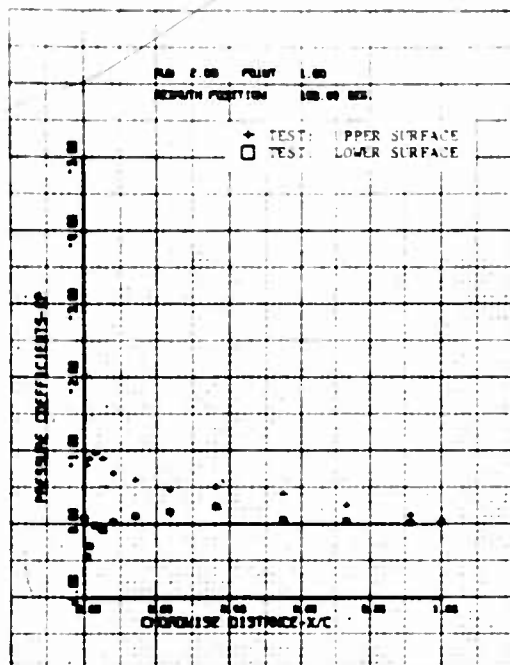


(c)  $\psi = 90^\circ$

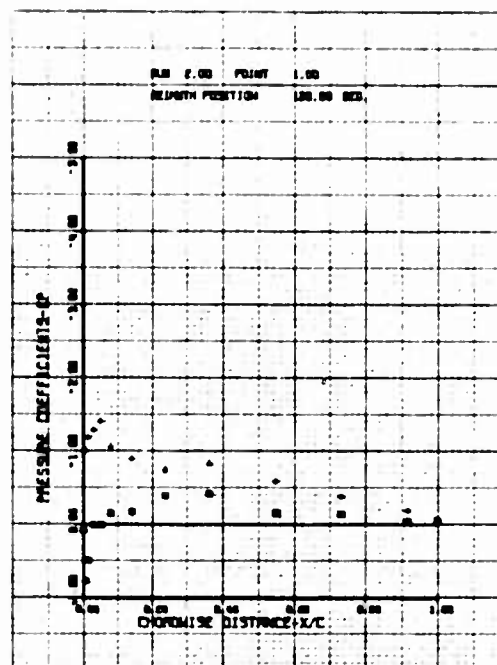


(d)  $\psi = 120^\circ$

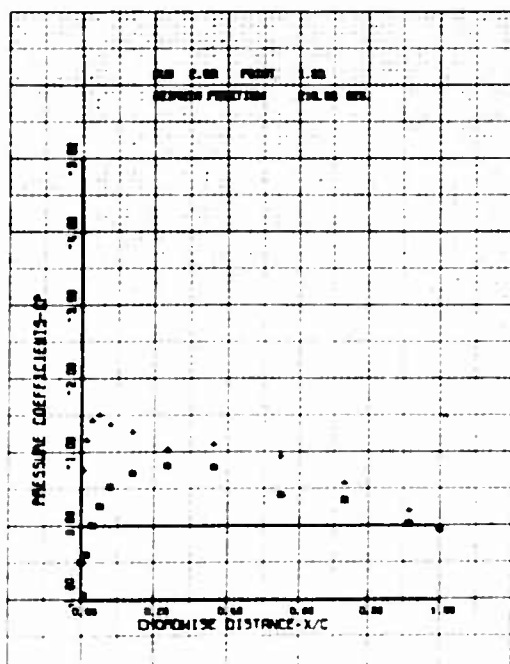
Figure 35. Chordwise Pressure Distribution (Run 2, Point 1);  
 $\mu = 0.20$ ,  $M_{(1.0, 90)} = 0.30$ ,  $\theta_{.75R} = 3.1^\circ$ ,  
 $\dot{\beta} \approx \ddot{\beta} \approx 0$ .



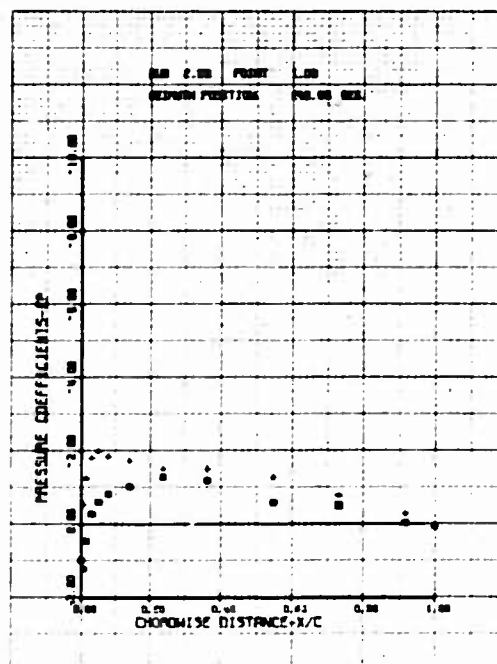
(e)  $\psi = 150^\circ$



(f)  $\psi = 180^\circ$

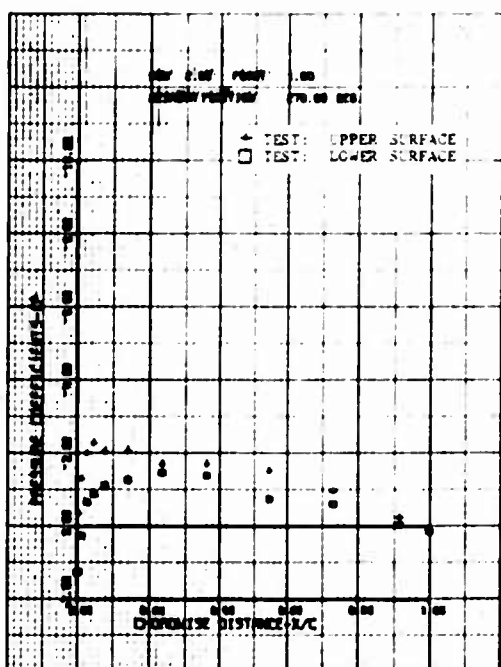


(g)  $\psi = 210^\circ$

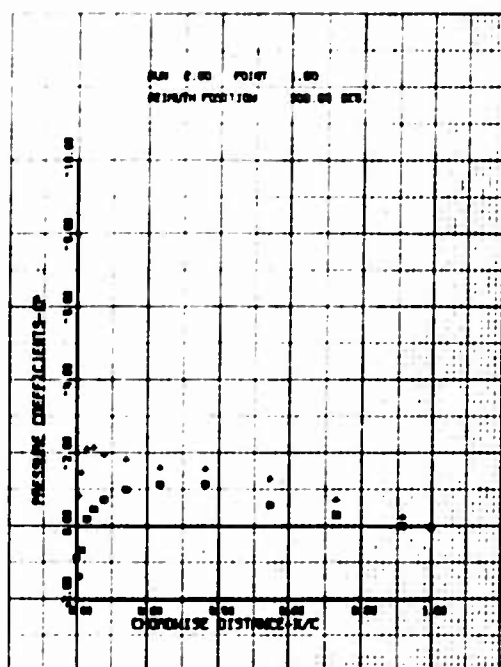


(h)  $\psi = 240^\circ$

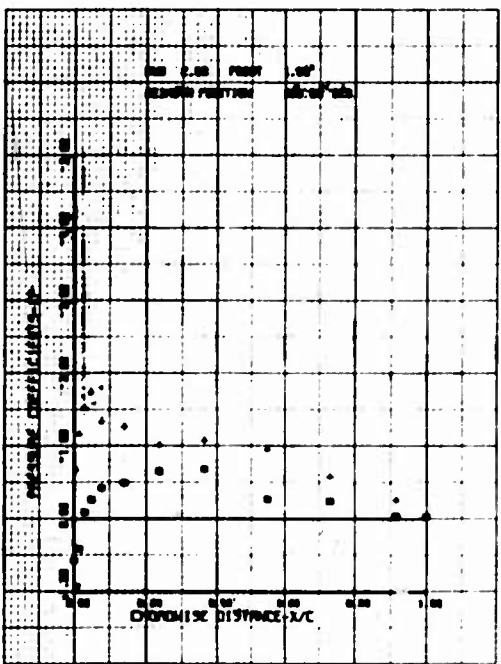
Figure 35. Continued.



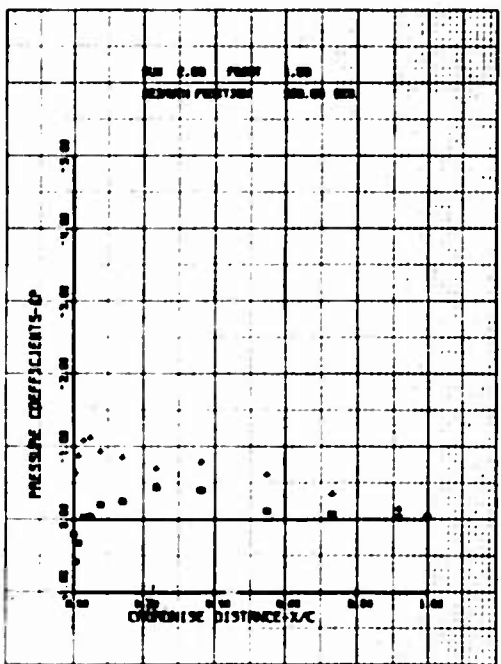
(i)  $\psi = 270^\circ$



(j)  $\psi = 300^\circ$

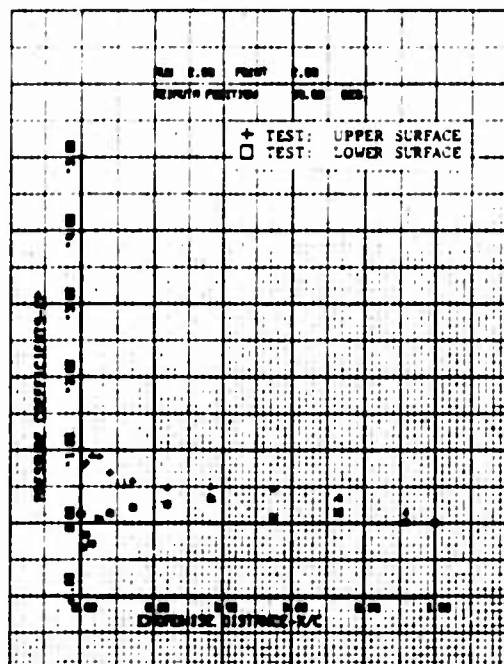


(k)  $\psi = 330^\circ$

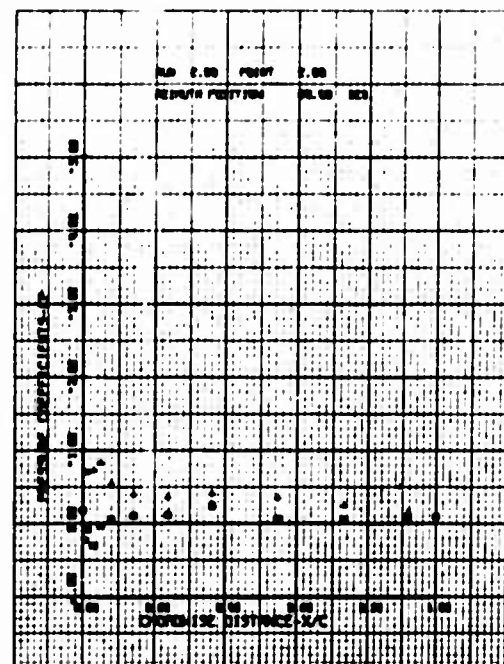


(l)  $\psi = 360^\circ$

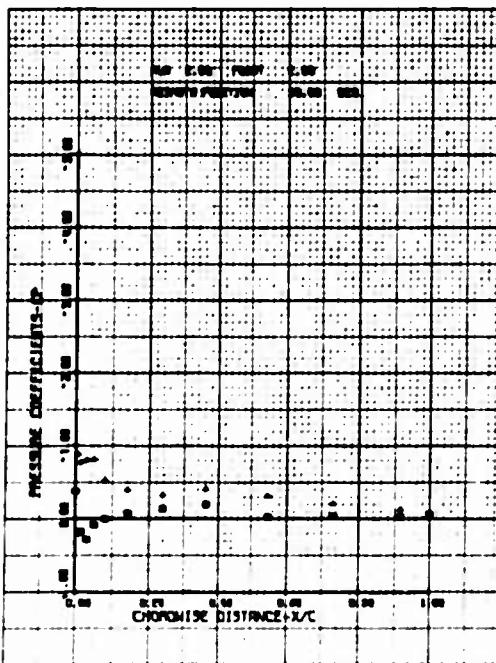
Figure 35. Concluded.



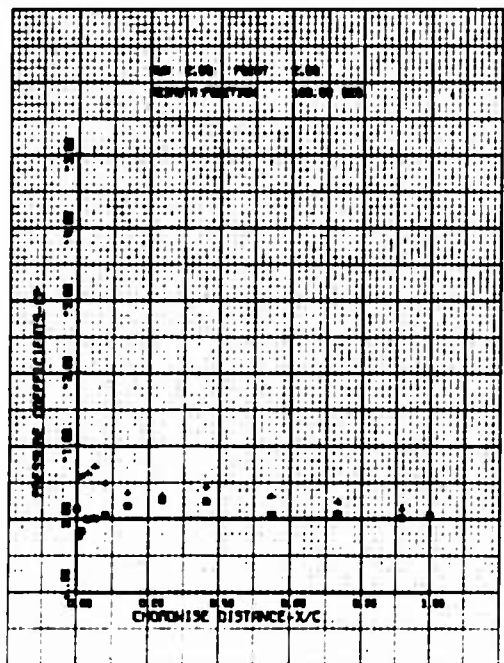
(a)  $\psi = 30^\circ$



(b)  $\psi = 60^\circ$

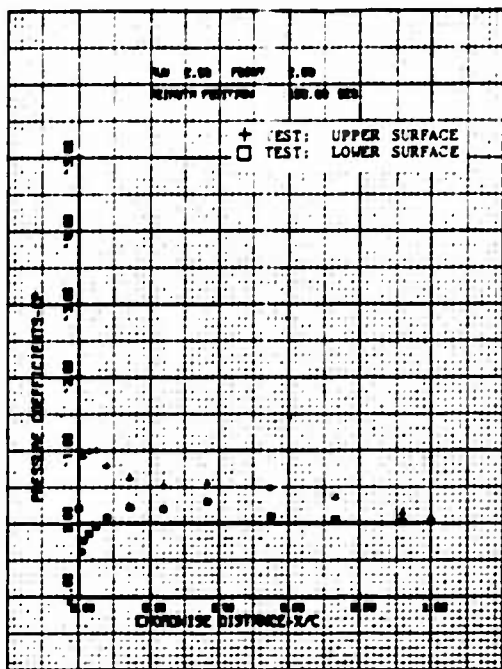


(c)  $\psi = 90^\circ$

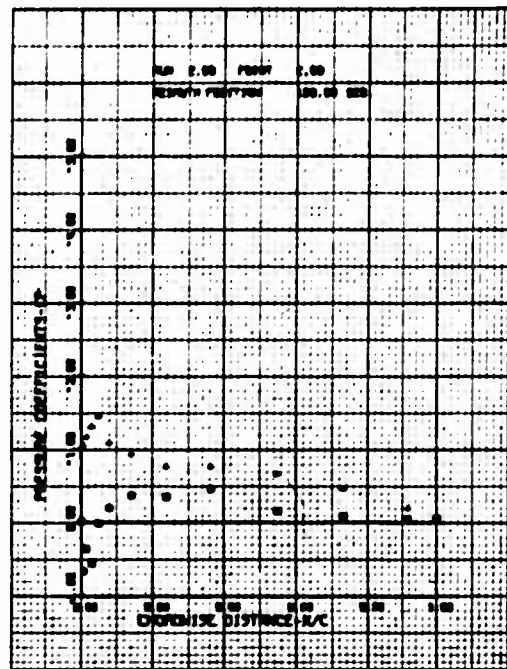


(d)  $\psi = 120^\circ$

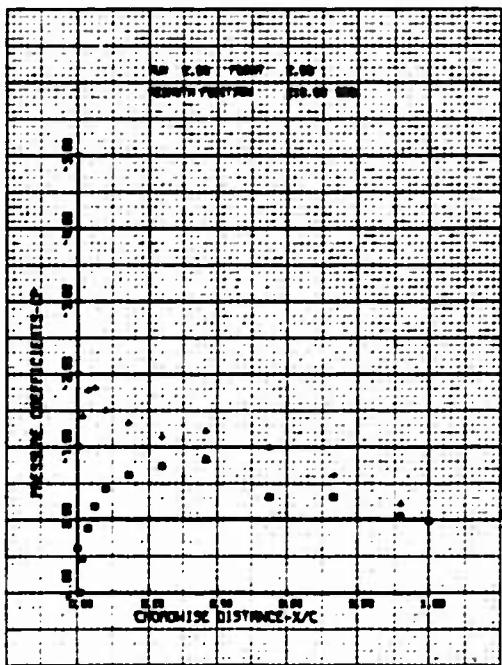
Figure 36. Chordwise Pressure Distribution (Run 2, Point 2);  
 $\mu = 0.20$ ,  $M_{(1.0, 90)} = 0.30$ ,  $\theta_{.75R} = 3.1^\circ$ ,  
 $\dot{\theta} \approx \theta \approx 0$ .



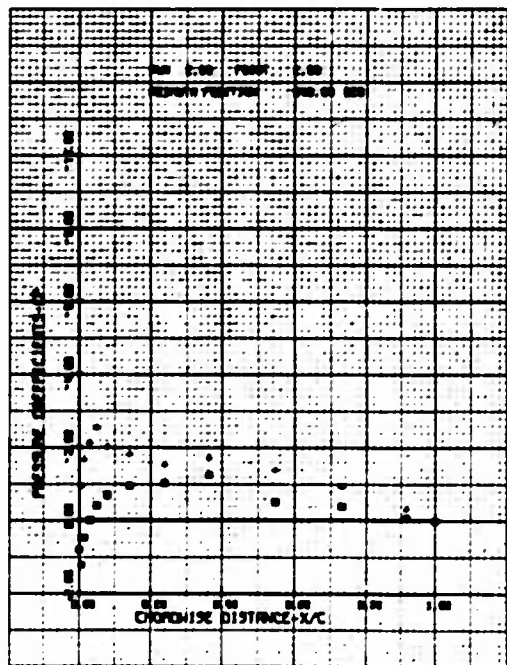
(e)  $\psi = 150^\circ$



(f)  $\psi = 180^\circ$

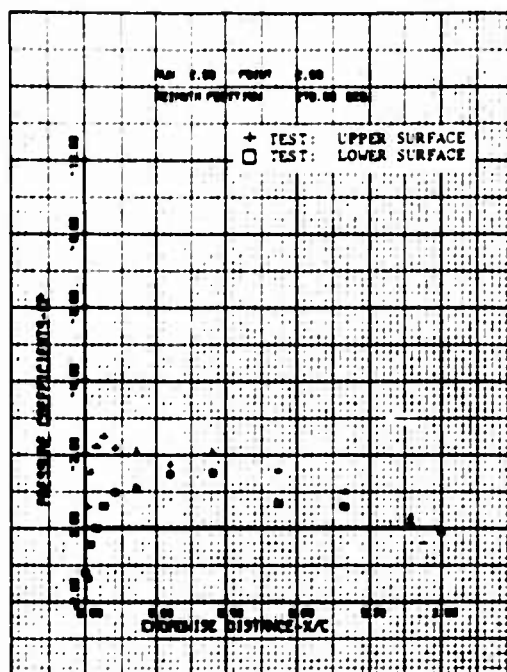


(g)  $\psi = 210^\circ$

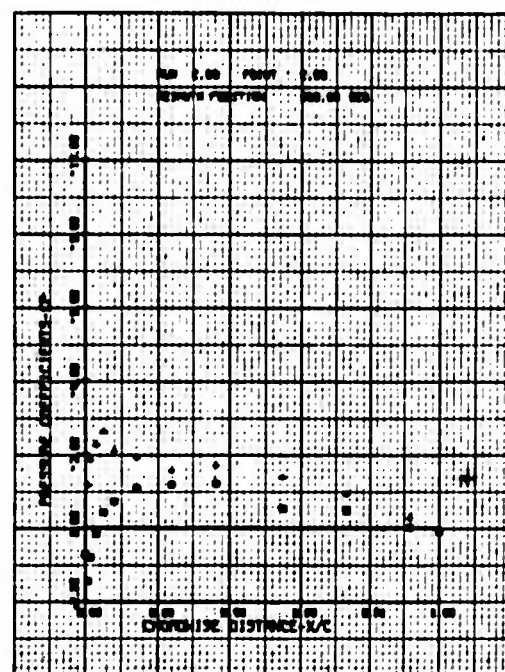


(h)  $\psi = 240^\circ$

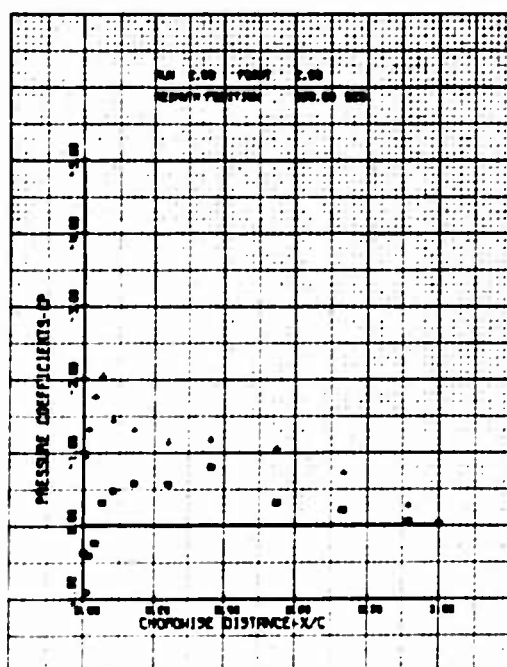
Figure 36. Continued.



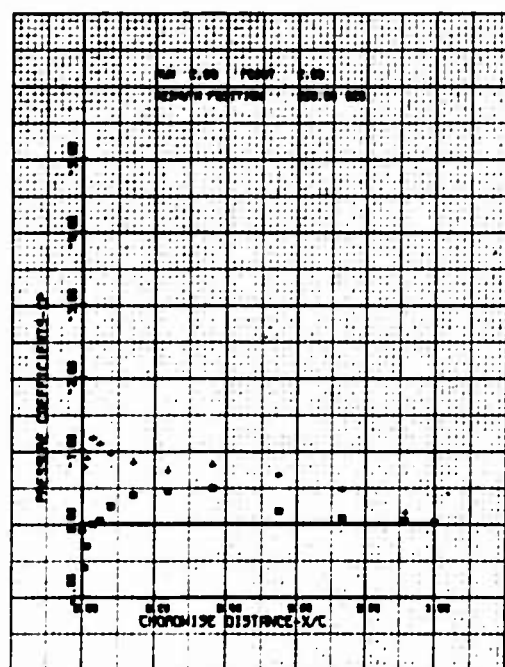
(i)  $\psi = 270^\circ$



(j)  $\psi = 300^\circ$

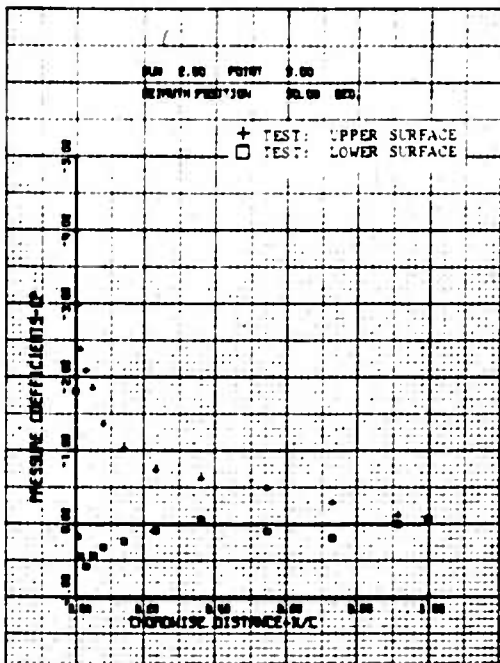


(k)  $\psi = 330^\circ$

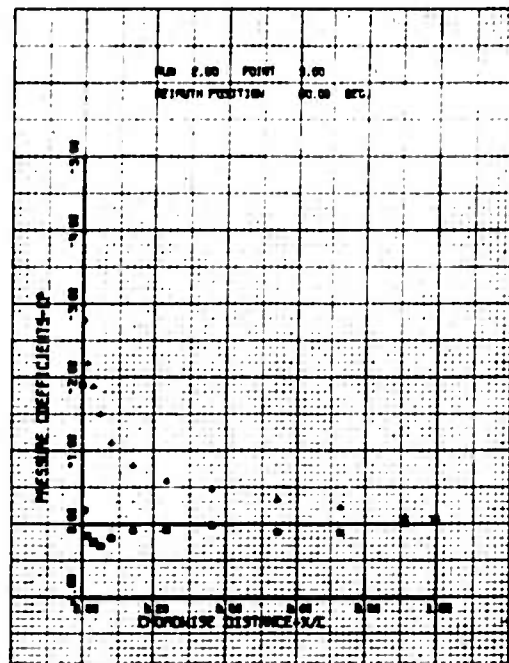


(l)  $\psi = 360^\circ$

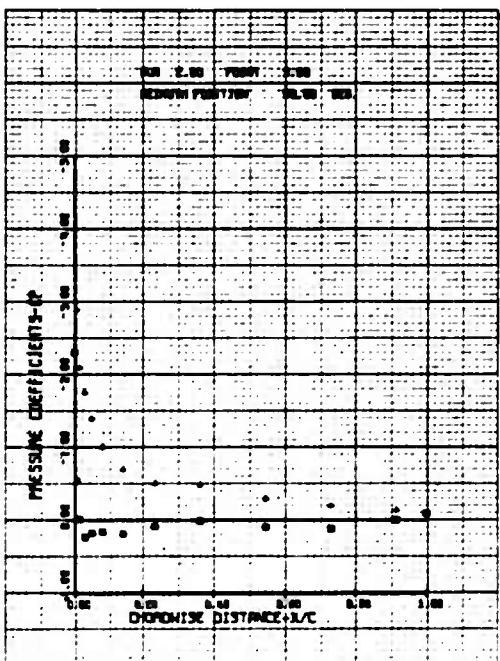
Figure 36. Concluded.



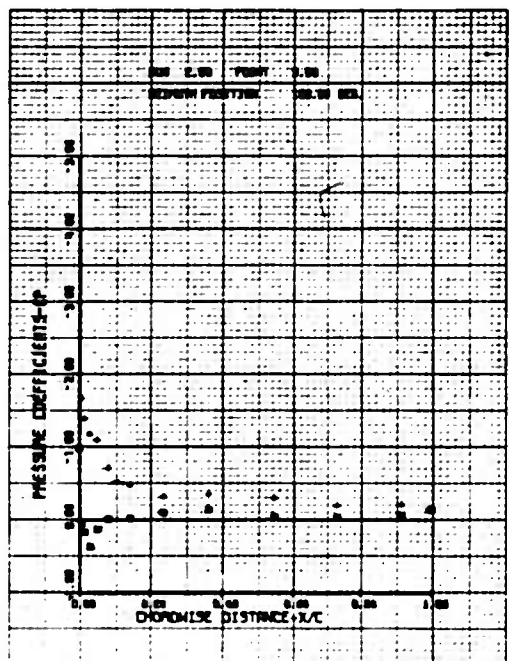
(a)  $\psi = 30^\circ$



(b)  $\psi = 60^\circ$

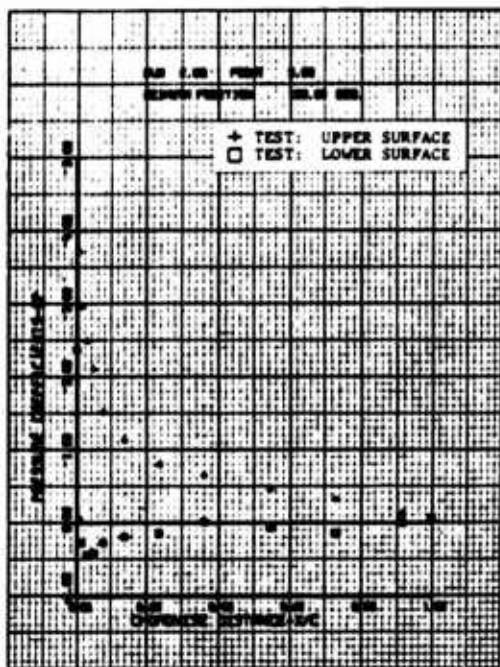


(c)  $\psi = 90^\circ$

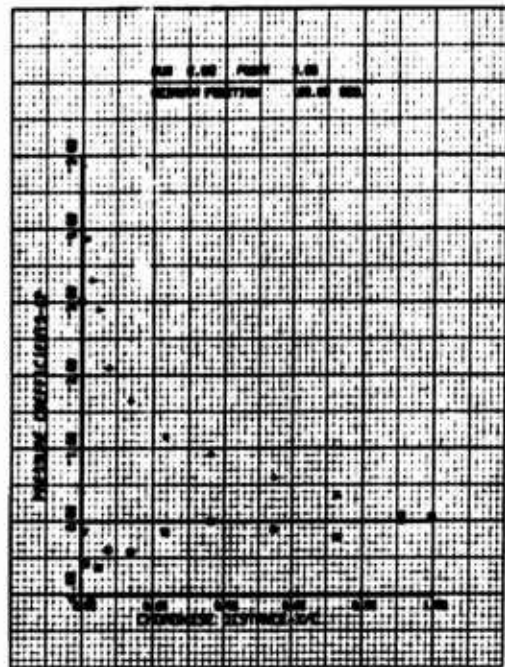


(d)  $\psi = 120^\circ$

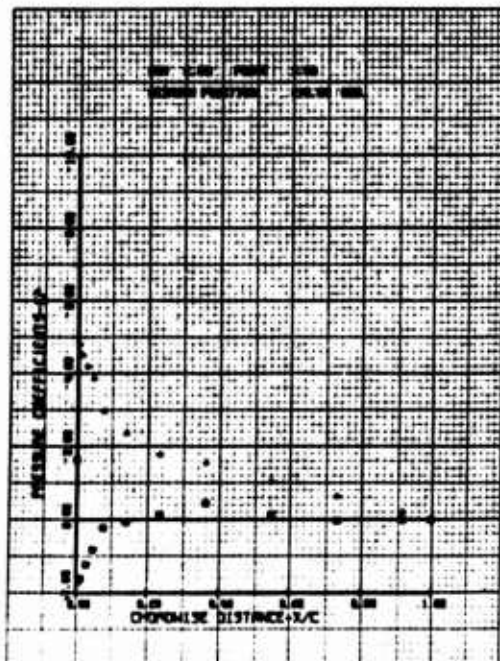
Figure 37. Chordwise Pressure Distribution (Run 2, Point 3);  
 $\mu = 0.20$ ,  $M_{(1.0, 90)} = 0.30$ ,  $\theta_{.75R} = 11.0^\circ$ ,  
 $\beta \approx \dot{\beta} \approx 0$ .



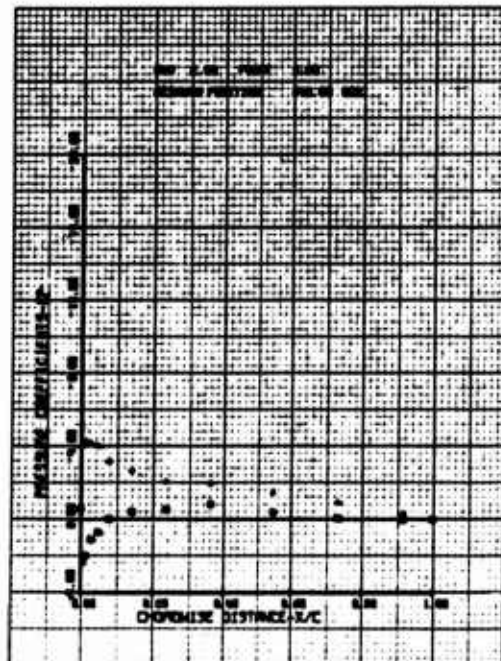
(e)  $\psi = 150^\circ$



(f)  $\psi = 180^\circ$

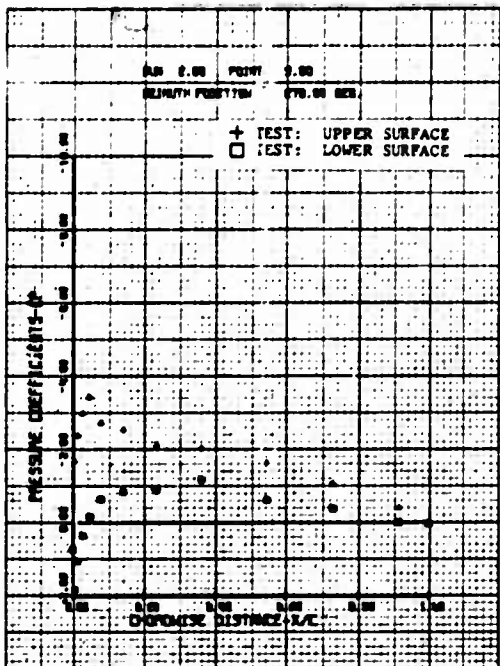


(g)  $\psi = 210^\circ$

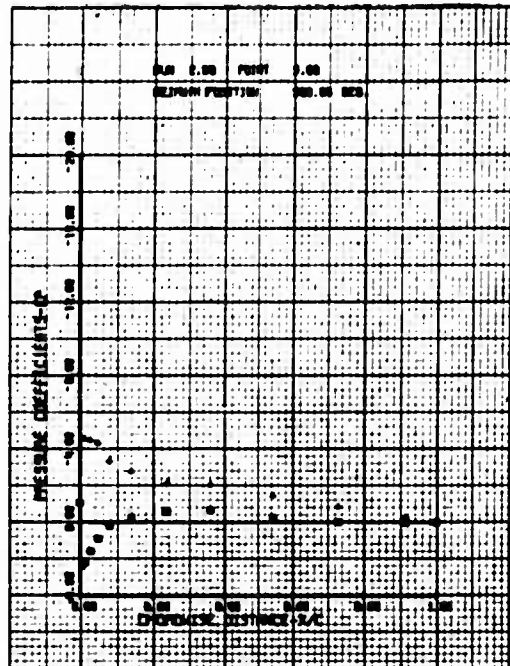


(h)  $\psi = 240^\circ$

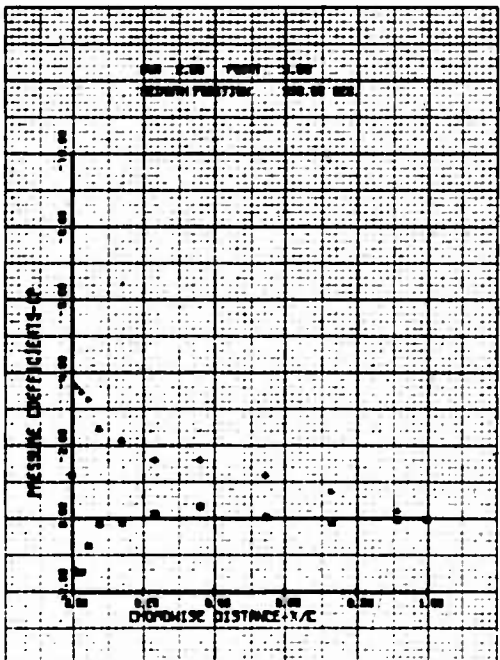
Figure 37. Continued.



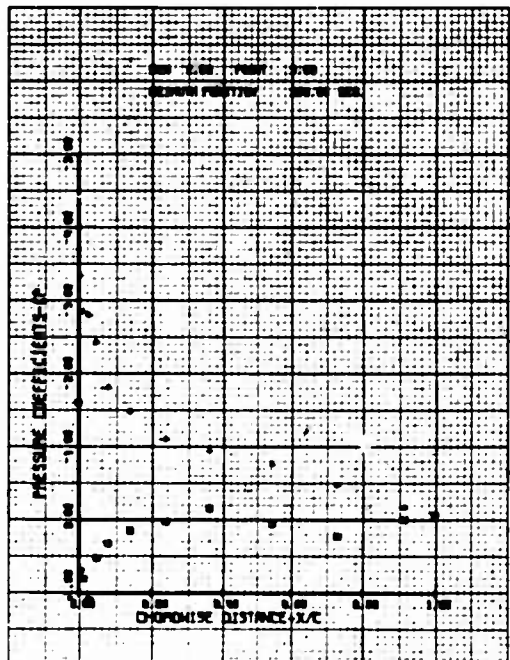
(i)  $\psi = 270^\circ$



(j)  $\psi = 300^\circ$

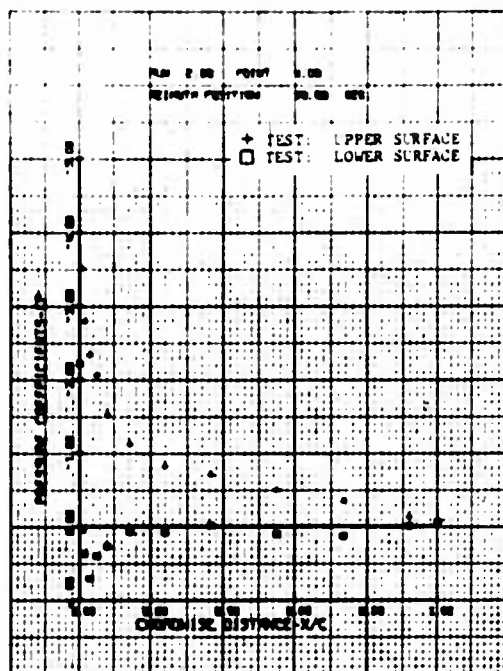


(k)  $\psi = 330^\circ$

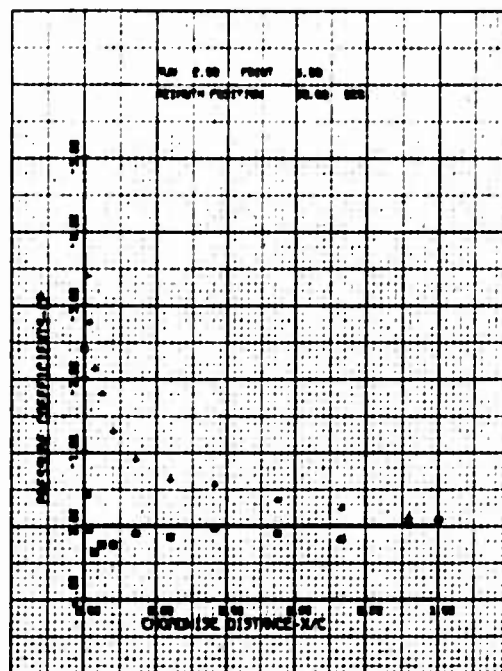


(l)  $\psi = 360^\circ$

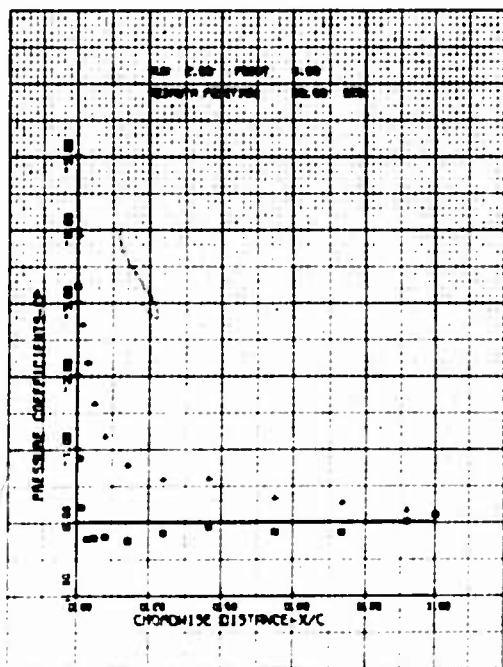
Figure 37. Concluded.



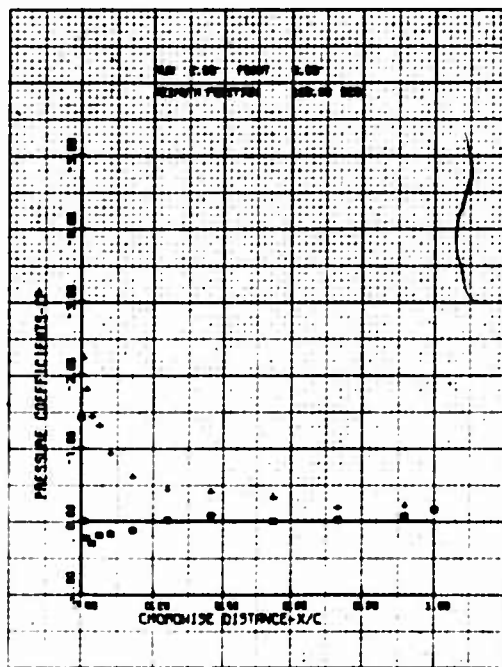
(a)  $\psi = 30^\circ$



(b)  $\psi = 60^\circ$

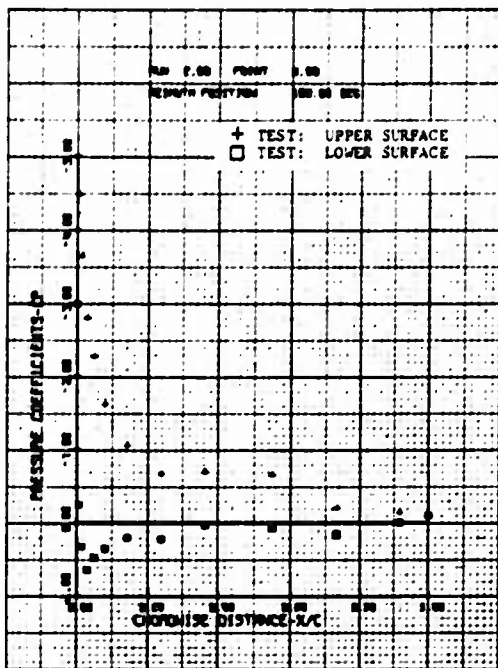


(c)  $\psi = 90^\circ$

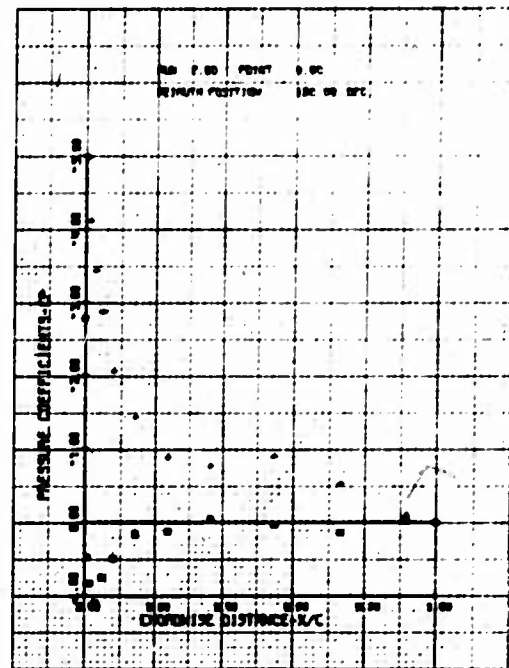


(d)  $\psi = 120^\circ$

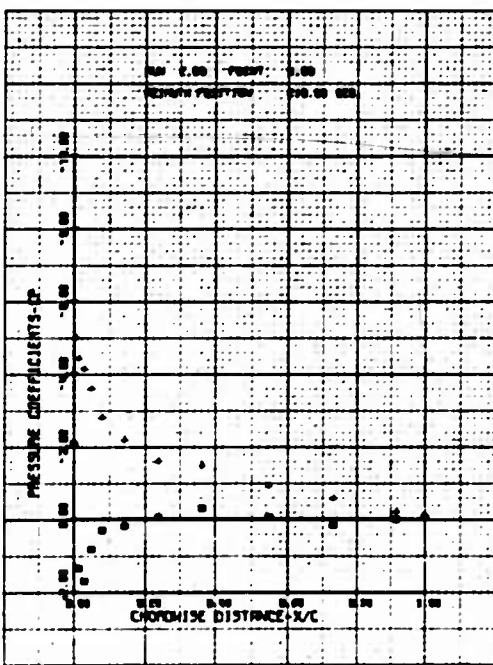
Figure 38. Chordwise Pressure Distribution (Run 2 Point 4);  
 $\mu = 0.20$ ,  $M_{(1.0, 90)} = 0.30$ ,  $\theta_{.75R} = 11.0^\circ$ ,  
 $\dot{\theta} \approx \ddot{\theta} \approx 0$ .



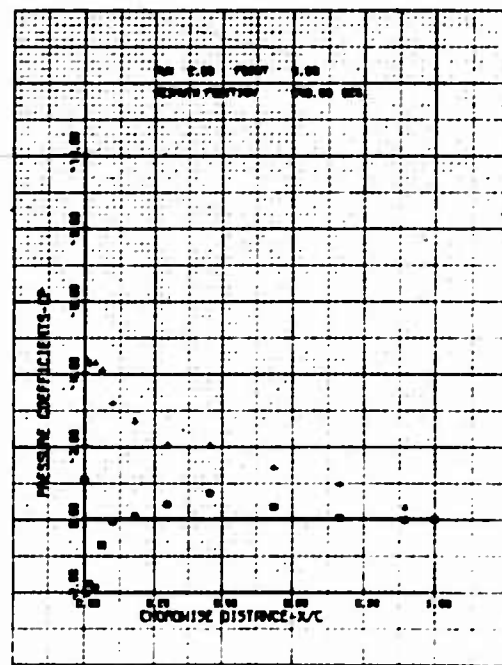
(e)  $\psi = 150^\circ$



(f)  $\psi = 180^\circ$

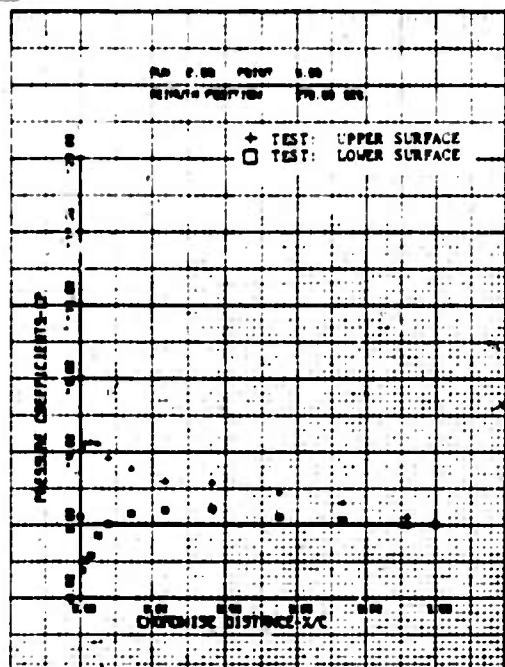


(g)  $\psi = 210^\circ$

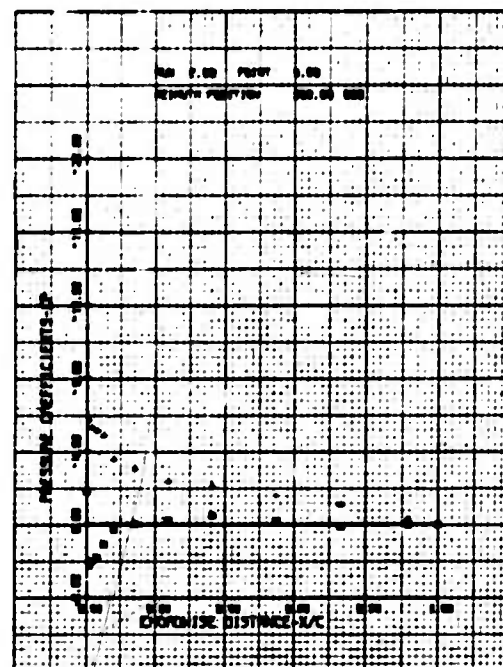


(h)  $\psi = 240^\circ$

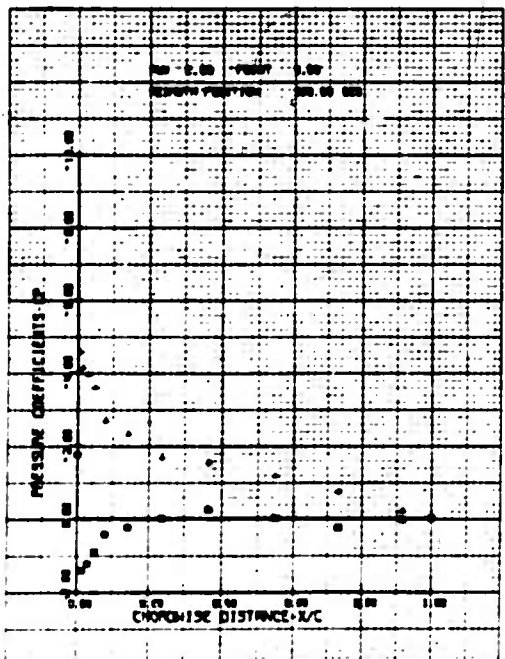
Figure 38. Continued.



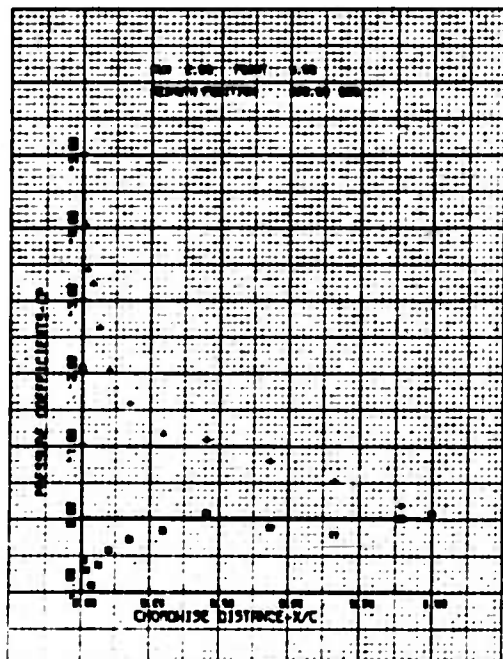
( i )  $\psi = 270^\circ$



( j )  $\psi = 300^\circ$

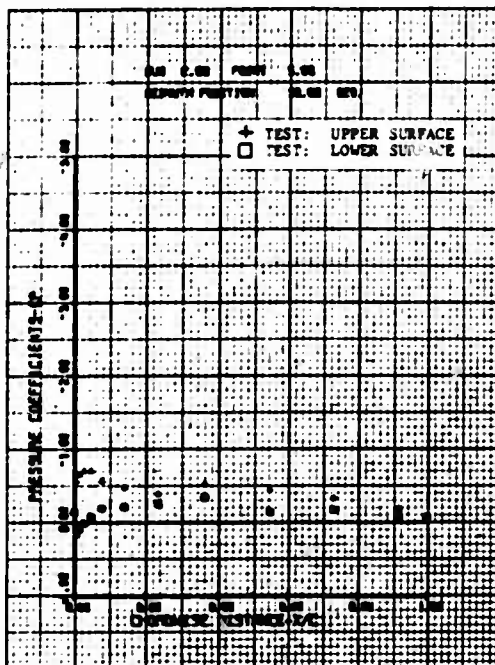


( k )  $\psi = 330^\circ$

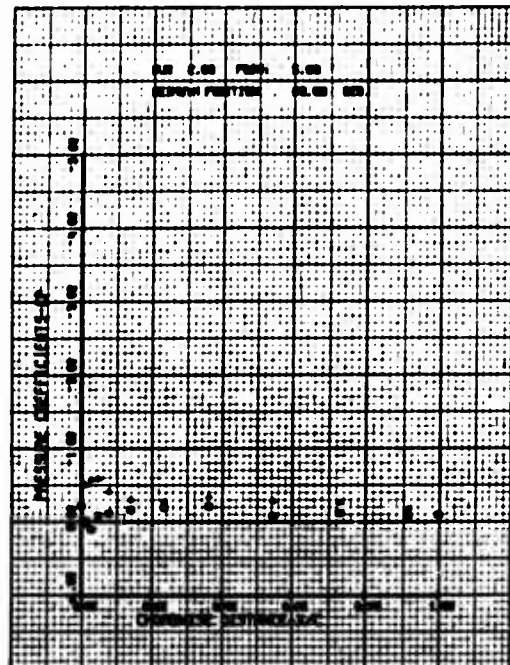


( l )  $\psi = 360^\circ$

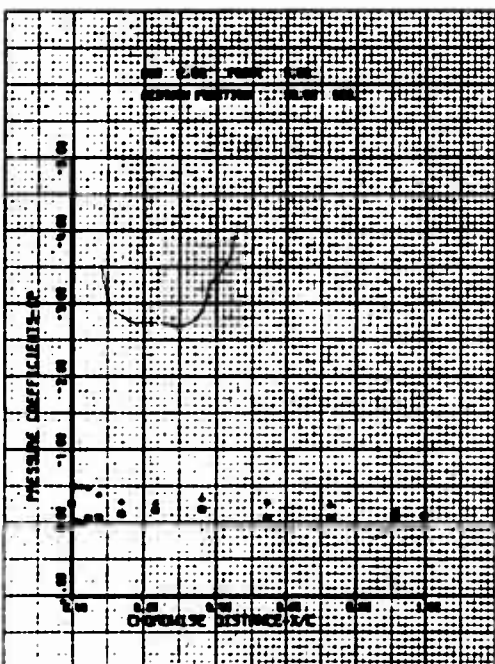
Figure 38. Concluded.



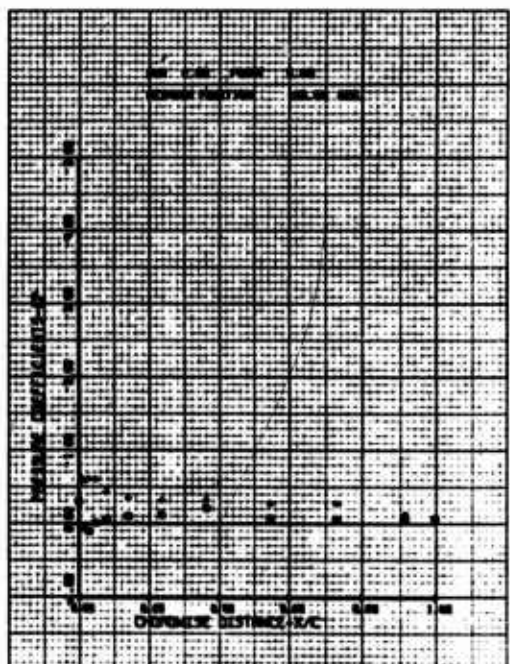
(a)  $\psi = 30^\circ$



(b)  $\psi = 60^\circ$

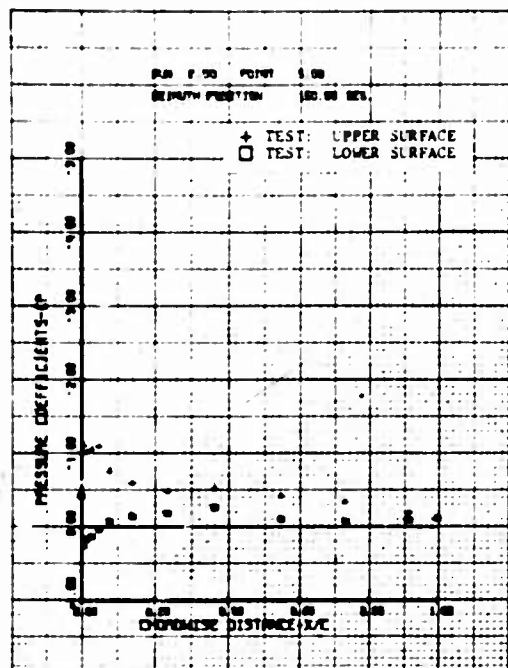


(c)  $\psi = 90^\circ$

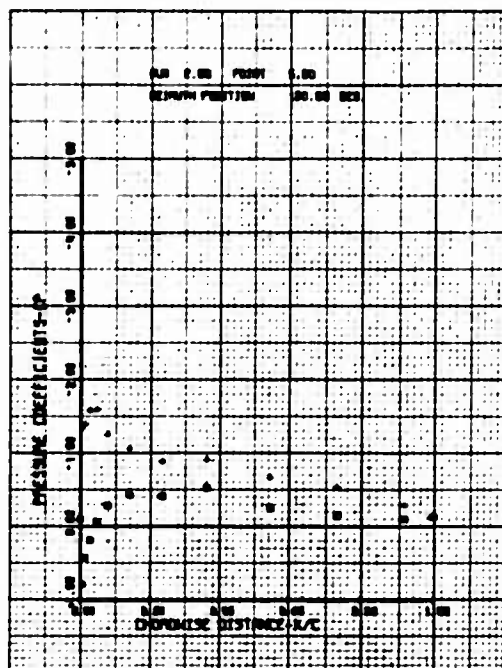


(d)  $\psi = 120^\circ$

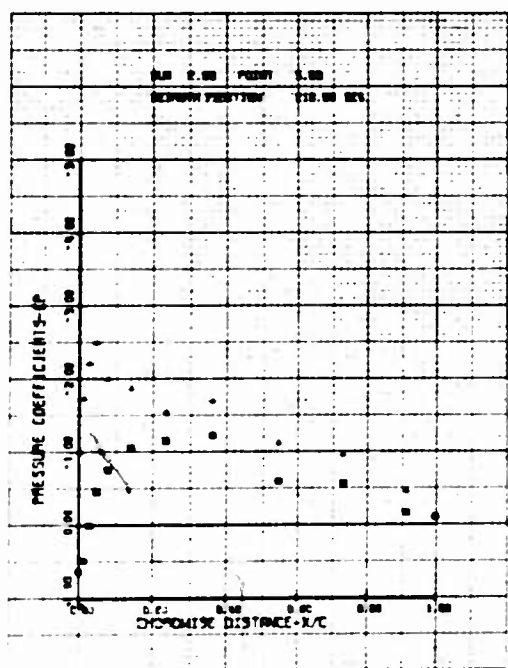
Figure 39. Chordwise Pressure Distribution (Run 2, Point 5);  
 $\mu = 0.30$ ,  $M_{(1.0, 90)} = 0.32$ ,  $\theta_{.75R} = 3.1^\circ$ ,  
 $\dot{\beta} \approx \ddot{\beta} \approx 0$ .



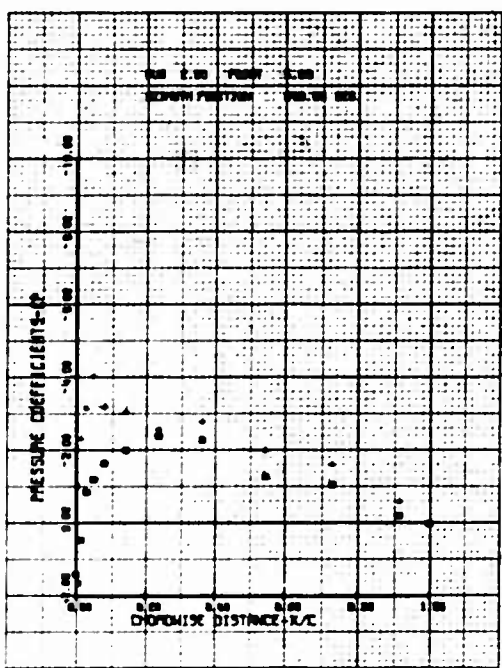
(e)  $\psi = 150^\circ$



(f)  $\psi = 180^\circ$

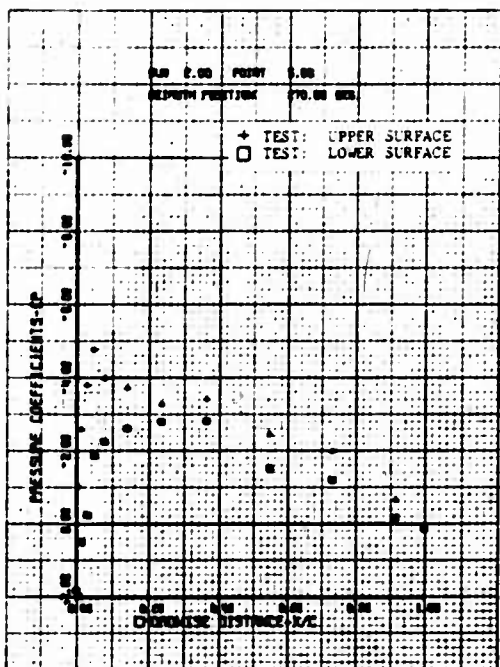


(g)  $\psi = 210^\circ$

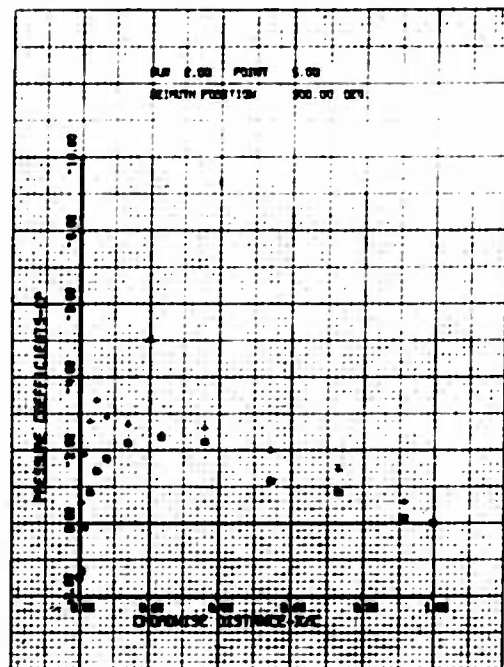


(h)  $\psi = 240^\circ$

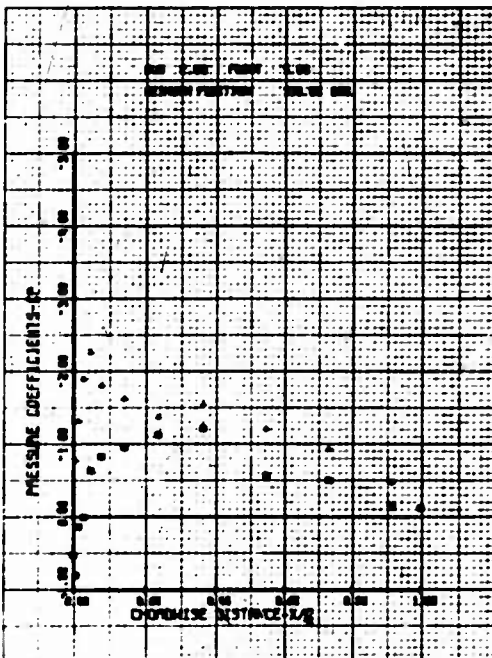
Figure 39. Continued.



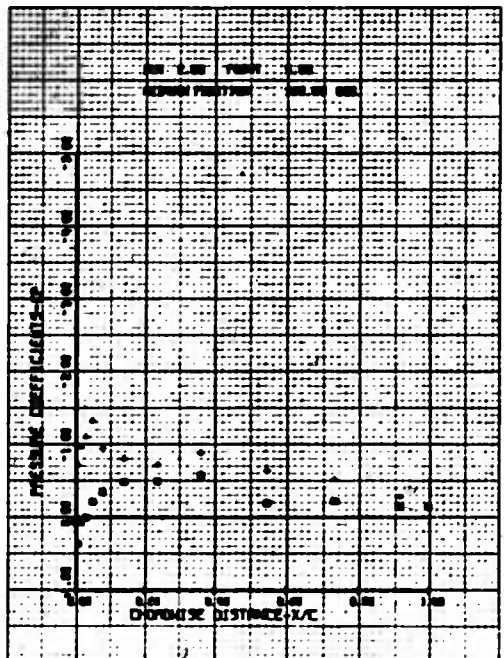
(i)  $\psi = 270^\circ$



(j)  $\psi = 300^\circ$

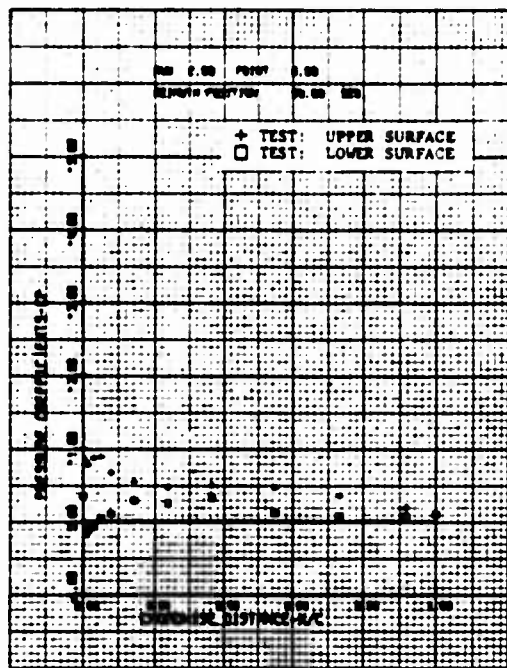


(k)  $\psi = 330^\circ$

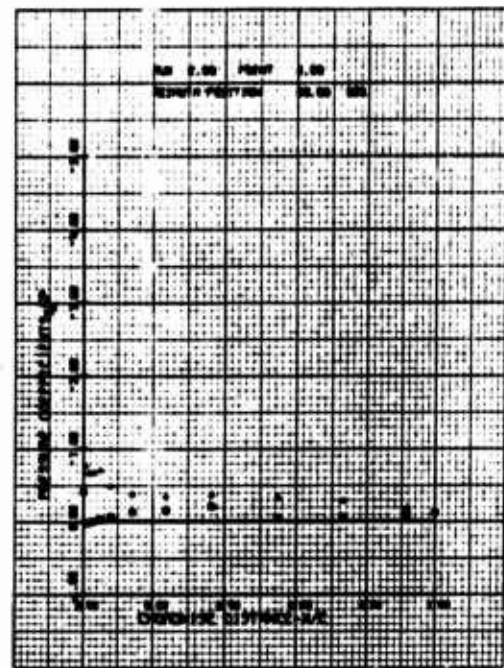


(l)  $\psi = 360^\circ$

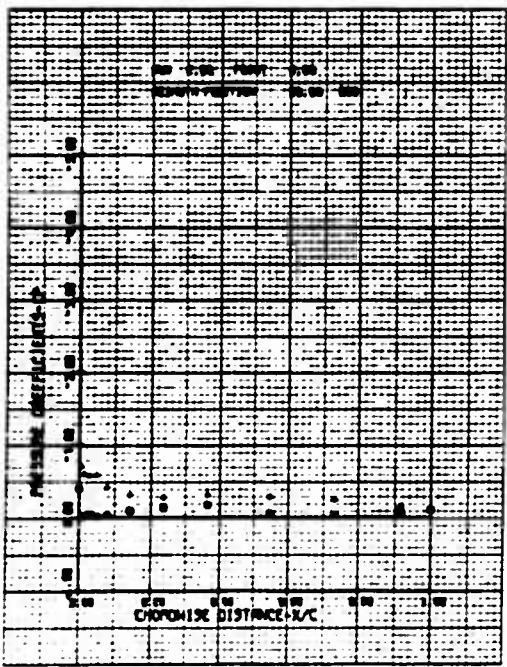
Figure 39. Concluded.



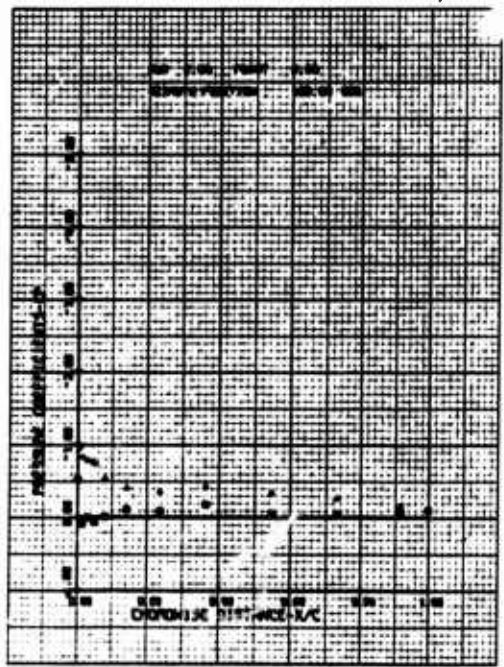
(a)  $\psi = 30^\circ$



(b)  $\psi = 60^\circ$

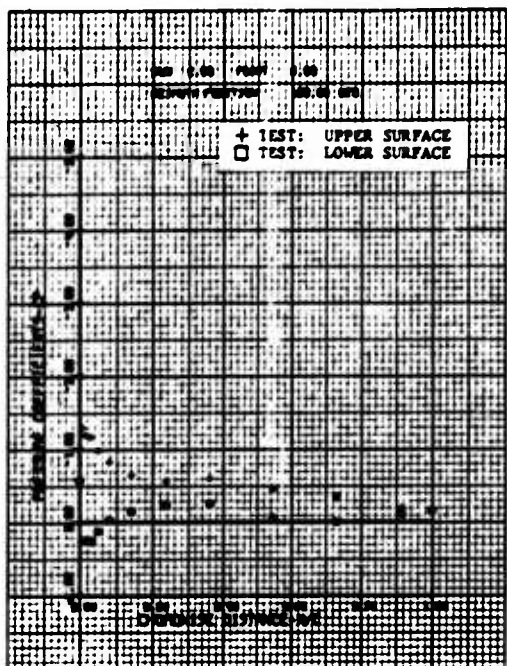


(c)  $\psi = 90^\circ$

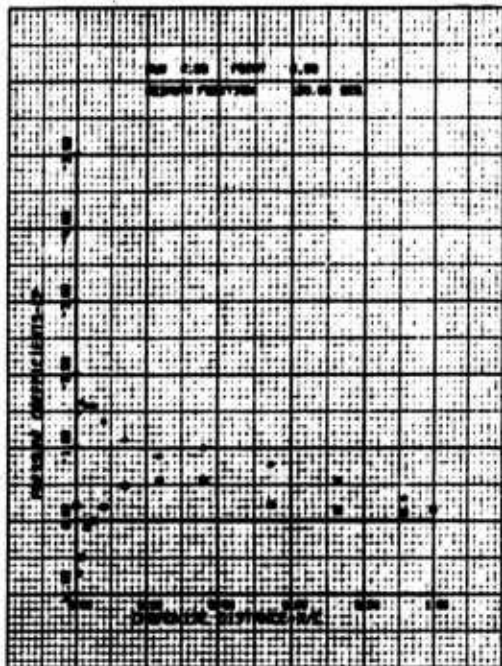


(d)  $\psi = 120^\circ$

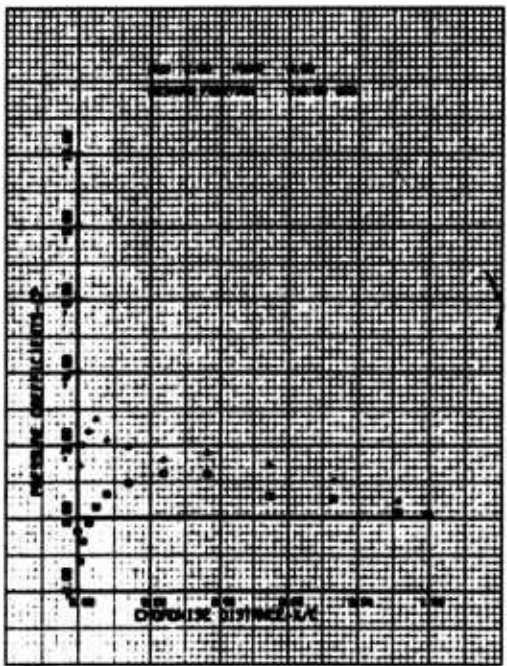
Figure 40. Chordwise Pressure Distribution (Run 2, Point 6);  
 $\mu = 0.30$ ,  $M_{(1.0, 90)} = 0.32$ ,  $\theta_{.75R} = 3.1^\circ$ ,  
 $\dot{\theta} \approx \ddot{\theta} \approx 0$ .



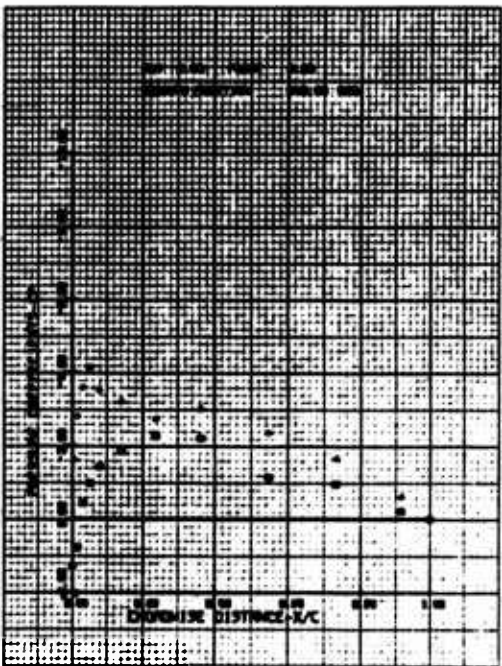
(e)  $\psi = 150^\circ$



(f)  $\psi = 180^\circ$

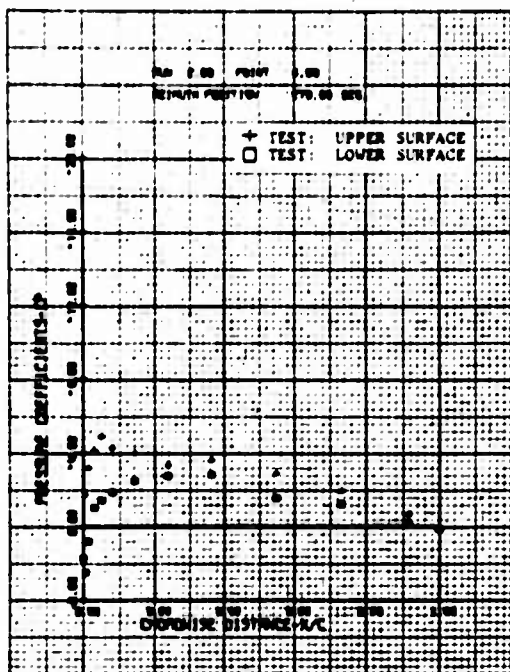


(g)  $\psi = 210^\circ$

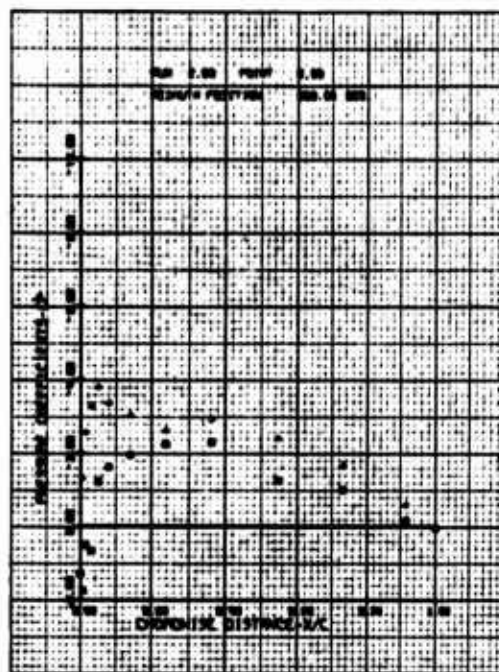


(h)  $\psi = 240^\circ$

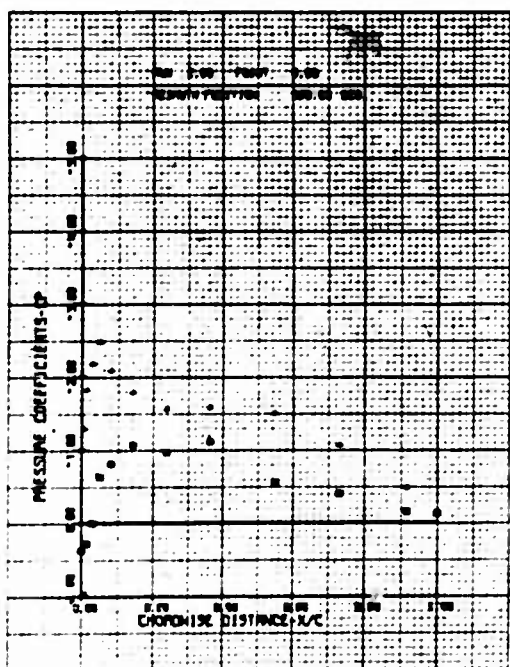
Figure 40. Continued.



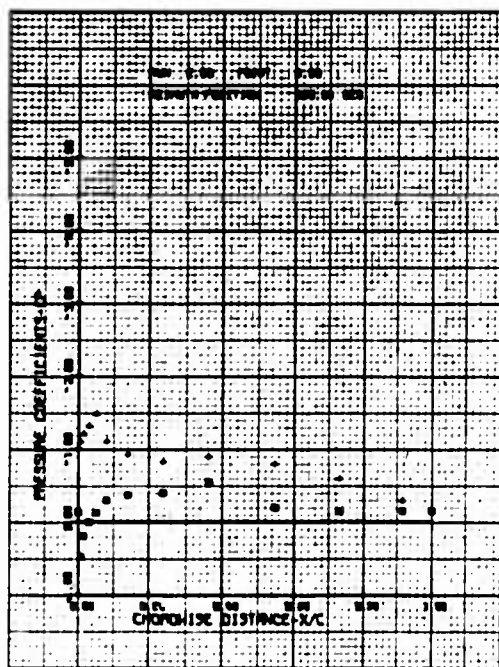
(i)  $\psi = 270^\circ$



(j)  $\psi = 300^\circ$

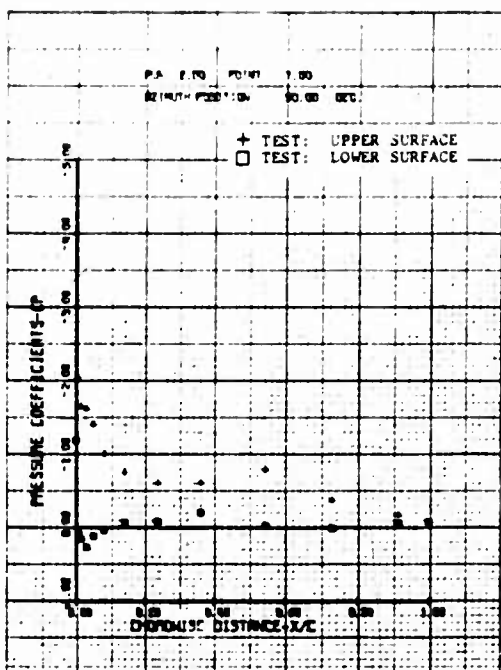


(k)  $\psi = 330^\circ$

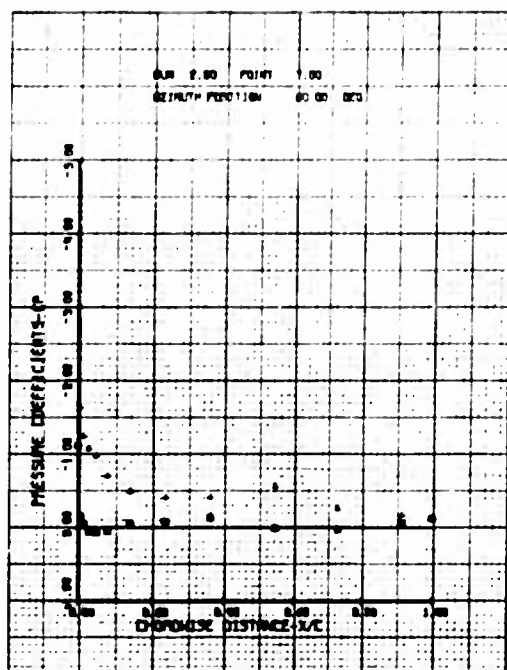


(l)  $\psi = 360^\circ$

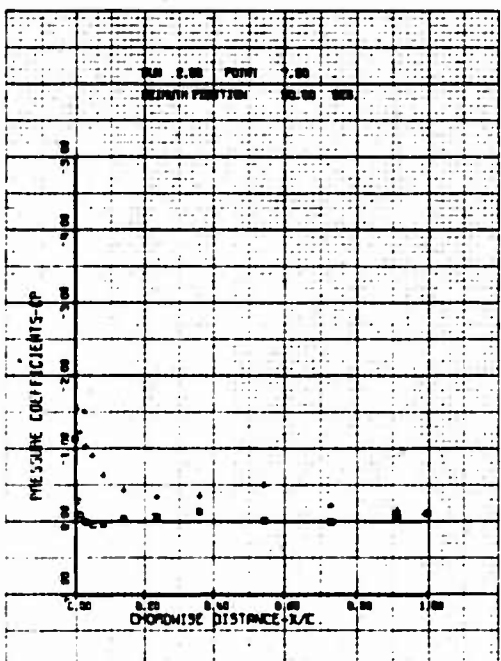
Figure 40. Concluded.



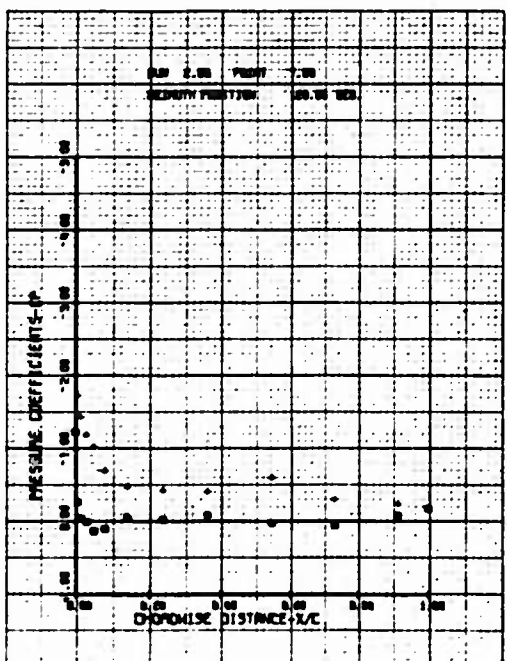
(a)  $\psi = 30^\circ$



(b)  $\psi = 60^\circ$

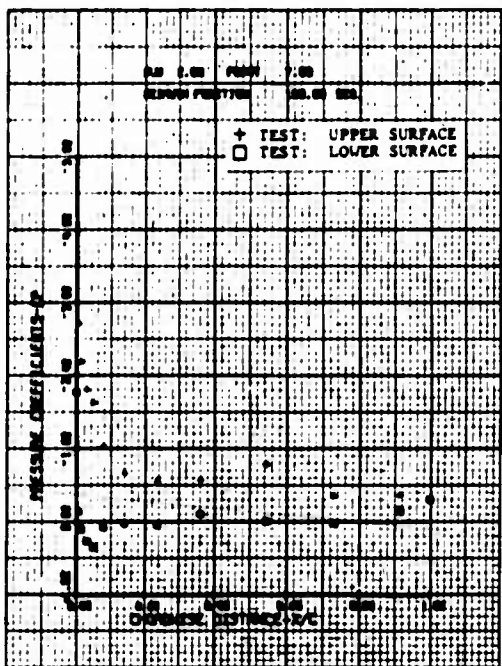


(c)  $\psi = 90^\circ$

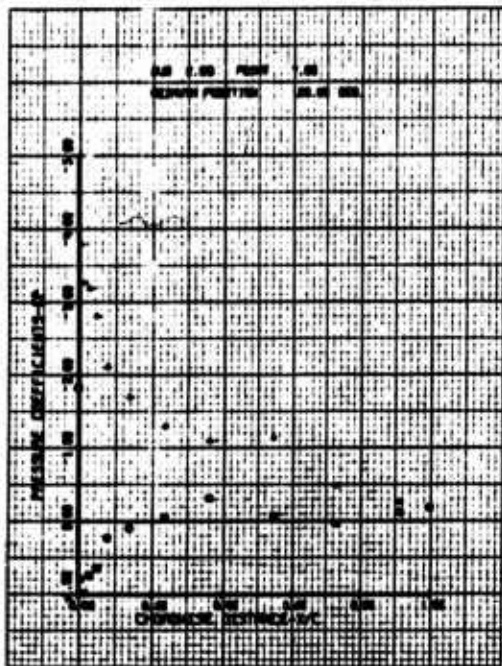


(d)  $\psi = 120^\circ$

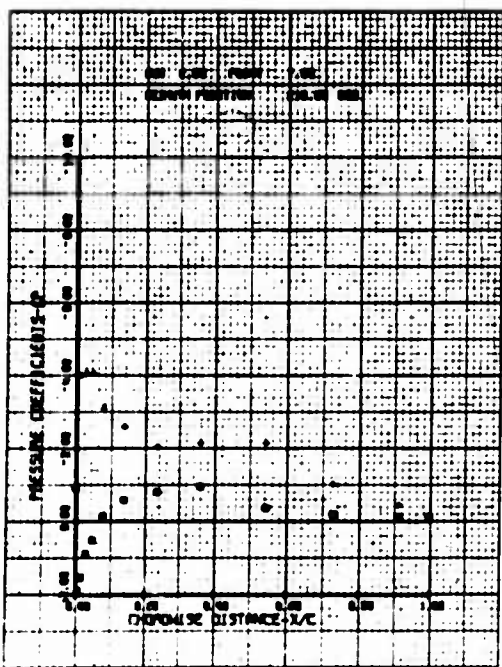
Figure 41. Chordwise Pressure Distribution (Run 2, Point 7);  
 $\mu = 0.30$ ,  $M_{(1.0, 90)} = 0.32$ ,  $\theta_{.75R} = 9.1^\circ$ ,  
 $\dot{\beta} \approx \ddot{\beta} \approx 0$ .



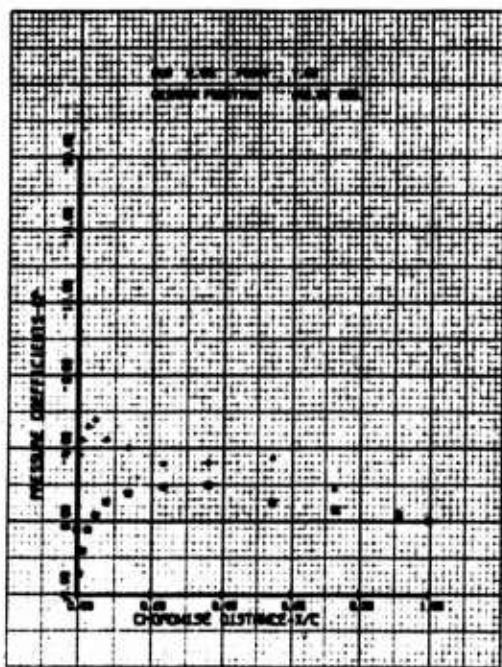
(e)  $\psi = 150^\circ$



(f)  $\psi = 180^\circ$

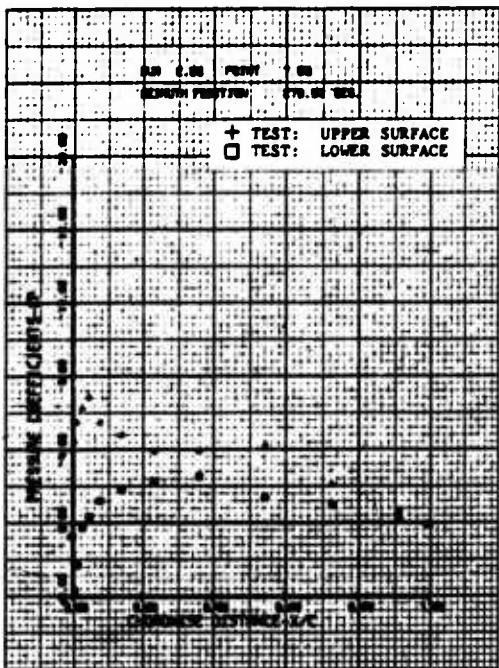


(g)  $\psi = 210^\circ$

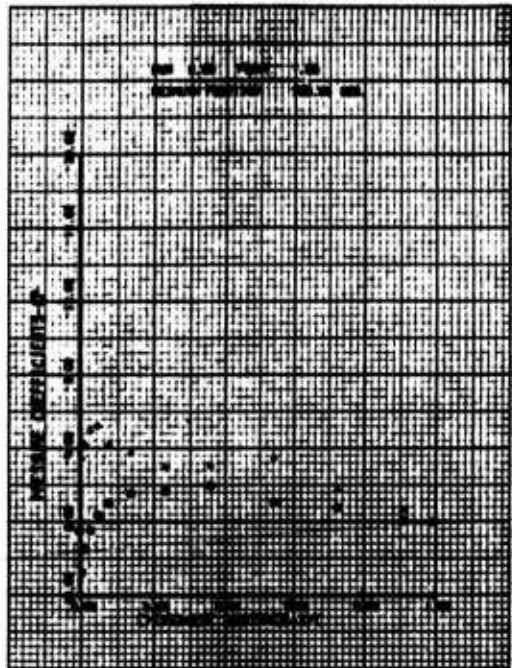


(h)  $\psi = 240^\circ$

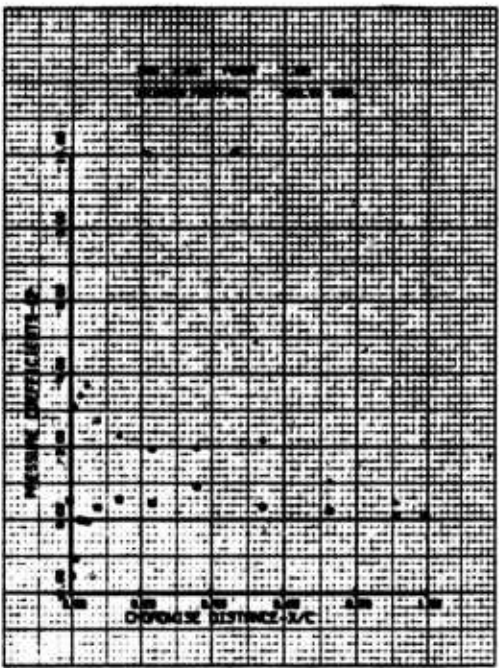
Figure 41. Continued.



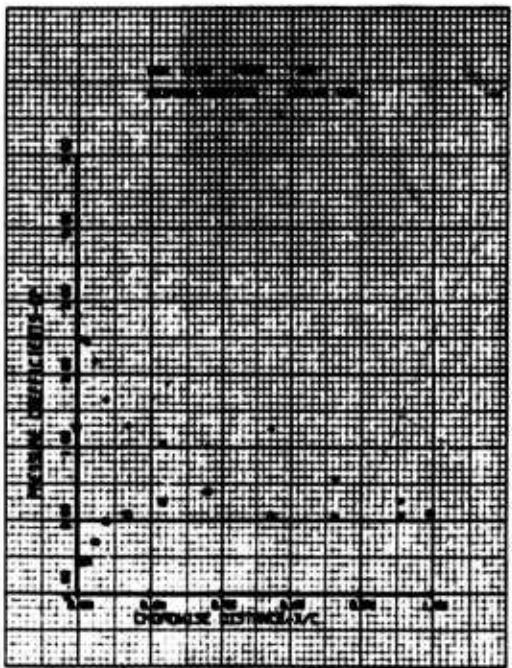
(i)  $\psi = 270^\circ$



(j)  $\psi = 300^\circ$

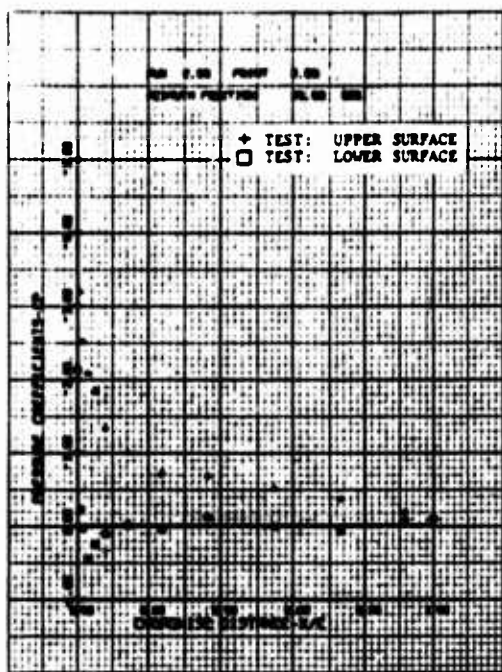


(k)  $\psi = 330^\circ$

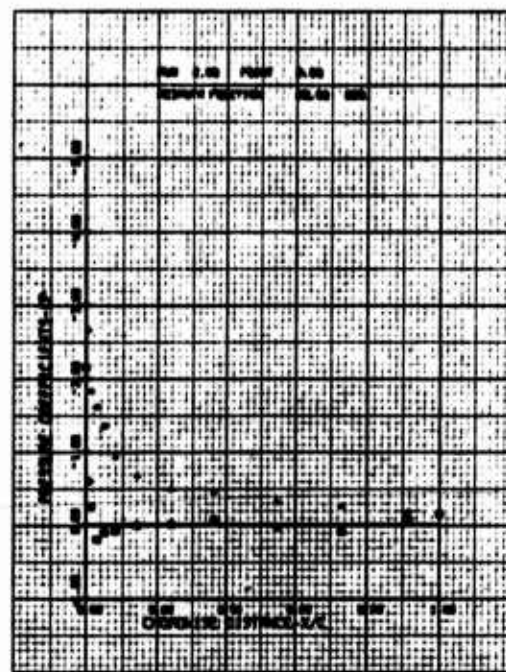


(l)  $\psi = 360^\circ$

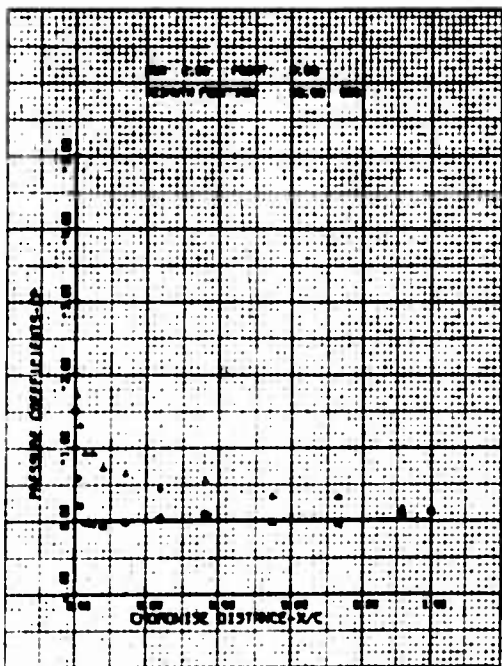
Figure 41. Concluded.



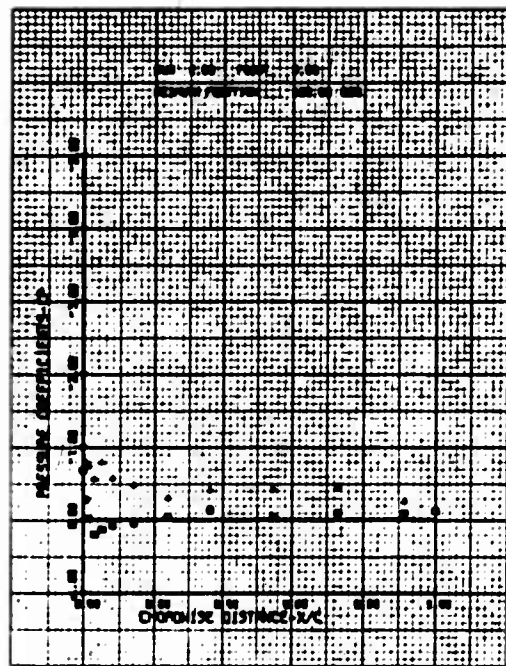
(a)  $\psi = 30^\circ$



(b)  $\psi = 60^\circ$

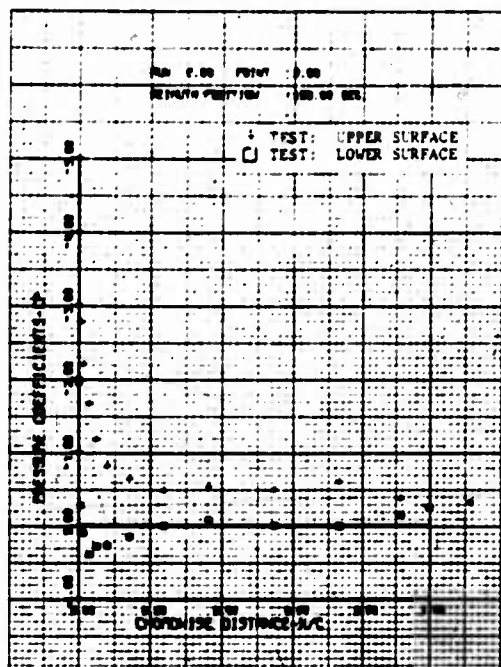


(c)  $\psi = 90^\circ$

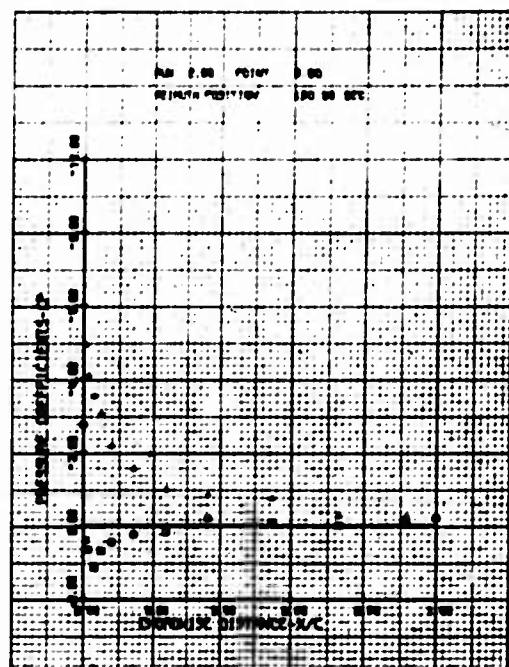


(d)  $\psi = 120^\circ$

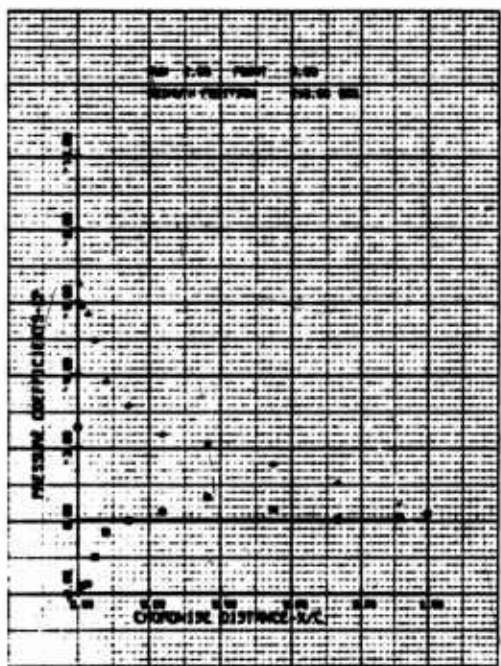
Figure 42. Chordwise Pressure Distribution (Run 2, Point 8);  
 $\mu = 0.30$ ,  $M_{(1.0, 90)} = 0.32$ ,  $\theta_{.75R} = 9.1^\circ$ ,  
 $\dot{\theta} \equiv \ddot{\theta} \equiv 0$ .



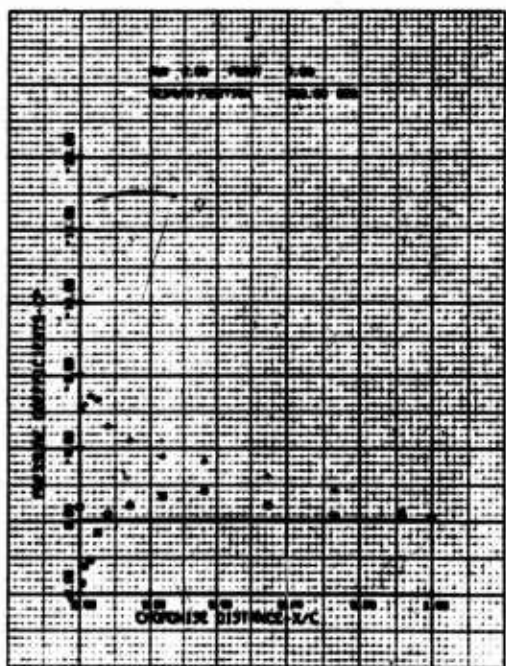
(e)  $\psi = 150^\circ$



(f)  $\psi = 180^\circ$

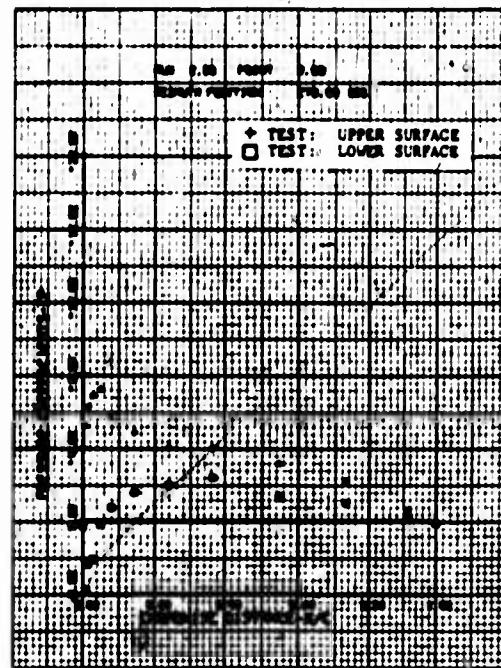


(g)  $\psi = 210^\circ$

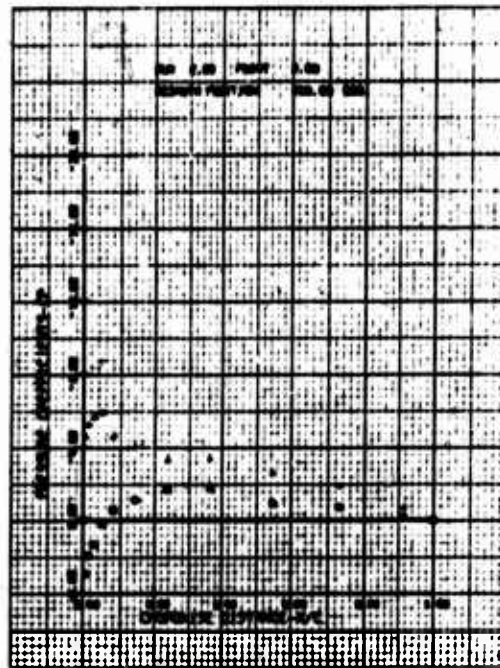


(h)  $\psi = 240^\circ$

Figure 42. Continued.



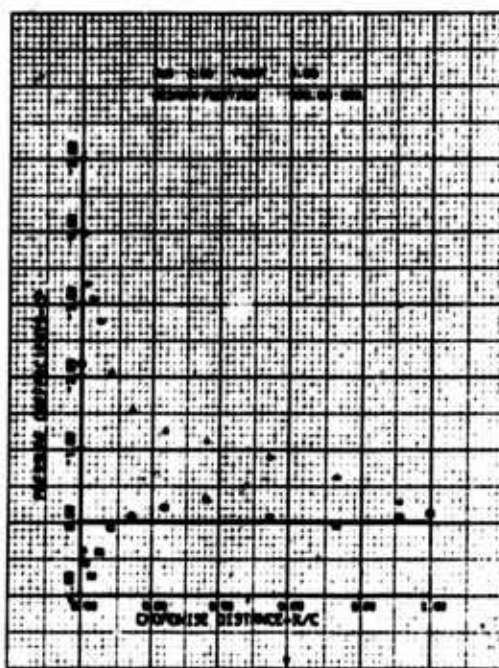
(i)  $\psi = 270^\circ$



(j)  $\psi = 300^\circ$

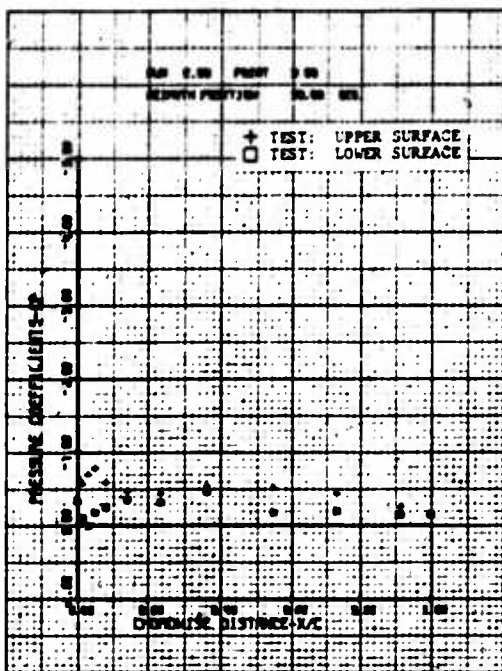


(k)  $\psi = 330^\circ$

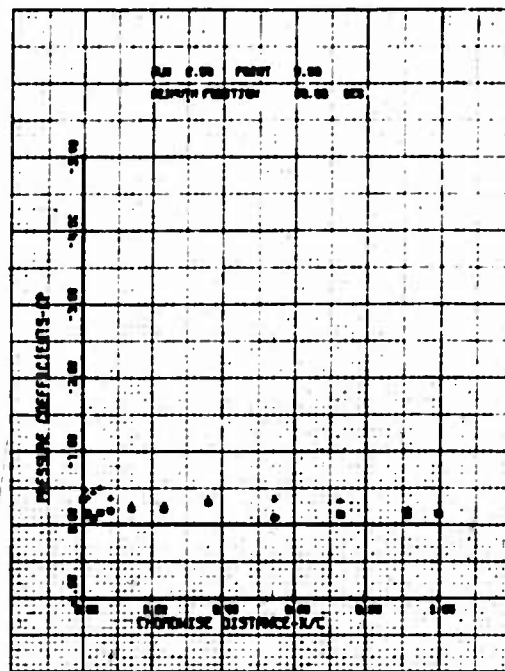


(l)  $\psi = 360^\circ$

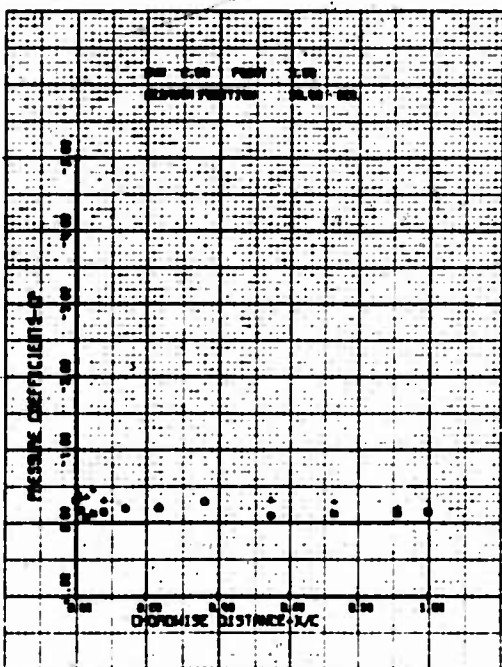
Figure 42. Concluded.



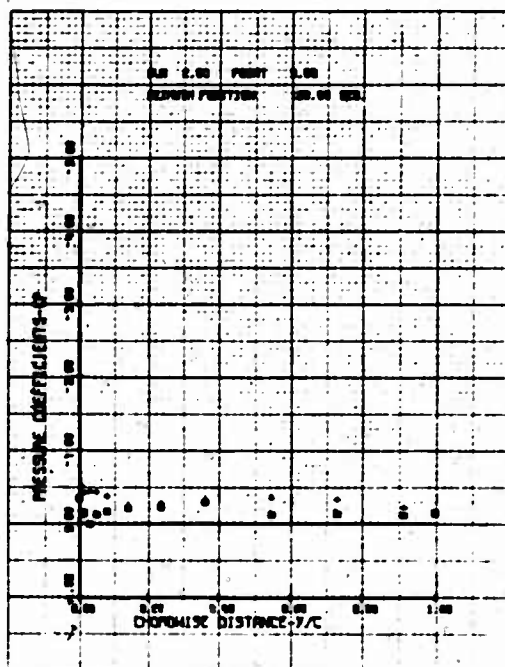
(a)  $\psi = 30^\circ$



(b)  $\psi = 60^\circ$

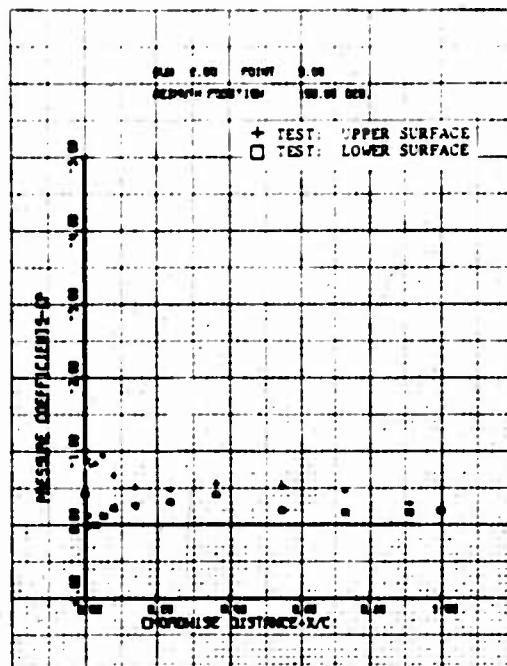


(c)  $\psi = 90^\circ$

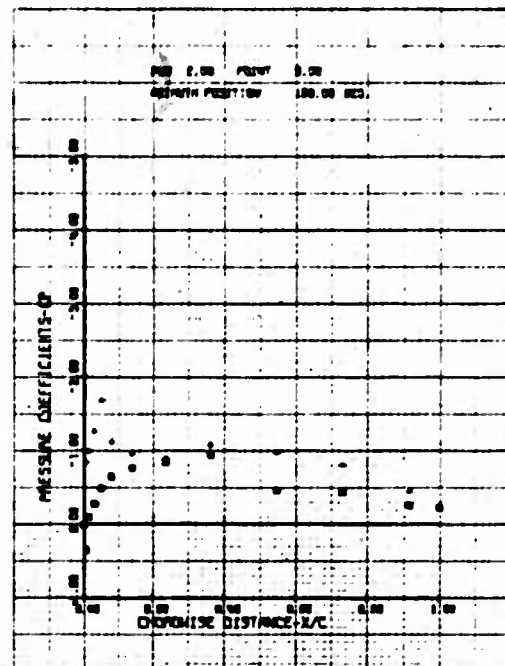


(d)  $\psi = 120^\circ$

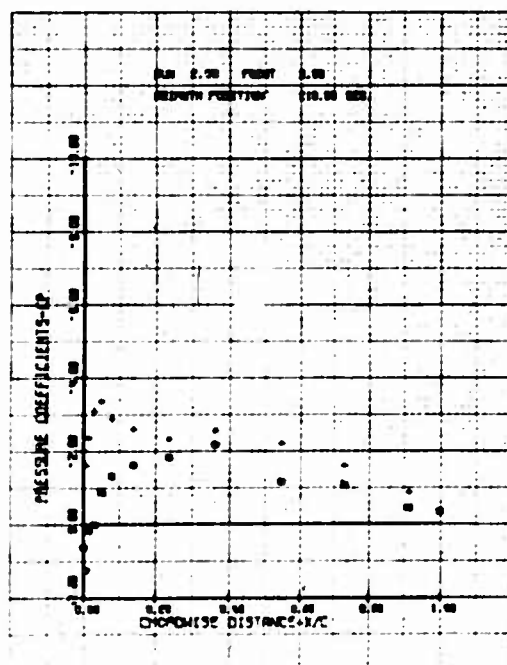
Figure 43. Chordwise Pressure Distribution (Run 2, Point 9);  
 $\mu = 0.40$ ,  $M_{(1.0, 90)} = 0.34$ ,  $\theta_{.75R} = 3.1^\circ$ ,  
 $\dot{\beta} \approx \ddot{\beta} \approx 0$ .



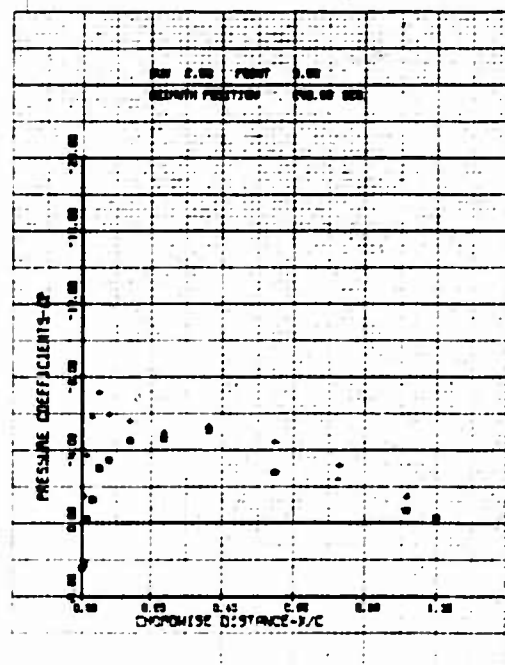
(e)  $\psi = 150^\circ$



(f)  $\psi = 180^\circ$

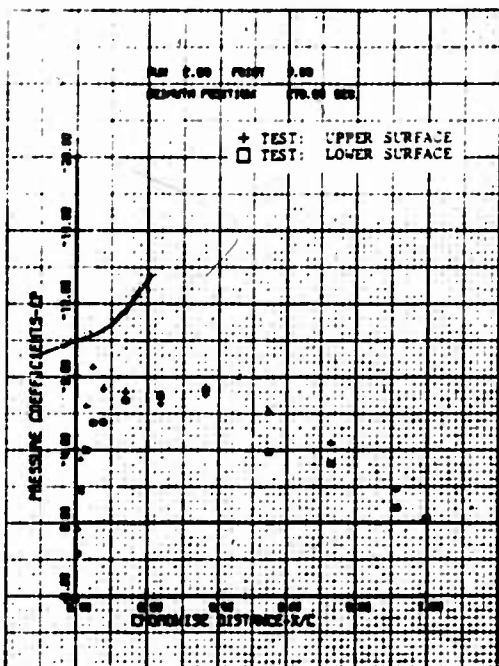


(g)  $\psi = 210^\circ$

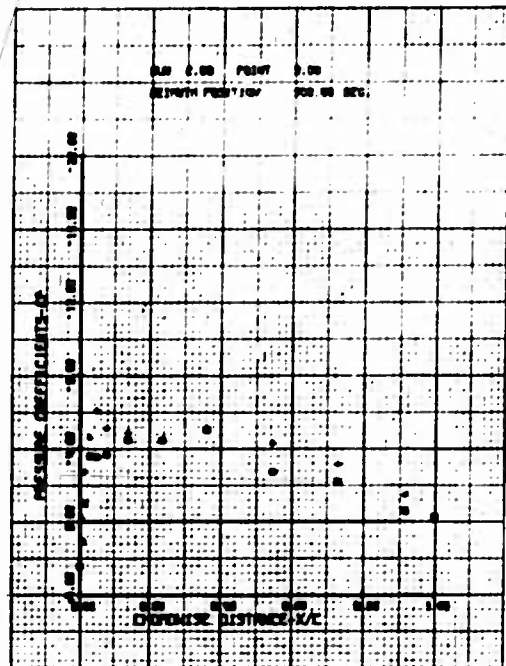


(h)  $\psi = 240^\circ$

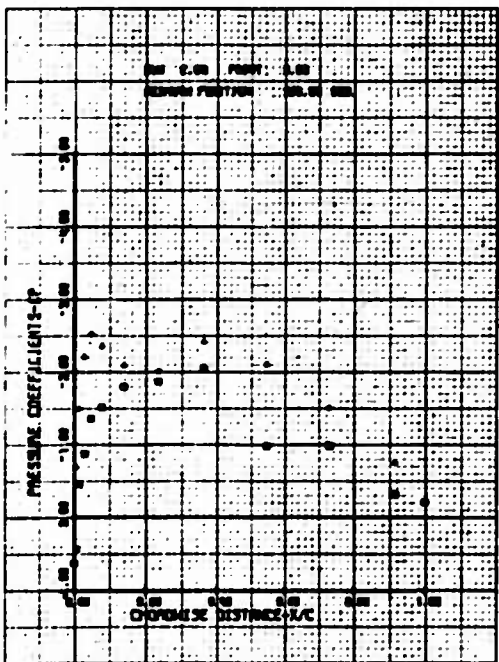
Figure 43. Continued.



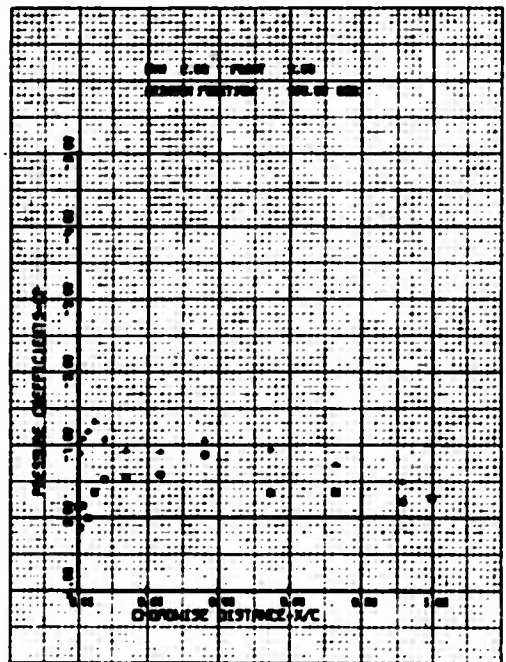
(i)  $\psi = 270^\circ$



(j)  $\psi = 300^\circ$

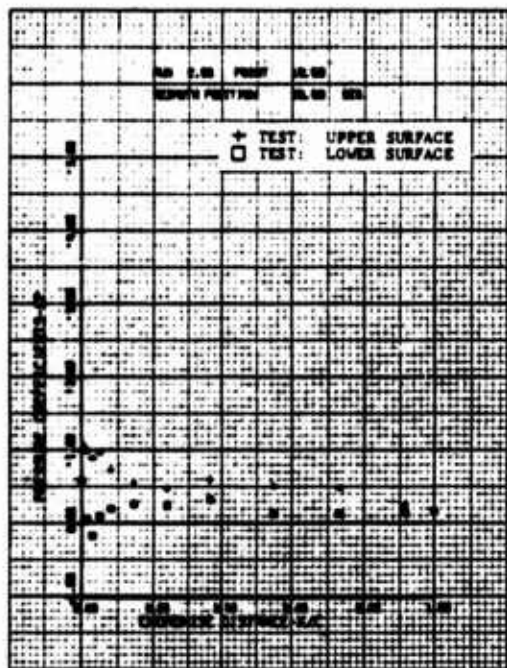


(k)  $\psi = 330^\circ$

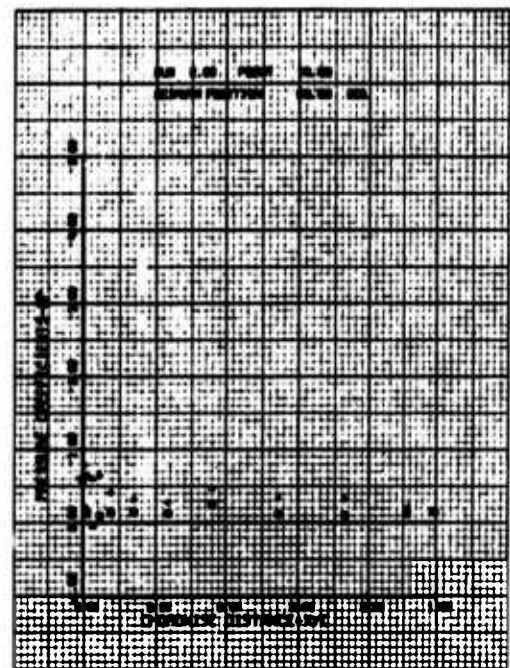


(l)  $\psi = 360^\circ$

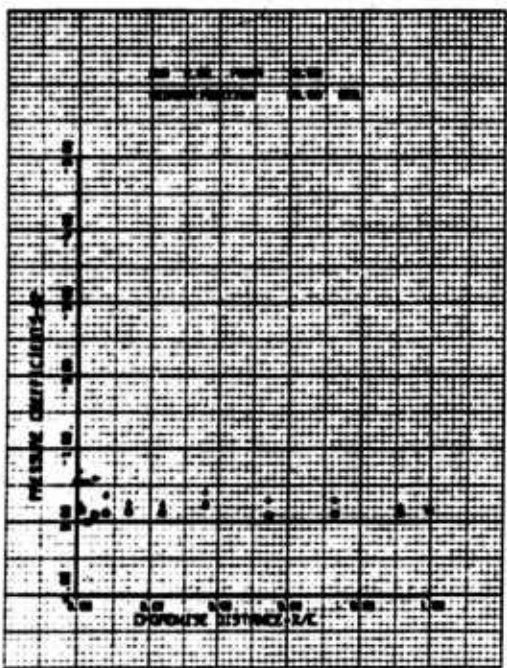
Figure 43. Concluded.



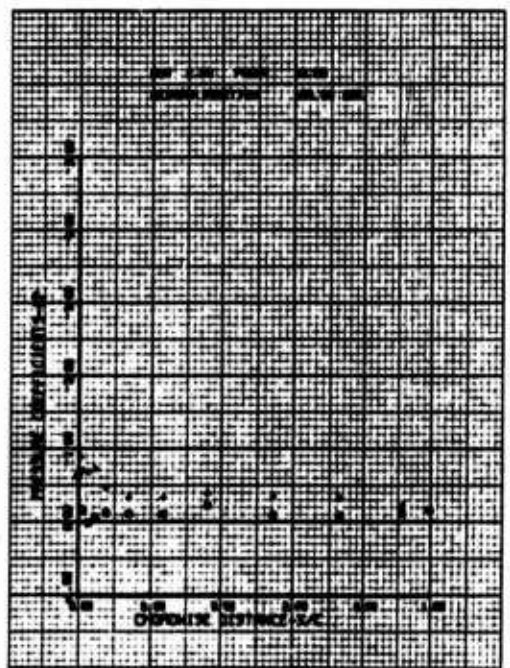
(a)  $\psi = 30^\circ$



(b)  $\psi = 60^\circ$

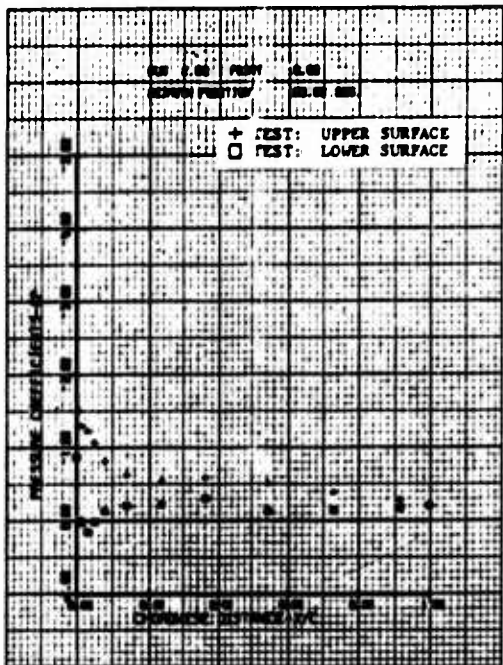


(c)  $\psi = 90^\circ$

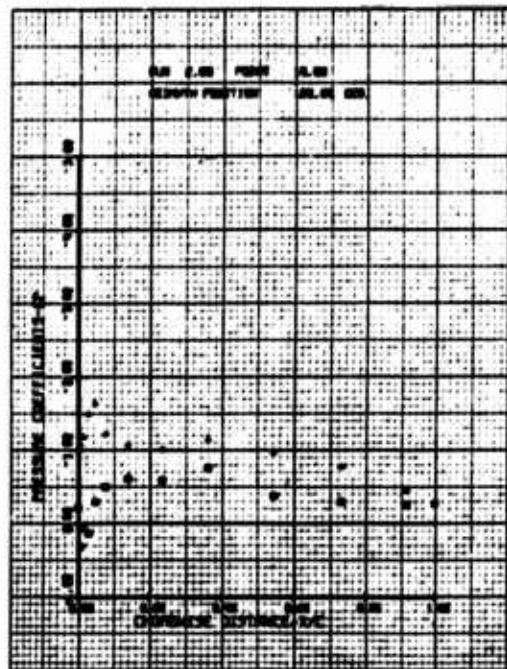


(d)  $\psi = 120^\circ$

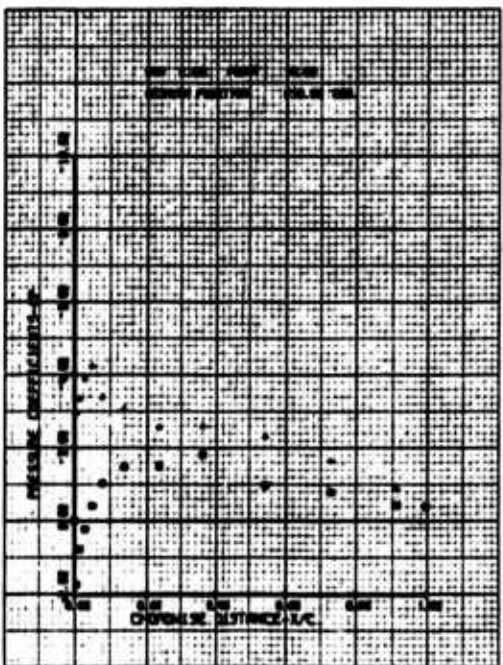
Figure 44. Chordwise Pressure Distribution (Run 2, Point 10);  
 $\mu = 0.40$ ,  $M_{(1.0, 90)} = 0.34$ ,  $\theta_{.75R} = 3.1^\circ$ ,  
 $\dot{\theta} \approx \ddot{\theta} \approx 0$ .



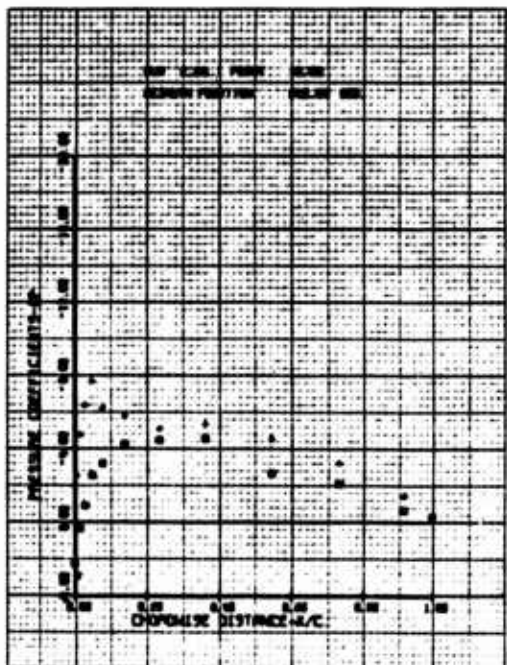
(e)  $\psi = 150^\circ$



(f)  $\psi = 180^\circ$

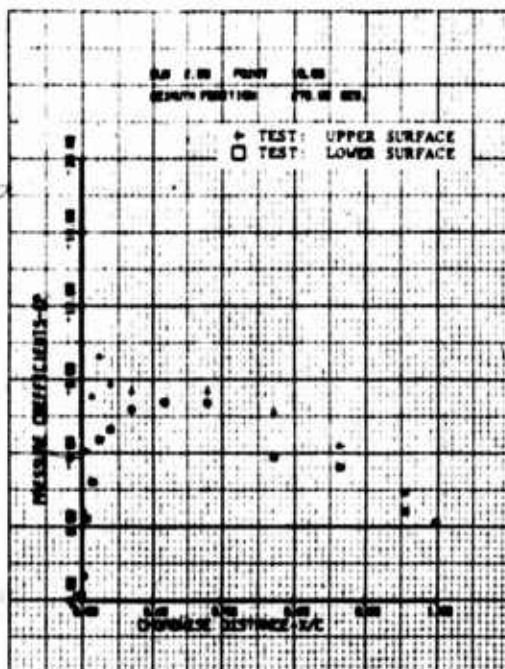


(g)  $\psi = 210^\circ$

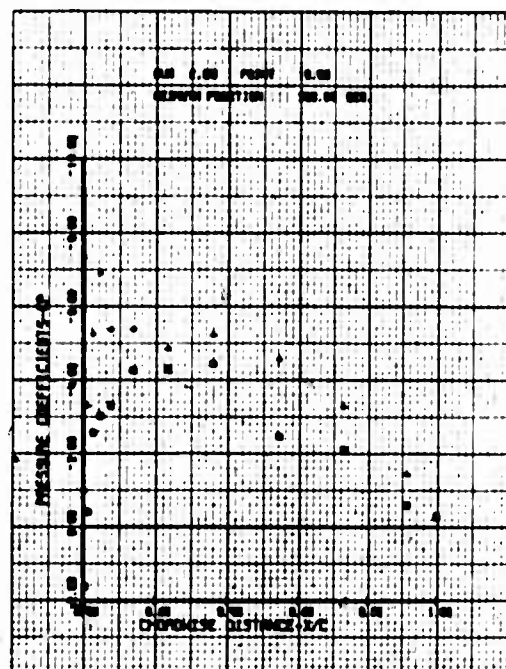


(h)  $\psi = 240^\circ$

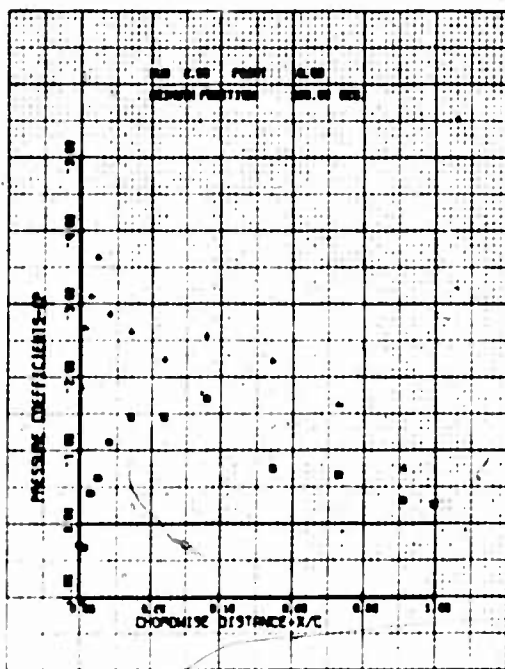
Figure 44. Continued.



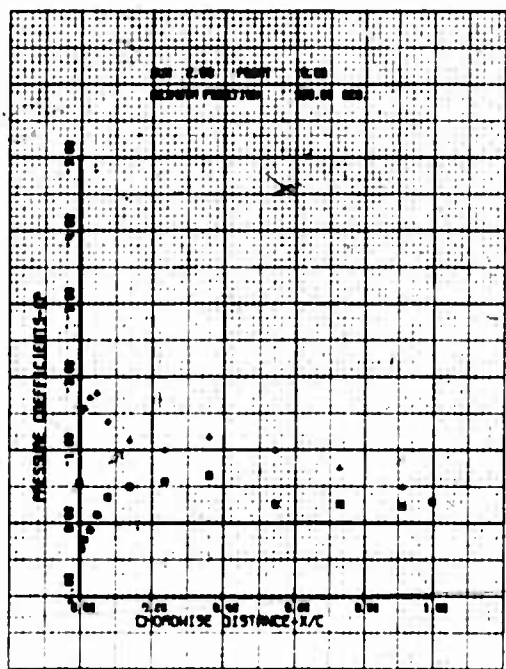
(i)  $\psi = 270^\circ$



(j)  $\psi = 300^\circ$

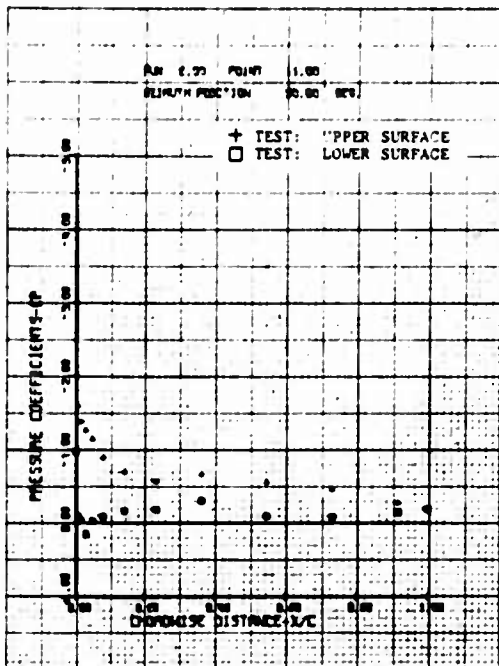


(k)  $\psi = 330^\circ$

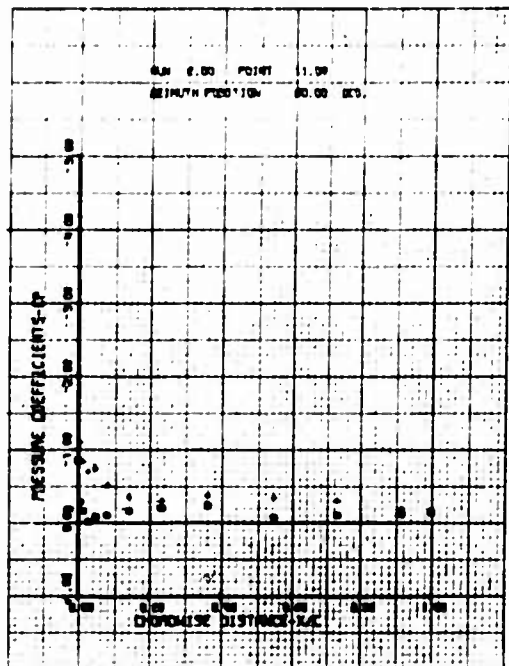


(l)  $\psi = 360^\circ$

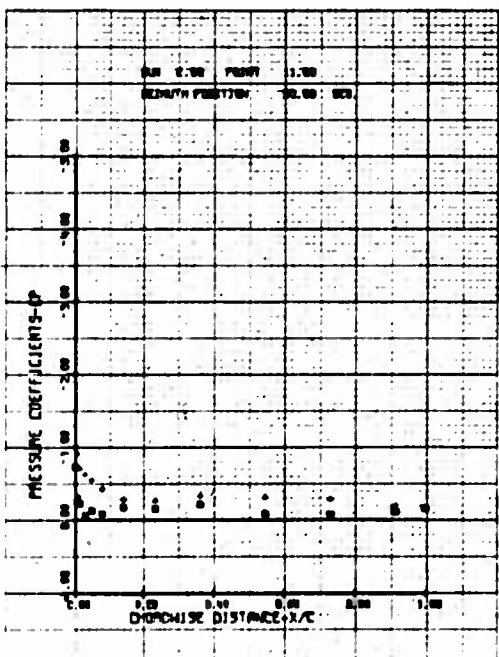
Figure 44. Concluded.



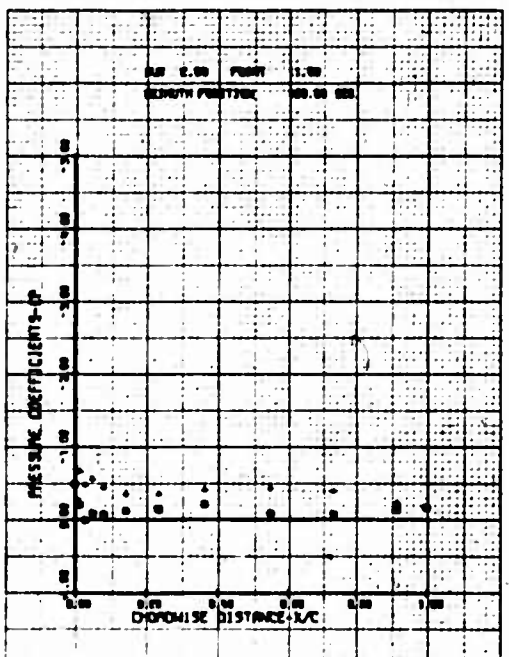
(a)  $\psi = 30^\circ$



(b)  $\psi = 60^\circ$

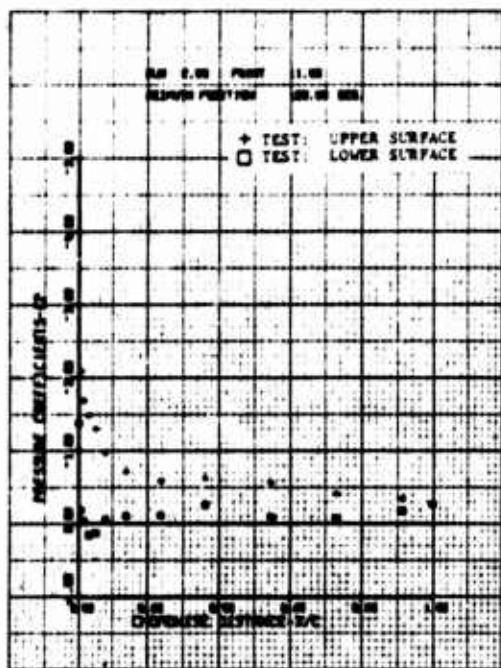


(c)  $\psi = 90^\circ$

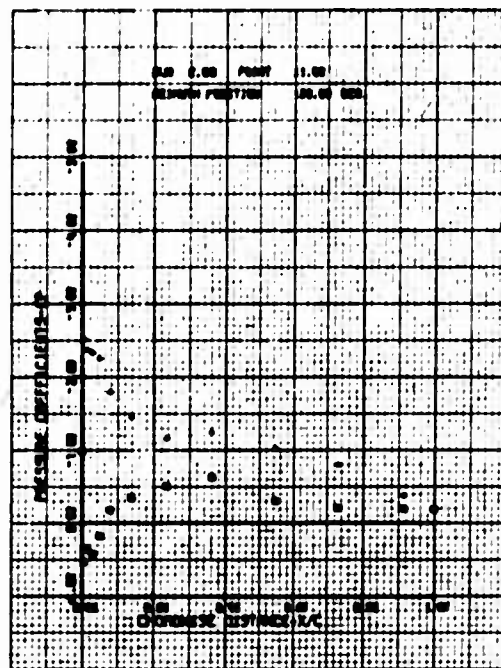


(d)  $\psi = 120^\circ$

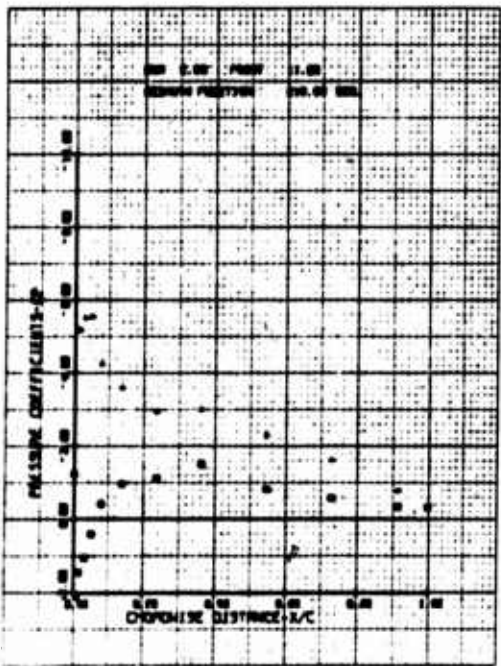
Figure 45. Chordwise Pressure Distribution (Run 2, Point 11);  
 $\mu = 0.40$ ,  $M_{(1.0, 90)} = 0.34$ ,  $\theta_{.75R} = 8.1^\circ$ ,  
 $\dot{\beta} \approx \ddot{\beta} \approx 0$ .



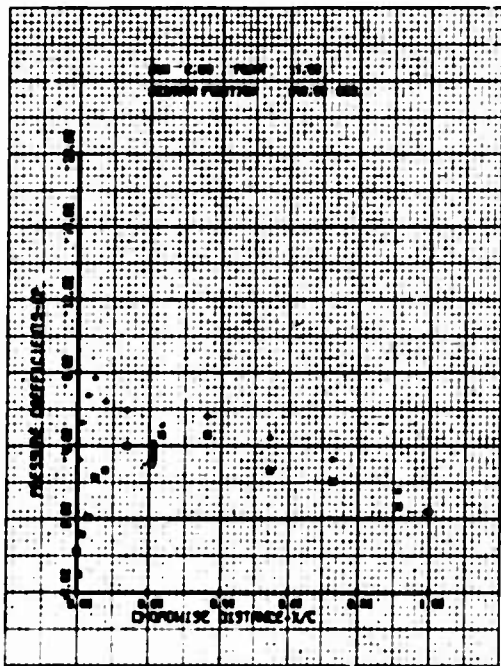
(e)  $\psi = 150^\circ$



(f)  $\psi = 180^\circ$

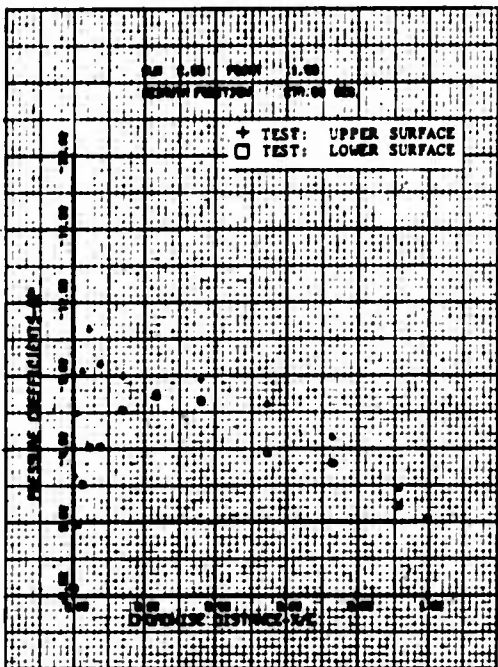


(g)  $\psi = 210^\circ$

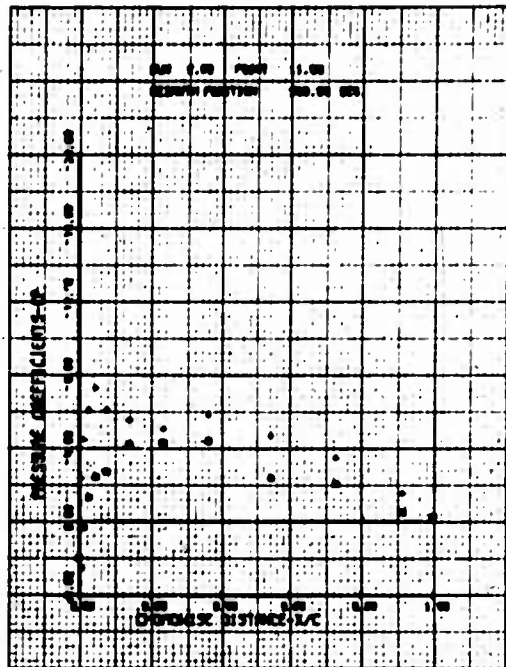


(h)  $\psi = 240^\circ$

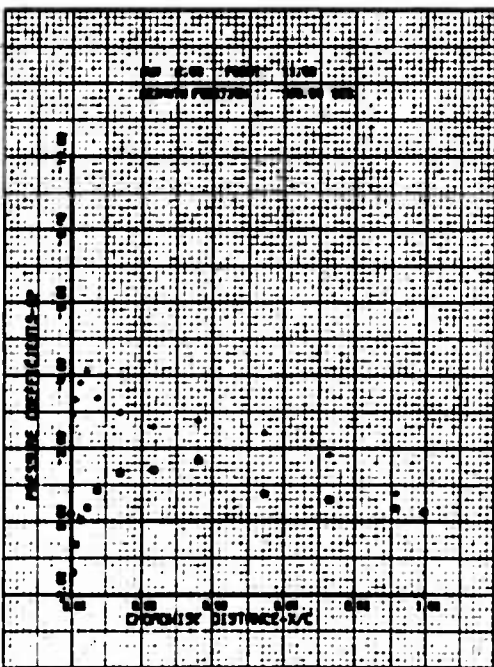
Figure 45. Continued.



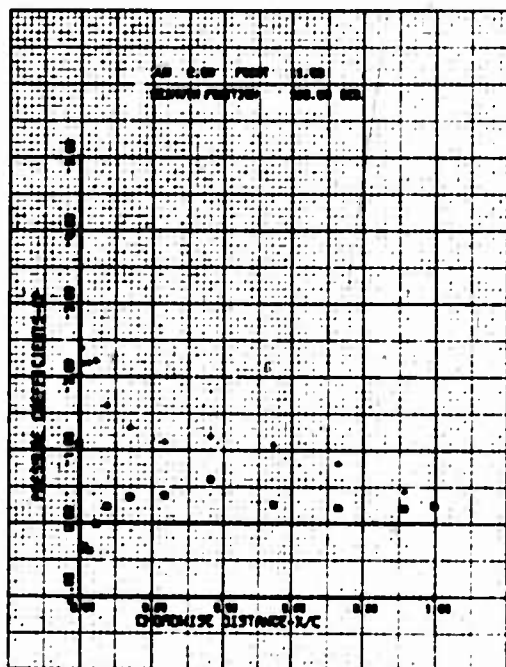
(i)  $\psi = 270^\circ$



(j)  $\psi = 300^\circ$

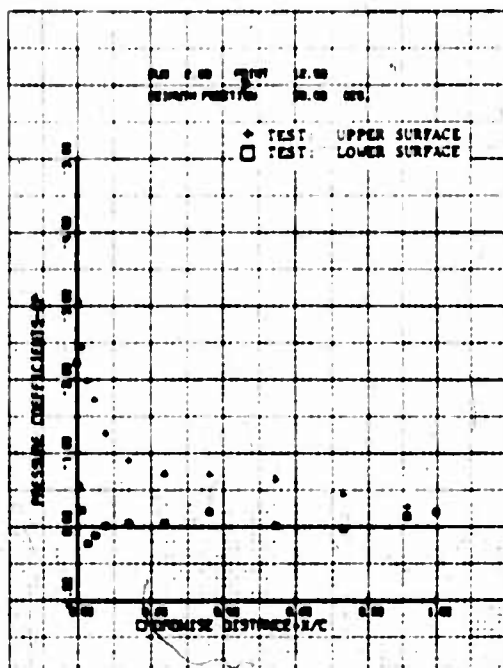


(k)  $\psi = 330^\circ$

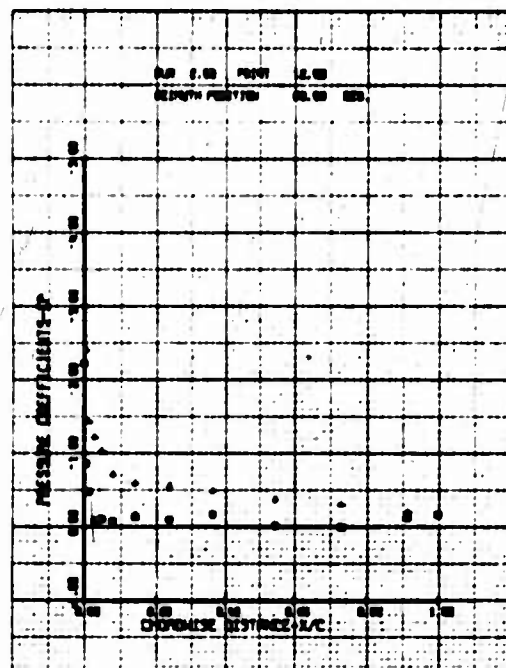


(l)  $\psi = 360^\circ$

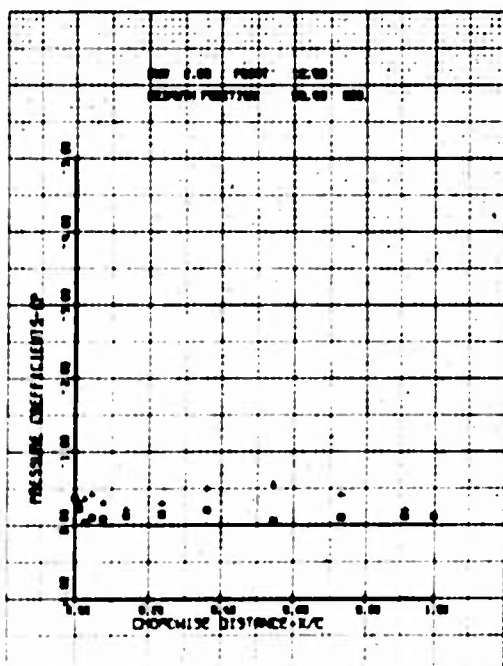
Figure 45. Concluded.



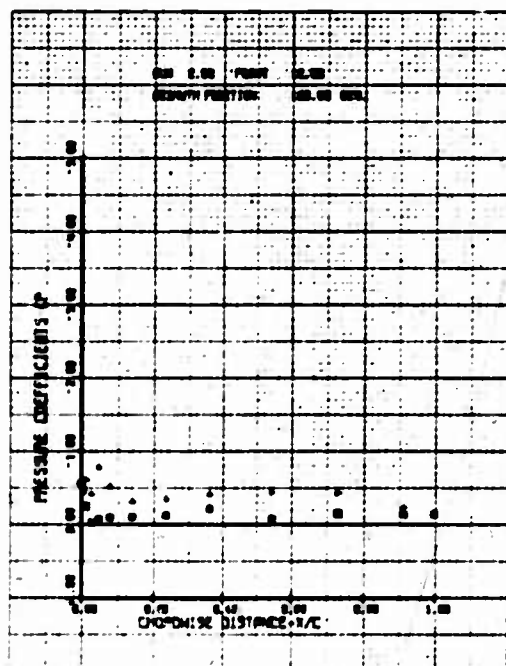
(a)  $\psi = 30^\circ$



(b)  $\psi = 60^\circ$

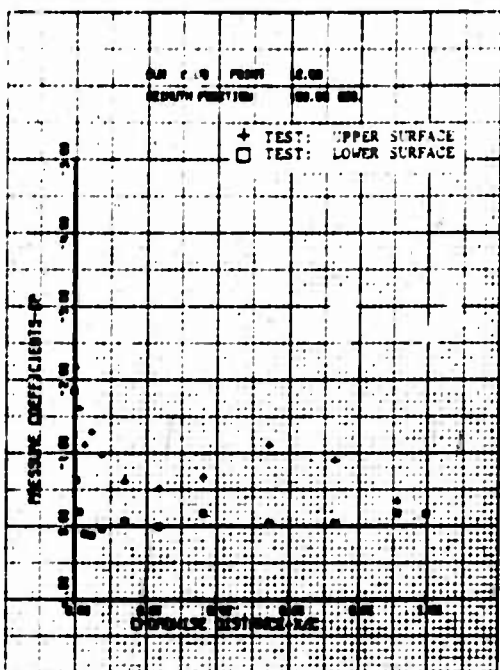


(c)  $\psi = 90^\circ$

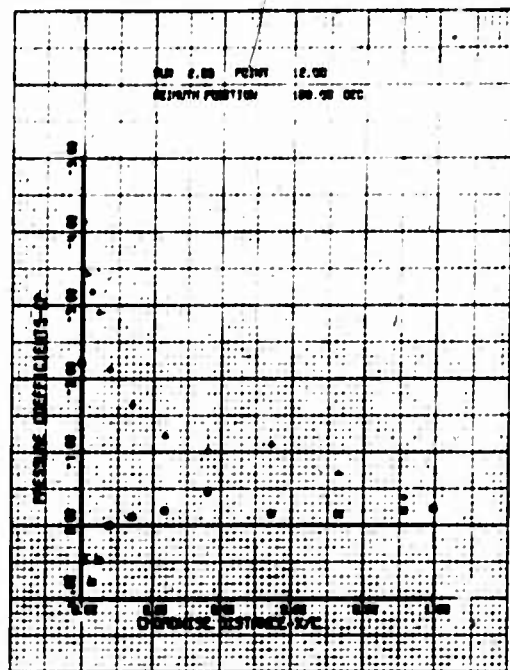


(d)  $\psi = 120^\circ$

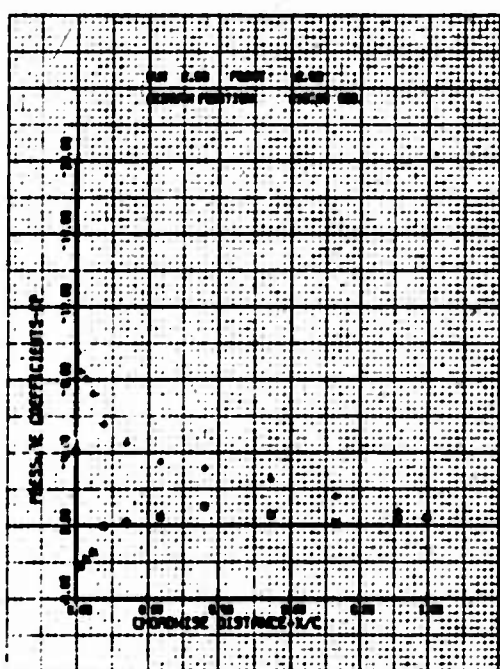
Figure 46. Chordwise Pressure Distribution (Run 2, Point 12);  
 $\mu = 0.40$ ,  $M(1.0, 90) = 0.34$ ,  $\theta_{.75R} = 8.1^\circ$ ,  
 $\dot{\theta} \geq \ddot{\theta} \geq 0$ .



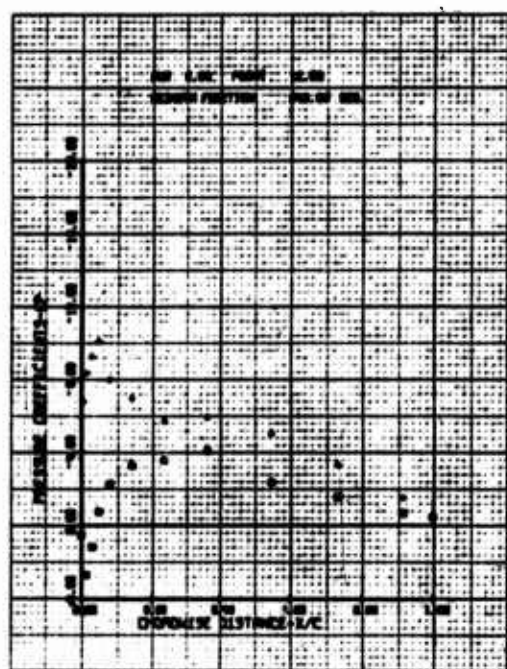
(e)  $\psi = 150^\circ$



(f)  $\psi = 180^\circ$

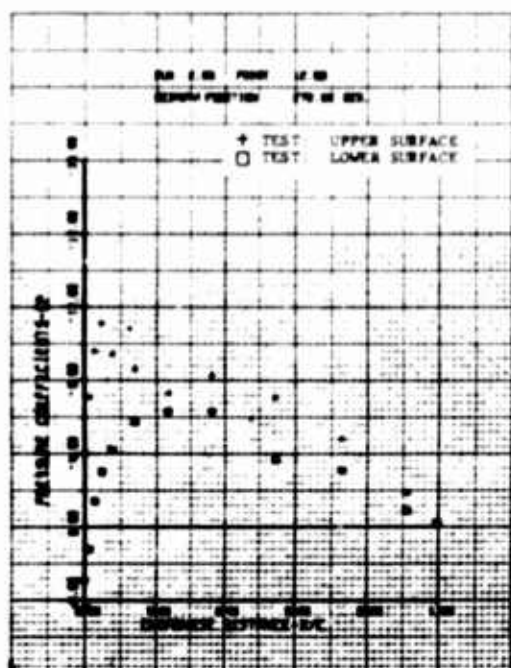


(g)  $\psi = 210^\circ$

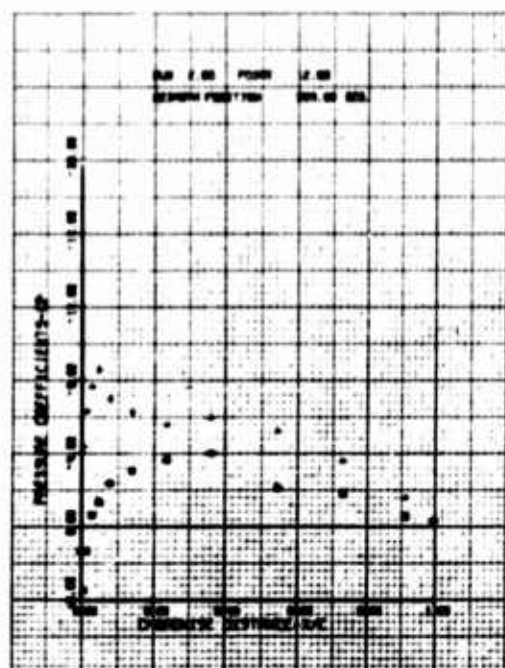


(h)  $\psi = 240^\circ$

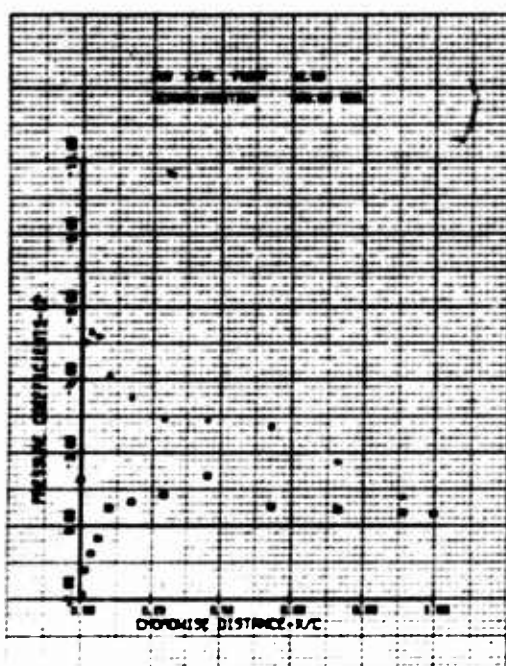
Figure 46. Continued.



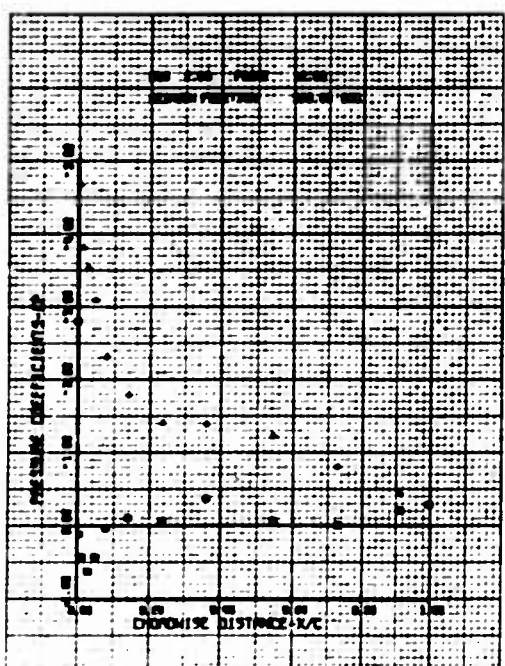
(i)  $\psi = 270^\circ$



(j)  $\psi = 300^\circ$

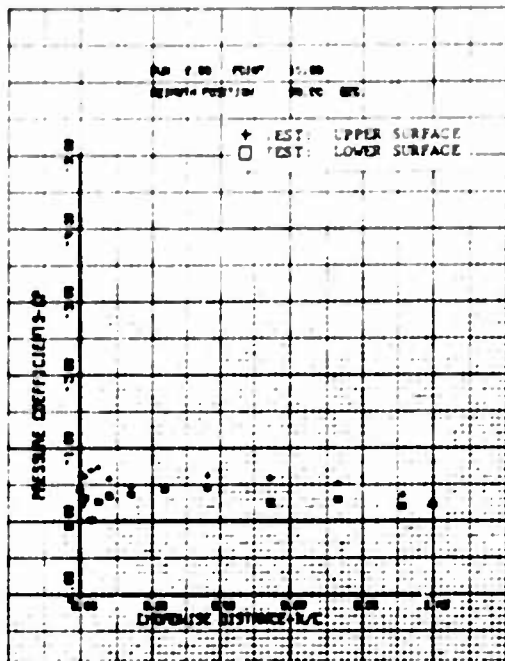


(k)  $\psi = 330^\circ$

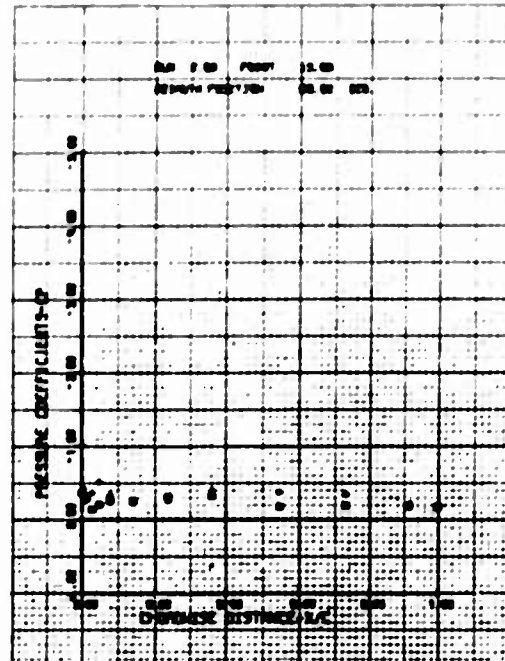


(l)  $\psi = 360^\circ$

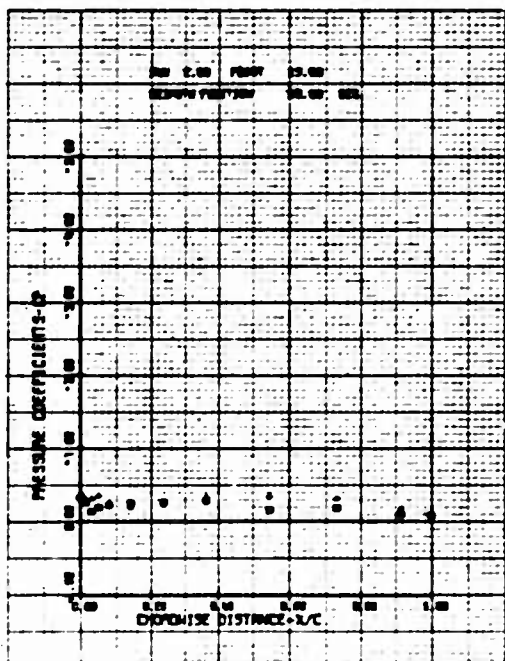
**Figure 46. Concluded.**



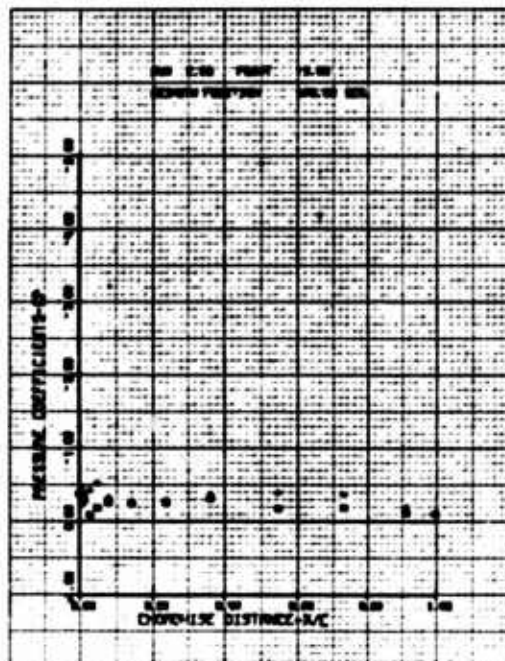
(a)  $\psi = 30^\circ$



(b)  $\psi = 60^\circ$

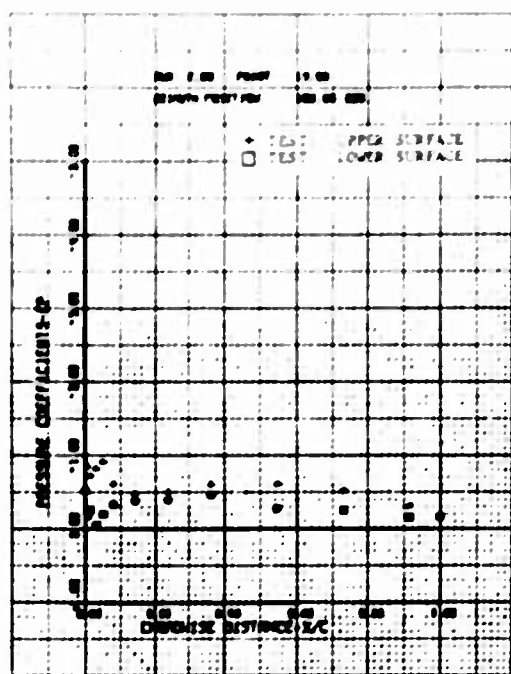


(c)  $\psi = 90^\circ$

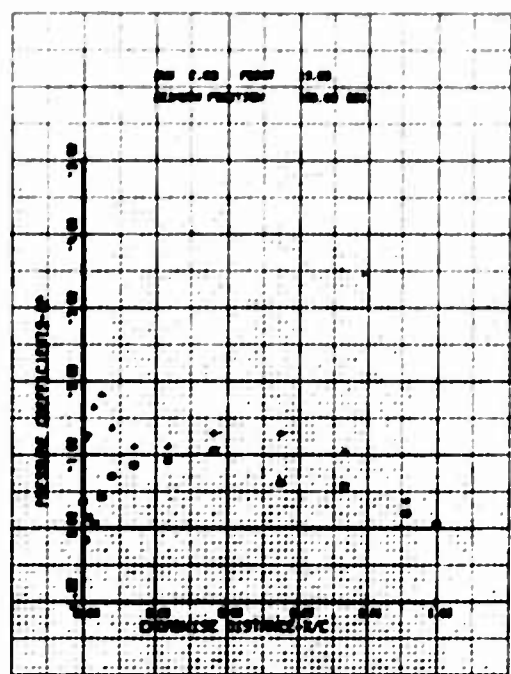


(d)  $\psi = 120^\circ$

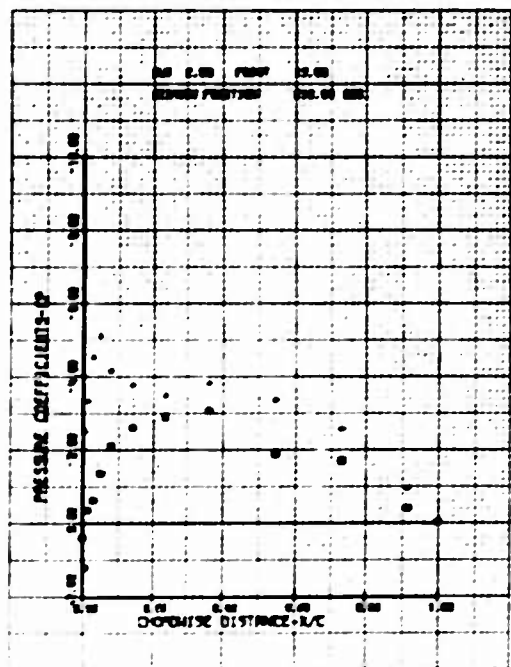
**Figure 47. Chordwise Pressure Distribution (Run 2, Point 13);**  
 $\mu = 0.50$ ,  $M_{(1.0, 90)} = 0.37$ ,  $\theta_{.75R} = 3.1^\circ$ ,  
 $\dot{\beta} \approx \ddot{\beta} \approx 0$ .



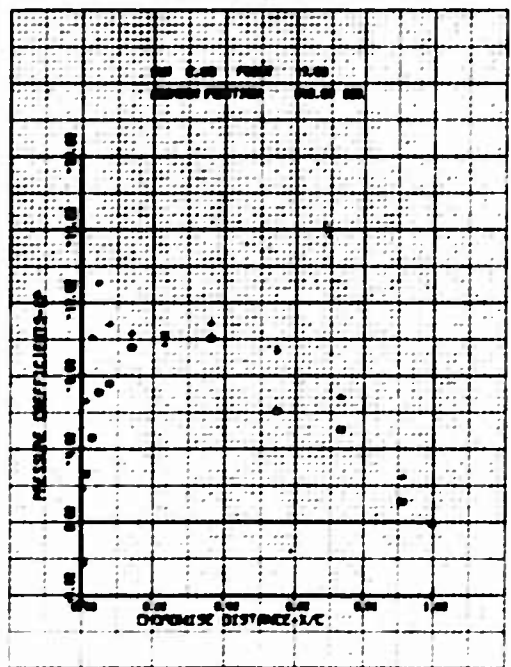
(e)  $\psi = 150^\circ$



(f)  $\psi = 180^\circ$

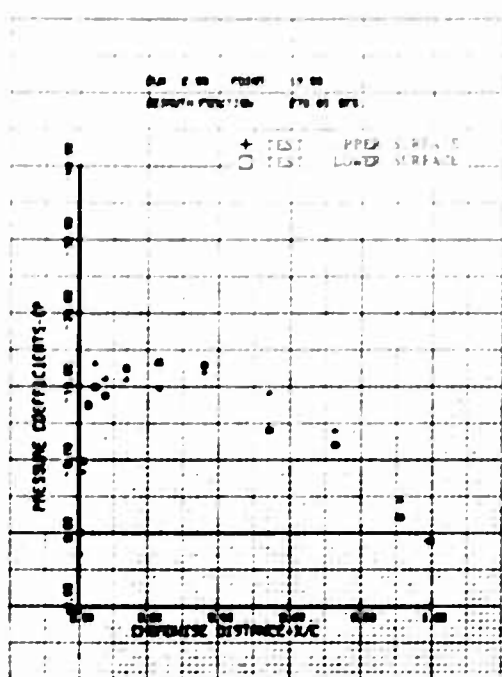


(g)  $\psi = 210^\circ$

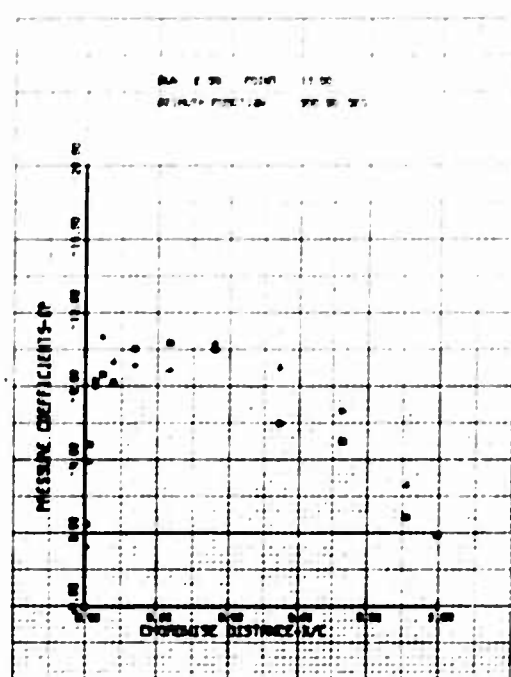


(h)  $\psi = 240^\circ$

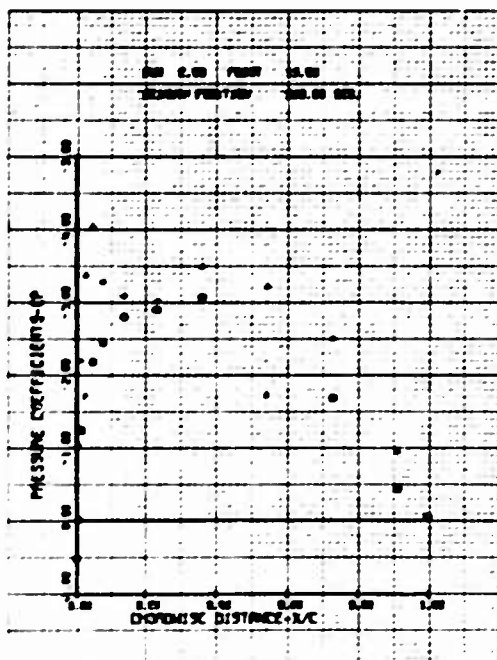
Figure 47. Continued.



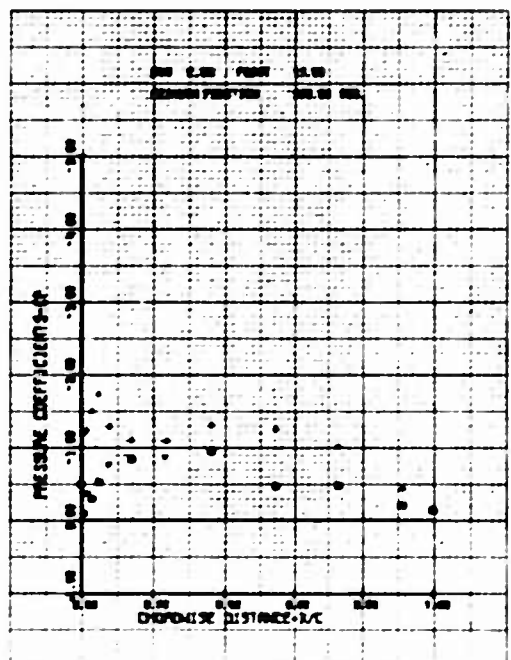
(i)  $\psi = 270^\circ$



(j)  $\psi = 300^\circ$

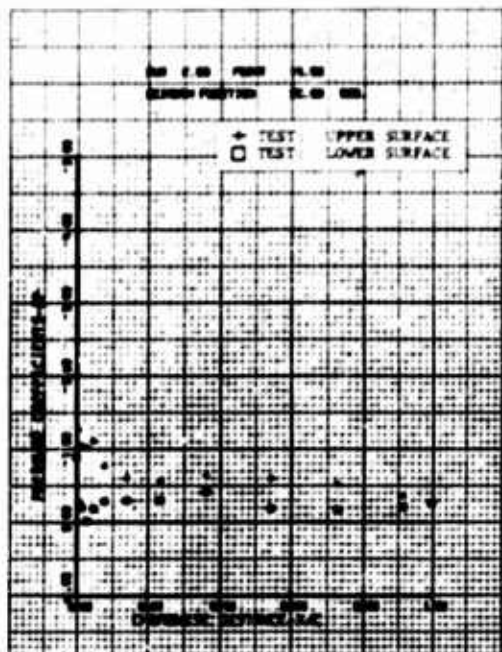


(k)  $\psi = 330^\circ$

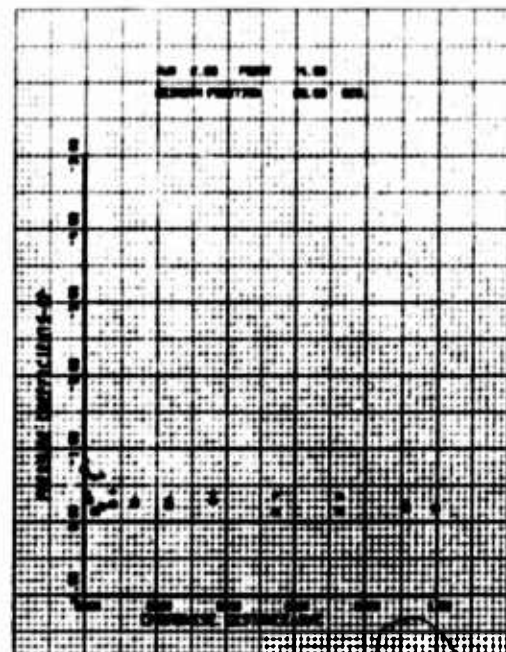


(l)  $\psi = 360^\circ$

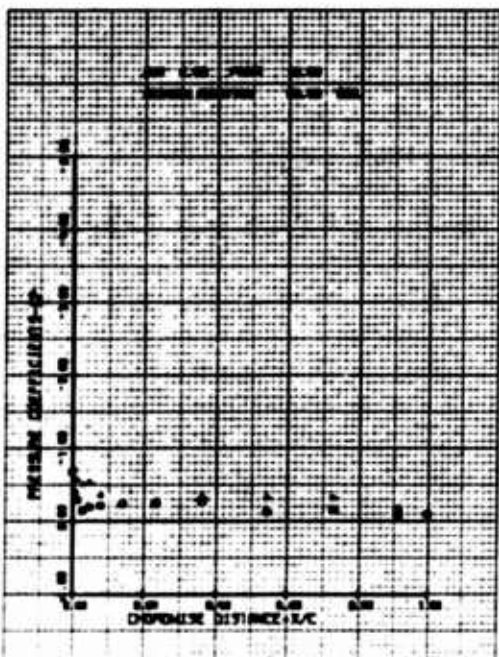
Figure 47. Concluded.



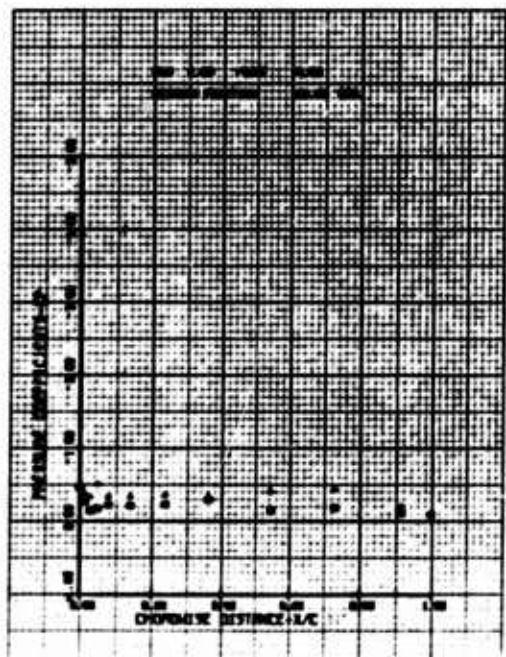
(a)  $\psi = 30^\circ$



(b)  $\psi = 60^\circ$

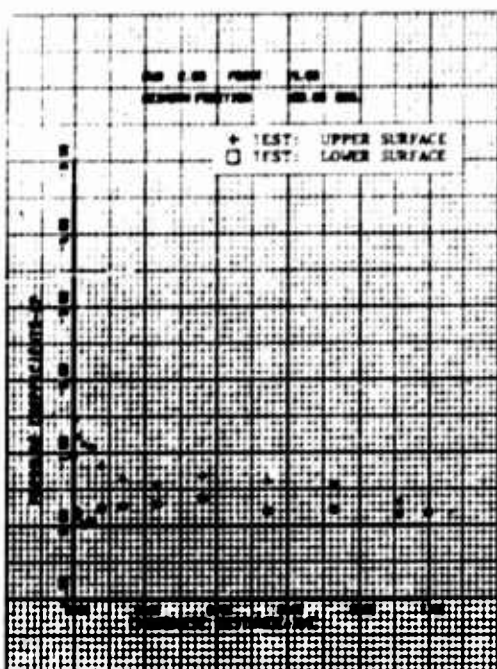


(c)  $\psi = 90^\circ$

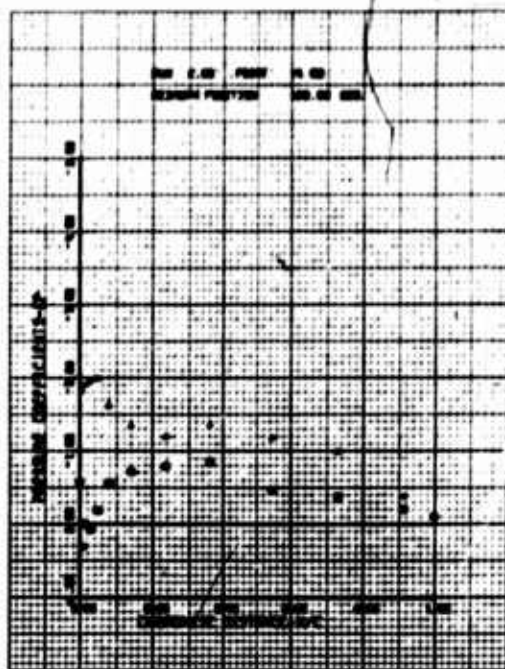


(d)  $\psi = 120^\circ$

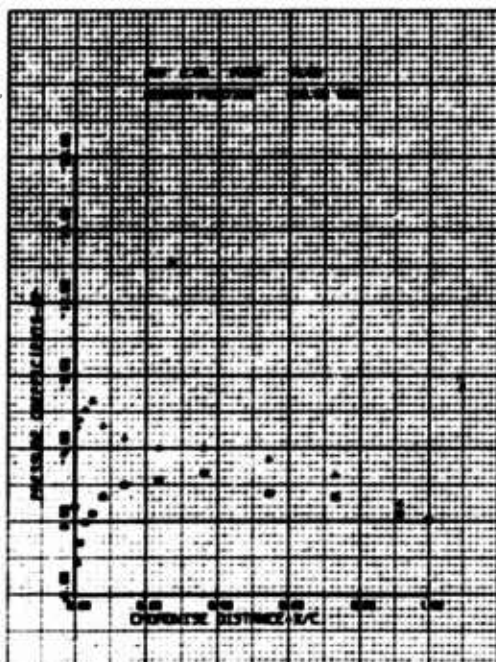
Figure 48. Chordwise Pressure Distribution (Run 2, Point 14);  
 $\mu = 0.50$ ,  $M_{(1.0, 90)} = 0.37$ ,  $\theta_{.75R} = 3.1^\circ$ ,  
 $\theta \approx \ddot{\theta} \approx 0$ .



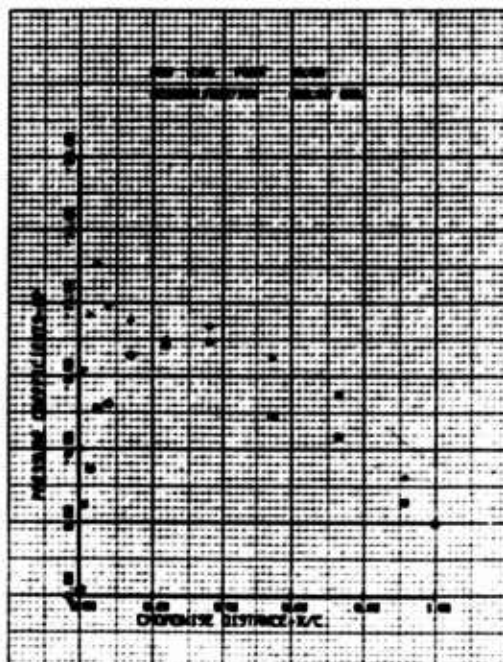
(e)  $\psi = 150^\circ$



(f)  $\psi = 180^\circ$

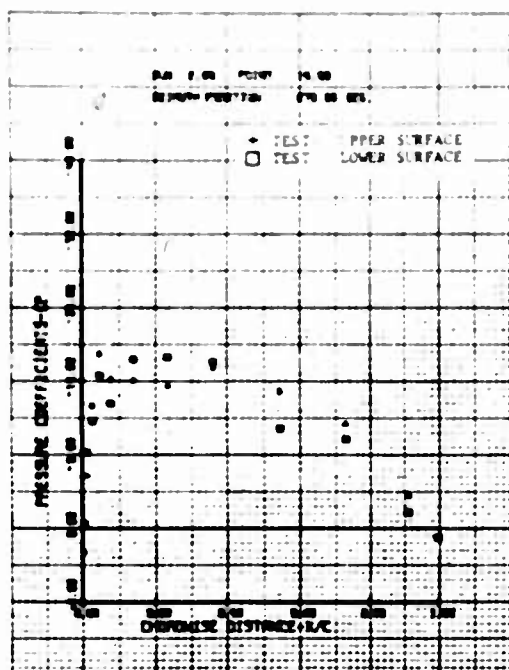


(g)  $\psi = 210^\circ$

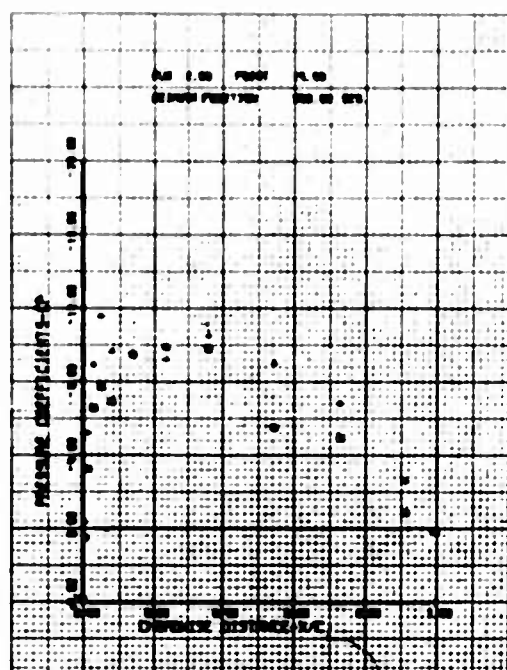


(h)  $\psi = 240^\circ$

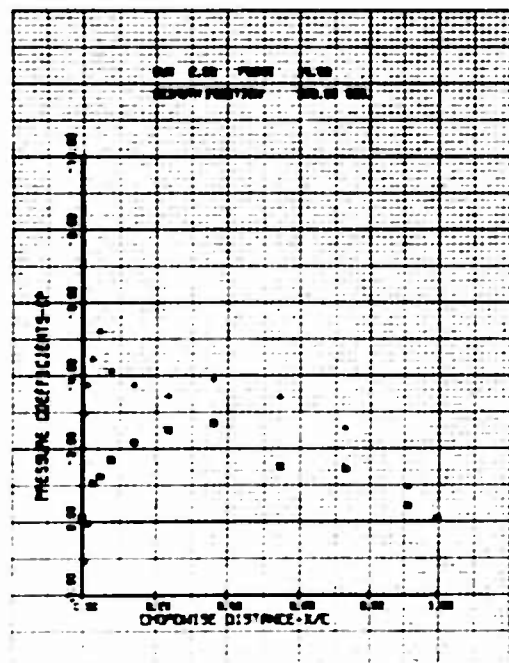
Figure 48. Continued.



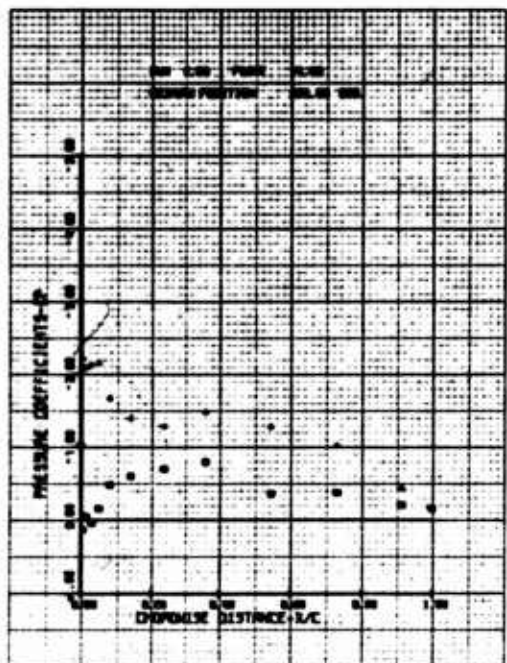
(i)  $\psi = 270^\circ$



(j)  $\psi = 300^\circ$

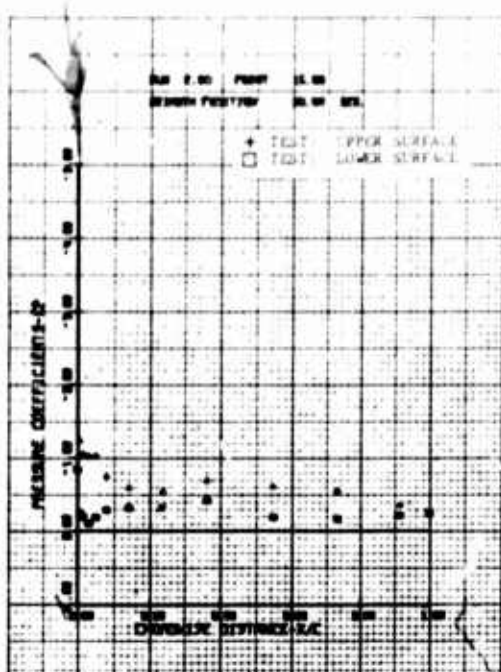


(k)  $\psi = 330^\circ$

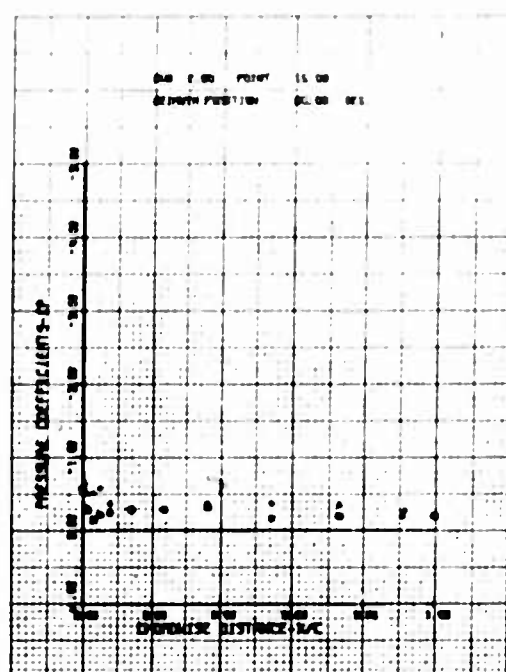


(l)  $\psi = 360^\circ$

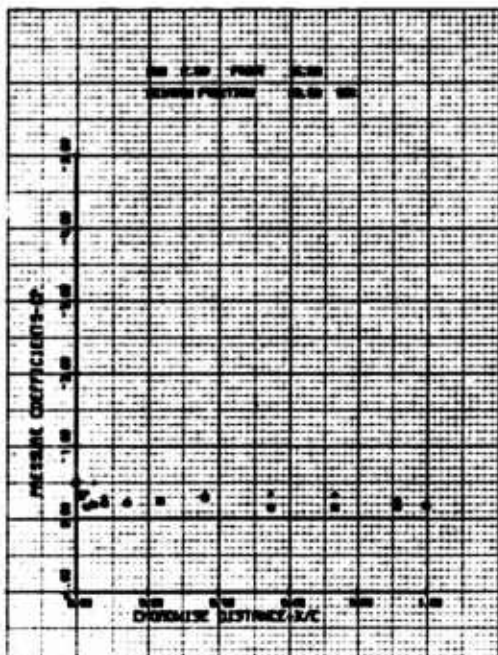
Figure 48. Concluded.



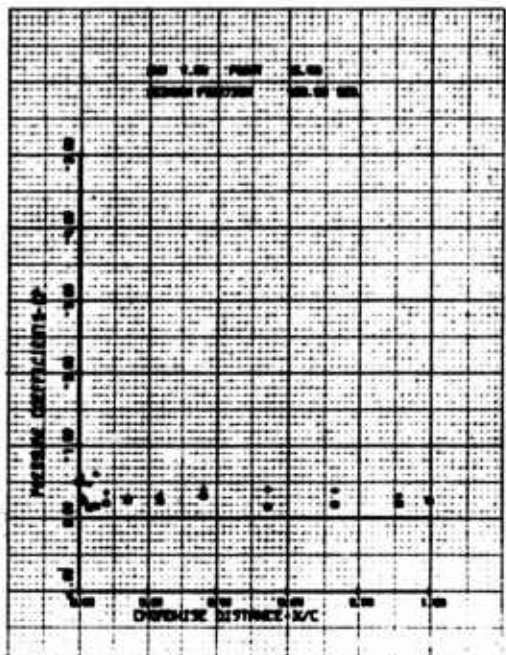
(a)  $\psi = 30^\circ$



(b)  $\psi = 60^\circ$

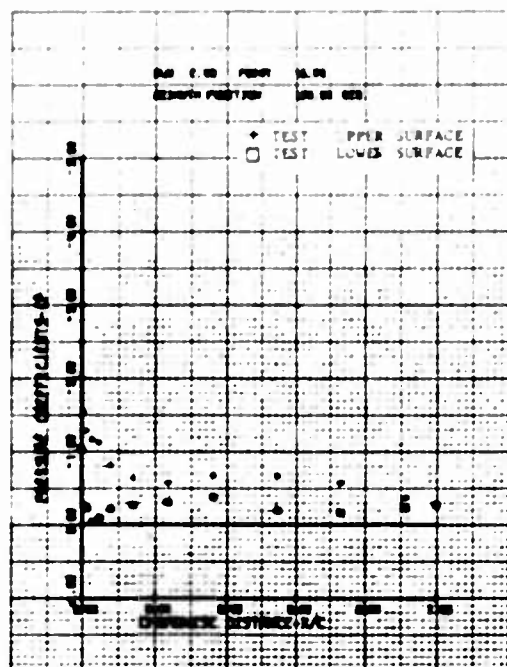


(c)  $\psi = 90^\circ$

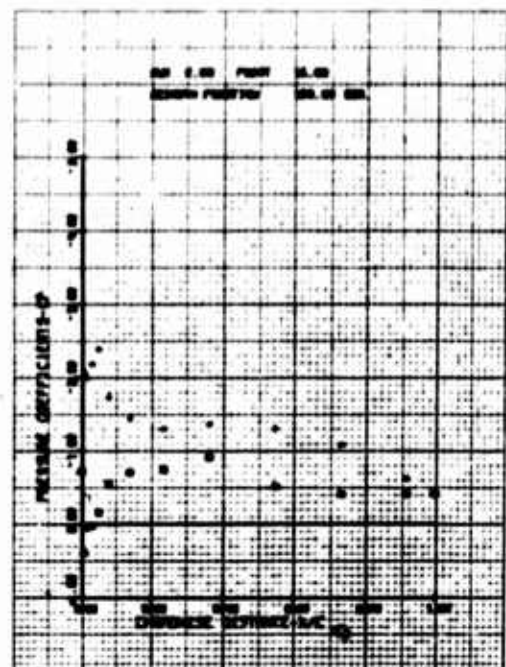


(d)  $\psi = 120^\circ$

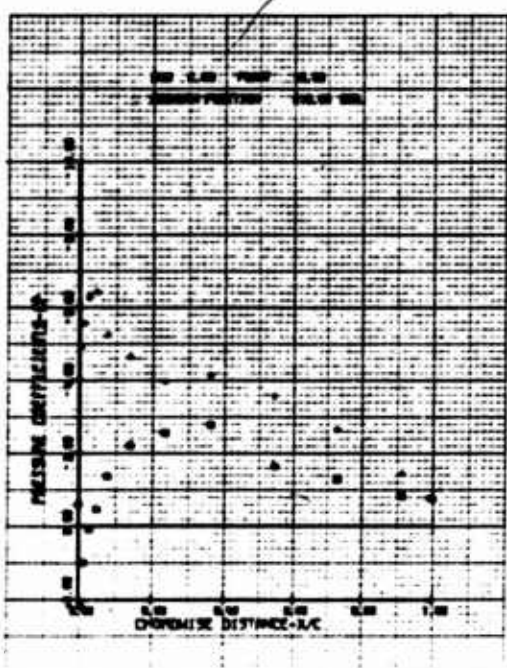
Figure 49. Chordwise Pressure Distribution (Run 2, Point 15);  
 $\mu = 0.50$ ,  $M_{(1.0, 90)} = 0.37$ ,  $\theta_{.75R} = 7.2^\circ$ ,  
 $\dot{\beta} \approx \ddot{\beta} \approx 0$ .



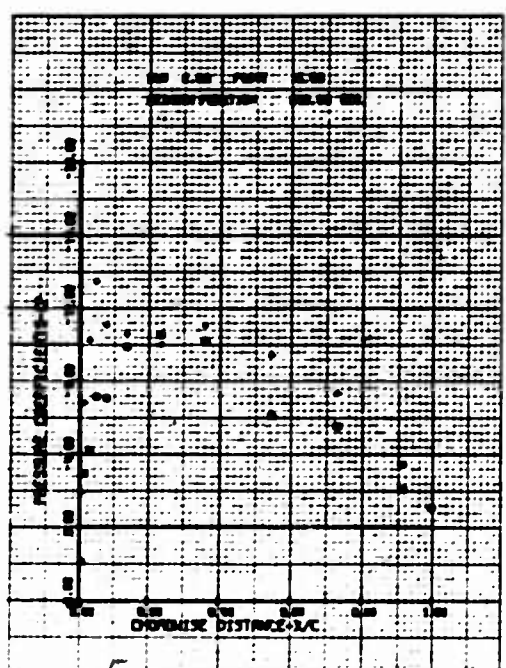
(e)  $\psi = 150^\circ$



(f)  $\psi = 180^\circ$

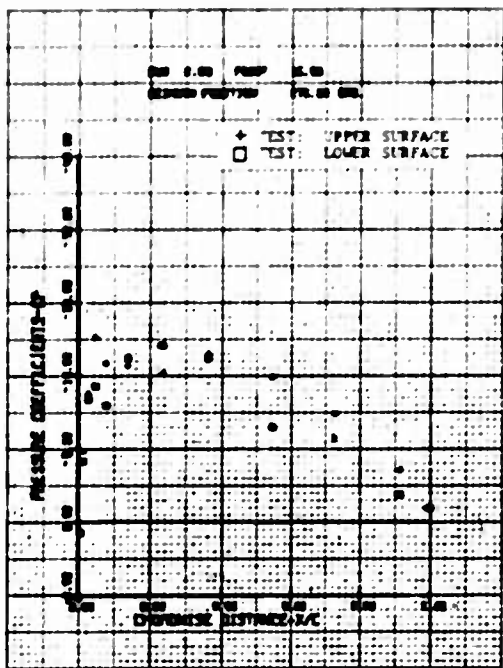


(g)  $\psi = 210^\circ$

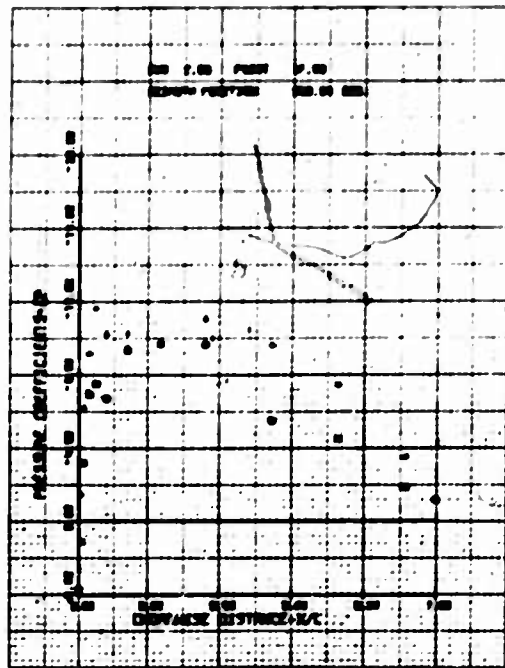


(h)  $\psi = 240^\circ$

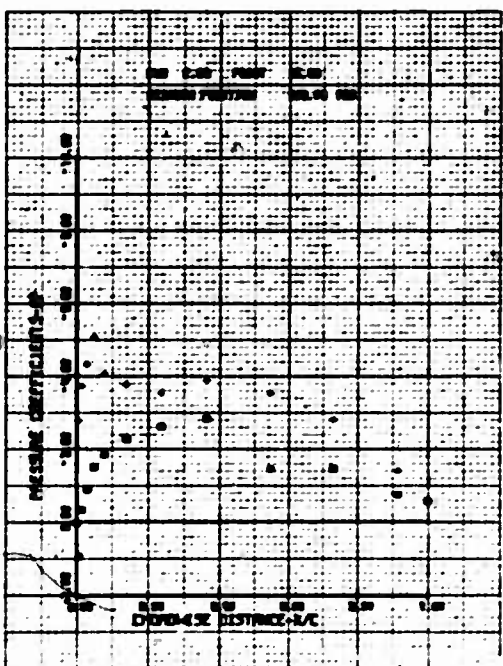
Figure 49. Continued.



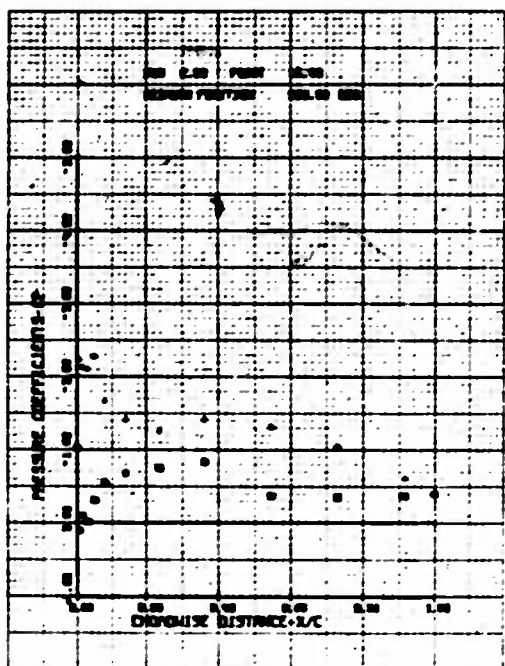
(i)  $\psi = 270^\circ$



(j)  $\psi = 300^\circ$

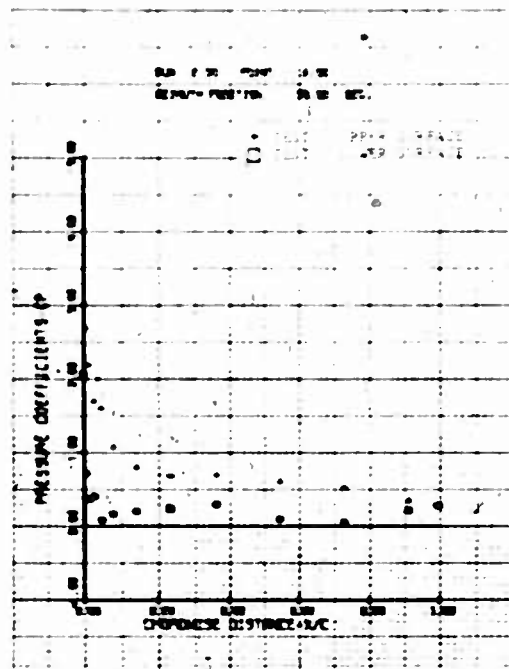


(k)  $\psi = 330^\circ$

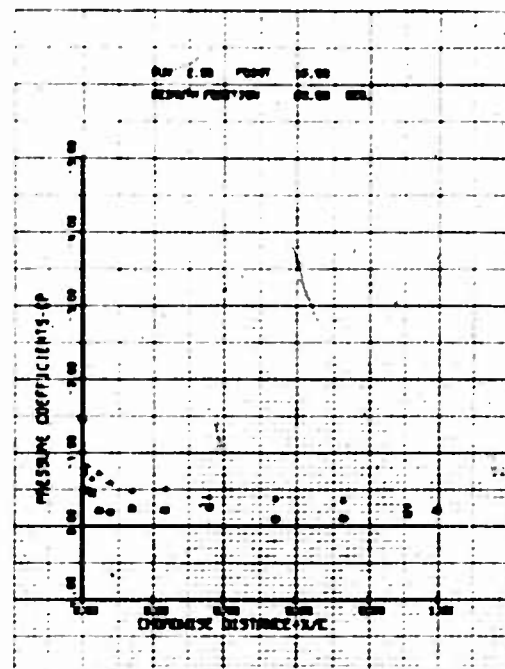


(l)  $\psi = 360^\circ$

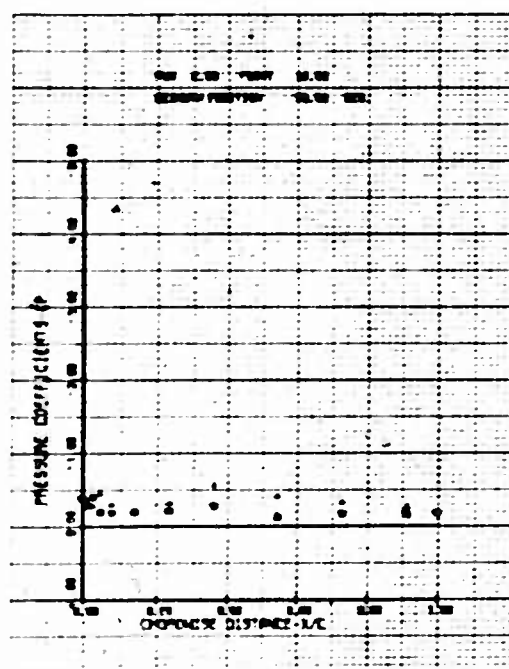
Figure 49. Concluded.



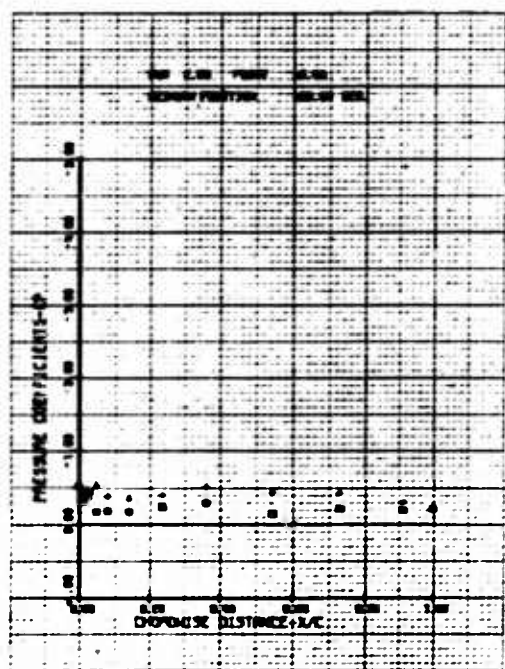
(a)  $\psi = 30^\circ$



(b)  $\psi = 60^\circ$

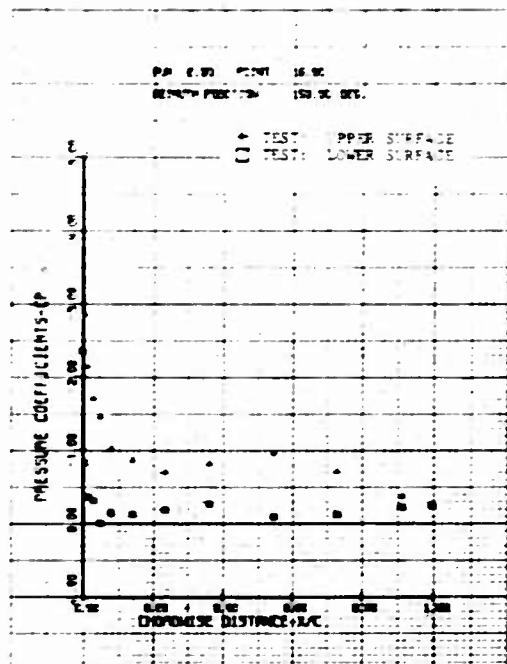


(c)  $\psi = 90^\circ$

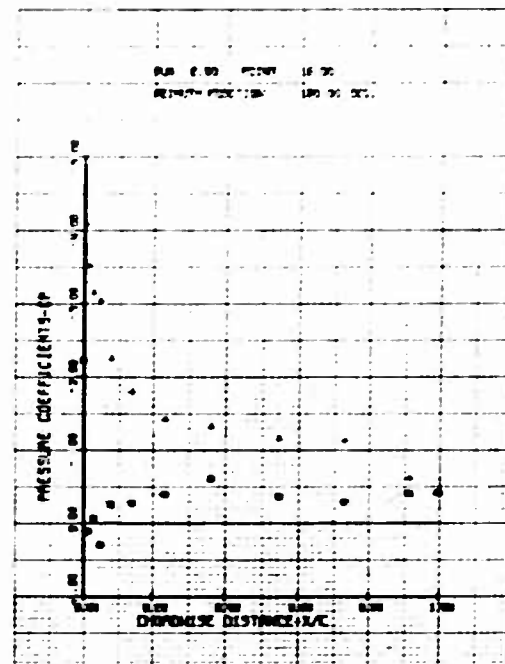


(d)  $\psi = 120^\circ$

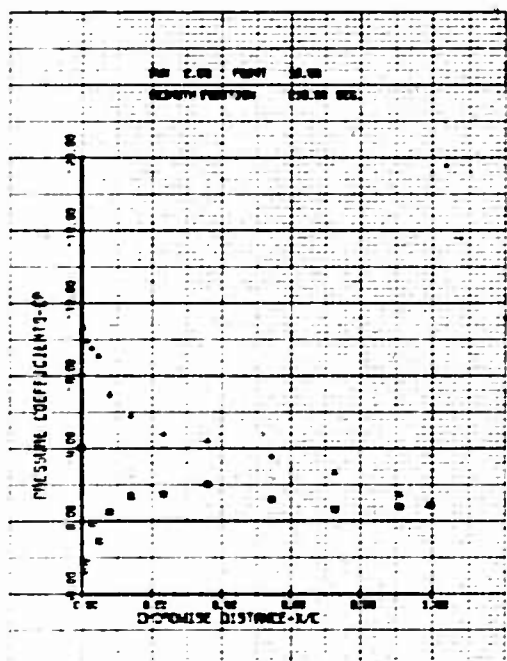
Figure 50. Chordwise Pressure Distribution (Run 2, Point 16);  
 $\mu = 0.50$ ,  $M(1.0, 90) = 0.37$ ,  $\theta_{.75R} = 7.2^\circ$ ,  
 $\dot{\theta} \approx \ddot{\theta} \approx 0$ .



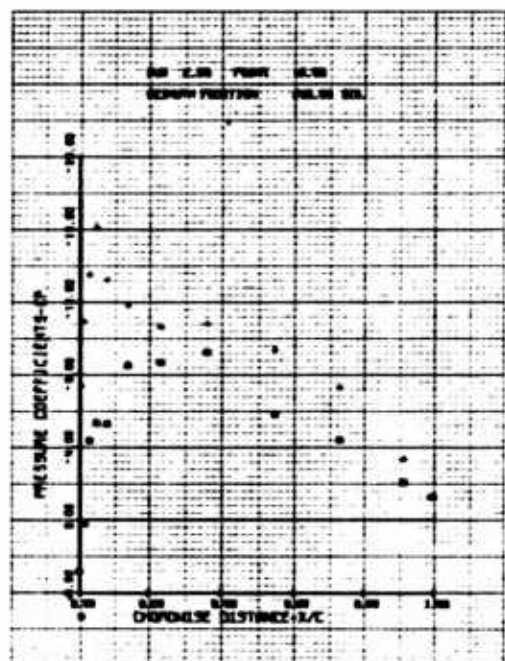
$$(e) \quad \psi = 150^\circ$$



$$(f) \quad \psi = 180^\circ$$

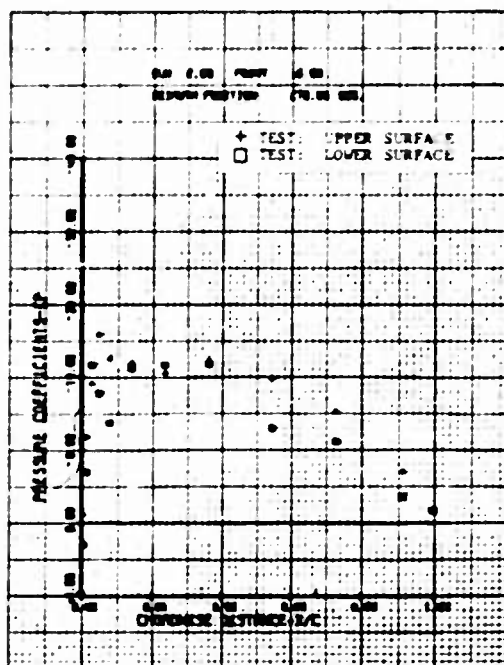


(g)  $\psi = 210^\circ$

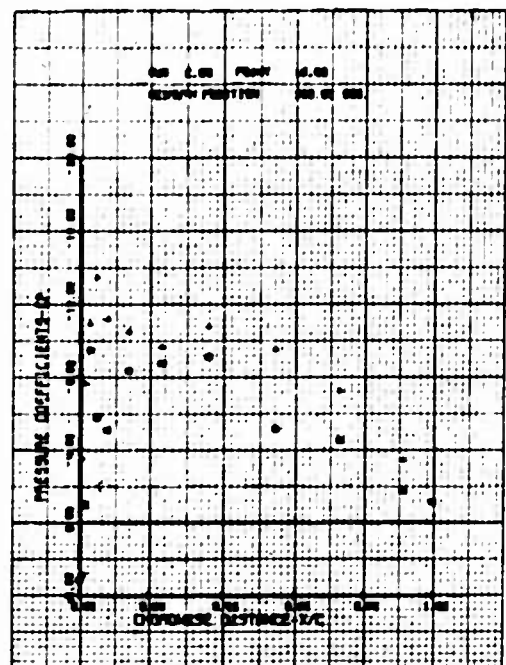


(h)  $\psi = 240^\circ$

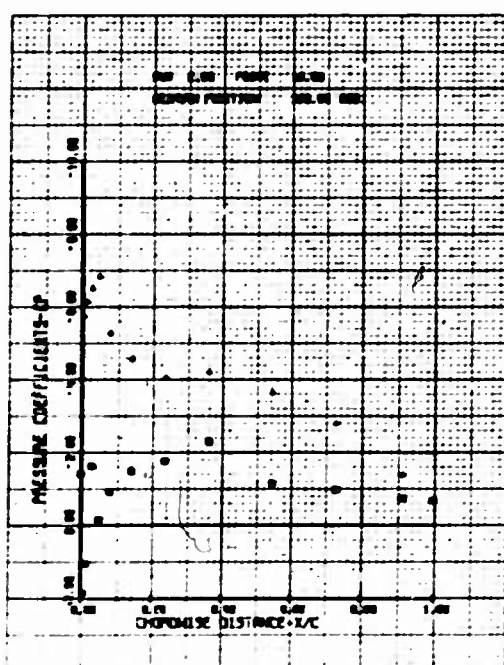
Figure 50. Continued.



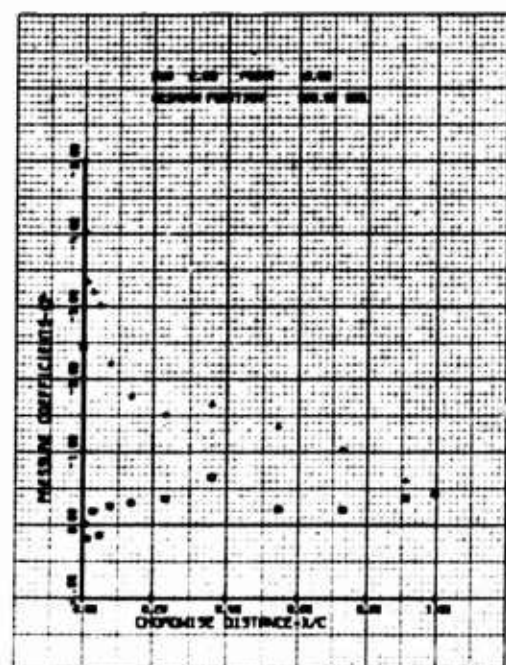
(i)  $\psi = 270^\circ$



(j)  $\psi = 300^\circ$



(k)  $\psi = 330^\circ$



(l)  $\psi = 360^\circ$

Figure 50. Concluded.

Unclassified

Security Classification

DOCUMENT CONTROL DATA - R & D

(Security classification of title, body of abstract and indexing annotation must be entered when the overall report is classified)

1. ORIGINATING ACTIVITY (Corporate author) Bell Helicopter Company Fort Worth, Texas		2a. REPORT SECURITY CLASSIFICATION Unclassified
2b. GROUP		
3. REPORT TITLE A Wind-Tunnel Investigation of the Aerodynamic Environment of a Full-Scale Helicopter Rotor in Forward Flight		
4. DESCRIPTIVE NOTES (Type of report and inclusive dates) Final		
5. AUTHOR(S) (First name, middle initial, last name) Thomas H. Bowden Gerald A. Shockey		
6. REPORT DATE July 1970	7a. TOTAL NO. OF PAGES 138	7b. NO. OF REPS 14
8a. CONTRACT OR GRANT NO. DAAJ02-69-C-0031 <i>me 64</i>	8b. ORIGINATOR'S REPORT NUMBER(S) USAABLabs Technical Report 70-35	
8d. PROJECT NO. IF162204A13903	9d. OTHER REPORT NO(S) (Any other numbers that may be assigned this report) BHC Report 576-099-054	
10. DISTRIBUTION STATEMENT This document is subject to special export controls, and each transmittal to foreign governments or foreign nationals may be made only with prior approval of U.S. Army Aviation Materiel Laboratories, Fort Eustis, Virginia 23604.		
11. SUPPLEMENTARY NOTES	12. SPONSORING MILITARY ACTIVITY U. S. Army Aviation Materiel Laboratories, Fort Eustis, Va.	
13. ABSTRACT An investigation of the aerodynamic environment of a low-twist, 34-foot-diameter helicopter rotor in forward flight was conducted in the NASA-Ames 40- by 80-foot wind tunnel. Forward-flight data obtained were: (1) angle of attack; (2) radial flow magnitude and direction; (3) chordwise absolute pressure distributions with corresponding chord forces, normal forces, and quarter chord pitching moments; (4) stall; and (5) unsteady effects. Continuous data were taken at a single blade station, 75 percent radius, for advance ratios of 0.20, 0.30, 0.40, and 0.50. A constant rpm of 160 and a constant shaft angle of 0 degrees were maintained. This test yielded some very unusual results, especially in the pressure distribution data. Of these, the more significant results were pressure coefficients greater than +1, and large negative pressure coefficients on both the upper and lower airfoil surfaces. The angle-of-attack and radial flow results are much more conventional and are in good agreement with theory. The agreement for all data taken is especially good on the advancing blade. This is because the wake influence is less prominent than it is on the retreating blade, and the oscillating velocities on the advancing blade are much less than the freestream velocity.		

DD FORM 1473

REPLACES DD FORM 1473, 1 JAN 64, WHICH IS  
OBSOLETE FOR ARMY USE.

Unclassified

Unclassified

Security Classification

16. KEY WORDS	LINK A		LINK B		LINK C	
	ROLE	WT	ROLE	WT	ROLE	WT
Rotor aerodynamic environment forward flight symmetrical airfoil section angle-of-attack pressure distributions force coefficients radial flow magnitude and direction						

Unclassified

Security Classification